Designing metal oxides for visible light induced photocatalysis by metal doping and graphene oxide mixing: Experimental and DFT studies

Thesis submitted in partial fulfillment

for the Award of Degree

Doctor of Philosophy

by

Sujeet Kumar Pandey

Rajiv Gandhi Institute of Petroleum Technology

Jais-229304

20CE0012 **2025**

CERTIFICATE

It is certified that the work contained in the thesis titled ***"Designing metal oxides for visible light induced photocatalysis by metal doping and graphene oxide mixing: Experimental and DFT studies"*** *has* been carried out under my supervision and that this work has not been submitted elsewhere for a degree.

It is further certified that the student has fulfilled all the requirements of Comprehensive, Candidacy, and SOTA.

Prof. Amit Ranjan

(Supervisor)

DECLARATION BY THE CANDIDATE

I, ***Sujeet Kumar Pandey***, certify that the work embodied in this thesis is my own bonafide work and was carried out by me under the supervision of ***Prof. Amit Ranjan*** from ***August 2020*** to ***December 2025***, at the *Department of Chemical and Biochemical Engineering,* Rajiv Gandhi Institute of Petroleum Technology, Jais. The matter embodied in this thesis has not been submitted for the award of any other degree. I declare that I have faithfully acknowledged and given credits to the research workers wherever their works have been cited in my work in this thesis. I further declare that I have not wilfully copied any other's work, paragraphs, text, data, results, etc., reported in journals, books, magazines, reports, dissertations, theses, etc., or available on websites and have not included them in this thesis and have not cited as my work.

Date:

Place: RGIPT, Jais, Amethi **Sujeet Kumar Pandey**

CERTIFICATE BY THE SUPERVISOR

It is certified that the above statement made by the student is correct to the best of my knowledge.

Prof. Amit Rajan

(Supervisor) Signature & Seal of Head of Department

CERTIFICATE

CERTIFIED that the work contained in the thesis titled **"*Designing metal oxides for visible light induced photocatalysis by metal doping and graphene oxide mixing: Experimental and DFT studies*"** by **Mr. Sujeet Kumar Pandey** has been carried out under my supervision. It is also certified that he fulfilled the mandatory requirement of TWO quality publications that arose out of his thesis work.

It is further certified that the two publications (copies enclosed) of the aforesaid **Mr. Sujeet Kumar Pandey** have been published in the Journals indexed by –

(a) SCI

(b) SCI Extended

(c) SCOPUS

Prof. Amit Rajan

(Supervisor) (Convener, DPGC)

COPYRIGHT TRANSFER CERTIFICATE

Title of the Thesis: Designing metal oxides for visible light induced photocatalysis by metal doping and graphene oxide mixing: Experimental and DFT studies

Name of the Student: Sujeet Kumar Pandey

Copyright Transfer

The undersigned hereby assigns to the Rajiv Gandhi Institute of Petroleum Technology Jais all rights under copyright that may exist in and for the above thesis submitted for the award of the **"DOCTOR OF PHILOSOPHY".**

Date:

Place: RGIPT, Jais, Amethi **Sujeet Kumar Pandey**

Note: However, the author may reproduce or authorize others to reproduce material extracted verbatim from the thesis or derivative of the thesis for the author's personal use provided that the source and the Institute's copyright notice are indicated

Dedicated to my family and teachers….

ACKNOWLEDGMENT

First and foremost, I express my deepest gratitude to the Almighty for granting me strength, wisdom, and perseverance throughout my Ph.D. journey.

I extend my sincere and profound appreciation to my doctoral supervisor, **Prof. Amit Ranjan**, Department of Chemical and Biochemical Engineering (CBE), Rajiv Gandhi Institute of Petroleum Technology (RGIPT), Jais, Amethi, Uttar Pradesh, India, for his unwavering guidance, encouragement, and invaluable support at every stage of my research. His insightful advice, patience, and open-minded approach have profoundly shaped my scientific thinking and research attitude. It has been an immense privilege to work under his supervision. His mentorship has not only made me a better researcher but also a more confident and curious learner. I am deeply thankful for his trust and for allowing me the scientific freedom to explore new ideas.

I would also like to acknowledge my RPEC members, Dr. Vipin Amoli (Department of Energy and Human science) and Dr. Milan Kumar (Department of CBE), for their constructive feedback, encouragement, and valuable suggestions that significantly improved the quality of my research. Their guidance and insightful discussions have left a lasting impression on my academic development. Special thanks to Dr. Deepak Dwivedi for their support.

My sincere thanks to the Director (RGIPT), Prof. A. S. K. Sinha, and the former directors for providing excellent research facilities in the Strength of Materials Laboratory and the Central Research Facility (CRF). I am also grateful for the institutional fellowship that supported my doctoral studies. My heartfelt thanks go to all the teaching and non-teaching staff of RGIPT particularly Anuj ji, Arun ji,

Mahesh ji, and the CCIS and Academic staff for their continuous cooperation and assistance.

I am deeply thankful to my lab colleagues of the Materials Group Dr. Shama Perween, Dr. Somendra Singh, Dr. Yogendra Yadawa and Anil Verma for their kind help, stimulating discussions, and friendship. I also express sincere appreciation to Dr. Maharshi Yadav, Mr. Aash Mohammad, and Mr. Niyamat Ullah Khan for contributing to a lively and collaborative research environment in the lab.

My heartfelt thanks go to my closest friends Amit Kumar Gomey, Suvadeep Panda, Deepak Yadav. Their companionship, humor, and unwavering support made the Ph.D. journey an enjoyable and memorable experience. I also thank my batchmates Mr. Harikeshvar Pandey, Mr. Ajeet Kumar Prajapati, Mr. Rohit Kumar Singh for their friendship and support along this journey. To all my junior colleagues Siddharth Atal, Saurabh Mishra, Sankat Mochan Upadhyay, Ekansh Kumar, Wasim, Arvind, Bhupendra Kumar, Amarendra Uttam, and many others thank you for your camaraderie, encouragement, and support during challenging times.

Above all, I am profoundly indebted to my parents, Sri Lalan Pandey, Smt. Siyamani Devi, and big brother Mr. Manish Pandey whose unconditional love, blessings, and faith have been the foundation of my life. Their encouragement has always given me the courage to pursue my goals with determination.

(Sujeet Kumar Pandey)

PREFACE

This thesis presents a comprehensive investigation into graphene oxide-metal oxide composites and doped metal oxides, aimed at enhancing visible light photocatalytic performance for environmental remediation and energy-relevant applications. The work integrates experimental synthesis, advanced characterization, and density functional theory (DFT) calculations to design materials capable of efficiently degrading organic pollutants such as dyes under visible light irradiation. The research is motivated by the pressing global need for sustainable technologies that can address water contamination and energy challenges by effectively harnessing a larger fraction of the solar spectrum.

The thesis begins by situating nanomaterials and photocatalytic semiconductors within the broader context of environmental remediation and clean energy production. Special emphasis is placed on oxide semiconductors such as ZnO, TiO_2 and NiO and their derivatives, which, despite their chemical stability and abundance, suffer from wide band gaps and rapid charge carrier recombination that restrict their activity mainly to the ultraviolet region. To overcome these intrinsic limitations, the work explores composite formation with graphene oxide, strategic metal and non-metal doping, and defect engineering as routes to extend light absorption into the visible region and improve charge separation.

To achieve these goals, the thesis employs sol-gel, hydrothermal, modified hummers method, plasma treatment, and deep eutectic solvent assisted approaches for the synthesis of nanostructured materials and their composites. These methods enable precise control over phase purity, morphology, surface area, and defect chemistry, which are crucial for photocatalytic performance. A suite of analytical techniques including X-ray diffraction

(XRD), electron microscopy (SEM), X-ray photoelectron spectroscopy (XPS), nitrogen adsorption-desorption (BET), diffuse reflectance spectroscopy (DRS), photoluminescence (PL), electrochemical impedance spectroscopy (EIS), and Mott-Schottky analysis is used to establish detailed structure-property-performance relationships.

A central part of the work focuses on rhombohedral zinc titanate ($ZnTiO_3$) and its derivatives, chosen due to their tunable band structure and potential for visible-light photocatalysis when suitably modified. The thesis systematically examines: (i) $ZnTiO_3$/graphene oxide composites synthesized via solid-state, liquid-state, and hydrothermal routes, highlighting how process conditions affect crystallinity, oxygen vacancy formation, band gap narrowing, interfacial binding, and charge transfer; (ii) plasma-induced defect engineering in $ZnTiO_3$ to generate oxygen vacancies and enhance methylene blue degradation under visible light; and (iii) Cu-doped $ZnTiO_3$ systems, where DFT calculations are employed to elucidate the impact of dopant incorporation on electronic structure and to rationalize experimental band gap trends. (iv) Mg- doped $ZnTiO_3$ system DFT calculations are performed which shows electronic structure and density of states and band gap changes as Mg doping is increases. Across these studies, an integrated experimental-computational approach is used to identify design principles for optimizing visible light absorption, charge carrier dynamics, and photocatalytic efficiency.

Beyond zinc titanate, the thesis expands the material space by investigating NiO-ZnO-graphene oxide heterostructures. In NiO-ZnO-GO composites, the work demonstrates how tailored heterojunction architectures and GO-induced band gap reduction synergistically enhance visible-light-driven degradation of methylene blue.

The theoretical component of the thesis leverages DFT calculations to complement and guide the experimental efforts. For doped $ZnTiO_3$ systems, first-principles calculations are used to determine formation energies, electronic band structures, density of states, and the nature of defect-induced energy levels within the band gap. These calculations confirm that appropriate dopant selection and concentration can significantly narrow the electronic structure gap while preserving or even enhancing key features, such as indirect-gap character and favorable band edge positions for photocatalysis. The close agreement between calculated and experimental band gaps in selected compositions validates the computational approach and underscores the utility of DFT as a predictive tool for materials design.

Overall, this thesis contributes to the field of photocatalytic materials by providing: (i) a systematic experimental exploration of composite and doped oxide systems for visible-light-driven dye degradation; (ii) mechanistic insight into how synthesis route, interfacial structure, defect chemistry, and heterojunction design influence photocatalytic performance; and (iii) a combined experimental-computational framework that can be extended to other doped oxide systems. The findings not only advance the understanding of graphene oxide-metal oxide photocatalysts and doped zinc titanates but also suggest practical guidelines and future directions for developing efficient, stable, and scalable materials for environmental remediation and solar energy conversion.

Table of Contents

CERTIFICATE ..... **iii**
ACKNOWLEDGMENT ..... **xi**
PREFACE ..... **xiii**
Table of Contents ..... **xvii**
List of Figures ..... **xxiii**
List of Tables ..... **xxix**
List of Abbreviations/Notations ..... **xxxi**
1. CHAPTER 1 ..... **1**
Introduction **1**
1.1. Motivation 1
1.1.1. Research gaps 3
1.2. Introduction to Nanomaterials 3
1.2.1. Classification of Nanomaterials 5
1.2.2. Inorganic Nanomaterials 6
1.2.3. Composite Nanomaterials 7
1.2.4. Doped Nanomaterials 8
1.3. Properties of Nanomaterials 9
1.3.1. Optical Properties 10
1.3.2. Electrical Properties 11
1.3.3. Thermal Properties 12
1.3.4. Chemical Properties 13
1.4. Photocatalytic Semiconductors 13
1.4.1. Classifications of Photocatalytic Semiconductors 14
1.5. Historical Background of Dyes and Their Classification 17
1.5.1. Methylene Blue (MB) Dye 19
1.6. Treatment Methods for Removal of Dyes 21
1.6.1. Photocatalysis and Photocatalysis Mechanism 22
1.6.2. Factors Affecting the Photocatalysis 24
1.6.3. Visible Light-Induced Photocatalysis 26
1.7. Metal Oxide Semiconductor for Visible Light-Induced Photocatalysis 27
1.7.1. Zinc Titanate ($ZnTiO_3$) Structure and Its Properties 28

1.7.2. NiO-ZnO Structure and Its Properties 31
1.8. 2D Layered Structure and Its Properties 32
1.8.1. Graphene Oxide and Their Properties 33
1.9. Metal Oxide Semiconductor and Graphene Oxide Composite Effect on Photocatalysis 35
1.9.1. Titanium Dioxide (TiO_2) and Graphene Oxide Composite Effect on Photocatalysis 36
1.9.2. Zinc Oxide (ZnO) and Graphene Oxide Composite Effect on Photocatalysis 37
1.9.3. Nickel Oxide (NiO) and Graphene Oxide Composite Effect on Photocatalysis 38
1.10. Density Functional Theory (DFT) 39
1.10.1. DFT for Metal Oxide Semiconductor 40
1.10.2. DFT for Composite of Metal Oxide Semiconductor 41
1.10.3. DFT for Doping in Metal Oxide Semiconductor 42
1.11. Objectives of Thesis Work 43
1.12. Thesis Outline 45
1.13. Novelty of the Thesis 50
2. CHAPTER 2 53
Synthesis Methods and Characterization Techniques 53
2.1. Synthesis method of nanomaterials 53
2.1.1. Sol-gel method 54
2.1.2. Hydrothermal method 55
2.1.3. Hummers' method 57
2.2. Analytical characterization techniques 58
2.2.1. X-ray diffractogram (XRD) 59
2.2.2. Scanning Electron microscopy (SEM)/Energy dispersive X-ray spectroscopy (EDX) analysis 60
2.2.3. X-ray photoelectron spectroscopy (XPS) 63
2.2.4. UV-Visible/diffuse reflectance spectroscopy (DRS) 65
2.2.5. BET surface area analyser 67
2.2.6. Photoluminescence (PL) spectroscopy 70
2.2.7. Dynamic Light Scattering (DLS) technique 72
2.2.8. Electrochemical measurements 74
2.3. Materials and technical specifications of characterizing instruments 76
2.3.1. Materials 76

2.3.2. Details of the characterization instruments used in this work 77
3. CHAPTER 3 79
Synthesis and characterization of zinc titanate-graphene oxide composites prepared by ambient and hydrothermal conditions 79
3.1. Abstract 79
3.2. Introduction 80
3.3 Experimental section 83
3.3.1. Materials 83
3.3.2. Synthesis of zinc titanate ($ZnTiO_3$) (ZTO) 84
3.3.3. Synthesis of graphene oxide (GO) 84
3.3.4. Synthesis of composite I 85
3.3.5. Synthesis of composite II 85
3.3.6. Synthesis of composite III 85
3.4 Electrochemical measurements 85
3.5 Result and discussion 86
3.5.1. X-ray diffraction (XRD) 86
3.5.2 Surface Area Analysis 91
3.5.3 Field Emission Scanning Electron Microscopy (FESEM) analysis 92
3.5.4 X-ray Photoelectron spectroscopy 96
3.5.5 Optical behavior from UV-Vis Diffuse Reflectance Spectroscopy 100
3.5.6 Photoluminescence Spectroscopy 102
3.5.7 Mott-Schottky Analysis 103
3.5.8 Nyquist plot from electrochemical impedance analysis 104
3.6 Conclusion 106
4 CHAPTER 4 107
Improving $ZnTiO_3$ dispersion in water and thereby its photocatalytic activity towards MB degradation by plasma exposure using custom designed set-up 107
4.1. Abstract 107
4.2. Introduction 108
4.3. Experimental section 110
4.3.1. Materials 110
4.3.2. Zinc titanate synthesis 111
4.3.3. Plasma treatment of zinc titanate 111
4.3.4. Test for photocatalytic MB degradation 112
4.4. Results and discussions 113
4.4.1. Suspension stability in water 113

4.4.2. Field Emission Scanning Electron Microscopy (FESEM) analysis 115
4.4.3. X-ray diffraction (XRD) 117
4.4.4. Surface Area Analysis 119
4.4.5. Optical behaviour from UV-Vis Diffuse Reflectance Spectroscopy 120
4.4.6. X-ray Photoelectron spectroscopy 120
4.5. Photocatalytic degradation of methylene blue 122
4.6. Conclusion 125
5. CHAPTER 5 127
Synthesis and characterization of deep eutectic solvent-assisted Cu doped zinc titanate and its DFT study 127
5.1 Abstract 127
5.2 Introduction 128
5.3 Experimental section 129
5.3.1 Materials 129
5.3.2 Synthesis of zinc titanate (ZTO) 129
5.3.3 Synthesis of Cu doped ZTO 130
5.3.4 Synthesis of DES 130
5.3.5 Synthesis of DES assisted Cu doped ZTO 131
5.4 Results and discussion 131
5.4.1 X-ray Diffraction (XRD) 131
5.4.2 Field Emission Scanning Electron Microscopy (FESEM) 134
5.4.3 Optical behavior from UV-Vis Diffuse Reflectance Spectroscopy 137
5.4.4 Surface Area Analysis 138
5.4.5 X-ray Photoelectron spectroscopy (XPS) 139
5.5 Computational section 144
5.5.1 Calculation method and crystal structure 144
5.5.2 Structural properties 145
5.5.3 Electronic properties 146
5.6 Conclusion 148
6. CHAPTER 6 149
The effect of Mg-doping on the structural and electronic properties of $ZnTiO_3$: A first-principles study and compared with experimental band gap of $ZnTiO_3$ 149
6.1. Abstract 149
6.2. Introduction 150
6.3. Calculation method and crystal structure 151
6.4. Results and discussions 154

6.4.1. Structural properties 154
6.4.2. Electronic properties 155
6.5. Experimental band gap 160
6.6. Comparison of band gap from theoretical, experimental and from literature 161
6.7. Conclusion 162
7. CHAPTER 7 163
Photocatalytic performance of NiZnO/graphene oxide composites towards visible light induced degradation of methylene blue dye 163
7.1. Abstract 163
7.2. Introduction 164
7.3. Experimental section 166
7.3.1. Materials 166
7.3.2. Synthesis of NiZnO 166
7.3.3. Synthesis of graphene oxide (GO) 167
7.3.4. Synthesis of NiZnO/graphene oxide (GO) composite 167
7.4. Results and discussion 168
7.4.1. X-ray diffraction (XRD) 168
7.4.2. Surface Area Analysis 170
7.4.3. Field Emission Scanning Electron Microscopy (FESEM) analysis 171
7.4.4. X-ray Photoelectron spectroscopy 173
7.4.5. Optical behavior from UV-Vis Diffuse Reflectance Spectroscopy 179
7.4.6. Photoluminescence Spectroscopy 184
7.5. Photocatalytic performance 186
7.6. Conclusion 190
8. CHAPTER 8 191
Solar-Powered Photocatalytic Reactor 191
8.1. Abstract 191
8.2. Introduction and main components 192
8.3. System Configuration and Flow Path 195
8.4. Conclusion 197
9. CHAPTER 9 199
Conclusions and Future Scope 199
9.1. Conclusions 199
9.1.1. Chapter 3 199
9.1.2. Chapter 4 201

9.1.3. Chapter 5 202
9.1.4. Chapter 6 201
9.1.5. Chapter 7 203
9.1.6. Chapter 8 204
9.2. Future Scope 204
References 207
Appendix 239
Thesis outcomes 245
Published Research Articles/Granted Patent 249
Curriculum vitae (CV) 257

List of Figures

Figure 1.1.Classification of photocatalytic semiconductor. 17

Figure 1.2.Classification of dyes..... 19

Figure 1.3. Chemical Structure of (a) Methylene blue (MB), (b) Methyl orange, (c) Congo Red and (d) Rhodamine B dyes. 21

Figure 1.4. Classifications of a dye removal and other related aspects. 22

Figure 1.5. Classification of photocatalytic semiconductors based on band gaps, mechanism, and composite heterojunction configuration. 24

Figure 1.6. Phase diagram of ZnO-TiO2 (adapted)[127]..... 29

Figure 1.7. (a) Rhombohedral zinc titanate with a lattice parameter a = b = 5.13 Å, and c = 14.08 Å, and (b) Cubic zinc titanate with a lattice parameter a = b = c = 3.84 Å. .. 31

Figure 1.8. (a) Cubic NiO with a lattice parameter a = b = c = 4.19 Å, and (b) Hexagonal ZnO with a lattice parameter a = b = 3.24 Å and c = 5.22 Å. 32

Figure 1.9. Illustration of (a) Graphene Oxide, and (b) Reduced Graphene oxide..... 35

Figure 2.1. Nanomaterials synthesis methods..... 54

Figure 2.2. Hydrothermal synthesis route. 56

Figure2.3. Synthesis of graphene oxide by modified Hummers' method. 58

Figure 2.4. Schematic diagram of X-ray diffractogram represents the diffraction of incident x-rays from parallel planes..... 60

Figure 2.5. Mechanism of photoelectron emission in XPS technique. 65

Figure 2.6. Physisorption isotherms,type- I to VI, in the classification of Bruauer, Emett and Teller. (Adapted from) [169] 69

Figure 3.1. XRD patterns of ZTO, composite I, II, III, and GO. 90

Figure 3.2. Deconvoluted XRD peaks for (311) and (110) planes of Zn2TiO4 and ZnTiO3 in (a) ZTO, and composite (b) I, (c) II, and (d) III. 91

Figure 3.3. The BET surface area and isotherm of (a) ZTO, and composites (b) I, (c) II, and (d) III. 92

Figure 3.4. FESEM images of samples at smaller magnification (left column) and larger magnification (right column). Images of GO (a, b), composite I (c, d), composite II (e, f), and composite III (g, h) samples. 94

Figure 3.5. EDX mapping of composite III. 95

Figure 3.6. XPS of C1s of (a) GO, (b) composite I, (c) composite II, and (d) composite III. 98

Figure 3.7. XPS of O1s of (a) GO, (b) ZTO, (C) composite I, (d) composite II, and (e) composite III. 99

Figure 3.8. (a) UV DRS data in terms of reflectance. The plot of the Kubelka-Munk function versus the energy of exciting light that results in the band-gap of (b) ZTO, (c) composite I, (d) composite II, (e) composite III. 102

Figure 3.9. Photoluminescence spectra of ZTO, composite I, composite II, composite III. 103

Figure 3.10. Mott- Schottky plot of ZTO, composite I, composite II, and composite III. 104

Figure 3.11. Nyquist plot of ZTO, composite I, composite II, and composite III. 106

Figure 4.1. Customized plasma treatment Instrument. 112

Figure 4.2. Viscosity of suspension of $ZnTiO_3$ and suspension obtained by plasma treatment of $ZnTiO_3$. 114

Figure 4.3. (a) Zeta potential of suspension of $ZnTiO_3$, (b) particle-size distribution of suspension of $ZnTiO_3$, (c) zeta potential of suspension of PT-$ZnTiO_3$, and (d) particle-size distribution of PT-$ZnTiO_3$ suspension. 115

Figure 4.4.FESEM images of (a, b) ZnTiO3, and (c, d) PT- ZnTiO3. Lower panels correspond to higher magnification. 116

Figure 4.5. FESEM images of native and plasma treated ZnTiO3 are respectively shown in (a) and (b), and their elemental composition mapping obtained by EDX are shown in (c) and (d). 117

Figure 4.6. X-ray diffractogram of $ZnTiO_3$, and PT- $ZnTiO_3$. 118

Figure 4.7. The BET surface area and isotherm of (a) $ZnTiO_3$, and (b) PT- $ZnTiO_3$...119

Figure 4.8. (a) UV–vis DRS, and (b) Tauc plots of $ZnTiO_3$ and PT-$ZnTiO_3$..... 120

Figure 4.9. XPS signals from (a) O1s of $ZnTiO_3$, (b) O1s of PT-$ZnTiO_3$, (c) Zn2p of $ZnTiO_3$, (d) Zn2p of PT-$ZnTiO_3$, (e) Ti2p of $ZnTiO_3$, and (f) Ti2p of PT-$ZnTiO_3$..... 122

Figure 4.10. The absorption spectra of MB dye after varying time for (a) $ZnTiO_3$ and (b) PT-$ZnTiO_3$. First order kinetics fit for the degradation of MB for (c) $ZnTiO_3$ and (d) PT-$ZnTiO_3$. 124

Figure 5.1. XRD patterns of ZnTiO3, ZnTiO3/Cu (14% with DES), $ZnTiO_3$/Cu (28% with DES), and ZnTiO3/Cu (14% with DI). 133

Figure 5.2. FESEM images of samples at smaller magnification (left column) and larger magnification (right column). Images of ZnTiO3 (a, b), ZnTiO3/Cu (14% with DES) (c, d), ZnTiO3/Cu (28% with DES) (e, f), and ZnTiO3/Cu (14% with DI) (g, h) samples. 135

Figure 5.3. FESEM images of (a) ZnTiO3, (c) ZnTiO3/Cu (14% with DES), (e) ZnTiO3/Cu (28% with DES), (g) ZnTiO3/Cu (14% with DI), and their elemental composition mapping obtained by EDX are shown in (b) ZnTiO3, (d) ZnTiO3/Cu (14% with DES), (f) $ZnTiO_3$/Cu (28% with DES), (h) $ZnTiO_3$/Cu (14% with DI). 137

Figure 5.4. (a) UV-Vis DRS, and (b) The tauc plot versus the energy of exciting light results in the band-gap of $ZnTiO_3$, $ZnTiO_3$/Cu (14% with DES), $ZnTiO_3$/Cu (28% with DES), and $ZnTiO_3$/Cu (14% with DI). 138

Figure 5.5. The BET isotherms of (a) $ZnTiO_3$, (b) $ZnTiO_3$/Cu (14% with DES), (c) $ZnTiO_3$/Cu (28% with DES), and (d) $ZnTiO_3$/Cu (14% with DI). 139

Figure 5.6. XPS of O1s of (a) $ZnTiO_3$, (b) $ZnTiO_3$/Cu (14% with DES), (c) $ZnTiO_3$/Cu (28% with DES), and (d) $ZnTiO_3$/Cu (14% with DI). 140

Figure 5.7. XPS of (a) Zn2p, (b) Ti2p for $ZnTiO_3$, $ZnTiO_3$/Cu (14% with DES), $ZnTiO_3$/Cu (28% with DES), and $ZnTiO_3$/Cu (14% with DI). 141

Figure 5.8. XPS of Cu2p for (a) $ZnTiO_3$/Cu (14% with DES), (b) $ZnTiO_3$/Cu (28% with DES), and (c) $ZnTiO_3$/Cu (14% with DI). 142

Figure 5.9. A schematic representation of the pure zinc titanate $ZnTiO_3$ using the VESTA package. 145

Figure 5.10. Band Structures of (a) $ZnTiO_3$ and (b) Cu doped $ZnTiO_3$. 147

Figure 5.11. Partial density of states (PDOS) of (a) $ZnTiO_3$ and (b) Cu doped $ZnTiO_3$. 148

Figure 6.1. An optimized structures of $Zn_{1-x}Mg_xTiO_3$ where (a) x = 0, (b) x = 0.167, (c) x = 0.333, (d) x = 0.5, (e) x = 0.667 using the VESTA package. 153

Figure 6.2. The formation energy of the Mg-doped ZnTiO3 material as a function of the lattice parameters (a) a (Å) and (b) c (Å), using the GGA approximation. 155

Figure 6.3. Band Structures of $Zn_{1-x}Mg_xTiO_3$ where (a) x = 0, (b) x = 0.167, (c) x = 0.333, (d) x = 0.5, (e) x = 0.667, and (f) formation energy and electronic structure gap of the doped $ZnTiO_3$ as a function of concentration (x) of impurities of Mg. 158

Figure 6.4. Partial density of states (PDOS) of $Zn_{1-x}Mg_xTiO_3$, where (a) x = 0, (b) x = 0.167, (c) x = 0.333, (d) x = 0.5, and (e) x = 0.667. 160

Figure 6.5. (a) absorption verses wavelength and (b) experimental band gap energy (E_g) for $ZnTiO_3$. 161

Figure 7.1. X-ray diffractogram of NiZnO, NiZnO/GO1, NiZnO/GO10, and GO. ... 169

Figure 7.2. X-ray diffractogram for (a) GO, (b) NiZnO/GO1, and (c) NiZnO/GO10 in region 21-23°. 170

Figure 7.3. The BET isotherms of (a) NiZnO, (c) NiZnO/GO10 and BET plots of (b) NiZnO, (d) NiZnO/GO10. 171

Figure 7.4. FESEM images of samples at smaller magnification (left column) and larger magnification (right column). Images of (a, b) GO, (c, d) NiZnO, (e, f) NiZnO/GO1, and (g, h) NiZnO/GO10 samples. 173

Figure 7.5. EDX mapping (a, b, c) of NiZnO and spot EDX (d, e) of NiZnO and (f) GO. 173

Figure 7.6. XPS of O1s of (a) GO, (b) NiZnO, (c) NiZnO/GO1, and (d) NiZnO/GO10. 175

Figure 7.7. XPS of C1s of (a) GO, (b) NiZnO/GO1, and (c) NiZnO/GO10. 176

Figure 7.8.XPS of Zn2p of (a) NiZnO, NiZnO/GO1, and NiZnO/GO10 and XPS of Ni2p of (b) NiZnO, NiZnO/GO1, and NiZnO/GO10. 176

Figure 7.9. Images of XPS deconvolute of Ni2p for (a) NiZnO, (b) NiZnO/GO1, and (c) NiZnO/GO10. 179

Figure 7.10. (a) UV DRS data in terms of reflectance. The plot of the Kubelka-Munk function versus the energy of exciting light that results in the band gap of (b) NiZnO, (c) NiZnO/GO1, (d) NiZnO/GO10, (e) GO. 181

Figure 7.11. Mechanism of charge separation in r-GO/NiO/ZnO. (a) Type II heterojunction when r-GO work function is larger than that of NiO, and (b) direct Z-scheme, when work function of r-GO is smaller than that of NiO. The dashed lines

imply the Fermi level. For representation, sample NiZnO/GO10 is considered here, with NiO band gap becoming 2.7 eV from 3.4 eV due to nickel binding with carbon of r-GO sheets after it is composited with the GO. The green vertical arrows represent carrier generation due to light illumination, blue arrows represent carriers moving across the junction to lower energy levels, and orange arrows represent recombination. Please see text for detail. 184

Figure 7.12. Photoluminescence spectra of NiZnO, NiZnO/GO1, and NiZnO/GO10 samples. 186

Figure 7.13. UV-Vis of degradation for (a) NiZnO, (b) NiZnO/GO1, and (c) NiZnO/GO10 and pseudo-first-order kinetic fit for the degradation of MB for (d) NiZnO, (e) NiZnO/GO1, and (f) NiZnO/GO10. 188

Figure 8.1. Design of Solar-Powered Photocatalytic Reactor (a) Right View, (b) bottom view, (c) front view, (d) top view and (e) left view. 194

Figure 8.2. Perspective view of photocatalytic reactor. 195

List of Tables

Table 3.1. Calculation of the percentage of phase present in the sample. 90

Table 3.2. The atomic composition of GO, composite I, composite II, composite III from areal EDX. 95

Table 4.1. Composition of phases present in $ZnTiO_3$ and PT- $ZnTiO_3$. 118

Table 4.2. Comparison of degradation efficiency and kinetics for different photocatalysts..... 125

Table 5.1. Calculation of the percentage of phase present in the sample. 133

Table 5.2. Calculation of lattice constants of different phases present in samples. 133

Table 5.3. Peak positions of XPS for $ZnTiO_3$, $ZnTiO_3$/Cu (14% with DES), $ZnTiO_3$/Cu (28% with DES), and $ZnTiO_3$/Cu (14% with DI). 143

Table 6.1. Lattice parameter of $ZnTiO_3$ and calculated lattice parameter of Mg-doped $ZnTiO_3$. 155

Table 6.2.Comparison tabulation of bandgap of $ZnTiO_3$ reported in the literature, experimental and theoretical bandgap of Mg-doped $ZnTiO_3$. 162

Table 7.1.Percentage of phase present in the sample. 169

Table 7.2. Peak positions of XPS for NiZnO, NiZnO/GO1, and NiZnO/GO10. 177

Table 7.3. Comparison of degradation kinetics rate constant for different photocatalysts. 189

List of Abbreviations/Notations

μm	:	micrometre
nm	:	nanometre
Å	:	Angstrom
mL	:	Mililitre
kN	:	Kilonewton
mPa.s	:	millipascal Second
DI	:	Deionised
MB	:	Methylene Blue
E_g	:	Energy Band Gap
UV	:	Ultra-Violet
HOMO	:	Highest Occupied Molecular Orbital
LUMO	:	Least Unoccupied Molecular Orbital
TNBT	:	Tetra-N-Butyl Orthotitanate
ZTO	:	Zinc Titanate
JCPDS	:	Joint-Committee on Powder Diffraction
MPa	:	Megapascal
kV	:	Kilovolts

XRD	:	X-Ray Diffraction
FWHM	:	Full Width Half Maxima
ATR	:	Attenuated Total Reflectance
FESEM	:	Field Emission Scanning Electron Microscopy
EDX	:	Energy Dispersive X-ray spectroscopy
XPS	:	X-ray Photoelectron Spectroscopy
K.E.	:	Kinetic Energy
B.E.	:	Binding Energy
UV-Vis	:	Ultraviolet Visible Spectroscopy
DRS	:	Diffuse Reflectance Spectroscopy
BET	:	Brunauer-Emmett-Teller
PL	:	Photoluminescence
CB	:	Conduction Band
VB	:	Valence Band
M.W.	:	Molecular weight
DLS	:	Dynamic Light Scattering
CTAB	:	cetyltrimethylammonium bromide

CHAPTER 1

Introduction

1.1. Motivation

The escalating global environmental crisis and the urgent need for sustainable energy solutions have positioned photocatalysis as a pivotal technology for addressing contemporary challenges in environmental remediation and clean energy production [1]. The development of efficient photocatalytic materials that can harness visible light, which constitutes approximately 45% of the solar spectrum, represents a critical advancement toward sustainable environmental technologies [2], [3]. Traditional photocatalysts such as titanium dioxide (TiO_2) primarily operate under ultraviolet (UV) light irradiation, which accounts for only 4-5% of solar radiation, thereby limiting their practical applications and economic viability [4], [5].

The increasing discharge of synthetic dyes from textile, pharmaceutical, and chemical industries into aquatic environments poses severe threats to ecological systems and human health [6]. These organic pollutants are characterized by their complex aromatic structures, high stability, and resistance to conventional biological degradation processes [7]. Methylene blue, a representative cationic dye widely used in industrial applications, exemplifies the persistent nature of these contaminants, necessitating the development of advanced treatment technologies [8], [9].

The practical application of many oxide semiconductor photocatalysts remains limited by their wide band gap, low visible-light utilization, and rapid recombination of photogenerated charge carriers. In addition, insufficient surface adsorption and limited interfacial charge transport further reduce their degradation efficiency. These limitations indicate that the performance of pristine oxide photocatalysts cannot be substantially improved by simple material selection alone, and targeted structural modification is required.

The integration of computational approaches, particularly Density Functional Theory (DFT) calculations, with experimental synthesis methods offers unprecedented opportunities to understand and predict the electronic properties of photocatalytic materials. This synergistic approach enables the rational design of composite materials with tailored band structures and optimized charge transfer mechanisms, ultimately leading to enhanced photocatalytic performance under visible light conditions. The motivation for incorporating DFT calculations lies in their ability to provide fundamental insights into the electronic structure modifications that occur upon doping and composite formation, thereby guiding the experimental design process [10], [11].

Accordingly, the present work has been motivated by the need to modify oxide photocatalysts through graphene oxide compositing, metal doping, and defect engineering. Graphene oxide is expected to improve surface adsorption and charge transport, while metal doping and defect formation are expected to tune the electronic structure, band gap, and charge-carrier dynamics. These strategies were therefore selected to develop visible-light-active photocatalysts with improved efficiency, stability, and mechanistic clarity.

1.1.1. Research gaps

Favorable band edge positions are exhibited by $ZnTiO_3$ for photocatalytic applications. However, significant phase complexity is frequently observed during synthesis. Visible light absorption is strictly limited by its intrinsic wide band gap. Furthermore, the modification of its electronic structure via GO compositing is insufficiently understood. The precise effects of defect engineering and transition metal doping on its photocatalytic behavior also remain unresolved.

Established p-n heterojunctions are formed by NiO-ZnO systems. Despite this, the modulation of interfacial band bending by rGO content is poorly defined. Practical dye degradation kinetics under visible light are rarely detailed for these specific heterostructures. This structural gap is highly evident for compositions matching the NiO-ZnO/GO systems. The dominant charge recombination mechanisms in these tailored composites require thorough investigation.

A coupled experimental and DFT framework is rarely applied to Cu-doped and Mg-doped $ZnTiO_3$. The explicit mapping of dopant concentration to electronic structure changes is required. Calculated band gaps must be directly compared with experimental band gap of $ZnTiO_3$. These theoretical insights are strictly necessary to rationally design visible light-active compositions.

1.2. Introduction to Nanomaterials

Nanomaterials represent a revolutionary class of materials characterized by at least one dimension in the nanometer scale (1-100 nm), exhibiting unique properties that differ significantly from their bulk counterparts [12]. The emergence of nanotechnology as a

driving force in materials science has opened new avenues for developing advanced functional materials with enhanced performance characteristics [13]. The distinctive properties of nanomaterials arise from their high surface-to-volume ratio, quantum confinement effects, and increased surface reactivity, making them particularly suitable for photocatalytic applications.

The field of nanomaterials has witnessed exponential growth over the past few decades, driven by advances in synthesis techniques and characterization methods [12]. The ability to control size, shape, morphology, and composition at the nanoscale has enabled the development of materials with precisely tailored properties for specific applications [12]. In the context of photocatalysis, nanomaterials offer several advantages including enhanced light absorption, increased active surface area, improved charge separation efficiency, and reduced recombination rates of photogenerated electron-hole pairs [14], [15].

The unique properties of nanomaterials stem from their quantum size effects, where the electronic and optical properties become size-dependent due to quantum confinement [16]. This phenomenon allows for the tuning of band gap energies and optical absorption characteristics, which is particularly important for developing visible light-active photocatalysts [17]. Furthermore, the high surface energy of nanomaterials promotes enhanced interaction with reactant molecules, leading to improved catalytic activity and selectivity.

When we move from the micro to the nano regime, we should expect the measured properties to change because surface effects, defect effects, and quantum confinement become much more important as particle size decreases. In simple terms, the material no

longer behaves like a bulk solid; instead, a much larger fraction of its atoms are at the surface, so surface reactivity, adsorption, and interfacial charge transfer increase.

In this study, the most relevant changes are usually in optical, structural, and catalytic behavior. Optical absorption can shift because the band gap may change at smaller sizes, electrical transport can improve or become more defect-sensitive depending on the dopant and interface, and photocatalytic activity often increases because the nano-sized material exposes more active sites and supports faster charge separation.

1.2.1. Classification of Nanomaterials

Nanomaterials can be systematically classified based on various criteria including dimensionality, composition, origin, and structural characteristics [18]. The dimensional classification divides nanomaterials into zero-dimensional (0D), one-dimensional (1D), two-dimensional (2D), and three-dimensional (3D) structures, each exhibiting distinct properties and applications. Zero-dimensional nanomaterials include quantum dots and nanoparticles, which exhibit quantum confinement effects in all three spatial dimensions, resulting in discrete energy levels and size-dependent optical properties.

One-dimensional nanomaterials such as nanowires, nanotubes, and nanorods possess high aspect ratios and anisotropic properties, making them suitable for applications requiring directional charge transport [19]. Two-dimensional nanomaterials, exemplified by graphene and layered metal oxides, offer unique properties arising from their sheet-like structures and high surface areas [20]. Three-dimensional nanomaterials encompass complex hierarchical structures and nanocomposites that combine multiple components to achieve synergistic effects [21].

Based on composition, nanomaterials can be classified into organic, inorganic, and hybrid organic-inorganic systems. Inorganic nanomaterials include metal oxides, metals,

semiconductors, and ceramics, while organic nanomaterials comprise polymers, carbon-based materials, and biomolecules [22]. Hybrid nanomaterials combine the advantages of both organic and inorganic components, offering enhanced functionality and versatility for various applications [23].

1.2.2. Inorganic Nanomaterials

Inorganic nanomaterials constitute a diverse class of materials including metal oxides, metals, semiconductors, and ceramic compounds that exhibit exceptional properties for photocatalytic applications [24]. Metal oxide nanomaterials such as TiO_2, ZnO, CeO_2, and SnO_2 have been extensively studied as photocatalysts due to their chemical stability, biocompatibility, and ability to generate reactive oxygen species under light irradiation [25]. These materials possess favorable electronic structures with suitable band positions for photocatalytic redox reactions [25].

The synthesis of inorganic nanomaterials can be achieved through various methods including sol-gel processes, hydrothermal synthesis, chemical vapor deposition, and precipitation techniques [12]. The sol-gel method, in particular, offers excellent control over composition, purity, and morphology while operating at relatively low temperatures [26]. Hydrothermal synthesis provides an environmentally friendly approach for producing crystalline nanomaterials with controlled size and morphology under mild conditions [27].

The photocatalytic activity of inorganic nanomaterials is primarily governed by their electronic band structure, surface area, crystallinity, and defect concentration. The band gap energy determines the wavelength of light that can be absorbed, while the band edge positions dictate the thermodynamic feasibility of photocatalytic reactions [3]. Surface

defects and oxygen vacancies can act as charge trapping sites, influencing the charge separation efficiency and overall photocatalytic performance [28].

1.2.3. Composite Nanomaterials

Composite nanomaterials represent an advanced class of materials that combine two or more distinct components at the nanoscale to achieve enhanced properties that cannot be obtained from individual components alone [29]. The design principle of composite nanomaterials relies on the synergistic interaction between different components, leading to improved functionality, stability, and performance characteristics [30]. In photocatalysis, composite materials offer unique advantages including extended light absorption range, enhanced charge separation, and reduced recombination rates.

The formation of heterojunctions in composite nanomaterials creates built-in electric fields that facilitate the separation of photogenerated charge carriers [31]. Type I, Type II, and Z-scheme heterojunctions represent different band alignment configurations that determine the charge transfer pathways and photocatalytic mechanisms [32]. The interface between different components plays a crucial role in determining the overall performance of composite materials, requiring careful control of synthesis conditions and interfacial interactions [32].

Two-dimensional layered composite photocatalysts have gained significant attention due to their unique properties arising from quantum confinement effects and high surface areas [33]. These materials offer advantages in band gap tuning, heterojunction formation, and enhanced light absorption capabilities [34]. The layered structure facilitates efficient charge transport and provides numerous active sites for photocatalytic reactions [34].

1.2.4. Doped Nanomaterials

Doped nanomaterials are created by introducing foreign atoms or ions into the host crystal lattice, resulting in modified electronic, optical, and catalytic properties [35], [36], [37]. The doping process can involve substitutional or interstitial incorporation of dopant atoms, leading to the formation of new energy levels within the band gap of the host material [38], [39]. This modification allows for the tuning of band gap energies, enhancement of visible light absorption, and improvement of charge separation efficiency [40], [41].

Metal doping of semiconductor nanomaterials has proven to be an effective strategy for enhancing photocatalytic activity under visible light irradiation [42]. Transition metal dopants such as Fe, Co, Ni, and Cu introduce d-orbital states that can act as electron traps or recombination centers, depending on their concentration and position within the band gap [43], [44]. The optimal doping concentration is critical, as excessive doping can lead to increased recombination rates and reduced photocatalytic efficiency [45].

Non-metal doping with elements such as N, C, S, and F has also been extensively studied for extending the light absorption of wide band gap semiconductors into the visible region [46]. These dopants typically introduce states above the valence band maximum, effectively narrowing the band gap and enabling visible light activation [47]. The success of doping strategies depends on factors such as dopant solubility, thermal stability, and the formation of compensating defects [48].

A suitable dopant is usually selected based on four basic criteria: its ionic radius should be close enough to the host ion to allow lattice substitution, its valence state should be compatible with charge compensation, it should not form unwanted secondary phases at

the chosen concentration, and it should introduce electronic states that improve light absorption or charge transport rather than acting mainly as a recombination center.

In this study, this means the dopant should fit into the ZnTiO3 lattice with minimal structural distortion while still modifying the band structure in a useful way. For Cu doping, the idea is to replace Zn sites without destroying the host framework, and for Mg doping the same principle applies, but the concentration must be tuned carefully so that the electronic structure is altered in a controlled manner.

The structural properties can be controlled mainly through dopant concentration because low to moderate doping can reduce crystallite size, change lattice parameters slightly, and adjust defect density, while excessive doping may produce strain, agglomeration, or even secondary phases. In practice, this is why dopant concentration is treated as an optimization variable rather than a fixed number.

The electrochemical properties are also concentration-dependent because dopants can shift the Fermi level, create trap states, change carrier density, and influence charge separation and transfer at interfaces. At an optimal concentration, these changes help improve conductivity and reduce recombination, but beyond that point the added dopant can create too many defects and start decreasing performance.

1.3. Properties of Nanomaterials

The unique properties of nanomaterials arise from their reduced dimensionality, high surface-to-volume ratio, and quantum confinement effects [49], [50]. These properties can be categorized into optical, electrical, thermal, and chemical characteristics, each playing a crucial role in determining the material's suitability for specific applications [51], [52]. Understanding these properties is essential for designing nanomaterials with tailored functionality for photocatalytic applications.

The size-dependent properties of nanomaterials distinguish them from their bulk counterparts, often exhibiting enhanced or entirely new characteristics [53]. Quantum confinement effects become prominent when the material dimensions approach the de Broglie wavelength of charge carriers, leading to discrete energy levels and size-dependent optical properties [54], [55]. Surface effects dominate in nanomaterials due to the high proportion of atoms located at or near the surface, resulting in increased reactivity and modified thermodynamic properties [56].

Nanomaterials show enhanced catalytic activity mainly because they expose a much larger active surface area, which gives more reactant-accessible sites and increases the probability of surface reactions. At the nanoscale, a greater fraction of atoms lies at edges, corners, and surfaces rather than inside the bulk, so a larger portion of the material can directly participate in catalysis.

They also benefit from shorter diffusion paths and faster interfacial charge transfer, which is especially important in photocatalysis where photogenerated electrons and holes must reach the surface before recombining. In addition, nanoscale materials often have more defects, vacancies, and tunable electronic states, which can improve adsorption of reactants and lower the activation energy for reaction pathways.

1.3.1. Optical Properties

The optical properties of nanomaterials are fundamentally different from bulk materials due to quantum confinement effects and surface plasmon resonances [57], [58]. The absorption and emission characteristics of semiconductor nanomaterials are strongly size-dependent, with smaller particles exhibiting blue-shifted absorption edges due to quantum confinement [59]. This size-dependent tunability allows for the precise control of optical properties for specific photocatalytic applications.

The band gap energy of semiconductor nanomaterials increases with decreasing particle size, following the effective mass approximation model [60]. This relationship enables the engineering of optical properties by controlling the synthesis parameters and particle size distribution [61]. For photocatalytic applications, the optimal band gap should be narrow enough to absorb visible light while maintaining sufficient driving force for redox reactions [62].

Surface plasmon resonances in metal nanoparticles provide additional mechanisms for light absorption and enhancement of local electromagnetic fields. The incorporation of plasmonic nanoparticles into photocatalytic composites can significantly enhance light absorption and improve charge separation efficiency through hot electron injection and near-field enhancement effects [63]. The plasmon resonance frequency depends on the particle size, shape, and surrounding dielectric environment [64].

1.3.2. Electrical Properties

The electrical properties of nanomaterials are governed by quantum confinement effects, surface states, and grain boundary effects [65]. The reduced dimensionality leads to modified density of states and altered charge transport mechanisms compared to bulk materials [66]. In semiconductor nanomaterials, the presence of surface states and defects can significantly influence the electrical conductivity and charge carrier mobility [67].

The conductivity of nanomaterials can vary dramatically with size, shape, and surface functionalization [68]. Quantum confinement effects can lead to either enhanced or reduced conductivity depending on the specific material and dimensional constraints [69]. For photocatalytic applications, the electrical properties determine the efficiency of charge separation and transport to reactive sites [63].

Interface effects in composite nanomaterials play a crucial role in determining the overall electrical behavior [70]. The formation of Schottky barriers or ohmic contacts at interfaces can facilitate or hinder charge transfer between different components [71]. Understanding and controlling these interfacial properties is essential for optimizing the performance of composite photocatalysts [70], [71].

1.3.3. Thermal Properties

The thermal properties of nanomaterials, including melting point, thermal conductivity, and thermal stability, differ significantly from bulk materials [72]. The high surface-to-volume ratio and increased surface energy lead to reduced melting points and enhanced thermal reactivity [73]. These modified thermal properties have important implications for synthesis conditions and operational stability of photocatalytic materials.

Thermal conductivity in nanomaterials can be either enhanced or reduced compared to bulk materials, depending on the specific structure and phonon transport mechanisms [74]. In layered materials, thermal conductivity is often anisotropic, with higher values in the plane direction and reduced values across layers [75]. For photocatalytic applications, thermal management is important for maintaining activity under concentrated solar irradiation [76].

The thermal stability of nanomaterials is influenced by surface energy, defect concentration, and grain size effects [74]. Phase transformations and sintering can occur at lower temperatures in nanomaterials, potentially affecting their photocatalytic performance [77]. Understanding thermal stability is crucial for determining the operational temperature range and long-term durability of photocatalytic systems [78].

1.3.4. Chemical Properties

The chemical properties of nanomaterials are dominated by surface effects and the high concentration of reactive sites [79]. The increased surface area provides more active sites for chemical reactions, while surface atoms exhibit higher reactivity due to unsaturated coordination [80]. These enhanced chemical properties make nanomaterials particularly suitable for catalytic applications [81].

Surface functionalization and modification strategies can be employed to tailor the chemical properties of nanomaterials for specific applications [80]. The introduction of functional groups can enhance selectivity, improve stability, and facilitate interfacial interactions in composite systems [68]. For photocatalytic applications, surface modification can improve light absorption, charge separation, and reactant adsorption [68], [80].

The chemical stability of nanomaterials in different environments is a critical factor for practical applications. Factors such as pH, temperature, and the presence of reactive species can influence the long-term stability and performance of photocatalytic materials [82], [83], [84]. Understanding degradation mechanisms and developing strategies for improving chemical stability is essential for commercial viability.

1.4. Photocatalytic Semiconductors

Photocatalytic semiconductors represent a class of materials capable of absorbing light energy and converting it into chemical energy through the generation of reactive species [85]. The fundamental principle of semiconductor photocatalysis involves the excitation of electrons from the valence band to the conduction band upon light absorption, creating electron-hole pairs that can participate in redox reactions [85]. The efficiency of this

process depends on factors such as band gap energy, band edge positions, charge carrier mobility, and surface properties [2].

The photocatalytic process begins with light absorption, where photons with energy equal to or greater than the band gap energy promote electrons from the valence band to the conduction band [86]. The photogenerated electrons and holes can then migrate to the surface and participate in reduction and oxidation reactions, respectively [87]. The overall efficiency of the photocatalytic process is determined by the competition between productive surface reactions and unproductive recombination of charge carriers [88].

The development of efficient photocatalytic semiconductors requires careful consideration of their electronic structure, optical properties, and surface characteristics. Wide band gap semiconductors such as TiO_2 and ZnO exhibit excellent photocatalytic activity under UV irradiation but have limited visible light absorption [4]. Strategies for extending the light absorption range include band gap engineering through doping, composite formation, and surface sensitization [89].

1.4.1. Classifications of Photocatalytic Semiconductors

Semiconductor photocatalysts represent a diverse class of materials that can be systematically categorized based on their chemical composition and structural complexity. The classification framework divides these materials into three primary categories: binary type, ternary type, and quaternary type photocatalysts.

Binary Type Semiconductor Photocatalysts

Binary-type photocatalysts consist of compounds containing two different elements and can be further subdivided into three main subcategories:

Oxides

Binary oxide photocatalysts include some of the most widely studied materials in photocatalysis: Titanium dioxide (TiO_2), Zinc oxide (ZnO), Nickel oxide (NiO), Tin dioxide (SnO_2), Zinc oxide (ZnO), Zirconium dioxide (ZrO_2), Tungsten trioxide (WO_3), Cerium dioxide (CeO_2), and Bismuth trioxide (Bi_2O_3)

Nitrides

Nitride-based photocatalysts demonstrate excellent properties for visible light absorption: Gallium nitride (GaN), Tantalum nitride (Ta_3N_5), Graphitic carbon nitride (g-C_3N_4)

Chalcogenide photocatalysts are further classified into two subgroups:

Sulfides

Cadmium sulfide (CdS), Copper sulfide (CuS), Zinc sulfide (ZnS), Bismuth sulfide (Bi_2S_3), Antimony sulfide (Sb_2S_3)

Selenides

Cadmium selenide (CdSe)

Ternary Type Semiconductor Photocatalysts

Ternary photocatalysts contain three different elements and exhibit more complex crystal structures, offering enhanced tunability of their electronic and optical properties.

Ternary Oxides

Ternary oxide photocatalysts encompass several structural types:

ABO_3-Perovskite Structures

Perovskite-type materials with the general formula ABO_3 include: Zinc titanate ($ZnTiO_3$), Bismuth ferrite ($BiFeO_3$), Strontium titanate ($SrTiO_3$)

AB_2O_4 Compounds

These materials feature spinel and related structures with diverse cation arrangements.

ABO_2 Materials

This category includes: Delafossite-structured materials and Cristobalite-structured materials for example copper iron oxide ($CuFeO_2$)

ABO_4 Materials: Scheelite-structured materials

Ternary Chalcogenides

This category encompasses ternary compounds containing chalcogen elements (sulfur, selenium, tellurium) combined with two other elements.

Quaternary Type

Quaternary photocatalysts represent the most complex category, consisting of four or more different elements. These materials offer the highest degree of compositional flexibility for tailoring photocatalytic properties: Calcium bismuth niobate ($CaBi_2Nb_4O_9$), Barium bismuth niobate ($BaBi_2Nb_4O_9$), and Strontium bismuth niobate ($SrBi_2Nb_4O_9$).

Significance of Classification

This hierarchical classification system provides a comprehensive framework for understanding the structural diversity of semiconductor photocatalysts. The increasing complexity from binary to quaternary types generally corresponds to greater tunability of electronic band structures, optical properties, and photocatalytic performance. This systematic approach facilitates the rational design and selection of photocatalyst materials for specific applications, including water splitting, pollutant degradation, and solar fuel production.

The classification serves as a foundation for researchers to navigate the vast landscape of semiconductor photocatalysts and guides the development of new materials with enhanced photocatalytic efficiency and stability.

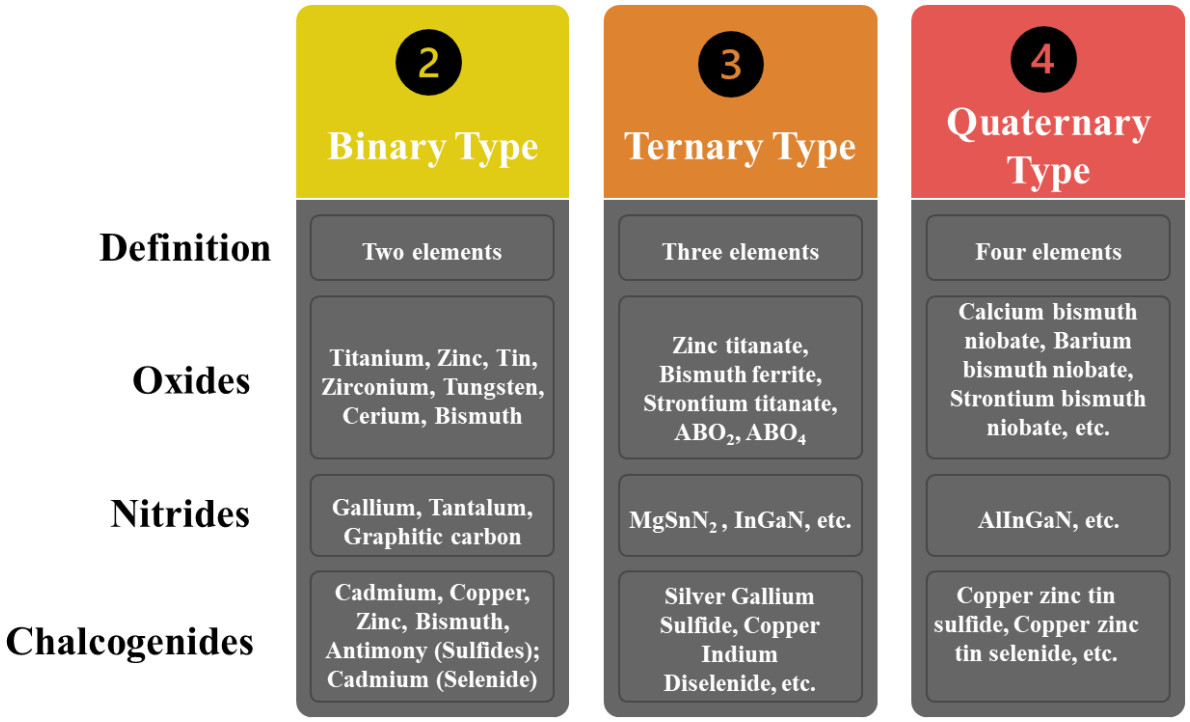

Figure 1.1.Classification of photocatalytic semiconductor.

1.5. Historical Background of Dyes and Their Classification

The history of dyes spans over years, beginning with natural colorants extracted from plants, animals, and minerals. Archaeological evidence indicates that the earliest use of natural dyes dates back to 2600 BC in ancient China, where various organic and inorganic materials were employed to color textiles [90]. The Stockholm Papyrus from the Hellenistic period contains over a hundred recipes for dye manufacturing and application, demonstrating the advanced understanding of dyeing processes in ancient civilizations [91].

The modern synthetic dye industry began in 1856 with William Perkin's accidental discovery of mauveine, the first synthetic dye, while attempting to synthesize quinine for malaria treatment [92]. This breakthrough revolutionized the textile industry and led to the rapid development of synthetic colorants with improved properties and colour fastness [93]. The transition from natural to synthetic dyes marked a significant milestone in industrial chemistry and materials science [93].

The classification of dyes has evolved with advances in chemical understanding and application requirements. Traditional classification systems were based on colour or natural source, while modern approaches consider chemical structure, application method, and fiber compatibility. The development of reactive dyes in the mid-20th century represented another major advancement, providing permanent chemical bonding with textile fibers [94].

Contemporary dye classification systems recognize various categories including acid dyes, basic dyes, direct dyes, reactive dyes, disperse dyes, and vat dyes [93]. Each class exhibits distinct chemical properties, application methods, and environmental behavior. Understanding these classifications is crucial for developing effective treatment strategies and designing targeted photocatalytic systems for dye degradation. Methylene blue (MB), methyl orange, Congo red, and Rhodamine B are synthetic organic dyes that are used a lot in industry (Figure 1.3).

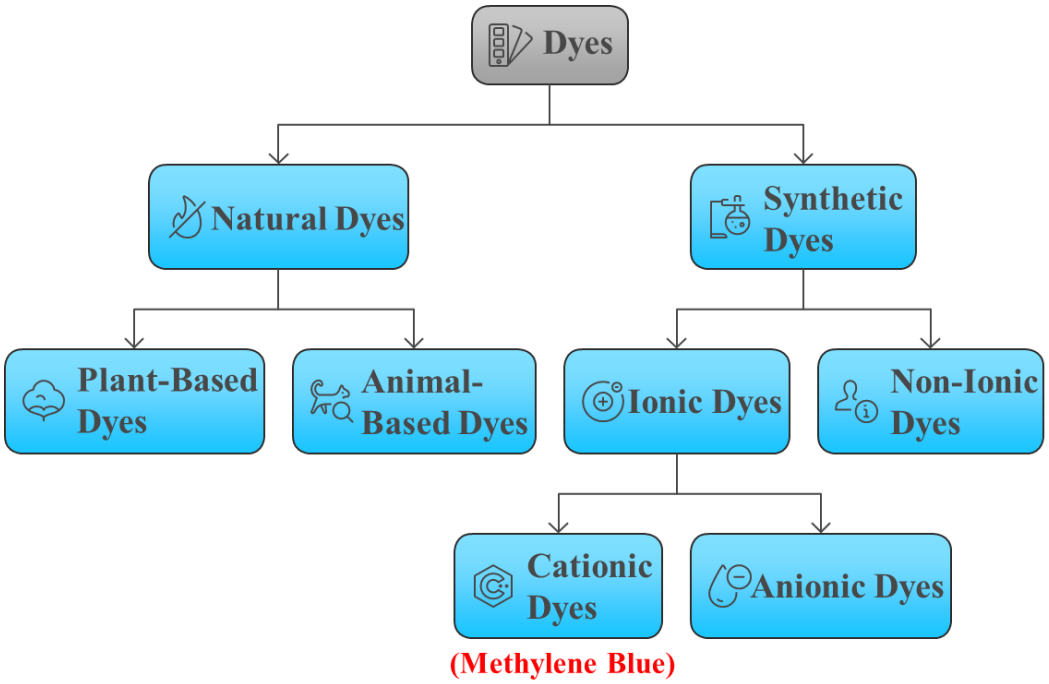

Figure 1.2.Classification of dyes.

1.5.1. Methylene Blue (MB) Dye

Methylene blue ($C_{16}H_{18}ClN_3S$) is a thiazine dye discovered by German chemist Heinrich Caro in 1876, representing one of the most widely studied and utilized synthetic dyes in both industrial and research applications [95]. This cationic dye is characterized by its intense blue color, high water solubility, and strong affinity for negatively charged surfaces, making it an ideal model compound for photocatalytic degradation studies [96]. The molecular structure consists of a phenothiazine core with dimethylamino substituents, providing characteristic optical and electrochemical properties [96].

The widespread use of methylene blue in textile, pharmaceutical, and biological applications has led to its frequent occurrence in industrial wastewater [96]. Despite its utility, methylene blue poses environmental and health concerns due to its persistence in aquatic systems and potential toxicity to marine organisms [97]. The dye can cause hemolysis and reduce the oxygen-carrying capacity of blood when present in significant

concentrations [98]. These factors have driven extensive research into effective removal and degradation methods.

Methylene blue serves as an excellent model pollutant for evaluating photocatalytic materials due to its well-characterized properties and standardized testing protocols [99], [100]. The dye exhibits strong absorption in the visible region with a characteristic peak around 664 nm, allowing for easy monitoring of degradation kinetics through UV-vis spectroscopy [99]. The photocatalytic degradation of methylene blue typically proceeds through the formation of reactive oxygen species, leading to the breakdown of the aromatic structure and eventual mineralization [100].

Methylene blue was chosen as the model pollutant because it is a widely used industrial dye, is highly visible in water, and is easy to monitor spectroscopically during degradation. It is also a persistent and toxic cationic dye, so it serves as a relevant representative contaminant for evaluating photocatalytic wastewater treatment materials.

In addition, MB has a strong absorption peak in the visible region, which makes its concentration changes simple to track by UV-Vis spectroscopy, allowing clear kinetic analysis of photocatalytic performance. For these reasons, it is commonly used as a standard probe molecule in photocatalysis studies.

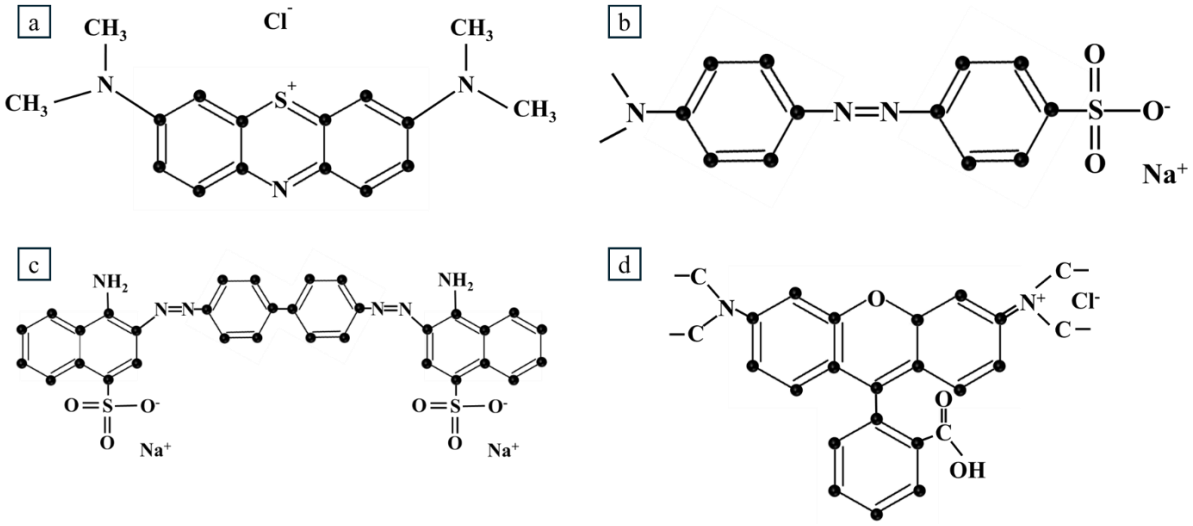

Figure 1.3. Chemical Structure of (a) Methylene blue (MB), (b) Methyl orange, (c) Congo Red and (d) Rhodamine B dyes.

1.6. Treatment Methods for Removal of Dyes

The removal of dyes from wastewater requires sophisticated treatment approaches due to their complex chemical structures, high stability, and resistance to conventional biological processes [101]. Traditional treatment methods include physical adsorption, chemical coagulation, membrane filtration, and biological treatment, each with distinct advantages and limitations [101]. The selection of appropriate treatment methods depends on factors such as dye concentration, chemical structure, discharge volume, and economic considerations [101].

Adsorption has emerged as one of the most widely adopted methods for dye removal due to its simplicity, effectiveness, and cost-efficiency [102]. Various adsorbent materials including activated carbon, metal oxides, biomass, and polymer-based materials have been investigated for their dye removal capabilities [103]. The adsorption mechanism typically involves physical attraction, electrostatic interactions, and chemical bonding between the dye molecules and adsorbent surface [104].

Advanced oxidation processes (AOPs) represent a promising category of treatment technologies that generate highly reactive species capable of mineralizing organic pollutants [105]. These processes include photocatalysis, ozonation, Fenton oxidation, and electrochemical oxidation, all of which can effectively degrade recalcitrant dye molecules. Among these, photocatalysis has gained particular attention due to its ability to utilize solar energy and achieve complete mineralization of organic pollutants [106].

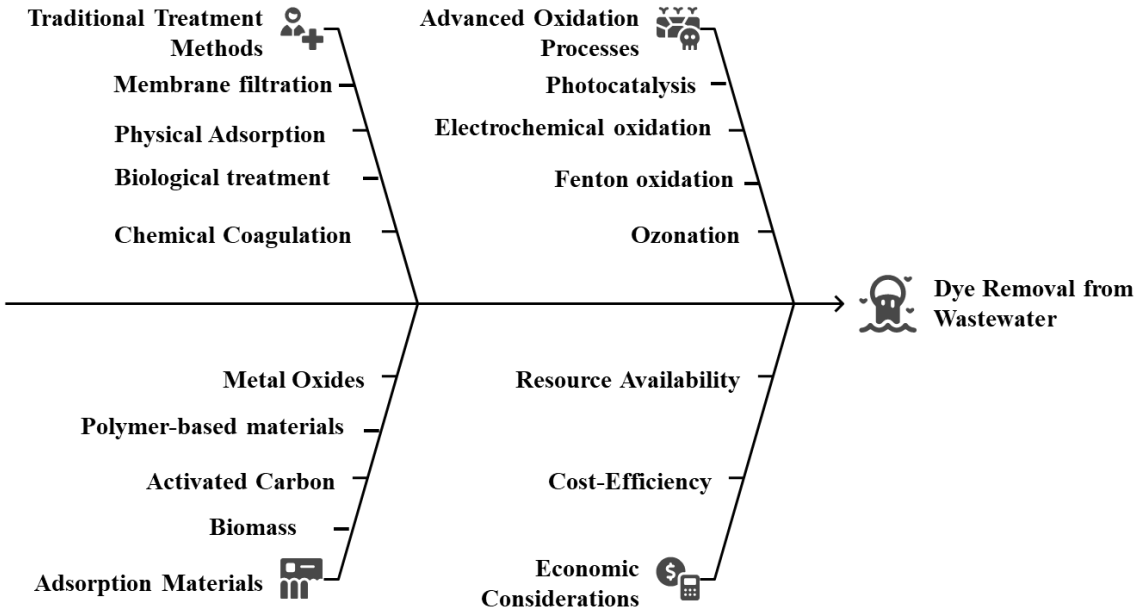

Figure 1.4. Classifications of a dye removal and other related aspects.

1.6.1. Photocatalysis and Photocatalysis Mechanism

Photocatalysis is a light-driven process that utilizes semiconductor materials to generate reactive species capable of degrading organic pollutants and facilitating various chemical transformations [107]. The fundamental mechanism involves three key steps: light absorption, charge carrier generation and separation, and surface redox reactions [108]. When a photocatalyst absorbs photons with energy equal to or greater than its band gap, electrons are promoted from the valence band to the conduction band, creating electron-hole pairs [109].

The photogenerated electrons and holes can migrate to the catalyst surface where they participate in reduction and oxidation reactions, respectively [2]. Electrons typically reduce molecular oxygen to form superoxide radicals ($O_2^{\cdot -}$), while holes can directly oxidize organic molecules or react with water/hydroxide ions to form hydroxyl radicals ($^{\cdot}OH$) [2]. These reactive oxygen species are highly oxidizing and can effectively degrade organic pollutants through various pathways including hydrogen abstraction, electron transfer, and addition reactions [2].

The efficiency of photocatalytic processes is governed by the competition between productive surface reactions and unproductive recombination of charge carriers [110]. Recombination can occur in the bulk material or at surface trap states, representing energy loss that reduces overall quantum efficiency [34]. Strategies for minimizing recombination include surface modification, composite formation, and the incorporation of electron acceptors or hole scavengers [34].

Photocatalytic semiconductors can be classified based on various criteria including chemical composition, crystal structure, band gap energy, and operational mechanisms [109]. The most common classification is based on the band gap energy, dividing materials into UV-active (band gap > 3.0 eV) and visible light-active (band gap < 3.0 eV) photocatalysts [111]. UV-active photocatalysts include TiO_2, ZnO, and $SrTiO_3$, while visible light-active materials encompass $BiVO_4$, WO_3, and various doped semiconductors.

Another classification approach considers the photocatalytic mechanism, distinguishing between direct and indirect band gap semiconductors [112]. Direct band gap materials exhibit stronger optical absorption and more efficient electron-hole pair generation, while indirect band gap materials require phonon assistance for optical transitions [112]. The

choice between direct and indirect semiconductors depends on the specific application requirements and operational conditions.

Composite photocatalysts represent a distinct class that combines multiple semiconductor components to achieve enhanced performance. These systems can be further classified based on their heterojunction type (Type I, Type II, or Z-scheme) and the nature of component interactions [38]. Z-scheme photocatalysts have gained particular attention due to their ability to maintain strong redox capability while achieving efficient charge separation.

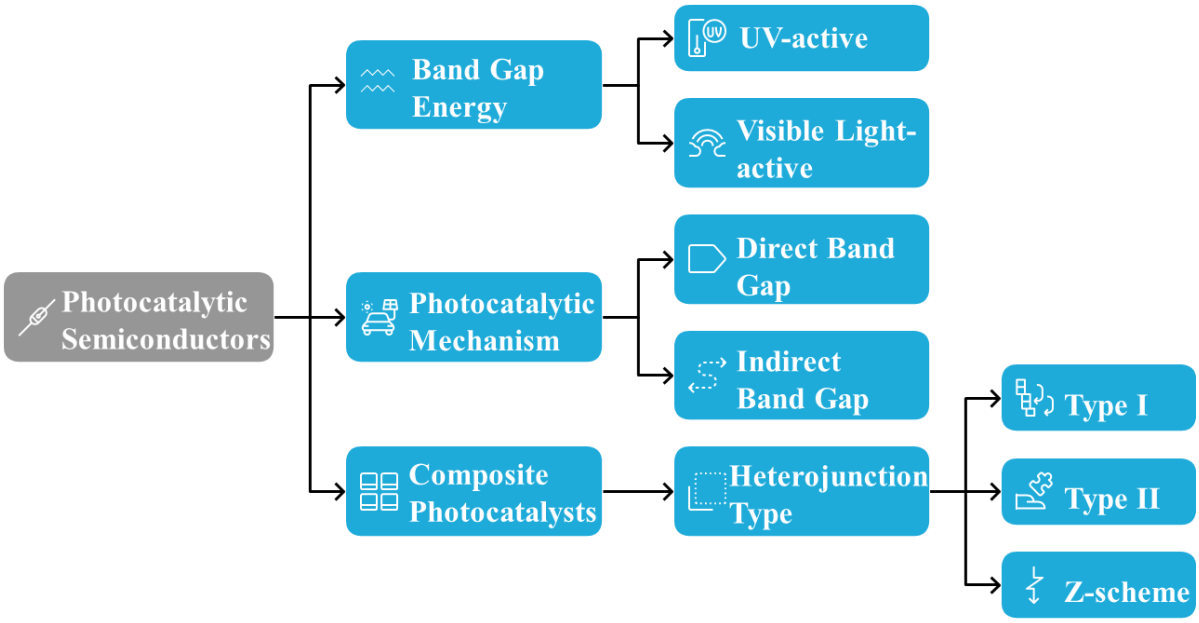

Figure 1.5. Classification of photocatalytic semiconductors based on band gaps, mechanism, and composite heterojunction configuration.

1.6.2. Factors Affecting the Photocatalysis

The efficiency of photocatalytic processes is influenced by numerous factors that can be broadly categorized into intrinsic material properties and external operational conditions [112]. Intrinsic factors include recombination time, band gap energy, crystal structure, surface area, particle size, and defect concentration, while external factors encompass

light intensity, pH, temperature, dissolved oxygen concentration, and pollutant concentration [107]. Understanding and optimizing these factors is crucial for achieving maximum photocatalytic efficiency.

Charge carrier recombination time is an important intrinsic factor in photocatalysis. It is the average time that photogenerated electrons and holes stay apart before they are recombine. Shorter recombination times cause charge carriers to lose their charge quickly, which lowers the quantum efficiency of photocatalytic reactions. However, techniques like heterojunction formation, doping, or surface passivation can increase this lifetime to microseconds or longer, making redox processes at the catalyst surface more effective. To improve overall photocatalytic performance, especially in applications like water splitting and pollutant degradation, it is important to optimise recombination time through material design.

Solar intensity and wavelength significantly affect the rate of electron-hole pair generation and overall photocatalytic activity [106]. Higher solar intensities generally lead to increased reaction rates up to a saturation point where all available photocatalyst sites are activated. The wavelength dependence is determined by the band gap energy of the photocatalyst, with optimal performance achieved when the incident photon energy matches or exceeds the band gap [112].

However, the effect is not unlimited. At very high intensity, the gain may level off because the catalyst surface becomes saturated, charge recombination can increase, and mass-transfer limitations may start to dominate.

Solution pH plays a critical role in photocatalytic processes by affecting the surface charge of the catalyst, the speciation of pollutants, and the formation of reactive species. The point of zero charge (PZC) of the photocatalyst determines the surface charge at

different pH values, influencing the adsorption of charged pollutants and the efficiency of charge transfer processes [86]. Optimal pH conditions vary depending on the specific photocatalyst and target pollutant.

Temperature effects in photocatalysis are complex, with opposing influences on different process steps [112]. While higher temperatures generally increase reaction rates and improve mass transfer, they can also promote undesirable recombination processes and reduce the adsorption of reactants. The optimal operating temperature represents a balance between these competing effects.

1.6.3. Visible Light-Induced Photocatalysis

Visible light-induced photocatalysis represents a significant advancement in environmental remediation and sustainable energy technologies, as it enables the utilization of solar radiation and artificial lighting for driving photochemical processes [113]. The development of visible light-active photocatalysts addresses the major limitation of conventional UV-active materials, which can only utilize a small fraction of the solar spectrum. This advancement has important implications for the practical application and economic viability of photocatalytic technologies.

The extension of photocatalytic activity into the visible light region can be achieved through various strategies including band gap narrowing, sensitization, and the creation of mid-gap states [2]. Band gap narrowing can be accomplished through doping with metal or non-metal ions, which introduces new energy levels within the forbidden gap. Sensitization involves the use of dye molecules or narrow band gap semiconductors that can absorb visible light and inject electrons into the conduction band of wide band gap photocatalysts.

The mechanism of visible light photocatalysis can involve direct excitation of the photocatalyst or indirect processes through sensitization [113]. In direct excitation, visible light photons promote electrons from dopant levels or defect states to the conduction band, while in sensitization mechanisms, visible light is absorbed by sensitizer molecules that subsequently inject electrons into the photocatalyst. The choice of mechanism depends on the specific material system and application requirements.

Recent advances in visible light photocatalysis have revealed new mechanisms such as the formation of intra-band transitions through organic compound adsorption on wide band gap semiconductors [114]. This mechanism enables visible light activity in materials traditionally considered UV-active, expanding the range of potential photocatalytic materials [115]. Understanding these mechanisms is crucial for the rational design of next-generation visible light-active photocatalysts.

1.7. Metal Oxide Semiconductor for Visible Light-Induced Photocatalysis

Metal oxide semiconductors represent the most extensively studied class of photocatalytic materials due to their chemical stability, biocompatibility, and favorable electronic properties [116]. Common metal oxides such as TiO_2, ZnO, Fe_2O_3, and WO_3 exhibit excellent photocatalytic activity, though many are limited to UV light activation due to their wide band gaps [117]. The development of visible light-active metal oxide photocatalysts has become a major research focus, with strategies including doping, composite formation, and morphological control.

The electronic structure of metal oxide semiconductors is characterized by oxygen 2p orbitals forming the valence band and metal d or s orbitals constituting the conduction band [118]. The band gap energy is determined by the energy difference between these

bands, which can be modified through various approaches [114]. The band edge positions relative to the water redox potentials determine the thermodynamic feasibility of photocatalytic water splitting and pollutant degradation reactions.

Binary metal oxides such as $ZnTiO_3$ and composite systems like NiO-ZnO have shown promise for visible light photocatalysis due to their tailored electronic structures and enhanced charge separation properties [119], [120], [121]. These materials often exhibit improved performance compared to their individual components due to heterojunction formation and synergistic effects [121] The design of such systems requires careful consideration of band alignment, interface engineering, and morphological control.

1.7.1. Zinc Titanate ($ZnTiO_3$) Structure and Its Properties

Zinc titanates ($ZnTiO_3$) are a type of oxide that has three parts and a perovskite-type (ABO_3) structure. Previous studies have demonstrated that $ZnTiO_3$ operates as an n-type semiconductor [122]. Zinc titanate has many different phases, and the ones that form depend on how it is heated. When ZnO and TiO_2 are mixed together, they can form many different crystalline phases of zinc titanate, such as cubic, rhombohedral, and spinel. The type of phase that forms depend on how the mixture is heated [123]. Additionally, the ZnO-TiO_2 combination, zinc titanate, can be found in different forms, such as cubic with the unit formula $ZnTiO_3$, rhombohedral (or hexagonal) with the unit formula $ZnTiO_3$, cubic spinel with Zn_2TiO_4, and cubic with the unit formula $Zn_2Ti_3O_8$ [124]. The phases appear at different temperatures, so the phase found in ZTO will be greatly affected by the thermal treatment history of ZnO-TiO_2 systems (Figure 1.6) [123], [124], [125]. There are two important phases of ZTO: one at low temperature that has cubic symmetry and the other at high temperature that has rhombohedral symmetry. Both of these phases have the same unit formula, $ZnTiO_3$ [122], [126].

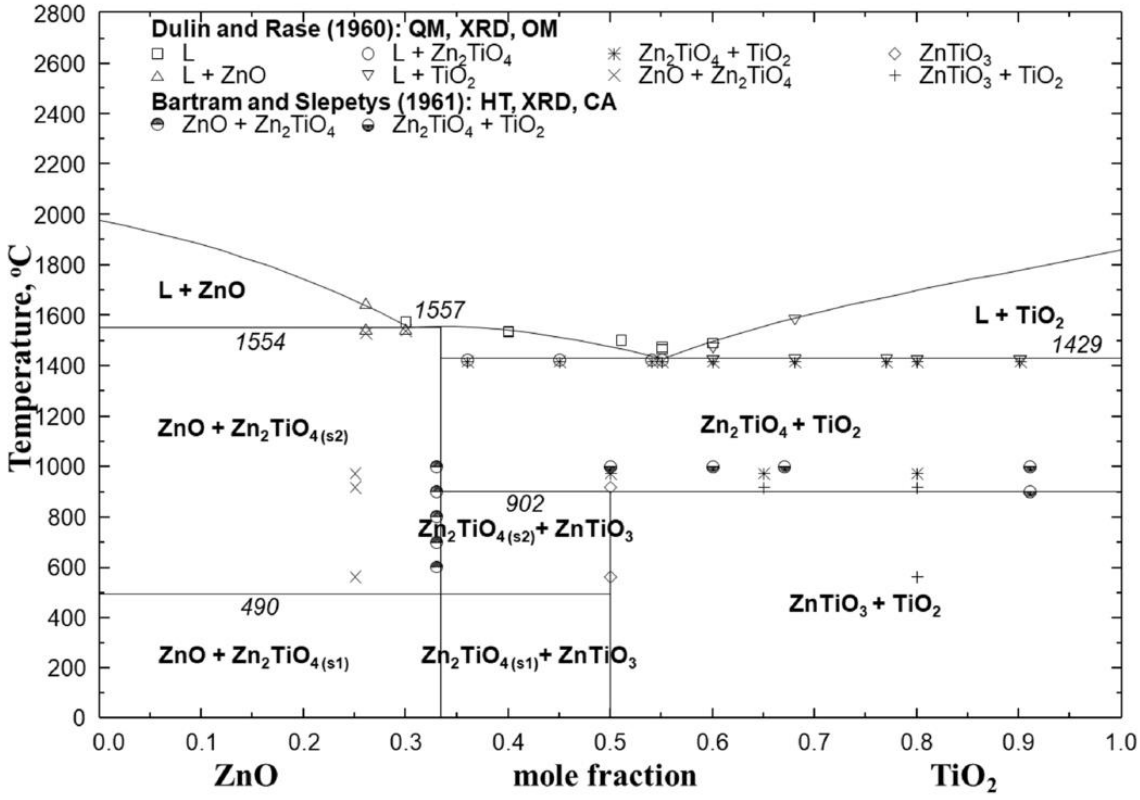

Figure 1.6. Phase diagram of ZnO-TiO2 (adapted)[127]

Zinc titanate cubic structure has a face-centered cubic lattice with Fm-3m space group symmetry (Figure 1.7 (b)), where Zn^{2+} cations mostly fill tetrahedral sites that are connected to four oxygen atoms. Ti^{4+} ions, on the other hand, fill octahedral sites that are surrounded by six oxygen atoms.

Zinc titanate ($ZnTiO_3$) crystallizes in the ilmenite structure with trigonal R-3 space group symmetry, where Ti^{4+} and Zn^{2+} cations occupy octahedral sites coordinated by six oxygen atoms (Figure 1.7 (a)) [119]. The crystal structure features distorted TiO_6 and ZnO_6 octahedra that share corners and edges, creating a three-dimensional framework with specific bond lengths and angles [128].

The electronic structure of $ZnTiO_3$ is characterized by a band gap energy suitable for visible light absorption, making it an attractive candidate for photocatalytic applications

[114]. The valence band is primarily composed of O 2p orbitals with some contribution from Zn 3d states, while the conduction band consists mainly of Ti 3d orbitals [129]. This electronic configuration results in favorable band edge positions for photocatalytic redox reactions and enables visible light activation.

$ZnTiO_3$ has demonstrated excellent photocatalytic activity for the degradation of various organic pollutants under visible light irradiation. Studies have shown that $ZnTiO_3$ synthesized through sol-gel methods exhibits high crystallinity and enhanced photocatalytic performance compared to other synthesis routes [120]. The photocatalytic mechanism involves the generation of reactive oxygen species, particularly hydroxyl radicals and superoxide ions, which effectively degrade organic contaminants.

The photocatalytic performance of $ZnTiO_3$ can be further enhanced through morphological control, surface modification, and composite formation [119]. Nanostructured $ZnTiO_3$ with high surface area and optimized crystal facets exhibits improved light absorption and charge separation efficiency.

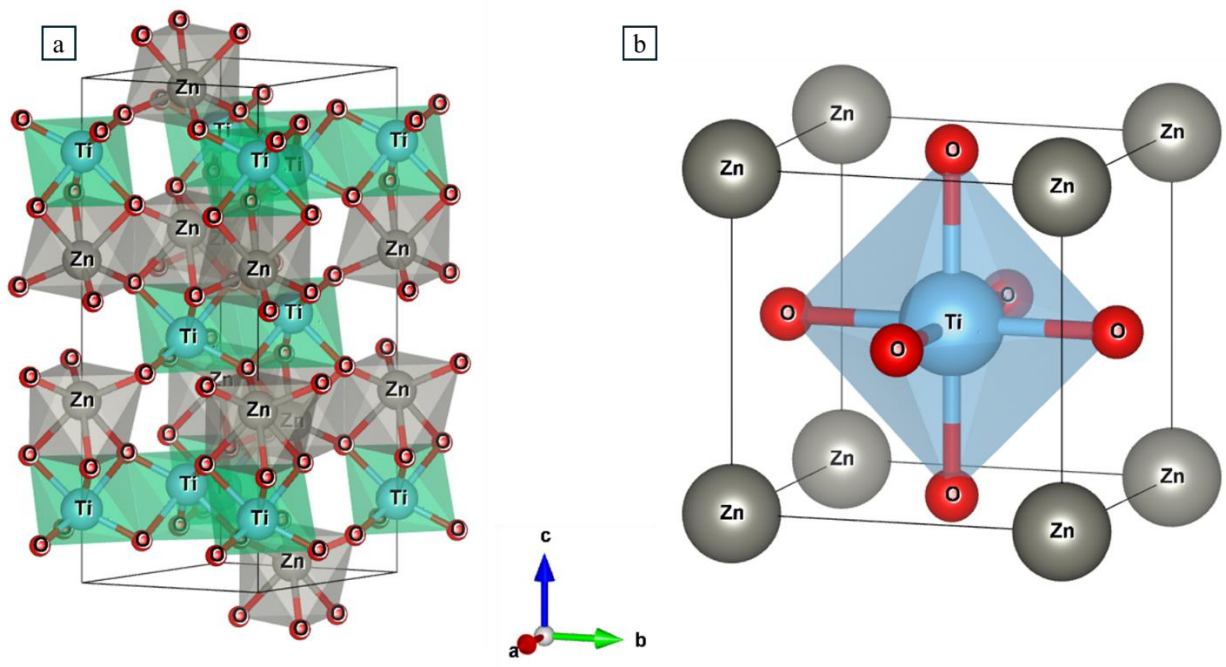

Figure 1.7. (a) Rhombohedral zinc titanate with a lattice parameter a = b = 5.13 Å, and c = 14.08 Å, and (b) Cubic zinc titanate with a lattice parameter a = b = c = 3.84 Å.

1.7.2. NiO-ZnO Structure and Its Properties

The NiO-ZnO composite system represents an important class of heterojunction photocatalysts that combines the unique properties of both component oxides [121]. NiO is a p-type semiconductor with a band gap of approximately 3.6-4.0 eV, while ZnO is an n-type semiconductor with a band gap of 3.37 eV [130]. The formation of p-n heterojunctions between these materials creates built-in electric fields that facilitate charge separation and enhance photocatalytic activity.

The crystal structure of NiO features a face-centered cubic rock salt structure, while ZnO adopts a hexagonal wurtzite structure (Figure 1.8) [38]. In composite systems, these materials can form intimate contact at the interface, enabling efficient charge transfer between the components. The morphology of NiO-ZnO composites can be controlled through various synthesis methods, with core-shell and dispersed configurations.

The photocatalytic mechanism in NiO-ZnO composites involves the migration of photogenerated electrons from ZnO to NiO and holes from NiO to ZnO, effectively separating charge carriers and reducing recombination rates [121]. This charge separation mechanism is facilitated by the appropriate band alignment between the two semiconductors. The composite system exhibits enhanced visible light absorption compared to pure ZnO due to the contribution of NiO and interfacial states.

NiO-ZnO composites have demonstrated superior photocatalytic performance for dye degradation under both UV and visible light irradiation [130]. The optimal NiO content and synthesis conditions significantly influence the photocatalytic activity, with excessive NiO loading potentially leading to increased recombination rates [121]. The magnetic

properties of NiO enable easy separation and recovery of the photocatalyst, making it attractive for practical applications.

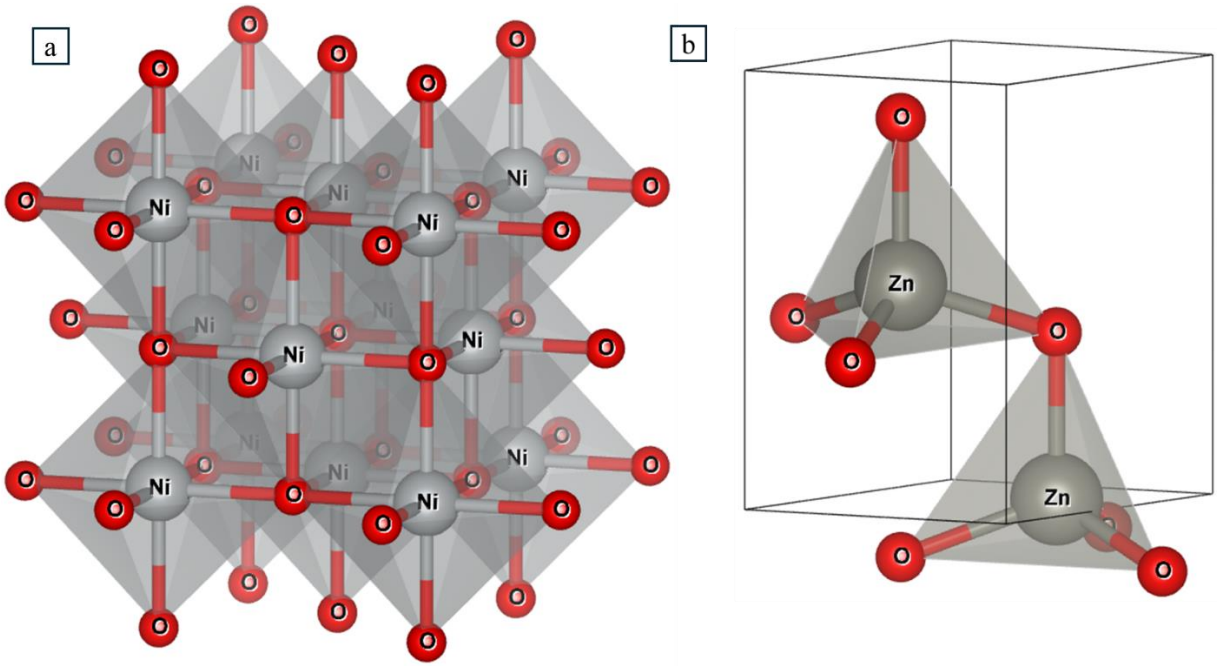

Figure 1.8. (a) Cubic NiO with a lattice parameter a = b = c = 4.19 Å, and (b) Hexagonal ZnO with a lattice parameter a = b = 3.24 Å and c = 5.22 Å.

1.8. 2D Layered Structure and Its Properties

Two-dimensional (2D) layered materials have emerged as a revolutionary class of nanomaterials with unique properties arising from their sheet-like structures and quantum confinement effects [131]. These materials are characterized by strong in-plane bonding and weak interlayer interactions, enabling easy exfoliation into individual layers with thicknesses ranging from single atomic layers to a few nanometers [132]. The reduced dimensionality leads to modified electronic, optical, and catalytic properties that differ significantly from their bulk counterparts.

The high surface-to-volume ratio of 2D materials provides abundant active sites for catalytic reactions, while the layered structure facilitates efficient charge transport and

mass transfer [132]. The electronic structure of 2D materials is often characterized by direct band gaps and high carrier mobility, making them suitable for optoelectronic and photocatalytic applications [131]. The ability to tune properties through layer stacking, chemical functionalization, and heterostructure formation offers unprecedented opportunities for materials design.

2D layered composite photocatalysts represent a promising approach for achieving enhanced photocatalytic performance through the combination of different materials [119]. These composites can exhibit unique properties such as extended light absorption, improved charge separation, and enhanced stability compared to individual components. The rational design of 2D composite photocatalysts requires understanding of interfacial interactions, band alignment, and charge transfer mechanisms.

1.8.1. Graphene Oxide and Their Properties

Graphene oxide (GO) is a heavily oxidized derivative of graphene containing various oxygen-containing functional groups including hydroxyl, epoxy, carboxyl, and carbonyl groups (Figure 1.9 (a)) [132]. The presence of these functional groups renders GO hydrophilic and provides numerous sites for chemical modification and functionalization. The electronic structure of GO is significantly different from pristine graphene, with an increased band gap due to the disruption of the π-conjugated system by oxygen functionalities [133].

The synthesis of graphene oxide is typically achieved through chemical oxidation methods such as the Hummers or modified Hummer's methods [134]. These approaches involve the treatment of graphite with strong oxidizing agents, resulting in the intercalation of oxygen-containing groups and the expansion of interlayer spacing [134].

The degree of oxidation can be controlled through reaction conditions, affecting the properties and applications of the resulting GO [134].

GO exhibits unique properties that make it attractive for photocatalytic applications, including high surface area, excellent dispersibility in aqueous solutions, and the ability to act as both electron acceptor and donor [131]. The oxygen-containing functional groups provide anchoring sites for the attachment of semiconductor nanoparticles, enabling the formation of stable composite materials [9]. The electronic properties of GO can be tuned through reduction processes, allowing for the optimization of charge transfer characteristics [131]. Reduced graphene oxide (Figure 1.9 (b)) is synthesized by removing oxygen functional groups through chemical, thermal, or electrochemical reduction methods. This restores the sp^2 carbon network and greatly improves electrical conductivity, mechanical strength, thermal and photocatalytic properties compared to graphene oxide.

The role of GO in photocatalytic composites is multifaceted, serving as a precursor for graphene, a cross-linked framework for constructing aerogel photocatalysts, a macromolecular surfactant, and a two-dimensional growth template [132]. GO can also function as a photocatalyst by itself under certain conditions, though its activity is generally lower than that of semiconductor-GO composites [117]. The versatility of GO makes it an ideal building block for designing advanced photocatalytic materials.

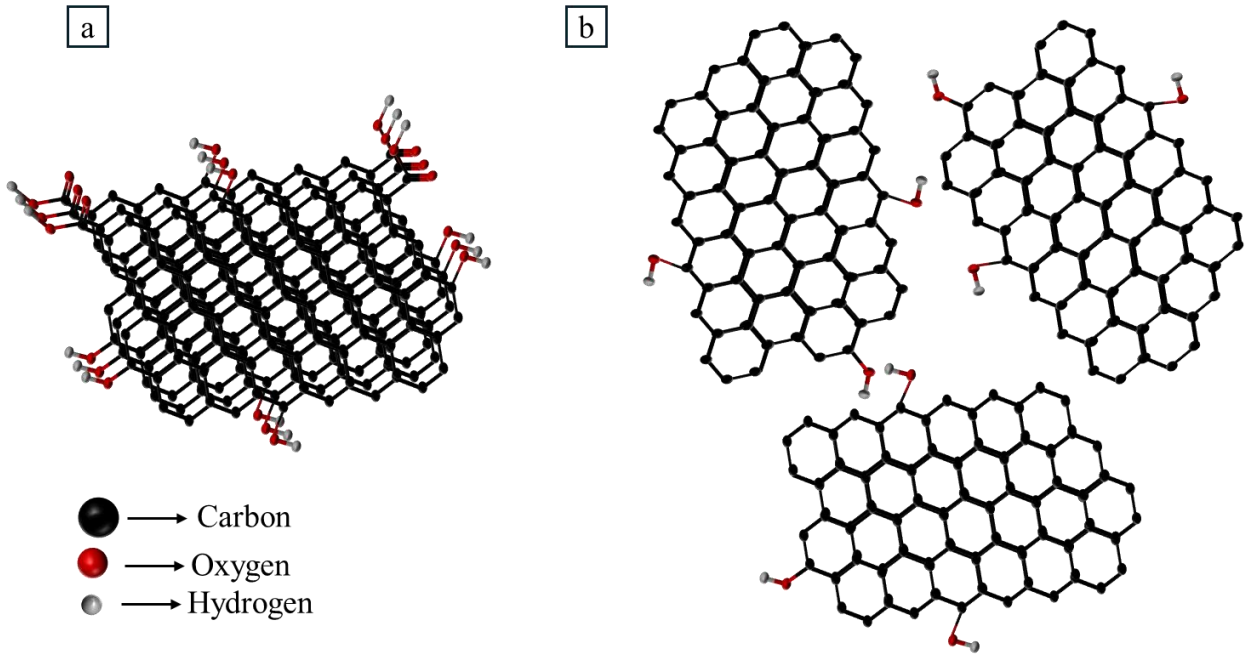

Figure 1.9. Illustration of (a) Graphene Oxide, and (b) Reduced Graphene oxide.

1.9. Metal Oxide Semiconductor and Graphene Oxide Composite Effect on Photocatalysis

The integration of metal oxide semiconductors with graphene oxide represents a significant advancement in photocatalytic materials design, offering synergistic effects that enhance overall performance [9], [117]. The unique properties of GO, including its high surface area, excellent electron mobility, and abundant functional groups, complement the photocatalytic activity of metal oxide semiconductors [131]. The formation of GO-semiconductor composites typically results in improved light absorption, enhanced charge separation, and reduced recombination rates [119].

The mechanism of enhancement in GO-semiconductor composites involves multiple factors including increased surface area, improved light scattering, enhanced charge transport, and modified band structure. GO acts as an electron acceptor, facilitating the separation of photogenerated charge carriers and extending their lifetime. The π-

conjugated structure of GO, even in its oxidized form, provides pathways for electron conduction and can suppress recombination processes [132], [135].

The synthesis of GO-semiconductor composites can be achieved through various methods including in-situ growth, hydrothermal treatment, sol-gel processes, and electrostatic assembly [136]. The choice of synthesis method affects the morphology, interfacial contact, and overall performance of the composite materials. Optimal GO loading is critical, as excessive amounts can lead to light screening effects and increased recombination centers.

Photocatalytic efficiency often increases with GO loading at first because GO improves dispersion, provides more adsorption sites, and helps separate photogenerated electrons and holes by acting as an electron-transport pathway. This usually enhances interfacial charge transfer and reduces recombination, which is why a moderate GO amount can improve activity.

Beyond the optimum concentration, the efficiency can decrease because excess GO starts to cover the active oxide surface, block light from reaching the semiconductor, and promote sheet restacking or agglomeration.

1.9.1. Titanium Dioxide (TiO_2) and Graphene Oxide Composite Effect on Photocatalysis

TiO_2-GO composites represent one of the most extensively studied systems in photocatalytic research due to the excellent properties of both components [137]. The integration of GO with TiO_2 addresses several limitations of pure TiO_2, including rapid charge recombination, limited visible light absorption, and poor adsorption of organic pollutants [137]. The composite formation typically results in enhanced photocatalytic activity under both UV and visible light irradiation.

The enhanced performance of TiO_2-GO composites can be attributed to several factors including improved charge separation through electron transfer from TiO_2 to GO, enhanced light absorption due to the optical properties of GO, and increased adsorption capacity for organic pollutants [138]. The oxygen-containing functional groups on GO provide strong interactions with TiO_2 nanoparticles, ensuring good interfacial contact and efficient charge transfer [138].

Studies have demonstrated that TiO_2-GO composites can achieve nearly 100% degradation efficiency for various organic dyes under natural sunlight irradiation [137]. The synthesis method significantly influences the properties of TiO_2-GO composites, with hydrothermal and sol-gel methods being most commonly employed.

The photocatalytic mechanism in TiO_2-GO composites involves the excitation of TiO_2 upon light absorption, followed by electron transfer to GO sheets [137]. This charge separation reduces recombination rates and allows for more efficient utilization of photogenerated charge carriers. The enhanced visible light activity can be attributed to the photosensitization effect of GO and the formation of Ti-O-C bonds at the interface [138].

1.9.2. Zinc Oxide (ZnO) and Graphene Oxide Composite Effect on Photocatalysis

ZnO-GO composites have attracted significant attention due to their enhanced photocatalytic performance and the complementary properties of both components [139]. ZnO is an n-type semiconductor with excellent photocatalytic activity, while GO provides high surface area and electron transport capabilities [140]. The formation of ZnO-GO composites typically results in improved charge separation, enhanced light absorption, and increased surface area for photocatalytic reactions.

The synthesis of ZnO-GO composites can be achieved through various methods including one-pot synthesis, hydrothermal treatment, and sol-gel processes [139]. The morphology of ZnO nanoparticles can be controlled through synthesis parameters, with common shapes including nanorods, nanoparticles, and nanoflowers [141].

Experimental studies have demonstrated that ZnO-GO composites exhibit superior photocatalytic activity compared to pure ZnO for the degradation of methylene blue and other organic dyes [140]. The enhancement factor can reach up to 3-4 times under visible light irradiation, depending on the GO content and synthesis conditions [139]. The improved performance is attributed to the efficient electron transfer from ZnO to GO, which suppresses recombination and extends charge carrier lifetime [140].

1.9.3. Nickel Oxide (NiO) and Graphene Oxide Composite Effect on Photocatalysis

NiO-GO composites represent an emerging class of photocatalytic materials that combine the p-type semiconducting properties of NiO with the exceptional electronic properties of GO [142]. The formation of NiO-GO composites creates unique heterojunctions that facilitate charge separation and enhance photocatalytic activity [143]. The p-type nature of NiO complements the electron-accepting properties of GO, creating efficient pathways for charge transport [143].

The synthesis of NiO-GO composites typically involves the reduction of nickel precursors in the presence of GO, followed by calcination or hydrothermal treatment [143]. The interaction between NiO and GO can occur through various mechanisms including electrostatic interactions, π-π stacking, and chemical bonding through oxygen-containing functional groups [143]. The morphology and composition of the composites can be controlled through synthesis parameters.

The photocatalytic mechanism in NiO-GO composites involves the generation of electron-hole pairs in NiO upon light absorption, followed by charge transfer processes that separate carriers and reduce recombination rates [144]. GO acts as an electron acceptor and transport medium, facilitating the movement of charges to reactive sites [136]. The composite formation also enhances light absorption and provides additional surface area for photocatalytic reactions.

Recent studies have demonstrated the potential of NiO-GO composites for various photocatalytic applications including dye degradation, water splitting, and air purification. The performance of these composites is highly dependent on the GO content, synthesis method, and operating conditions. The development of three-dimensional NiO-GO architectures has shown promise for improving mass transfer and light utilization efficiency.

1.10. Density Functional Theory (DFT)

Density Functional Theory (DFT) has emerged as a powerful computational tool for understanding and predicting the electronic, structural, and optical properties of metal oxide semiconductors [145]. DFT provides a quantum mechanical framework for calculating the ground-state properties of many-electron systems by expressing the total energy as a functional of the electron density [145]. This approach has been instrumental in advancing the fundamental understanding of photocatalytic materials and guiding experimental design efforts.

The application of DFT to metal oxide semiconductors involves solving the Kohn-Sham equations within appropriate exchange-correlation functionals [146]. Common functionals include the local density approximation (LDA), generalized gradient approximation (GGA), and hybrid functionals that incorporate exact exchange [145]. The

choice of functional significantly affects the accuracy of calculated properties, particularly band gaps and magnetic properties.

DFT calculations can provide valuable insights into various properties of metal oxide semiconductors including band structure, density of states, formation energies, and optical absorption spectra [147]. These calculations complement experimental characterization techniques and can help explain observed phenomena such as photocatalytic activity, defect formation, and dopant incorporation [148]. The predictive capability of DFT enables the screening of potential materials before synthesis, significantly accelerating materials discovery processes.

1.10.1. DFT for Metal Oxide Semiconductor

The electronic structure calculations of metal oxide semiconductors using DFT provide fundamental insights into their photocatalytic properties [147]. The band structure calculations reveal the nature of electronic transitions, band gap energies, and the dispersion of electronic states throughout the Brillouin zone [145]. The density of states (DOS) analysis helps identify the contribution of different atomic orbitals to the valence and conduction bands, providing information about the chemical bonding and electronic properties.

DFT calculations have been extensively applied to study the electronic properties of common photocatalytic materials such as TiO_2, ZnO, and other metal oxides [10]. These studies have revealed the orbital contributions to band edges, the role of crystal structure on electronic properties, and the effects of different polymorphs on photocatalytic activity [10]. The calculated band edge positions can be compared with experimental values to validate the computational approach and provide thermodynamic insights into photocatalytic reactions.

The challenges in DFT calculations of metal oxide semiconductors include the accurate treatment of correlation effects, particularly in materials containing transition metals with partially filled d orbitals [149]. Standard DFT functionals often underestimate band gaps and fail to describe strongly correlated systems accurately. The use of DFT+U methods or hybrid functionals can improve the description of these systems by better accounting for electron correlation effects.

1.10.2. DFT for Composite of Metal Oxide Semiconductor

DFT calculations of composite metal oxide semiconductors present additional challenges due to the need to model interfaces, heterojunctions, and complex structures. The computational modeling of composite materials requires careful consideration of interface structures, charge transfer mechanisms, and band alignment at heterojunctions [145]. These calculations provide insights into the enhanced photocatalytic performance observed in experimental composite systems.

The study of heterojunction formation in composite materials involves calculating the band alignment between different semiconductor components. DFT calculations can predict the type of heterojunction (Type I, Type II, or Z-scheme) based on the relative positions of band edges. This information is crucial for understanding charge transfer mechanisms and designing efficient photocatalytic systems. The formation of interface states and their effects on electronic properties can also be investigated through DFT calculations [46].

Composite materials involving 2D materials such as graphene oxide require special attention to van der Waals interactions and interlayer coupling effects [150]. Standard DFT functionals may not accurately describe these weak interactions, necessitating the use of dispersion-corrected functionals or van der Waals density functionals. The

electronic properties of graphene oxide composites are particularly sensitive to the degree of oxidation and the nature of interfacial interactions.

The computational cost of studying composite materials can be significant due to the need for large supercells and the complexity of the systems. Various approximations and modeling strategies have been developed to make these calculations tractable while maintaining accuracy.

1.10.3. DFT for Doping in Metal Oxide Semiconductor

DFT calculations of doped metal oxide semiconductors provide valuable insights into the effects of dopant incorporation on electronic structure, stability, and photocatalytic properties [10]. The theoretical study of doping involves calculating formation energies, electronic structures, and defect levels introduced by foreign atoms in the host lattice [46]. These calculations help predict optimal doping concentrations and identify the most effective dopant species for specific applications.

The formation energy calculations determine the thermodynamic stability of doped systems and the conditions under which dopant incorporation is favorable. The formation energy depends on factors such as chemical potentials of constituent elements, defect charge states, and the Fermi level position [145]. These calculations can predict the solubility limits of dopants and the conditions for avoiding secondary phase formation.

The electronic structure of doped systems reveals the effects of dopant incorporation on band structure, density of states, and the formation of localized defect states [147]. Metal dopants in oxide semiconductors can introduce d-orbital states within the band gap, affecting optical absorption and charge transport properties [147]. The position and nature of these states determine whether the dopant acts as a shallow donor/acceptor or a deep trap center.

DFT calculations can predict the effects of doping on optical properties, including changes in band gap energy, absorption spectra, and photocatalytic activity. The comparison between calculated and experimental optical properties provides validation of theoretical models and helps interpret experimental observations. These calculations are particularly valuable for understanding the mechanisms of visible light activation in doped photocatalysts.

In this work, we perform theoretical analysis using the pseudopotential DFT-based first-principle method to simulate and analyze the structural, electrical, and optical characteristics of pure and doped $ZnTiO_3$. Quantum Espresso (QE) was utilized to conduct a computation-based analysis of properties. The QE code package utilizes the Generalized Gradient Approximation (GGA) function for performing geometrical optimization and calculating various attributes. $ZnTiO_3$ has a hexagonal symmetrical structure at a temperature near to 900°C, specifically belonging to the 'R-3' space group which has a hexagonal structure. Unit cell that contains 6 Zn atoms, 18 oxygen atoms, and 6 Ti atoms, for a total of 30 atoms. The atom is doped for zinc (Zn). which means $ZnTiO_3$ has undergone A site doping. The computation and analysis of QE were conducted using density functional theory, which incorporates the plane-wave pseudopotential method to provide fast and accurate findings. The electron-ion interaction has been examined using the ultrasoft pseudopotential proposed by GGA. The energy cutoff was set at 340 eV, and a k mesh of 5 × 5 × 2 was used to produce Brillouin zone integrations for geometrical optimization and other calculations.

1.11. Objectives of Thesis Work

The primary objective of this thesis work is to design and develop composite of graphene oxide and metal oxide semiconductor with various methods to enhanced photocatalytic

performance under visible light irradiation and to develop metal doped metal oxide semiconductor with various methods to enhanced photocatalytic performance under visible light irradiation through the systematic integration of experimental synthesis methods and theoretical DFT calculations. The research aims to address the critical limitations like wide band gap and rapid recombination of conventional photocatalysts by creating materials that can efficiently utilize solar radiation for environmental remediation applications. The comprehensive approach combines materials synthesis, characterization, performance evaluation, and computational analysis to achieve fundamental understanding and practical advancement.

The specific objectives include the synthesis of novel composite nanomaterials incorporating metal oxide semiconductors, graphene oxide, and strategic doping elements to achieve optimal photocatalytic performance. The research will investigate various synthesis methods including solid state mixing, liquid state mixing, hydrothermal, and plasma treatment to control morphology, composition, and interfacial properties. The systematic variation of synthesis parameters will enable the optimization of material properties for photocatalytic applications.

A key objective is to establish structure-property relationships through comprehensive characterization using techniques such as X-ray diffraction, electron microscopy, spectroscopic methods, and electrochemical measurements. The photocatalytic performance will be evaluated using methylene blue as a model pollutant under visible light irradiation, with detailed kinetic studies and mechanism investigation. The research aims to achieve superior degradation efficiency compared to existing photocatalytic materials while maintaining long-term stability and reusability.

The integration of DFT calculations represents a crucial objective for providing theoretical understanding of the observed experimental results. The computational studies will focus on electronic structure analysis, band alignment calculations, and the prediction of optimal doping concentrations. The theoretical insights will guide experimental design and help explain the enhanced photocatalytic performance of the developed materials.

1.12. Thesis Outline

This thesis is organized into several chapters that systematically address the design, synthesis, characterization and theoretical understanding of composite materials for enhanced visible light photocatalysis. The structure follows a logical progression from fundamental concepts and literature review to experimental methodology, results discussion, and theoretical analysis.

The present work systematically investigates several modification strategies, including metal oxide-graphene oxide composites, plasma treatment of metal oxides, and doping in $ZnTiO_3$-based systems. Chapter 1 provides a detailed introduction and motivation, while Chapter 2 describes the synthesis routes and characterization techniques used throughout the thesis. In Chapter 3, the influence of graphene oxide compositing on the structural, surface, and electronic properties of $ZnTiO_3$ is examined using different synthesis methods. Chapter 4 focuses on enhancing the photocatalytic activity of $ZnTiO_3$ via nitrogen plasma treatment. Chapter 5 investigates Cu doping in $ZnTiO_3$ assisted by deep eutectic solvents and employs density functional theory to analyse the electronic structure and density of states of Cu-doped $ZnTiO_3$, thereby correlating experimental and computational findings. Chapter 6 extends the doping study by examining Mg-doped $ZnTiO_3$ at different concentrations using DFT to understand how Mg substitution modifies the structural and electronic properties. Chapter 7 then explores the effect of

graphene oxide compositing on other metal oxide systems by studying NiO-ZnO-GO heterostructures. In Chapter 8, the knowledge obtained from these photocatalyst systems is used to design a solar-powered photocatalytic reactor intended for future deployment of these materials, and Chapter 9 presents the overall conclusions and outlines the future scope of the thesis.

Chapter 1: Introduction provides comprehensive background information on nanomaterials, photocatalysis, and the motivation for developing visible light-active composite materials. This chapter establishes the theoretical foundation and identifies the research gaps that the thesis aims to address. It covers various aspects including nanomaterial properties, photocatalytic mechanisms, and computational approaches. It also presets literature review of recent advances in photocatalytic materials, with emphasis on composite systems and visible light activation strategies. This chapter examines the current state of the art, identifies key challenges, and positions the thesis work within the broader context of photocatalytic research. The review covers experimental and theoretical studies relevant to the proposed research objectives.

Chapter 2: Experimental Methodology describes the synthesis procedures, characterization techniques, and experimental protocols used in the research. This chapter provides detailed information on material preparation methods, instrumental techniques, and data analysis procedures. The reproducibility and reliability of experimental methods are emphasized to ensure the validity of research findings.

Chapter 3: In this chapter, we prepare reduced graphene oxide-zinc titanate (ZTO) composite powders by mixing ZTO with 1 wt.% graphene oxide (GO) in solid and liquid states under open environments, and under hydrothermal conditions. The treatment temperature was 400 ^{o}C in the first two cases and 180 ^{o}C in hydrothermal. Structural and

chemical characterizations performed using XRD, SEM, BET, XPS, DRS, and PL are correlated with their photocatalytic performance. Mixing leads to significant structural and chemical changes in GO and ZTO particles but of different natures depending on the process. All the mixing routes reduce GO to r-GO. Unlike hydrothermal mixing, mixing under an open environment converts the rhombohedral $ZnTiO_3$ to cubic $Zn2TiO_4$ due to loss of oxygen. However, hydrothermal mixing leads to a loss in crystallinity of the $ZnTiO_3$ particles resulting into a larger specific surface area. XPS results suggest good binding between the r-GO sheets and the oxide particles. Liquid state mixing leads to the highest reduction in bandgap, probably due to maximal oxygen vacancy formation in this process. Mott-Schottky analysis is done to estimate the charge carrier density in all the samples. EIS shows that the hydrothermally prepared composite has the smallest R_{ct}. High surface area, less conversion to Zn_2TiO_4, changes in bandgap, good binding of ZTO with GO sheets, and more facile charge transfer in hydrothermally prepared composites have important implications in photocatalytic applications.

Chapters 4: In this chapter, we show that photocatalytic activity of rhombohedral zinc titanate under visible light irradiation can be enhanced by nitrogen plasma exposure. The sol-gel prepared rhombohedral zinc titanate was treated with nitrogen plasma prepared in a custom-designed setup that allowed the plasma-treated particles to be immersed in liquid immediately after plasma treatment without bringing them into contact with the ambient environment. We found that plasma treatment resulted in an enhancement of the first-order rate constant of methylene blue (MB) degradation under visible light by approximately 56%. Characterizations of the particles using Scanning Electron Microscopy (SEM), X-ray Photoelectron Spectroscopy (XPS), X-Ray Diffraction (XRD), (Diffuse Reflectance Spectroscopy) DRS, and Brunauer–Emmett–Teller (BET) suggest

that the enhancement can be ascribed to the creation of oxygen vacancies and enhancement in the surface area due to etching.

Chapters 5: This chapter reports the successful synthesis of Cu-doped zinc titanate ($ZnTiO_3$) nanoparticles using a deep eutectic solvent (DES)-assisted approach for enhanced photocatalytic applications. The chloride-based DES system enabled controlled doping and uniform particle morphology at moderate temperatures, offering a greener alternative to conventional high-temperature solid-state methods. Comprehensive characterization through X-ray diffraction (XRD), scanning electron microscopy (SEM), UV-visible spectroscopy, and energy-dispersive X-ray spectroscopy (EDX) confirmed the successful incorporation of Cu dopants into the $ZnTiO_3$ lattice structure. Density functional theory (DFT) calculations revealed that Cu doping introduces intermediate energy states within the bandgap, effectively narrowing the optical bandgap from the pristine $ZnTiO_3$ value and enhancing visible light absorption. The modified electronic structure promotes efficient charge carrier separation and reduces electron-hole recombination rates. The synergistic combination of DES-mediated synthesis and strategic Cu doping presents a promising pathway for developing high-performance photocatalysts for environmental remediation and solar energy conversion applications.

Chapters 6: This chapter shows a detailed analysis of the structural and electronic properties of pure zinc titanate ($ZnTiO_3$) and magnesium (Mg)-doped $ZnTiO_3$ ($Zn_{1-x}Mg_xTiO_3$, where x = 0.167, 0.333, 0.5, and 0.667) and compared with experimental band gap of $ZnTiO_3$. We conducted the analysis using first-principles and density-functional-theory calculations using the Quantum Espresso package. The objective was to investigate the effect of Mg substitution on zinc titanate $ZnTiO_3$. In the pure $ZnTiO_3$ system, calculations reveal an indirect electronic structure gap. At a doping level of 0.333, $ZnTiO_3$ with Mg impurities have an indirect electronic structure gap of 1.81 electron volts

(eV). The investigation of structural and electronic characteristics indicates that x = 0.333 Mg doped $ZnTiO_3$ significantly reduce the electronic structure gap of $ZnTiO_3$ while maintaining the same kind of electronic structure gap, which is an indirect electronic structure gap. The density functional theory study shows that Mg substitution in $ZnTiO_3$ change their electronic structure and density of states and experimental band gap is nearly same as computational band structure gap which validates the exchange-correlation treatment and pseudopotentials employed for the band-structure calculation for this system.

Chapters 7: In this chapter, we prepare composites of NiO, ZnO, and GO with 1% and 10% GO and measure their photocatalytic activity in the MB degradation reaction under visible light illumination. The oxides are prepared by the sol-gel route, and GO is mixed using a hydrothermal method. The rate constant value in the 1% GO and 10% GO composites are, respectively, 1.76 and 2.35 times higher as compared to that in the binary composite of NiO-ZnO. The rate constants with our GO-based composites also compare favourably with previously reported composites. Structural and chemical characterizations performed using XRD, SEM, BET, XPS, DRS, and PL are correlated with their photocatalytic performance. It is found that GO is reduced in the composites to r-GO, and the NiO band gap decreases to the visible range, which we attribute to the bonding of the NiO particles with the GO sheets. We also propose that the composite forms a double heterojunction structure of r-GO/NiO/ZnO. Because of the work function difference between the GO and NiO, the bands bend-up from r-GO to NiO. Since NiO is a p-type semiconductor and ZnO an n-type, the bands bend-down from NiO to ZnO. The band structure thus formed leads to an efficient carrier separation. Overall, we attribute the enhanced rate constants in our samples to the reduction in the NiO band gap so as to

lie in the visible range, causing higher carrier generation, and the formation of double heterostructures, causing more effective carrier separation.

Chapter 8: This chapter explain design of solar-powered photocatalytic reactor system for wastewater treatment by combining solar energy with oxidation methods in a slanted framework that accommodates horizontally positioned photocatalytic tubes and high-efficiency microreactor modules, all energized by a photovoltaic (PV) panel equipped with real-time monitoring electronics. Wastewater continuously enters an inlet manifold, which evenly distributes it into parallel channels lined with economical semiconductor photocatalysts in primary tubes and visible-light-active catalysts in secondary microreactors. Solar irradiation generates electron-hole pairs that produce reactive oxygen species, which mineralize pollutants. The microreactors use microchannels to optimize the catalyst-water interface, improve mass transfer, and increase photon utilization through light scattering, while the photovoltaic system manages pumps, flow, and pressure using sensors. This concept provides swift, nearly total deterioration at a low cost, making it suitable for scalable, decentralized applications in off-grid locations.

Chapters 9: In this chapter, we bring our thesis work to a conclusion and outline some potential scope and suggestions for future work.

1.13. Novelty of the Thesis

The multitype strategy adopted in this work is used to link graphene oxide compositing, plasma treatment, and density functional theory analysis within a unified framework for metal oxide photocatalysts. Several modification routes are designed for $ZnTiO_3$ and related oxides, including plasma treatment and graphene oxide compositing is systematically evaluated. In addition, doping is investigated experimentally, and

complementary DFT calculations are performed to correlate dopant concentration with changes in the electronic structure and band gap.

A detailed literature survey presented in this chapter confirms that, to the best of our knowledge, no prior study has (i) examined nitrogen-plasma-treated $ZnTiO_3$ using a custom reactor that preserves the treated surface during quenching, while correlating oxygen-vacancy formation, dispersion behaviour, and visible-light MB degradation, (ii) established the role of GO content in forming a double heterojunction rGO-NiO-ZnO structure with quantified improvements in photocatalytic kinetics, and (iii) combined DES-assisted Cu doping and systematic Mg doping of $ZnTiO_3$ with first-principles DFT calculations to link dopant concentration with electronic-structure changes and to validate calculated band gaps against experimental values. Therefore, this thesis constitutes the first integrated experimental-computational effort to address these specific gaps for $ZnTiO_3$- and NiO-ZnO-based visible-light photocatalysts

CHAPTER 2

Synthesis Methods and Characterization Techniques

2.1. Synthesis method of nanomaterials

Nanomaterials are typically synthesised using two primary methodologies: the "Top-down" approach and the "Bottom-up" approach [151]. The Top-down method breaks larger bulk materials into smaller molecules, while the Bottom-up method combines smaller atomic-sized materials to make larger bulk materials. Because nanoparticles are smaller, they have more surface area, which makes their properties different from those of bulk materials. This change in size and shape affects properties like how well electricity and heat flow through them. Nanomaterials are used in many fields, including catalysis, medicine, semiconductors, and energy, because they have unique properties. There are many ways to make nanomaterials, such as sol-gel, soft-template, chemical vapour deposition (CVD), hydrothermal synthesis, thermal deposition, green synthesis, and solvothermal approaches. In our current thesis, we employed two methodologies, sol-gel and hydrothermal, to synthesise metal oxide-based nanoparticles and their composites. Figure 2.1 shows a picture of the different steps used to make nanomaterials.

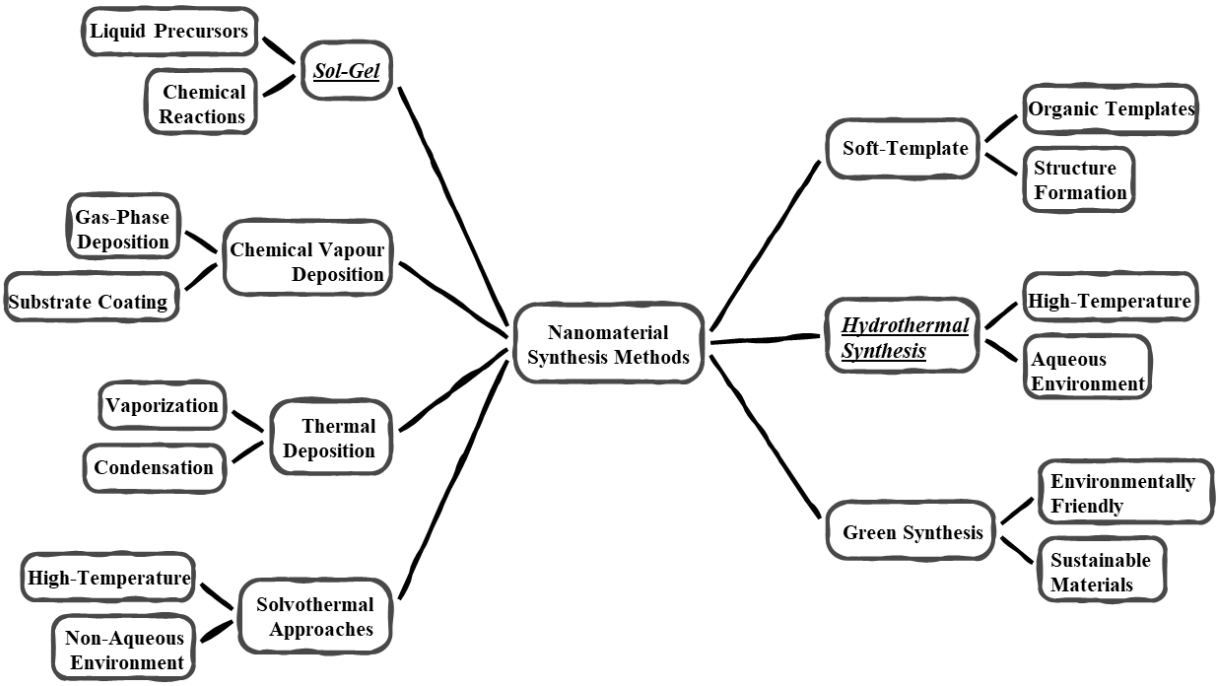

Figure 2.1. Nanomaterials synthesis methods.

2.1.1. Sol-gel method

The sol-gel process is an easy way to change the properties of materials by changing a number of factors, such as the types of precursors, solvents, reaction medium pH, temperature, reaction time, concentration, reagent and catalyst properties, the addition of organic additives, the duration of gelation, and the temperature of calcination [152]. The wet chemical method for making inorganic metal oxides is called "sol-gel processing." The chemistry behind it is based on the hydroxylation and condensation of molecular precursors. Metal alkoxides are likely the most versatile precursors for the sol-gel synthesis of oxides, due to their high reactivity with nucleophilic agents like water [153]. There are two types of solvents used in the sol-gel process: "aqueous" and "non-aqueous." So, in the aqueous sol-gel method, water was the solvent, and in the non-aqueous sol-gel method, organic compounds were the solvents [154]. The chemical reactivity of metal alkoxides concerning hydrolysis and condensation primarily depends on the

electronegativity of the metal atom and its ability to increase its coordination number [155]. A top-down strategy uses a suitable precursor that is smaller in size to make nanoparticles [156]. A top-down approach to the surface architecture of nanoparticles leads to flaws, which are a major problem because surface chemistry and other physical properties depend heavily on surface structure [118]. In bottom-up synthesis, nanoparticles are made by putting together smaller parts [119]. This method starts by making smaller parts, which are then put together to make final particles that are in the nanometre range [157].

2.1.2. Hydrothermal method

The hydrothermal method to synthesise materials using high-temperature, high-pressure water solutions in closed containers (Autoclave) (Figure 2.2). It was first developed from geological research and is now very important for making crystals and nanomaterials. In autoclaves, reactions happen at temperatures above 100 ^{o}C and pressures above 1 atm. Water can dissolve precursors that would normally not dissolve, and it can also help with dissolution-recrystallization pathways with precise control. To help solutes dissolve in the hotter area and settle on seeds in the cooler area, a temperature gradient is usually set up. This allows for controlled nucleation and growth through solution transport and supersaturation. Process parameters, including temperature, pressure, pH, mineralisers, precursor concentration, and duration, affect supersaturation kinetics, nucleation density, and crystal habit, which in turn determine the morphology and phase purity. The main benefits are precise control of particle size, shape, and crystallinity; the ability to reach metastable phases at moderate temperatures; and higher purity through in situ recrystallisation.

Using water as the reaction medium makes the method relatively safe for the environment and eco-friendly. It also encourages environmentally friendly synthesis methods and

lowers the risks that come with using solvents. This method works on a wide range of materials, including oxides, sulphides, phosphates, zeolites, and composites. It makes it easier to grow single crystals and nanostructures with less agglomeration. Some examples are solvothermal methods that use solvents that aren't water, microwave-assisted hydrothermal processes that speed up and even out heating, and near/supercritical water systems that help nucleation and growth. Continuous-flow hydrothermal reactors enable scalable and reproducible nanoparticle synthesis by merging precursor streams with near or supercritical water to induce instantaneous hydrolysis and precipitation. The field progressed from geochemical research to the development of engineered autoclaves that safely contain reactive substances under extreme conditions, thereby improving the range of chemistries and the quality of products. Hydrothermal synthesis has become one of the most popular ways to make functional nanomaterials in both research and industry because it is simple, flexible, and works well at low temperatures. By changing the chemistry of the precursors, mineralisers, and heating methods, it is possible to improve features like phase composition, defect density, and surface area for use in catalysis, electronics, and energy.

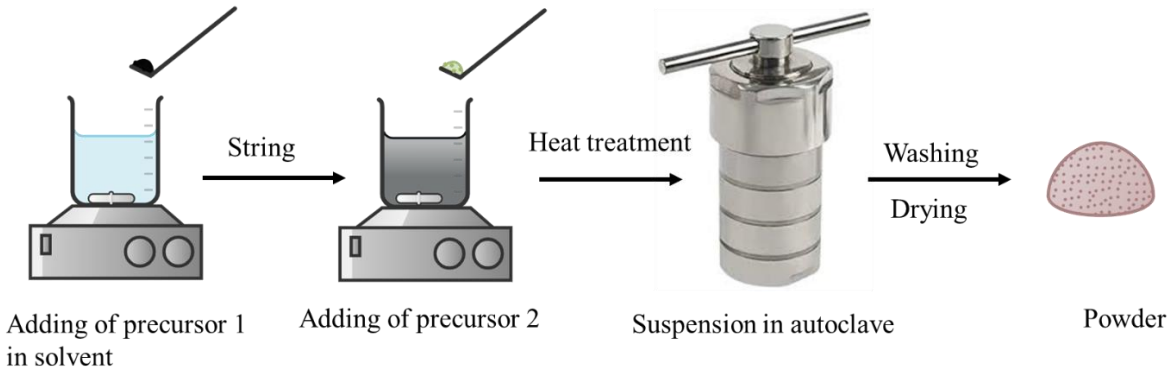

Figure 2.2. Hydrothermal synthesis route.

2.1.3. Hummers' method

The Hummers' method is a standard wet-chemical oxidation process that turns graphite into graphite oxide. This is then broken down into graphene oxide (GO) using $KMnO_4$ and $NaNO_3$ in concentrated H_2SO_4. Modified Hummers' methods make acids and oxidants stronger to make them more useful and efficient. The original Hummers' process, which was first used in 1958, mixes graphite with concentrated sulphuric acid and sodium nitrate. Then, potassium permanganate is added to turn the graphitic lattice into graphite oxide, which is a layered precursor of GO when it is exfoliated. Strong acids first intercalate to make graphite intercalation compounds. Then, permanganate-derived oxidants (like Mn_2O_7 in situ) come in and add oxygen functionality by targeting basal planes and edges. The reaction starts at a low temperature to control exothermicity. It is then heated to complete oxidation, and finally, water is added to help hydrolysis and break the material down into graphene oxide sheets. A hydrogen peroxide quench at about 90-95 °C turns manganese residues into soluble forms and clears up suspensions. This makes brown graphene oxide dispersions with typical high mass yields for graphite oxide (e.g., ~188 g per 100 g graphite), which are then turned into graphene oxide. The resulting substance has epoxide, hydroxyl, carbonyl, and carboxyl groups that make it hydrophilic and make it easier to change the chemical structure and make composites. Modified Hummers' methods (Figure 2.3) get rid of $NaNO_3$ and add more $KMnO_4$, using a mixed acid system (usually 9:1 H_2SO_4/H_3PO_4). This system has been shown to oxidise better than the original formulation. These changes lower the number of reagents needed while keeping high yields and shortening the reaction time, which makes the process more cost-effective and easier to scale up. Despite these differences, the basic order stays the same: acid intercalation, strong permanganate-based oxidation, and water-induced hydrolysis/exfoliation. After that, peroxide quenching is used to get rid of manganese

species. Protocols always say that cold baths should start when $KMnO_4$ is added, that heating should be controlled during deep oxidation, that dilution should be done carefully to avoid uncontrolled exothermic reactions, and that H_2O_2 should be added at the end to make stable GO dispersions. The 9:1 H_2SO_4/H_3PO_4 method is a well-known improvement that gets rid of $NaNO_3$ and raises $KMnO_4$. It is a safe, $NaNO_3$-free way that is widely used in modern laboratory syntheses of GO. Modified Hummers' methods, improve oxidant and acid chemistries to make GO production more efficient and scalable for modern research and applications.

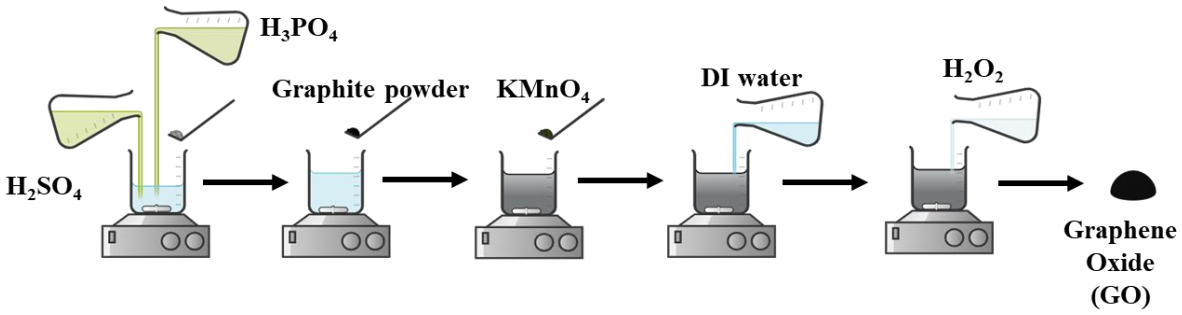

Figure 2.3. Synthesis of graphene oxide by modified Hummers' method.

2.2. Analytical characterization techniques

Analytical characterisation techniques refer to an extensive set of methodologies and instruments utilised to investigate and elucidate the properties, composition, structure, and behaviour of substances and materials. These methods are used in many areas of science, such as chemistry, materials science, biology, environmental science, and pharmaceuticals, to name a few.

The main goal of analytical characterisation is to learn as much as possible about a sample's qualities and characteristics. This information may include things like the elemental makeup, molecular structure, component concentration, surface shape, thermal properties, and more. Analytical characterisation techniques are crucial for advancing

scientific knowledge, promoting technological innovation, and facilitating various industrial applications. Here are some commonly used analytical characterization techniques:

2.2.1. X-ray diffractogram (XRD)

X-ray diffraction (XRD) is a technique for characterising the structure of a crystal by looking at how dispersed X-rays interfere with each other [158]. Furthermore, XRD techniques are utilised to determine the crystal structure of materials by analysing the diffraction pattern produced when X-rays interact with a crystalline sample. X-ray diffraction occurs when the inter-planar distance (d) within a crystal is close to the wavelength (λ) of the X-ray radiation, which is usually the Cu Kα emission line (λ = 1.5406 Å). Diffraction occurs at an angle (θ) when Bragg's law is satisfied as following equation (2.1).

$$2d \sin\theta = n\lambda \tag{2.1}$$

Where, n is an integer value.

A plot of diffraction intensity vs. the angle of reflection (2θ) (diffraction pattern) [159] shows the crystallographic structure of materials. The peak locations can tell you: (i) the average distance between atomic rows, (ii) the direction of a single crystal or grain, (iii) the structure of an unknown material, and (iv) the size, shape, and internal stress of small crystalline areas. As a result, the XRD patterns are used to find out what the materials are made of and how their crystalline phase structure works.

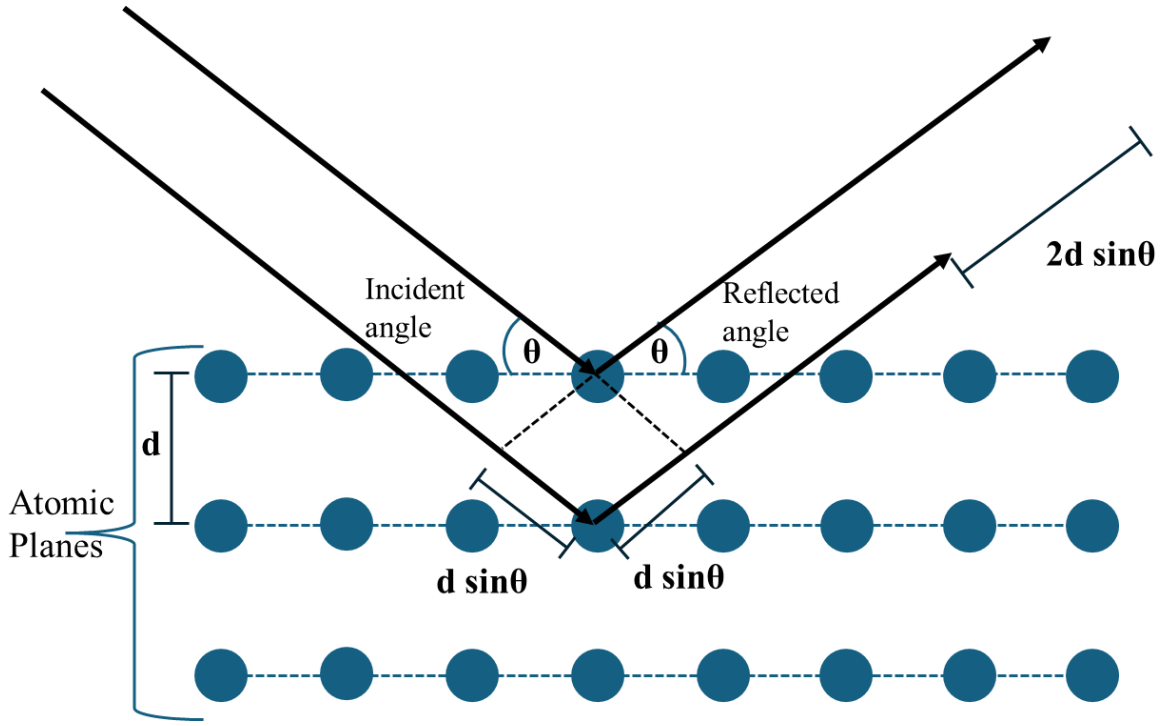

Figure 2.4. Schematic diagram of X-ray diffractogram represents the diffraction of incident x-rays from parallel planes.

2.2.2. Scanning Electron microscopy (SEM)/Energy dispersive X-ray spectroscopy (EDX) analysis

Scanning Electron Microscopy (SEM) is a very adaptable and extensively utilised analytical technique for materials characterisation, providing exceptional insights into surface morphology, topography, and microstructural characteristics at the nanoscale. A scanning electron microscope functions by utilising a precisely focussed electron beam produced by a thermionic or field emission electron cannon, which methodically scans the sample surface in a regulated raster pattern. High-energy electrons, typically accelerated at voltages ranging from 1 to 30 kV, interact with the sample material through elastic and inelastic scattering, producing various signals that convey essential information regarding the sample's surface properties and composition [160].

The core principle of SEM operation is based on the production of secondary electrons (SE), backscattered electrons (BSE), and distinctive X-rays, which serve as the main source of analytical data. Secondary electrons, generated by inelastic scattering with loosely bound outer shell electrons, offer remarkable topographical contrast and are especially responsive to differences in surface shape and roughness. Backscattered electrons, on the other hand, arise from elastic scattering with atomic nuclei and provide compositional contrast due to variations in atomic number, facilitating qualitative phase differentiation in multiphase systems. The spatial correlation between signal intensity and electron beam position, along with suitable magnification levels, enables the production of high-resolution surface images with dimensional accuracy at sub-nanometer scales, significantly surpassing the optical diffraction limit of traditional light microscopy.

A significant constraint of electron microscopy examination of electrically insulating materials arises from electron buildup on the sample surface during electron bombardment. The buildup of surface charge generates localised electrostatic fields that alter the trajectory of the incoming electron beam, leading to significant image deterioration marked by geometric distortion, diminished contrast, and unpredictable beam deflection. This process, referred to as "charging," poses a significant challenge when analysing nanocomposite materials, hydroxide compounds, and oxide systems that typically have high electrical resistivity.

The method for alleviating charging effects entails the application of a conductive metallic overlayer over the insulating sample surface before SEM examination. The sputter-coating method, usually executed with high-purity metals like gold (Au), platinum (Pt), or carbon (C), produces a thin, highly conductive surface sheet typically measuring between 5 and 20 nanometres in thickness. The deposition occurs by physical vapour deposition (PVD) processes, in which metal atoms are released from a target cathode

through energetic ion bombardment in an inert gas environment, and later condense onto the cooled sample substrate. This metallic layer efficiently grounds surface charge while maintaining the essential morphology of the sample, as the coating thickness is significantly less than the typical microstructural characteristics of interest.

Energy Dispersive X-ray Spectroscopy (EDS), also known as Electron Dispersive X-ray Analysis (EDXA) or Energy Dispersive Spectroscopy, is a powerful semi-quantitative analytical method for ascertaining the elemental composition of materials at spatial resolutions near the diameter of the SEM beam. The fundamental principle of EDS analysis is based on the characteristic X-ray emission that results when an incoming electron beam dislodges inner-shell electrons from sample atoms, thereby generating vacancies in low-binding-energy orbitals. Subsequent relaxation processes, during which electrons from higher-energy shells occupy these vacancies, lead to the emission of distinctive X-rays with energies that perfectly correspond to the atomic identity of the emitting element [161].

The morphological characterisation of synthesised nanomaterials in this study was performed using a field emission scanning electron microscope (FE-SEM, JSM-7900 F, JEOL, Tokyo, Japan). Field emission electron sources utilise tunnelling emission from a pointed tungsten cathode under elevated electric field gradients, resulting in significant enhancements in beam brightness and spatial resolution relative to traditional thermionic sources. The JSM-7900 F platform has operational features such as ultra-high-resolution imaging, concurrent imaging modalities (secondary electron and backscattered electron imaging), and integrated analytical functions enabling real-time characterisation. The device features both secondary electron (SE) and backscattered electron (BSE) detectors, facilitating thorough morphological and compositional analysis.

Analysis of elemental composition and chemical dispersion was conducted using a Zeiss electron microscope with an integrated Energy Dispersive X-ray (EDS) analyser. The analytical EDS system functioned at accelerating voltages from 5 to 20 kV, chosen to enhance X-ray production efficiency while reducing sample contact volume and mitigating spatial resolution deterioration. The 5 kV operating condition primarily improves surface-sensitive analysis with superior lateral spatial resolution (generally 0.5-1.0 μm), whereas the 20 kV condition significantly boosts X-ray generation efficiency, enhancing detection sensitivity for trace element analysis, albeit with an increased interaction volume.

Before electron microscopic analysis, all samples preliminary treatment to reduce surface charging artefacts. A thin conductive layer of high-purity gold (Au) was applied to the sample surface via physical vapour deposition (sputter coating) procedures, with the coating thickness regulated to roughly 5-10 nanometres. The gold coating, although providing metallic contrast at high magnifications, does not significantly hinder the visualisation of nanostructural features due to its negligible thickness compared to the sample size.

2.2.3. X-ray photoelectron spectroscopy (XPS)

X-ray photoelectron spectroscopy (XPS) is an advanced surface characterisation method that yields quantitative elemental composition, chemical oxidation states, and electronic structure data from material surfaces. The technique is based on the fundamental concept of the photoelectric effect, in which the absorption of sufficiently intense X-ray photons by a sample result in the emission of core electrons from the surface atoms [162]. X-ray photoelectron spectroscopy functions by irradiating a sample with monochromatic X-rays, usually produced by magnesium (Mg Kα, 1253.6 eV) or aluminium (Al Kα, 1486.6

eV) sources. Upon the impact of high-energy photons on the sample surface, atoms experience photoionisation, resulting in the ejection of core electrons from inner electron shells, each possessing distinct kinetic energies (Figure 2.5). The energy relationship dictating this process is articulated by the fundamental photoelectric equation: [163].

$$E_k = h\nu - BE - \phi \tag{2.2}$$

E_K stands for the kinetic energy of the photoelectrons that are released, BE stands for the binding energy of the electron in an orbital, h stands for Planck's constant, ν stands for the frequency of the incoming radiation, and ϕ stands for the work function of the material's surface. Given that the incident X-ray energy (hν) is constant and accurately determined, the binding energy of each detected photoelectron can be directly computed by measuring its kinetic energy. This binding energy is distinctive to each element and orbital, functioning as an elemental "fingerprint" that facilitates accurate identification [163].

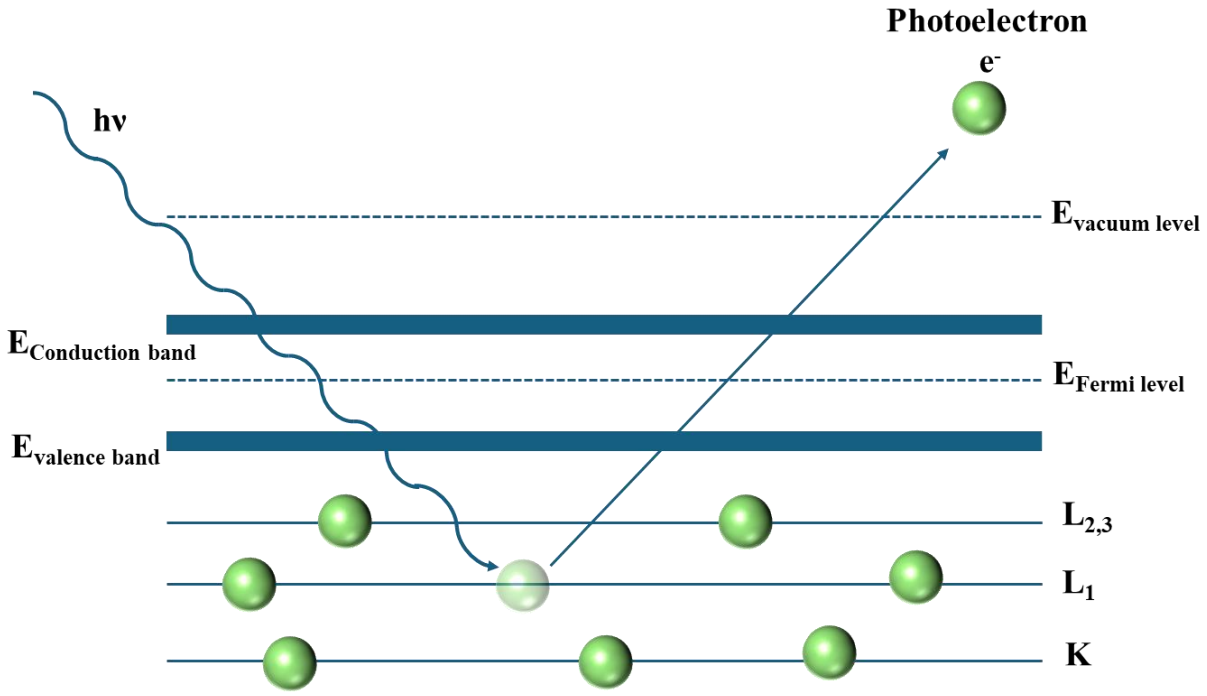

Figure 2.5. Mechanism of photoelectron emission in XPS technique.

XPS necessitates ultra-high vacuum (UHV) conditions with pressures between 10^{-8} and 10^{-10} mbar to avert collisional interactions between emitted photoelectrons and remaining gas molecules, which could distort spectrum characteristics and diminish analytical sensitivity. The approach has remarkable surface sensitivity, with photoelectrons mostly emanating from the uppermost 1-10 nanometres of the material, but the theoretical sample depth may reach around 20 nanometres, contingent upon the photoelectron kinetic energy and matrix composition.

XPS possesses a significant advantage in its capacity to identify not only elemental composition but also the oxidation states and chemical surroundings of individual elements via binding energy (BE) alterations. When an atom engages in chemical bonding or undergoes a change in oxidation state, its core electrons encounter modified electrostatic surroundings, leading to observable variations in binding energy. An elevation in oxidation state (removal of valence electrons) leads to augmented binding energy, whereas the addition of valence electrons diminishes binding energy.

XPS measurement data are generally displayed as intensity (counts per second) vs binding energy. Each peak in an XPS spectrum represents photoelectrons emitted from distinct electron shells or subshells with varying binding strengths. The correlation between observed photoelectron kinetic energy and binding energy via Equation 2.2 facilitates the systematic comparison of XPS data with reference material databases, hence allowing for unequivocal identification of elemental and chemical states.

2.2.4. UV-Visible/diffuse reflectance spectroscopy (DRS)

The UV-Vis spectrophotometer is widely regarded as one of the most common and flexible ways to analyse materials. This method often depends on most molecules taking

in UV-Vis light [137]. This technique is based on the fundamental principle of the Beer-Lambert law, as described in the equation (2.3) [164].

$$A = log \frac{I_0}{I} = \varepsilon cl \tag{2.3}$$

Where A is the absorbance, I_0 is the intensity of the light coming into the sample cell, and I is the intensity of the light leaving the sample cell. c (M = mol dm^{-3}) is the molar concentration of the solute, l is the length of the sample cell in centimetres, and ε ($M^{-1}cm^{-1}$) is the molar absorptivity. This method scans the sample from the UV range of 200 nm to 400 nm and into the visible range of 400 nm to 800 nm.

Samples usually take in light energy, which makes the UV-Vis spectrum. When molecules absorb energy, electrons move from lower-energy orbitals that are already filled (HOMO) to higher-energy orbitals that are not filled (LUMO) [165]. Antibonding orbitals (π* and σ*) are the empty orbitals, while σ orbitals, π orbitals, and nonbonding (n) orbitals are the occupied orbitals [165]. There are certain selection rules that tell us which transitions between orbitals are allowed and which ones aren't. The conservation of the spin quantum number of electrons must be followed for allowed transitions. If this is not the case, the transition is called a "forbidden transition" [165].

A graph of absorbance (A) against wavelength (λ) is the most common way to show the UV-Vis spectrum. The wavelength that corresponds to the highest absorption is called λ_{max}, which is a unique value for the specimen [165]. Also, UV-Vis spectroscopy is very important for studying photocatalysis and adsorption because it helps us understand how fast the reactions happen by measuring the concentration of the molecules.

Also, UV-Vis DRS is an optical method that shows the electrical band structure of semiconducting materials. An Agilent Cary 5000 UV-Vis-NIR spectrophotometer was used to get the UV-Visible diffuse reflectance spectra. The wavelength range was 200-

800 nm. The NIR inactive area reference sample, barium sulphate ($BaSO_4$), was used to make baseline corrections.

In order to extract the band gap (E_g) value, the Kubelka-Munk method is used, which described by equation (2.4).

$$E_g = [F(R) * hv]^{1/n} \tag{2.4}$$

$$F(R) = \frac{(1-R)^2}{2R} \tag{2.5}$$

In this case, *h* stands for Planck's constant, *v* stands for the radiation frequency, *R* stands for diffuse reflectance, and *n* is the exponent constant [166]. For indirect allowed transitions, *n* is 2, and for direct allowed transitions, *n* is 1/2. The Kubelka-Munk theory in which F(R) is the Kubelka-Munk function. The band gap of the semiconductor is the wavelength at which absorption starts to increase.

2.2.5. BET surface area analyser

Brunauer-Emmett-Teller (BET) used to find out the specific surface area, average pore diameter (BJH), and specific pore volume [167]. As the size of a nanomaterial's particles grows, its surface area decreases. This is an important factor in determining how well it works as a catalyst. Gas adsorption-desorption techniques are commonly employed to determine the surface area and pore size distribution of solid materials. The data that was collected is shown as a BET isotherm, which shows how much gas was adsorbed in relation to the pressure (P/P_0). There are five different types of adsorption isotherms, which are shown below:

Type I isotherm: This is often used for microporous materials that don't have a lot of surface area on the outside, like those with pore diameters less than 2 nm. As shown in Figure 2.6, it is divided into two groups: Type I(a), which includes microporous materials with mostly narrow micropores that are less than 1 nm wide, and Type I(b), which includes materials with wider micropores and possibly thin mesopores that are less than 2.5 nm wide.

Type II isotherm: refers to materials that are either nonporous or macroporous, distinguished by diameters exceeding those of micropores. At low pressures in Type II isotherms, nitrogen gas fills up the micropores. The knee is where monolayer formation starts, and medium pressure is where multilayer formation happens. Capillary condensation also happens at higher pressures.

Type III isotherm is distinguished by feeble interactions between the adsorbent and adsorbate. Because the curve doesn't have an asymptote, it can't form a monolayer. Because of this, we can't give you any information about monolayer coverage or formation.

Type IV isotherms are linked to mesoporous adsorbents with pore diameters ranging from 2 to 50 nm. Figure 2.6 shows that it can be divided into two groups: Type IV(a) isotherm comes from capillary condensation, while Type IV(b) isotherm comes from conical and cylindrical mesopores. A monolayer appears in areas of lower pressure, and then multilayers form [168].

At low relative pressure (P/P_0), the Type V isotherm looks a lot like the Type III isotherm. This means that the adsorbent and the adsorbate don't interact very strongly. When pressure rises (higher P/P_0), molecules start to stick together before the pores are full.

Type V isotherms are often observed in the adsorption of water onto hydrophobic microporous and mesoporous adsorbents.

Type VI isotherm: shows how molecules stick to a very smooth, nonporous surface in layers, one on top of the other. The step height shows how much each adsorbed layer can hold, but the sharpness of the step changes depending on the system and temperature.

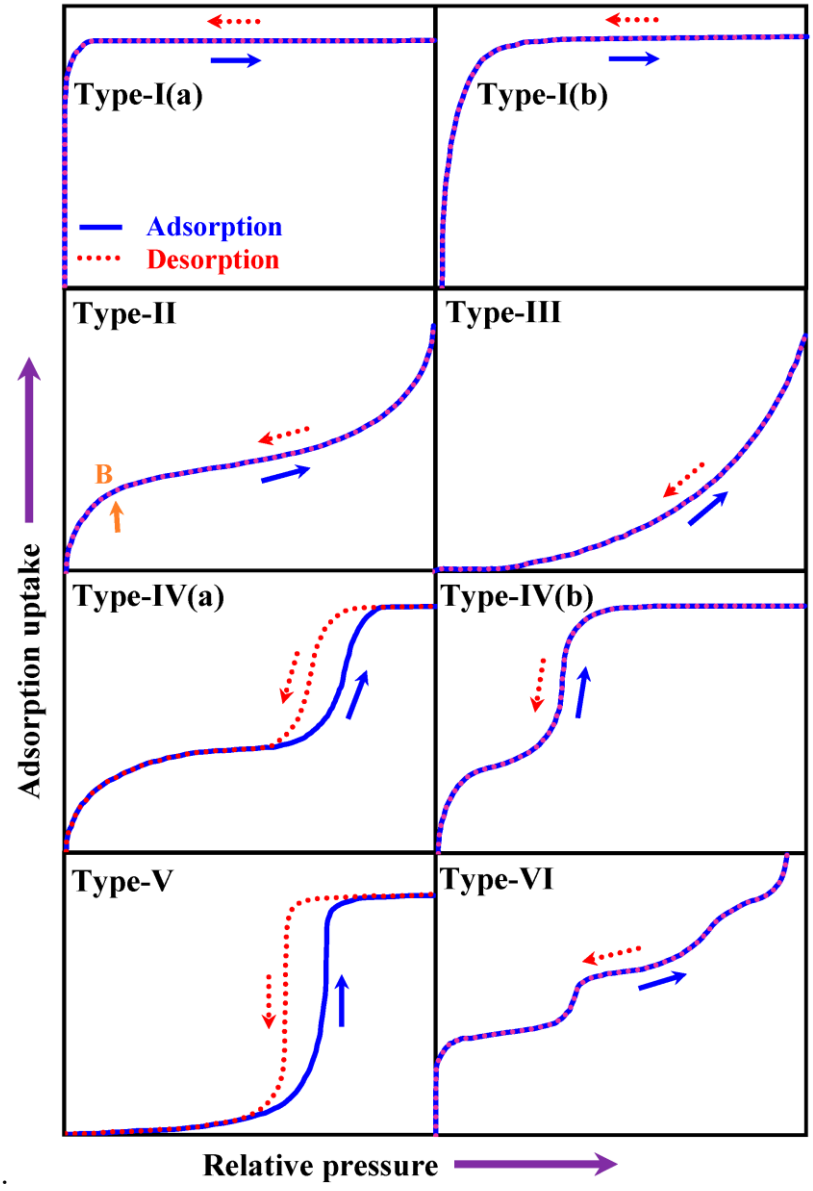

Figure 2.6. Physisorption isotherms,type- I to VI, in the classification of Bruauer, Emett and Teller. (Adapted from) [169]

2.2.6. Photoluminescence (PL) spectroscopy

Photoluminescence spectroscopy is a non-invasive and very sensitive optical method used to analyse the electronic structure, optical characteristics, and photophysical behaviour of materials, especially semiconductors and photocatalytic systems [165]. In contrast to ground-state approaches, PL spectroscopy specifically investigates excited-state behaviour by observing the radiative recombination of photogenerated charge carriers [170].

When a material absorbs photons with energy equal to or greater than its optical bandgap (E_g), electrons in the valence band (VB) acquire adequate energy to transition to the conduction band (CB), concurrently generating positively charged holes in the VB. Subsequent to photoexcitation, these charge carriers experience energy relaxation via phonon-electron scattering, ultimately reaching the band edges. The radiative recombination process, in which electrons from the conduction band recombine with holes from the valence band, releases energy as radiated photons. The energy of the released photon directly correlates with the energy difference between the conduction and valence band edges, providing insights on the material's electrical structure and the behaviour of photogenerated carriers [170].

Photoluminescence data can be acquired via two complementing techniques: steady-state photoluminescence (SSPL) and time-resolved photoluminescence (TRPL). Steady-state photoluminescence delivers spectral intensity data throughout a wavelength range, producing metrics including peak position, full-width at half-maximum (FWHM), and integrated intensity. Time-resolved photoluminescence, in contrast, quantifies the temporal decrease of luminescence intensity after pulsed excitation, yielding quantitative data on carrier lifetimes and the kinetics of recombination events.

The intensity and temporal dynamics of photoluminescence directly indicate the equilibrium between radiative and nonradiative recombination mechanisms. In photocatalytic applications, the photoluminescence intensity is directly related to the rate of charge carrier recombination. Materials with elevated luminescence intensity generally have minimal defect concentrations and extended carrier lifetimes, while diminished photoluminescence intensity suggests effective nonradiative recombination and/or fast entrapment of carriers at defect locations.

Radiative Recombination: Electrons from the conduction band directly recombine with holes in the valence band by k-conserving vertical transitions, releasing photons at energies that correspond to the bandgap or marginally below (for Stokes-shifted emission). The likelihood and frequency of radiative transitions are contingent upon the material's band structure, selection procedures, and the density of accessible states.

Nonradiative Recombination: This mechanism releases energy as thermal energy instead of photons. Shockley-Read-Hall (SRH) recombination entails recombination via intermediary deep-level defect states, whereas Auger recombination is a triadic process in which the energy liberated by one recombining pair is imparted to a third charge carrier, elevating it to higher energy levels. In photocatalysts, nonradiative paths are not entirely adverse; defect states can serve as charge separation centres, promoting electron transfer to catalytic sites.

The apex of the photoluminescence spectrum offers an optical approximation of the material's bandgap energy; however, this value may underestimate the actual bandgap derived from absorption spectroscopy because of Stokes shifting. The Stokes shift, defined as the energy difference between absorbed and emitted photons, results from the structural relaxation of the excited state and signifies the existence of defect states. A

larger Stokes shift generally correlates with more disorder and elevated defect concentration.

2.2.7. Dynamic Light Scattering (DLS) technique

Dynamic light scattering (DLS), alternatively referred to as photon correlation spectroscopy (PCS) or quasi-elastic light scattering (QELS), is a non-invasive optical method utilised to ascertain the hydrodynamic particle size distribution and colloidal stability properties of nanoparticle suspensions and molecular solutions. The integration of electrophoretic light scattering (ELS) with this technique facilitates the concurrent determination of zeta potential, offering thorough colloidal characterisation vital for comprehending particle behaviour in pharmaceutical, cosmetic, and materials scientific domains [171].

The DLS methodology is based on the observation of Brownian motion, which is the random and continuous movement of suspended particles caused by heat collisions with solvent molecules. As dispersed particles experience Brownian diffusion inside the medium, the continual redistribution of their positions produces variations in the intensity of scattered light when irradiated by a monochromatic laser. The primary equation determining particle size determination is the Stokes-Einstein equation:

$$D = \frac{K_\beta T}{6\pi\eta R_H} \tag{2.6}$$

D represents the translational diffusion coefficient (m^2/s), K_β denotes the Boltzmann constant (1.38×10^{-23} J/K), T signifies the absolute temperature (K), η indicates the dynamic viscosity of the dispersant (Pa·s), and R_H refers to the hydrodynamic radius (m). This equation indicates that particle diffusion is inversely related to size; smaller particles diffuse quickly due to less inertia and undergo proportionately more thermal impulses

compared to their mass, whereas bigger particles exhibit slower movement. The assessment of particle motion thus offers a quantitative foundation for size estimation when temperature and solvent viscosity are accurately established.

The instrumental setup focusses a monochromatic laser beam through an optically clear cuvette filled with a dilute particle suspension. The incident photons engage with dispersed particles, producing scattered light at all angles in accordance with the Rayleigh scattering regime. The dispersed light, gathered at a specific angle, displays temporal intensity variations that directly convey information regarding particle diffusion rates.

The hydrodynamic diameter (Z-average size) obtained from the Stokes-Einstein equation signifies the effective diameter of a spherical particle that would diffuse at the observed rate, considering the hydration shell and any electrical double layer enveloping the particle surface. This measure fundamentally varies from morphological sizes obtained using electron microscopy or atomic force microscopy, as the hydrodynamic diameter includes contributions from surface-associated solvent layers, ions, and any surface-bound polymers or ligands. Significant discrepancies between DLS-derived hydrodynamic size and transmission electron microscopy (TEM) measurements typically indicate particle non-sphericity (especially pertinent for rod-like or plate-like morphologies), anisotropic hydration, or surface functionalisation effects, rather than instrumental error.

The application of an electric field within a specialised electrophoresis cell converts dynamic light scattering (DLS) into electrophoretic light scattering (ELS), also known as laser Doppler electrophoresis or phase analysis light scattering (PALS). When an alternating or direct electric field is applied across the cell, charged particles undergo directed motion superimposed on their random Brownian motion. This electrophoretic

mobility appears as a frequency or phase change in the scattered laser light, resembling the Doppler effect seen with acoustic signals from moving sources.

The zeta potential value measures the electrostatic potential at the hydrodynamic shear plane, which is the theoretical border separating ions firmly attached to the particle surface (Stern layer) from ions in the diffuse outer region. Zeta potentials of ±30 mV or greater generally signify robust electrostatic stabilisation and a diminished propensity for aggregation, whereas values around zero denote potential colloidal instability and an increased danger of flocculation. The measurement thus offers essential insight into dispersion stability and particle-particle interaction dynamics.

Samples must be optically transparent or demonstrate only slight turbidity to allow laser penetration without significant multiple scattering, which produces erroneous large-size artefacts in the correlation function. Highly concentrated particle dispersions generally necessitate dilution into the original dispersant medium to mitigate concentration dependent electrostatic interactions and measurement artefacts.

2.2.8. Electrochemical measurements

The electrochemical characterisation of the synthesised materials was conducted via a three-electrode setup linked to a electrochemical workstation. The configuration included an indium tin oxide (ITO) glass substrate coated with the synthesised semiconductor material functioning as the working electrode (anode), a platinum (Pt) wire serving as the counter electrode, and an Ag/AgCl (3 M KCl) electrode utilised as the reference electrode [172]. All measurements were conducted at ambient temperature in an aqueous NaOH electrolyte solution (0.5 M) to guarantee adequate ionic conductivity and stability of the working electrode. Before utilisation, the electrolyte solution was purged with nitrogen gas for around 15 minutes to eliminate dissolved oxygen and stabilise the system.

The Electrochemical Impedance Spectroscopy (EIS) analysis was conducted to examine the charge-transfer resistance (R_{ct}), interfacial kinetics, and electronic conductivity of the electrode-electrolyte interface. Impedance measurements were collected across the frequency spectrum of 100 kHz to 0.1 Hz, utilising an applied AC perturbation amplitude of 10 mV centred at the open-circuit potential (OCP). The resultant Nyquist graphs (imaginary versus real impedance) were examined with equivalent circuit modelling via Nova software. The semicircular region in the Nyquist plot typically represents the charge-transfer process at the electrode/electrolyte interface, where a smaller semicircle diameter signifies a lower R_{ct} and consequently accelerated charge-transfer kinetics.

Mott-Schottky tests were performed to investigate the semiconductor's intrinsic electronic characteristics within a frequency range of 1-10 kHz and an AC amplitude of 5-10 mV. The M-S plots ($1/C^2$ vs applied potential) were utilised to ascertain the flat-band potential (E_{fb}) and charge carrier density (N_d) of the semiconductor material in accordance with the Mott-Schottky equation:

$$\frac{1}{C^2} = \frac{2}{e\varepsilon\varepsilon_0 N_d}\left(E - E_{fb} - \frac{KT}{e}\right) \tag{2.7}$$

The variables ε, ε_o, e, C, E, E_{fb}, K, T, and N_d denote the dielectric constant, permittivity of free space, elementary charge, space charge region capacitance, applied potential, flat band potential, Boltzmann constant, absolute temperature, charge carrier density, respectively.

A positive slope of the M-S figure denotes n-type conductivity, while a negative slope shows p-type behaviour. The linear segment of the curve was extrapolated to $1/C^2 = 0$ to determine the flat-band potential. The carrier density was derived from the slope of the M-S curve, offering insights into the dopant concentration and photoelectrochemical efficacy of the synthesised material.

The EIS and M-S studies combined furnish extensive insights into charge transport kinetics, semiconductor band energetics, and electrode/electrolyte interface behaviour, which together dictate the electrochemical and photoelectrocatalytic efficiency of the synthesised materials.

2.3. Materials and technical specifications of characterizing instruments

2.3.1. Materials

All the chemicals, such as zinc acetate dihydrate [$Zn(CH_3COOH)_2 \cdot 2H_2O$: M.W = 219.50 g/mol] from RFCL Limited in India, tetrabutyl orthotitanate [$Ti(OC_4H_9)_4$: M.W. = 340.32 g/mol] from TCI in Japan, glacial acetic acid [CH_3COOH: M.W = 60.05 g/mol] from SDFCL, India and Copper nitrate trihydrate [$Cu(NO_3)_2$. $3H_2O$: M.W. = 241.60 g/mol) purchased from molychem, India.

Sodium nitrate [$NaNO_3$: M.W = 84.99 g/mol], graphite, potassium permanganate [$KMnO_4$: M.W = 158.03 g/mol], hydrochloric acid (HCl: M.W = 36.46 g/mol), and hydrogen peroxide [H_2O_2: M.W = 34.01 g/mol] were purchased from molychem, India. Sulphuric acid [H_2SO_4: M.W = 98.08 g/mol] and phosphoric acid [H_3PO_4: M.W = 97.99 g/mol] purchased from rankem, India, are used to synthesize graphene oxide.

Zinc nitrate hexahydrate [$Zn\ (NO_3)_2.6H_2O$, M.W. = 297.48 g/mol], terephthalic acid [$C_8H_6O_4$, M.W. = 166.13 g/mol], C-tab [$C_{19}H_{42}BrN$, M.W. = 364.46 g/mol], and nickel nitrate hexahydrate [$Ni\ (NO_3)_2.6H_2O$, M.W. = 290.80 g/mol] were procured from Molychem Limited. Solvents used during synthesis of NiZnO, DMF [$HCON(CH_3)_2$, M.W. = 73.09 g/mol] and methanol [CH3OH, M.W. = 32.04 g/mol], were procured from Loba Chemie Pvt. Ltd. and Molychem Limited, respectively. All materials were of

analytical grade and were used without further purification. In addition to this, methylene blue [M.W. is 319.85 g/mol] is used for photocatalysis studies.

2.3.2. Details of the characterization instruments used in this work

We used a PANalytical X'pertpro MPD diffractometer with monochromatic Cu Kα radiation (λ = 1.5406 Å) across a diffraction angle (2θ) range of 10 to 90 degrees and a step size of 0.03 degrees to get X-ray diffraction (XRD) data for powder and grazing incidence angle. We took field emission scanning electron microscopy (FESEM) pictures of powder and using a JSM-7900F machine from JEOL, Japan. We then confirmed the chemical composition using an EDX analyser in FESEM. The accelerating voltage for the SEM pictures was between 5 and 10 kV. We used UV-Visible diffuse reflectance spectroscopy (DRS) on an Agilent Cary 5000 UV-Vis-NIR spectrophotometer to look at the optical properties (absorbance, reflectance, and transmittance) across a wavelength range of 200-800 nm. We used a UV-Vis spectrometer (LAB INDIA spectrometer) to study degradation of pollutants in water. An Agilent Cary Eclipse was used to get the steady-state photoluminescence emission spectra of particles at an excitation wavelength of 380 nm. A Micromeritics Flex 3 BET analyser was used to study the BET surface area and pore size distribution of powder samples. We used a Zetasizer (model: Zetasizer Nano ZS) from Malvern Panalytical to look at the average particle size and zeta potential (ZP) of the particles. The experiments in X-ray Photoelectron Spectroscopy (XPS) were done with a PHI 5000 Versa Probe spectrometer that had an Al Kα X-ray anode. The C 1s peak of carbon at 284.8 eV was used as a reference for binding energy calibration. All measurements were taken at room temperature. We used a Multi Autolab M204 electrochemical instrument to measure the electrochemical properties in a quantitative way. The system had a standard three-electrode setup, with catalyst-coated ITO glass as

the anode, coiled platinum as the counter electrode, and Ag/AgCl as the reference electrode.

CHAPTER 3

Synthesis and characterization of zinc titanate-graphene oxide composites prepared by ambient and hydrothermal conditions

3.1. Abstract

We prepare reduced graphene oxide-zinc titanate (ZTO) composite powders by mixing ZTO with 1 wt.% graphene oxide (GO) in solid and liquid states under open environments, and under hydrothermal conditions. The treatment temperature was 400 ºC in the first two cases and 180 ºC in hydrothermal. Structural and chemical characterizations performed using XRD, SEM, BET, XPS, DRS, and PL are correlated with their photocatalytic performance. Mixing leads to significant structural and chemical changes in GO and ZTO particles but of different natures depending on the process. All the mixing routes reduce GO to r-GO. Unlike hydrothermal mixing, mixing under an open environment converts the rhombohedral $ZnTiO_3$ to cubic $Zn2TiO_4$ due to loss of oxygen. However, hydrothermal mixing leads to a loss in crystallinity of the $ZnTiO_3$ particles resulting into a larger specific surface area. XPS results suggest good binding between the r-GO sheets and the oxide particles. Liquid state mixing leads to the highest reduction

in bandgap, probably due to maximal oxygen vacancy formation in this process. Mott-Schottky analysis is done to estimate the charge carrier density in all the samples. EIS shows that the hydrothermally prepared composite has the smallest R_{ct}. High surface area, less conversion to Zn_2TiO_4, changes in bandgap, good binding of ZTO with GO sheets, and more facile charge transfer in hydrothermally prepared composites have important implications in photocatalytic applications.

3.2. Introduction

In this chapter, different synthesis routes are used to prepare composites of graphene oxide with $ZnTiO_3$, and the resulting materials are analysed to understand how the structural, surface, and electronic properties of $ZnTiO_3$ are modified for visible-light photocatalysis. By comparing composites obtained via solid-state, liquid-state, and hydrothermal processing, the roles of phase composition, surface area, bandgap, and interfacial binding with GO are systematically evaluated.

Diverse categories of catalysts employed in photocatalysis include transition metal-centered complexes, organic photosensitizers, metal oxides, two-dimensional materials, quantum dots, and plasmonic metals [173]. Photocatalytic reactions involve charge generation on the catalyst and a subsequent charge transfer from the catalyst to the reacting species to trigger the desired reaction. Hence the concerned reactions are redox reactions. Metal oxides serve to be good photocatalytic materials because photogenerated electrons can help with reduction reactions, and holes in the valence band can help with oxidation reactions [174]. Moreover, metal oxides are the most prevalent minerals in the Earth's crust, resulting in lower prices relative to other wide-bandgap semiconductor materials. Certain metal oxides, like zinc oxide and tin oxide, demonstrate both conductivity and optical transparency, allowing the extensive application of transparent

conducting oxides in optoelectronic devices [175][176]. Transparency to light and facile conduction of electrons are the features that make these metal oxide semiconductors especially attractive for optoelectronic processing.

The electron-hole generation depends on the bandgap, and it should be smaller than the photon energy, as it signifies the minimal energy necessary to elevate an electron to the conduction band, enabling its participation in electrical conductivity. For photocatalysis and photovoltaics, a more efficient absorption of solar light is preferable, one that spans a far broader spectrum of wavelengths. This deficiency is propelling the pursuit of broad-bandgap metal oxide materials exhibiting optical responses in the visible to near-infrared ranges. Bandgap in oxides has been engineered to adjust to the visible spectrum using several approaches such as varying processing conditions, particle size, [177], [178], [179], [180] doping with metals, [181], [182] non-metals, [183][184] and generation of vacancies [185][186]. Doping not only reduces the bandgap but also introduces new spectral characteristics in the visible to near-infrared ranges, hence enhancing overall absorption efficiency [187]. The investigation of emergent behavior via oxygen vacancy manipulation has catalyzed a surge of scientific interest [188], [189], [190], [191].

To ensure that the diffusive transport occurs to the particle surface before recombination, the particles' specific area may be enhanced by making them porous. A larger surface area also ensures a higher number of active reaction sites for charge transfer. However, the mass transfer starts being a limiting process with the porous particles [192]. The processing conditions and calcination temperature are seen to affect crystalline phase and porosity characteristics and thereby influence the photocatalytic effectiveness of zinc titanate [193], [194], [195].

The charge separation of the electron-hole pairs generated upon shining the light can be achieved by several approaches, and creating a heterojunction that generates an internal electric field separating the electron-hole pairs has been the most effective approach. Using ultra-thin film geometry, sandwich substructures, applying external electrical bias, metal doping and modification, creating vacancies, creating surface defects by using pits, and applying magnetic fields [196], [197], [198], [199], [200], [201], [202], [203] have been several other approaches to separate the charges of opposite polarities and utilize them for surface active redox reactions.

Charge transfer resistance (R_{ct}), a parameter measured by electrochemical impedance spectroscopy (EIS) that quantifies the resistance against the transfer of charge (electrons or holes) from the immobilized solid electrode to redox species in the liquid phase occurring at the heterogeneous interface, is also crucial in determining the homogeneous photocatalytic performance in liquid phase [204].

Zinc titanate shows multiple phases such as cubic and rhombohedral [205], [206] with favorable band gaps matching the energy of visible light. Porosity in zinc titanate materials can also be engineered by processing conditions; for example, zinc titanate prepared by the electrospinning route and calcined at 800 °C has shown improved photocatalytic activity [207]. The pore size of zinc titanate facilitates the adsorption of organic contaminants. Prior research has shown that graphene composites can enhance the light absorption capacity [208]. The nanoscale dimensions of TiO_2/graphene photocatalysts yield an extensive surface area [137]. Metal-CNT composites can decrease electron-hole recombination [209]. Carbon has been incorporated in TiO_2 by using sol-gel as well as mechanochemical treatment, and the sol-gel method yielded samples with a narrower bandgap [210], [211]. In view of the observed bandgap narrowing in TiO_2 resulting from carbon, here we explore the ZTO-GO composites

prepared by three different routes and assess their potential application in photocatalysis based on the characterization results of these samples.

In this work, we study changes in the surface area, bandgap, binding of ZTO with GO sheets, and charge transfer of zinc titanate in composites of these particles with graphene oxide prepared using three different methods. These three methods are as follows: (i) The solid-state mixing, in which we mix laboratory prepared ZTO powders with GO powder and treat the mixture at 400 ºC, (ii) the liquid state mixing, wherein we mix GO with the ZTO suspension under stirring, the resulting mixture was dried to obtain a solid precursor, and the dried composite powder was then heat-treated at 400 °C for 1 h, and (iii) mixing under hydrothermal conditions, in which the treatment temperature was 180 ºC. Detailed analysis of the characterization data shows hydrothermally prepared samples show a reduction in the bandgap, an increase in surface area, increased charge separation, and reduced charge transfer resistance and hence can serve as a potential material for photocatalytic applications.

3.3 Experimental section

3.3.1. Materials

All materials were of analytical grade and were used without further purification. The zinc and titanium precursors were zinc acetate dihydrate from RFCL Limited in India and tetra butyl ortho titanate from TCI in Japan. SDFCL, India, supplied acetic acid glacial.

Sodium nitrate, graphite, potassium permanganate, hydrochloric acid, and hydrogen peroxide were purchased from MOLYCHEM, India. Sulphuric acid and phosphoric acid purchased from RANKEM, India, are used to synthesize graphene oxide.

3.3.2. Synthesis of zinc titanate ($ZnTiO_3$) (ZTO)

ZTO powder was synthesized using the sol-gel method. The mole ratio of Zn: Ti was determined to be 1:0.9 [207]. In a typical synthesis, 2.25 g of zinc acetate dihydrate and 3.14 mL of titanium tetra butoxide were dissolved in 3.33 mL of acetic acid (CH_3COOH) separately. Both solutions were mixed with magnetic stirring and heated to around 50 °C followed by mixing with deionized water (10 mL). After mixing deionized water, a transparent sol was obtained, which over time formed a gel. During the gel aging process, it was realized that maintaining a constant temperature is critical for getting a transparent and homogeneous gel. To remove excess solvent, dry for 10 hours at 120 °C. The resulting gel was calcined at 800 °C equilibrated for 3 hours at a heating rate of 10 °C/min to obtain the final powders.

3.3.3. Synthesis of graphene oxide (GO)

Graphene oxide (GO) was synthesized from graphite powder (GP) via a modified Hummer method [212]. Under constant stirring, 6 g of sodium nitrate was mixed into 230 mL of concentrated sulphuric acid and phosphoric acid (9:1 weight ratio), followed by the addition of 10.0 g of graphite. After 4 hours, 30 g of $KMnO_4$ was gradually added to the above solution while maintaining a temperature below 20 °C. The mixture was stirred at 35 °C for 48 hours, and the resulting solution was diluted by vigorously stirring in 460 mL of water. To ensure that the reaction with $KMnO_4$ was completed, the suspension was treated with a 5 mL H_2O_2 solution (30 %). The resulting mixture was filtered, and the graphite oxide residue was washed repeatedly with HCl and H_2O before drying; graphite oxide was thus obtained. We get graphene oxide after sonicating it several times.

3.3.4. Synthesis of composite I

Composite I was synthesized by a solid-state method. Initially, 3 g of the GO powder and 300 g of ZTO were highly mixed in powder form and then put in a furnace at 400 ºC for 1 hr. to reduce GO.

3.3.5. Synthesis of composite II

Composite II was synthesized in the presence of solvent (deionized water). Initially, 3 g of the GO powder and 300 g of ZTO are dispersed in 40 mL of water. Vigorously stir it for 4 hr. and then sonicate for 2 hr. to get ZTO-GO suspension. Then, dried to obtain a solid precursor, and the dried composite powder was then heat-treated at 400 °C for 1 h. to reduce GO.

3.3.6. Synthesis of composite III

Composite III was synthesized by the hydrothermal method. All the compositions and processes are the same as a composite II synthesis until the formation of ZTO-GO suspension. After that, we transferred this suspension into a 50 mL Teflon autoclave and held it at 180 ºC for 12 hr. Then, final composite was obtained by centrifuge and dried at 60 ºC.

3.4 Electrochemical measurements

The electrochemical characteristics were quantitatively determined using a Multi Autolab M204 electrochemical system. The system consisted of a typical three-electrode configuration, with catalyst-deposited ITO glass serving as the anode, coiled Pt as the counter electrode, and Ag/AgCl as the reference electrode. A 0.5 M KOH solution was employed as the electrolyte. The operational anodes were fabricated in the following manner: A suspension was prepared by mixing a 100 mg sample with a 300 μL mixed

solution of tritron X, ethanol, and acetic acid. Then the mentioned mixture was evenly distributed over a 47 mm^2 ITO glass and dried at a temperature of 40 °C.

3.5 Result and discussion

3.5.1. X-ray diffraction (XRD)

Figure 3.1 presents the X-ray diffraction patterns of GO and composite samples I, II, and III. The majority phase present in the composites was the hexagonal $ZnTiO_3$ (JCPDS file number 25-0671) with R-3 space group symmetry. Some residual impurities of rutile-TiO_2, ZnO, and cubic-Zn_2TiO_4 were also found as suggested by indexing the peaks in the diffraction pattern. The relative fractions of each phase were estimated from calculating the areas under the respective peaks and are presented in Table 1.

The GO samples show its characteristic strong peak at a 2θ value close to 10.9° [213]. These samples also show graphitic peak at around 27° and r-GO reflections at around 22°. The characteristic GO peak at 10.9° was found absent in the XRD diffraction patterns of composites. The composite samples show weak signals at 2θ value close to 23°. These observations are taken to conclude that in composite samples the GO has been reduced to r-GO. Yang et al. have observed gradual disappearance of the GO peak near 10° as the TiO_2 fraction is increased, with complete disappearance of this peak at a GO:TiO_2 ratio of 1:2.5 [214]. They have also attributed the disappearance of the GO peak to the transformation of GO to r-GO in the presence of TiO_2.The reduction of GO to rGO in the presence of TiO_2 during heat treatment is attributed to thermal deoxygenation of the oxygen-containing functional groups of GO. Epoxy, hydroxyl, and carboxyl groups are removed at elevated temperature, leading to the release of gaseous species such as CO and CO_2 and partial restoration of the sp^2 carbon framework. The TiO_2 surface can further assist this process through interfacial interactions that promote charge redistribution and

facilitate oxygen removal from GO. In the presence of the oxide matrix, interfacial interactions may further assist this process by promoting defect formation and accelerating oxygen removal from the GO surface [215]. As a result, GO is transformed into a more conductive rGO-like phase in the composite system [216]. In our samples, the GO fraction is much smaller (1%). Due to a significantly smaller fraction of GO present in our samples as compared to the crystalline oxides, the corresponding peaks in the XRD are weak and noisy, but still their presence is discernible as seen in Figure S1. The XRD patterns of the composites when magnified near the 2θ value close to 22° as presented in supplementary material Figure S1 show that the rGO peak gradually shifts to smaller angles, suggesting that due to the reduction of the graphene oxide, the graphene sheets become less compact. This is expected since oxygen atoms responsible for mediating the bonding between the neighboring sheets are lost upon reduction, thereby loosening the graphene sheets. Formation of graphite is also seen in composite I and II, formed by allowing the gases to escape, but not in composite III. Our first conclusion from XRD analysis is that GO is reduced to r-GO in the presence of zinc titanate [217], and even some graphite is formed if heat treatment occurs in an open environment.

We also notice that two higher order peaks at 2θ of 38.5° and 51° which are respectively due to (015) and (107) reflections from hexagonal ZTO, are more prominent in composites than in native ZTO (Figure 3.1). It could be due to the hexagonal symmetry of the graphene oxide that matches with ZTO and thereby promotes long-range ordering of ZTO atoms in these higher order planes.

Composite I, II, and III are prepared by three different routes where samples are finally heat treated at the same temperature of 400 °C in each case. GO is known to undergo thermal reduction at 200 °C [218]. Botta *et al.* [219] have shown that a mixture of zinc and anatase TiO_2 when activated, undergoes chemical transformation upon heat treatment

to produce Zn_2TiO_4 and $ZnTiO_3$. However, conversion to Zn_2TiO_4 is observed to occur above 600 ºC with an optimal duration of activation only (unlike conversion to $ZnTiO_3$ that speeds up monotonically as the activation time is increased). The optimally activated mixture is found to undergo high conversion to Zn_2TiO_4 above 600 ºC. The Zn_2TiO_4 is also susceptible to converting to $ZnTiO_3$ from the following reaction: $Zn_2TiO_4 + TiO_2 \rightarrow 2ZnTiO_3$. However, our results show that in the presence of GO, heat treatment at a much lower temperature in an open environment impedes the forward conversion of Zn_2TiO_4 to $ZnTiO_3$ and promotes the reverse reaction.

GO acts as a powerful reducing agent and electron-dense support. During heat treatment, GO can undergo thermal decomposition or reduction, creating local structural defects and oxygen vacancies. This localized reducing atmosphere actively favors the reformation of the inverse spinel structure Zn_2TiO_4, promoting the reverse tendency [220].

A comparison of the XRD patterns of the three composites shows that the formation of Zn_2TiO_4 is promoted in composite I and II but not in composite III. This is concluded from the enhanced peak intensities observed at the 2θ value close to 30º and 35.3º, the former of which is assigned to the (220) reflection from Zn_2TiO_4, whereas the latter peak results from an overlap of the (311) reflection from Zn_2TiO_4 and the (110) reflection from $ZnTiO_3$ phases. Chantelle et al. [221] have observed the (311) reflection to be the plane that crystallizes first in Zn_2TiO_4. A deconvolution of the peak at 35.3º is presented in Figure 3.3. The Zn_2TiO_4 has a lower oxygen fraction than $ZnTiO_3$. The preferential formation of Zn_2TiO_4 can be attributed to the loss of oxygen during heating. Since the composite I and II are prepared in an open environment unlike the composite III, therefore loss of oxygen is more facile in these samples. In general, Zn_2TiO_4 is formed at a higher temperature of 700 ºC [221], but in the presence of GO, we observe it to form at a much lower temperature. A comparison of the deconvoluted reflections of the Zn_2TiO_4 and

$ZnTiO_3$ phases in Figure 3.2 shows that the peak width of the $ZnTiO_3$ is higher compared to that of Zn_2TiO_4 in composite I and II, whereas an opposite trend is observed in composite III. This suggests that the crystallinity is better restored for $ZnTiO_3$ in composite III, whereas composite I and II have better crystallinity for Zn_2TiO_4. This observation also suggests that in composite I and II, the formation of Zn_2TiO_4 is favored over $ZnTiO_3$, unlike in composite III. Formation of TiO_2 is also higher in composite I and II as compared to composite III as listed in Table 1. This is because $ZnTiO_3$ transforms to Zn_2TiO_4 according to the following reaction: $2ZnTiO_3 \rightarrow Zn_2TiO_4 + TiO_2$, and the presence of GO at ambient conditions allows decreasing oxygen content in such a case. The lower rGO contribution in Composites I and II can be attributed to partial thermal reduction in open environment and decomposition of GO during calcination, whereas the comparatively higher rGO contribution in Composite III is consistent with the hydrothermal route, which better preserves the carbonaceous phase and promotes its incorporation into the composite.

We also note that in all the samples, the (311) reflection from Zn_2TiO_4 near 35^o is almost double its (220) reflection near 30^o. This would be expected because the number of Zn:Ti:O atoms is 12:24:48 in the (311) plane, which is nearly double than 5:11:22 in the (220) plane.

Another evidence of loss of oxygen from the $ZnTiO_3$ phase comes from a comparison of its (104) and (110) reflections in the composite samples. The plane (110) in Rh-ZTO has only Zn and Ti atoms, whereas (104) is from 6 oxygen atoms. In composite I and II, the relative intensity of the (104) reflection is significantly smaller, whereas in composite III they are comparable. Therefore, this relative decrease of the (104) reflection in composite I and II suggests that oxygen atoms are lost from the (104) plane in these samples, whereas the loss of oxygen is prevented in composite III.

The composite III also shows the XRD reflections to have larger FWHM values (Table S1). This suggests less crystallinity and hence a larger surface area in these samples. The amorphousness may play an important role in enhancing the photocatalytic property of the particles either by enhancing the surface area or by favorably altering the electronic density of states [189].

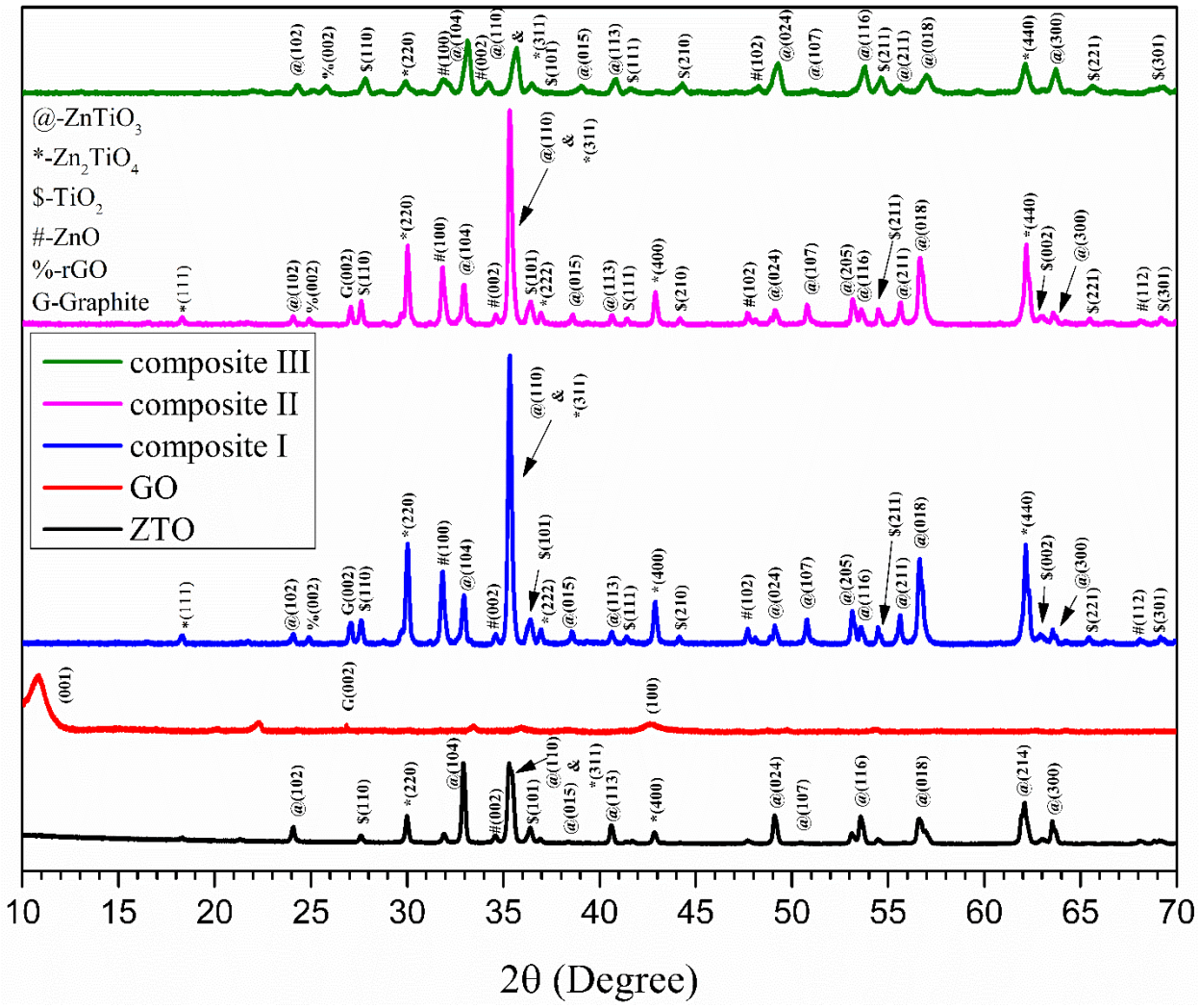

Figure 3.1. XRD patterns of ZTO, composite I, II, III, and GO.

Table 3.1. Calculation of the percentage of phase present in the sample.

	$ZnTiO_3$	**Composite I**	**Composite II**	**Composite III**
$ZnTiO_3$	74.04%	27.21%	27.79%	65.05%

Zn_2TiO_4	18.42%	42.98%	40.63%	14.45%
TiO_2	4.63%	18.48%	20.35%	6.00%
ZnO	2.90%	9.08%	9.19%	13.58%
rGO	-	0.42%	0.43%	0.91%
Graphite	-	1.83%	1.60%	0

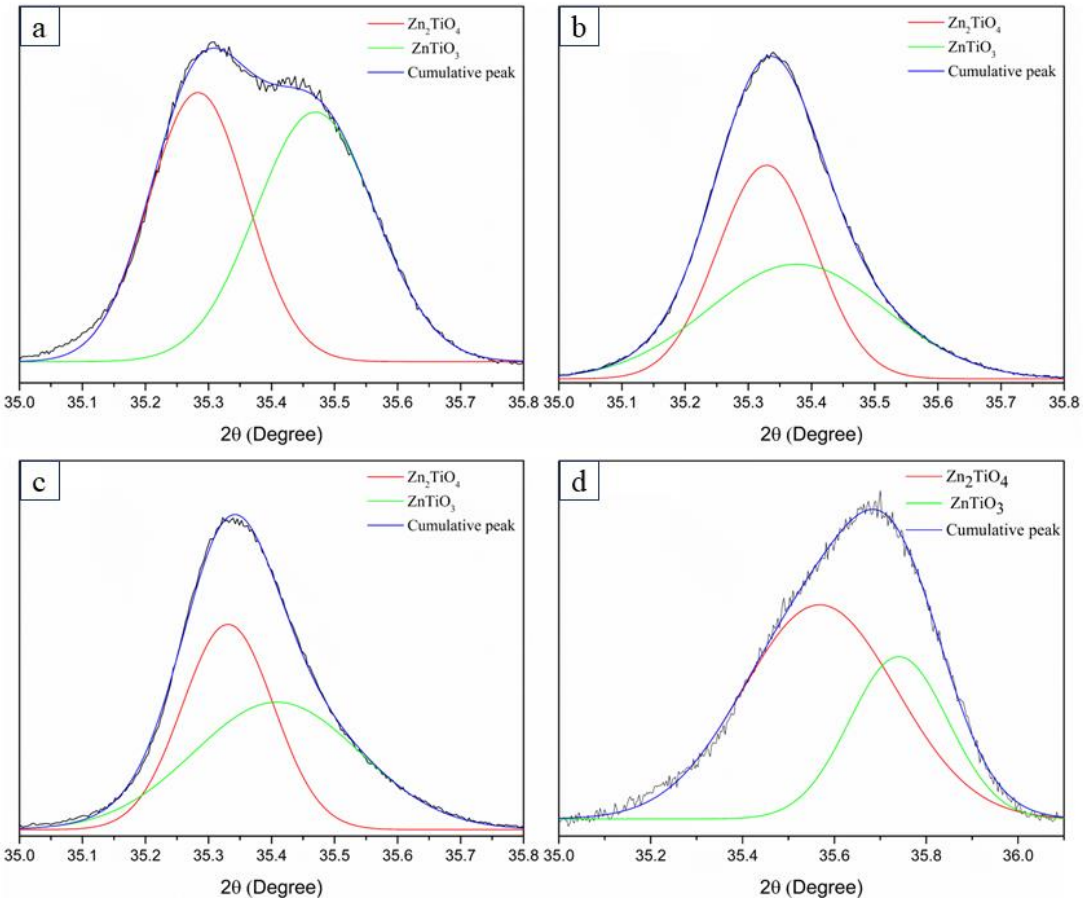

Figure 3.2. Deconvoluted XRD peaks for (311) and (110) planes of Zn2TiO4 and ZnTiO3 in (a) ZTO, and composite (b) I, (c) II, and (d) III.

3.5.2 Surface Area Analysis

Nitrogen adsorption-desorption isotherms of composites are shown in Figure 3.3. The specific BET Surface area of ZTO, composite I, composite II, and composite III are 1.0

m^2/g, 1.3 m^2/g, 1.3 m^2/g and 1.4 m^2/g, respectively. If we compare the surface area of composite III with ZTO, then there is a 40% increase in surface area. Figure 3.3(a-d) shows type II isotherms with a very steep capillary condensation step in the relative pressure (p/p_0) range of 0.8–1.0, as indicated by the hysteresis, which is typical of an ordered mesostructured with a large and uniform pore size. A high relative pressure uptake (p/p_0~0.9) is observed, indicating the presence of inter-crystalline pores.

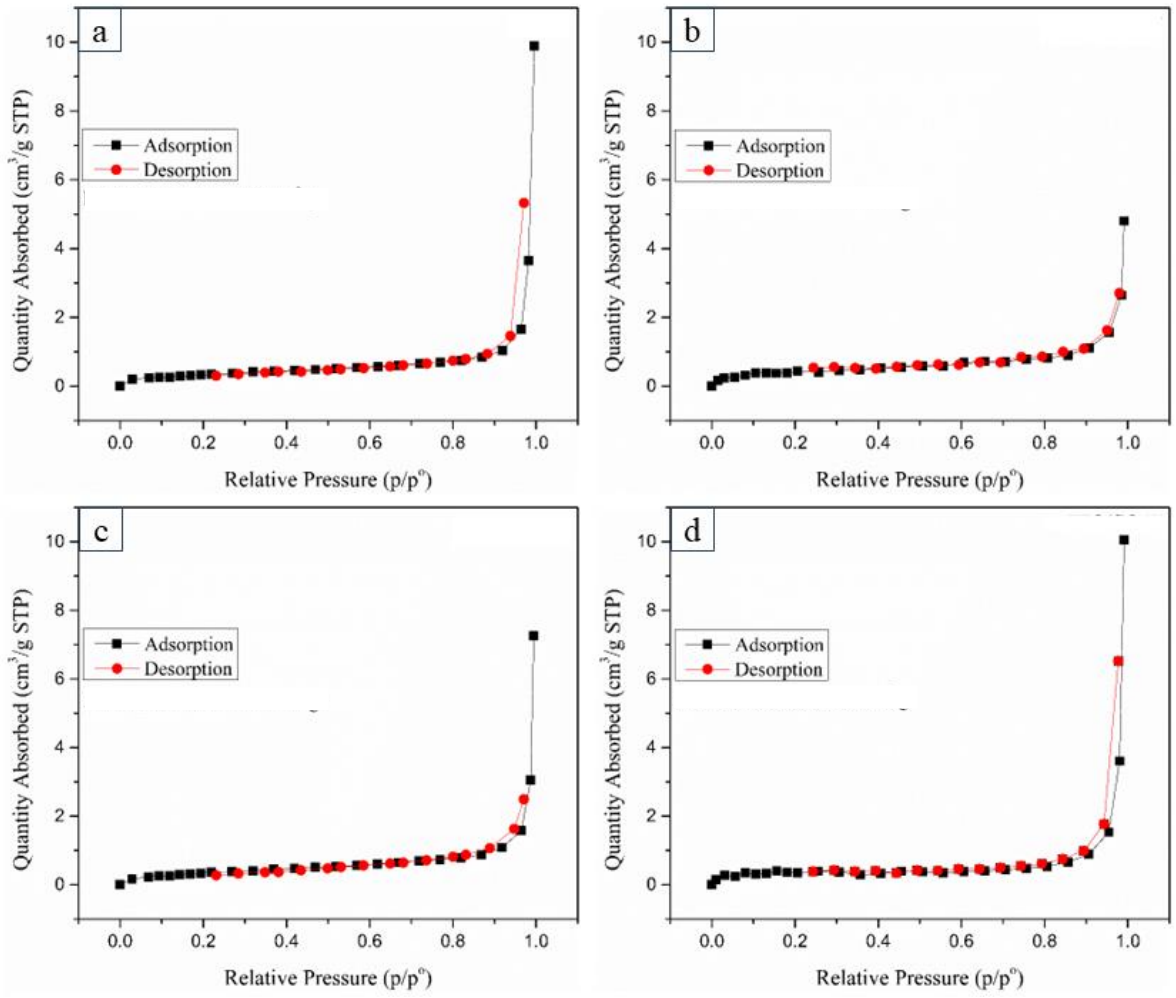

Figure 3.3. The BET surface area and isotherm of (a) ZTO, and composites (b) I, (c) II, and (d) III.

3.5.3 Field Emission Scanning Electron Microscopy (FESEM) analysis

FESEM images of GO and various composite samples are presented in Figure 3.4. In Figures 3.4 (a) and (b), GO sheets in stacked form are clearly visible, with a C/O ratio of

1.9 as obtained from the EDX data (Figure S2). Typical values of this ratio lie around 1.4 [222]. Whereas in composite II and III obtained by liquid phase processing, the detached graphene sheets decorated with the oxide particles are visible (Figures 3.4 (e) and (f) for composite II, and Figures 3.4 (g) and (h) for composite III), the composite I obtained by solid state processing did not show detached graphene sheets (Figures 3.4 (c) and (d)). This may be expected since the detachment of r-GO sheets will be better facilitated in the liquid phase. The composite III also has a higher fraction of ZnO rods (Figure 3.4(g)), as confirmed from the elemental mapping through EDX as presented in Figure 3.5. Rods are those of ZnO. Formation of ZnO is found to be facilitated in the hydrothermal method in the presence of graphene oxide. The atomic composition of GO, composite I, composite II, composite III from areal EDX is shown in Table 2. The variation in C, Zn, and Ti contents between Composites I and II is attributed to local inhomogeneity in GO distribution, particle packing, and interfacial aggregation, because different method is used in synthesis of composite I and II. The carbon content differs across all three samples because the synthesis route affects GO dispersion, surface coverage, and the extent of partial thermal reduction of the carbonaceous phase.

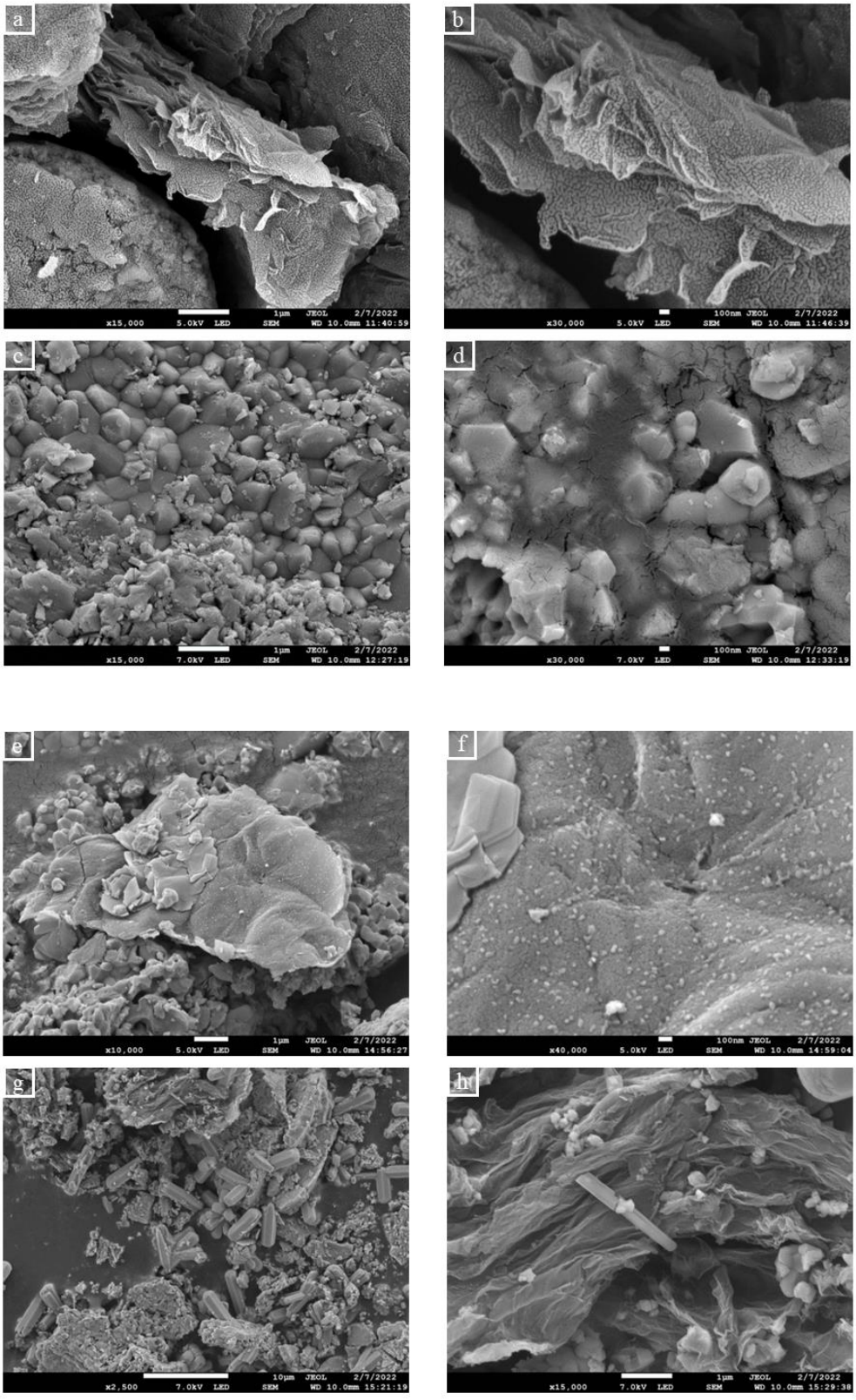

Figure 3.4. FESEM images of samples at smaller magnification (left column) and larger magnification (right column). Images of GO (a, b), composite I (c, d), composite II (e, f), and composite III (g, h) samples.

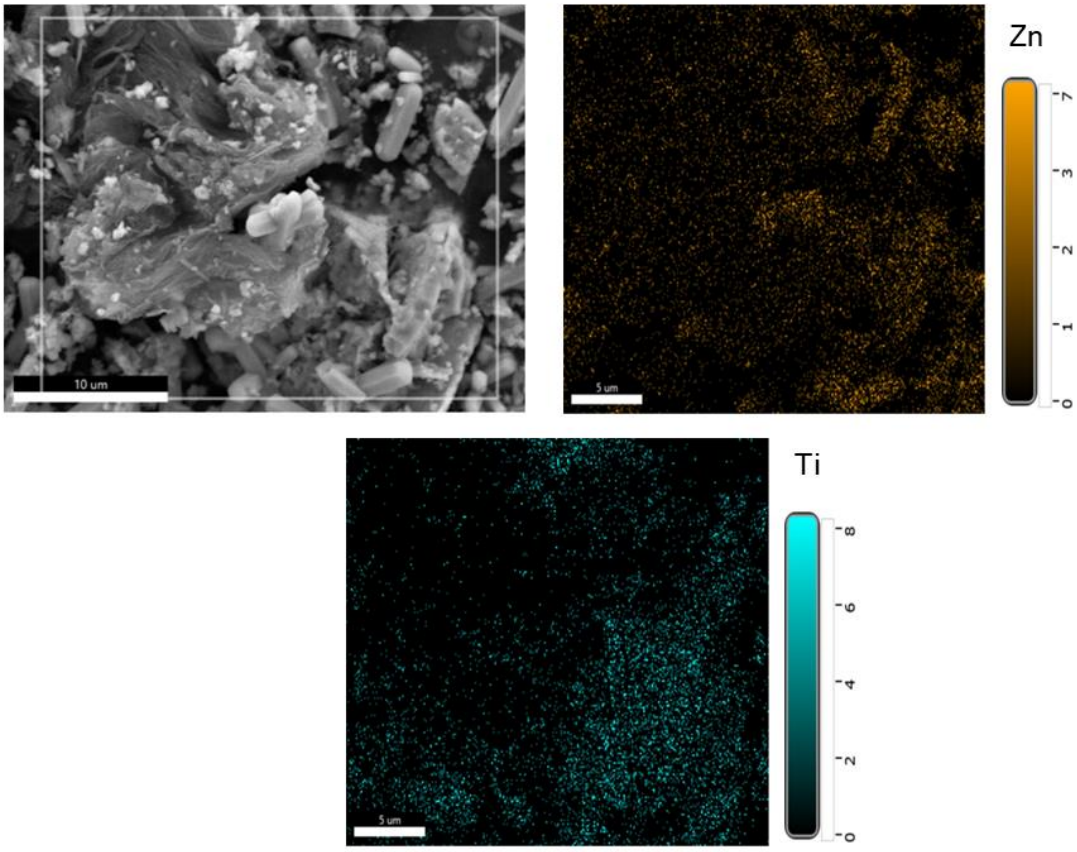

Figure 3.5. EDX mapping of composite III.

Table 3.2. The atomic composition of GO, composite I, composite II, composite III from areal EDX.

	C%	O%	Zn%	Ti%
GO	62.2	37.8	-	-
Composite I	9.5	49.4	30.7	10.4
Composite II	68.5	23.6	2.9	5
Composite III	58.3	26.9	6.7	8

3.5.4 X-ray Photoelectron spectroscopy

One of the important factors influencing photocatalytic reactions is the separation of electron-hole pairs, which in turn depends, among other things, on the intimacy of the contact between the materials at the junction. In our samples, the oxide particles form a junction with the r-GO, as seen in the SEM images, and by analyzing the XPS spectra of these samples, we conclude that the quality of binding between the oxides and r-GO is the best in the composite III.

The C1s and O1s XPS spectra from all the samples are presented respectively in Figures 3.6 and 3.7. The C1s electrons from C-O bonds show significantly weaker signals in composited samples, thereby suggesting the reduction in the GO and forming r-GO in these cases [223].

The de-convoluted spectra of the O1s signal in all the samples presented in Figure 3.7 shows two major peaks, one at a higher binding energy close to 532 eV and the other closer to 530 eV. The higher binding energy peak is attributed to the oxygen from the hydroxyl group adsorbed on the surface [224], [225]. The lower binding energy peak is attributed to the lattice oxygen, which may be bonded to zinc or titanium. Although these lattice oxygen atoms bonded to different cations show their XPS peaks at slightly different binding energy values [226], [227], we assume here that the first peak is due to the joint contribution of the two different lattice oxygen atoms. We note that, among the composites (Figures 3.7 (c), (d), and (e)), the composite III in Figure 3.7(e) has a hydroxyl signal significantly dominant compared to the lattice oxygen signal, unlike in the other two composites seen in Figures 3.7(c) and (d). This could be due to the fact that the third composite prepared under hydrothermal conditions undergoes high temperature, high

pressure treatment in presence of water that may lead to much higher irreversible hydroxyl group attachment to the particle surface.

A comparison of the peak positions in Figures 3.6 and 3.7 shows that the O1s peaks in the ZTO-GO composite samples from lattice oxygen generally shift towards lower binding energy values as compared to ZTO samples implying comparatively easier release of electrons in the composites. This could be caused by the loss of oxygen in composites that leaves behind excess electrons with the lattice that raises the chemical potential of the electrons such that release of electrons is easier in the composite samples. Although the bulk carbon percentage is low, XPS is a surface-sensitive technique and therefore records the chemistry of only the near-surface region, where the GO-derived carbonaceous phase is preferentially distributed. The C1s electrons also show a shift towards lower BE values as compared to pure GO samples. This can be explained by the observation that in composites, the GO reduces to r-GO making the GO richer in electrons, so that binding energy of the C1s electrons decreases in the r-GO present in the composite samples. The maximal shift is observed in the composite III (Table S2, Supporting Document) suggesting the highest reduction occurring in the hydrothermal method, which is in agreement with the XRD result presented in Table 1. The O1s signal in composites is not being compared with the Figure 3.7(a) because in composites, the oxygen has been significantly lost from the GO samples due to reduction, and the oxygen signal in the composites is assumed to be dominated by the oxygen atoms associated with the metal oxide.

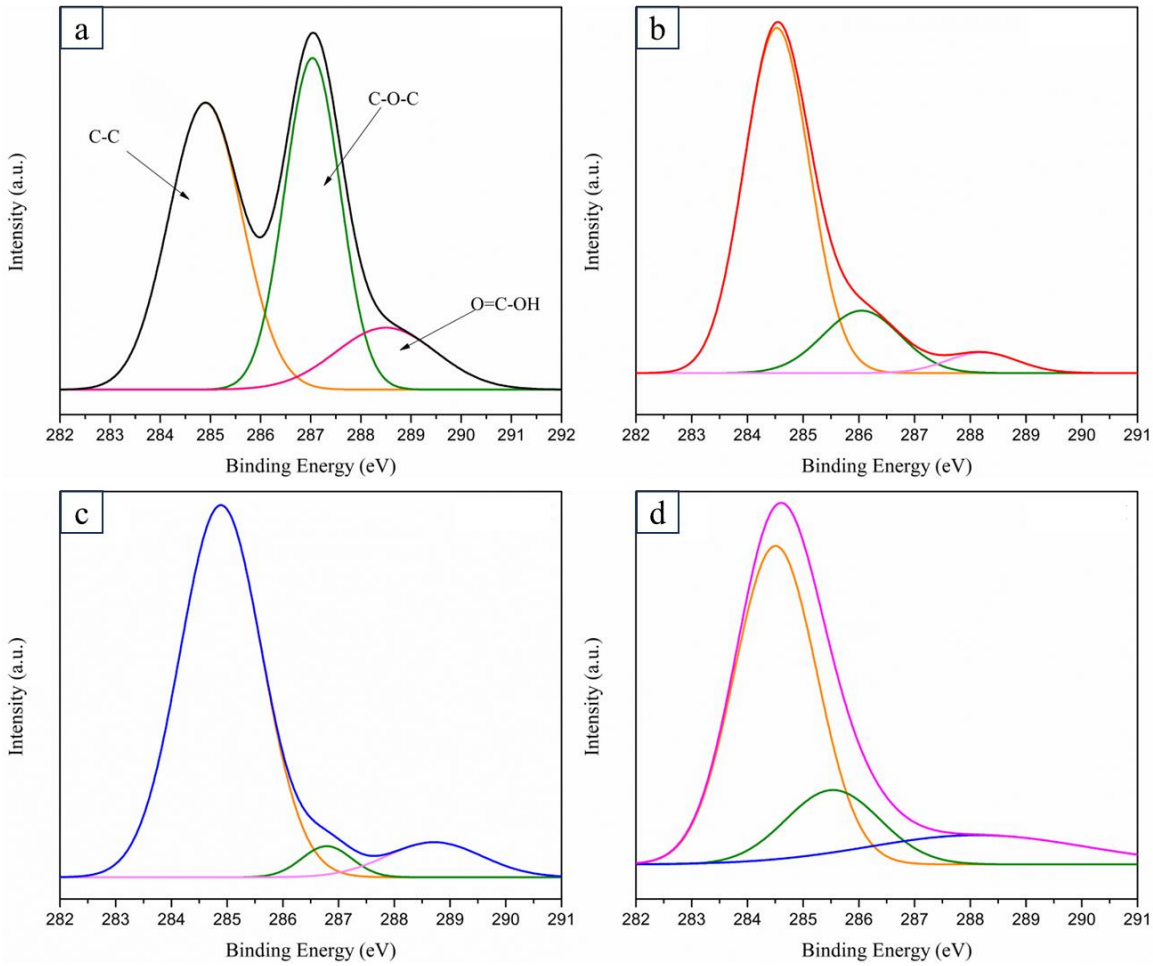

Figure 3.6. XPS of C1s of (a) GO, (b) composite I, (c) composite II, and (d) composite III.

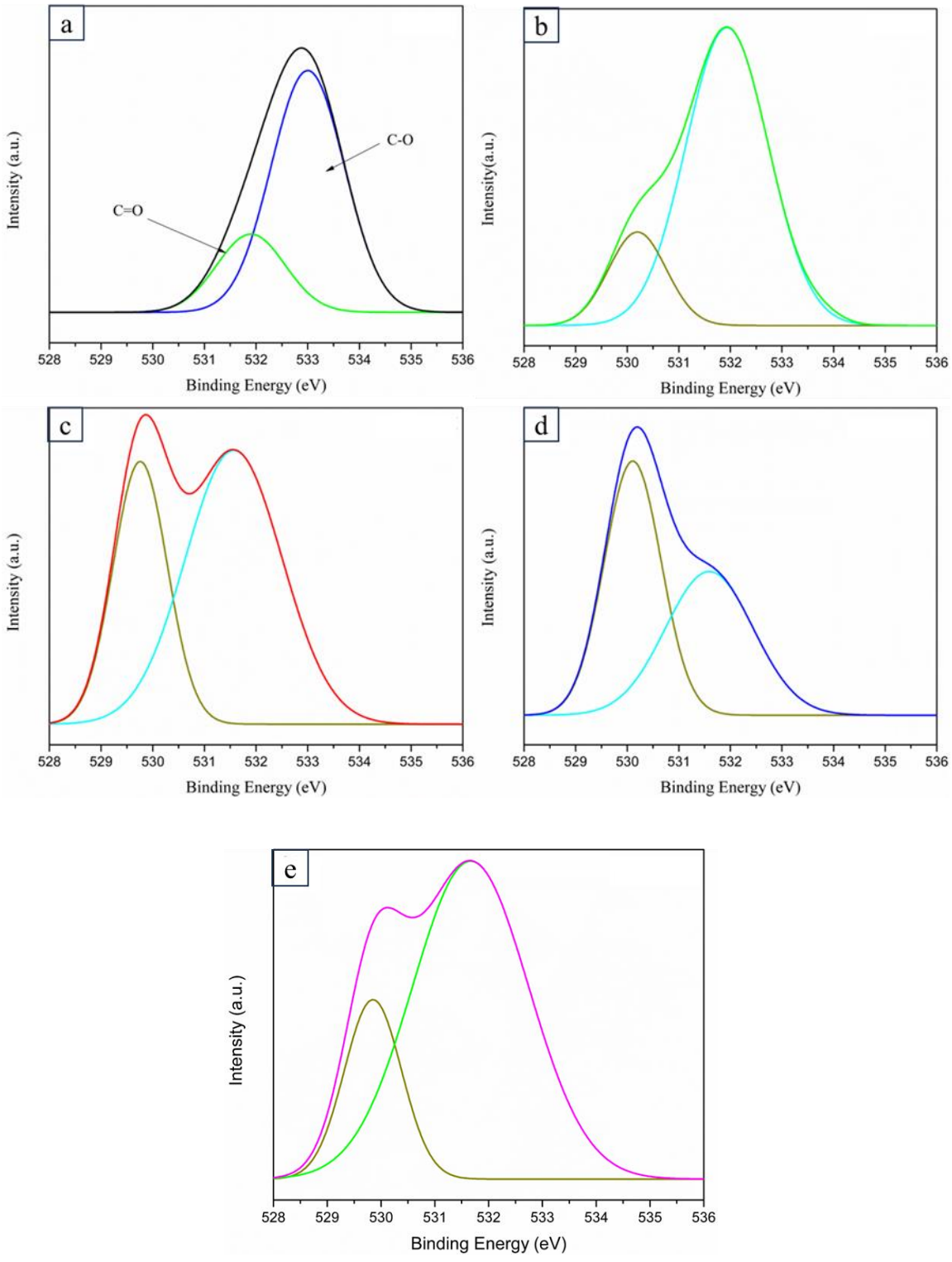

Figure 3.7. XPS of O1s of (a) GO, (b) ZTO, (C) composite I, (d) composite II, and (e) composite III.

3.5.5 Optical behavior from UV-Vis Diffuse Reflectance Spectroscopy

The band gap of the samples is determined by analyzing the reflectance spectra obtained from UV-Vis DRS spectroscopy [228]. We plot $[F(R)\times h\nu]^n$ against energy $h\nu$ (Tauc plot) using the reflectance R measured by DRS, as shown in Figure 3.8. The Kubelka Munk function, $F(R)$, is defined by the following relationship:

$$F(R) = \frac{(1-R)^2}{2R} \tag{3.1}$$

Here $n = 2$ denotes a direct allowed transition, and $n = 1/2$ denotes an indirect allowed transition [228]. We have assumed $n = 1/2$.

Figure 3.8(a) shows the raw data on reflectance of all the samples from DRS measurements, and Figures 3.8(b)-(e) shows the transformed data where $[F(R)\times h\nu]^n$ is plotted against $h\nu$, and the linear part of the curves are extrapolated to obtain the band-gap. The bandgaps measured for various samples are 2.85 eV for ZTO, 2.81 eV for composite I, 2.59 eV for composite II, and 2.73 eV for composite III. We attribute this decrease in bandgap to the loss of oxygen that results into the formation of oxygen vacancies. These oxygen vacancies are known to introduce donor states and lead to the narrowing down of the bandgap. In composite I, the reduction is not very effective due to solid state mixing leading to a small reduction in bandgap. Between composite II and III, oxygen loss is inhibited in composite III, thereby causing less oxygen vacancy. Hence, in composite II the highest change in bandgap occurs. However, due to the surface area effect, the specific surface area has been found to be highest in the composite III.

In the Tauc plots of the composite I and II, we also observe a second linear rise in the curve, which can be attributed to Zn_2TiO_4 in the samples. When extrapolated to the energy axis, the bandgap values corresponding to these second rises in the curves range between 3-3.4 eV. The Zn_2TiO_4 has been reported to have a bandgap in the range of 3.3eV to 3.7

eV [229] .The second rise in the curve is not prominent in the composite III because the composite III has $ZnTiO_3$ as a majority phase with much smaller fraction of Zn_2TiO_4, as was concluded from the XRD data.

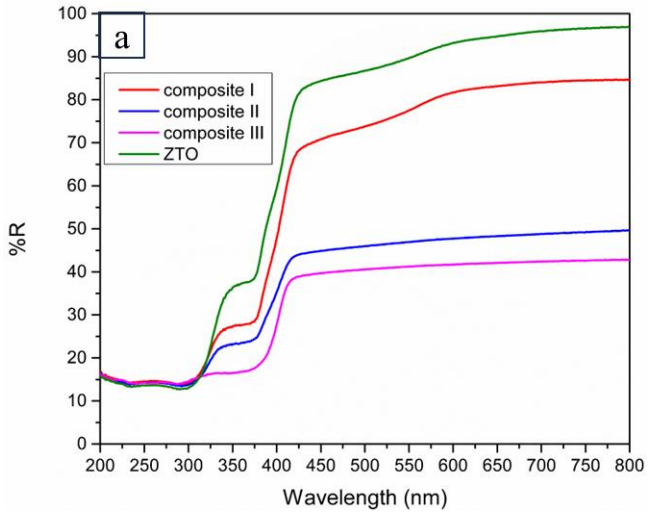

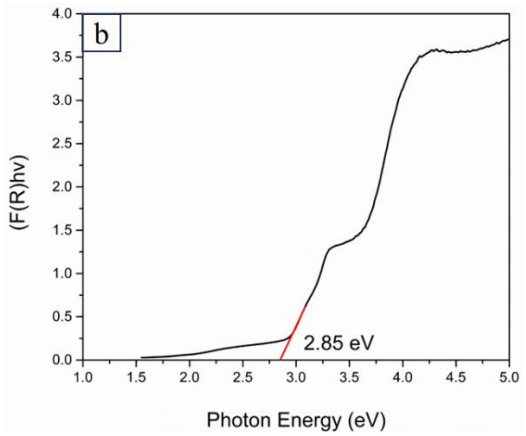

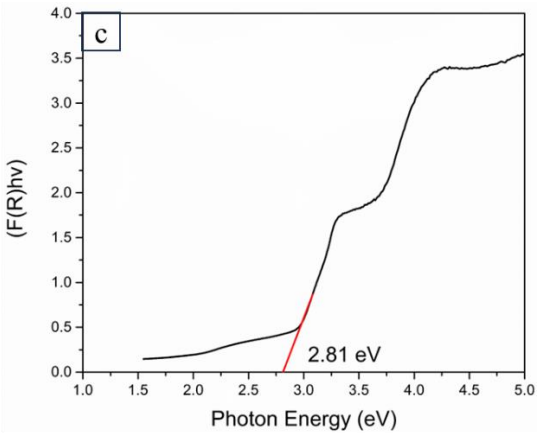

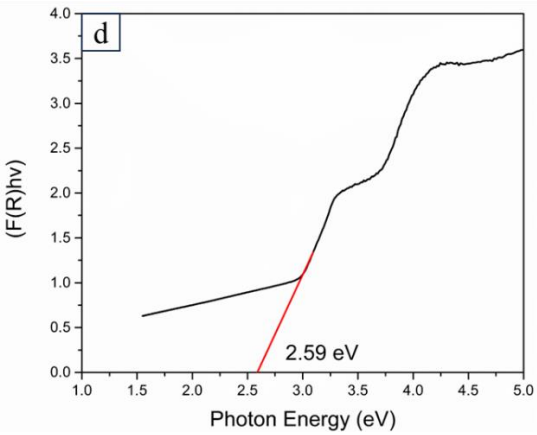

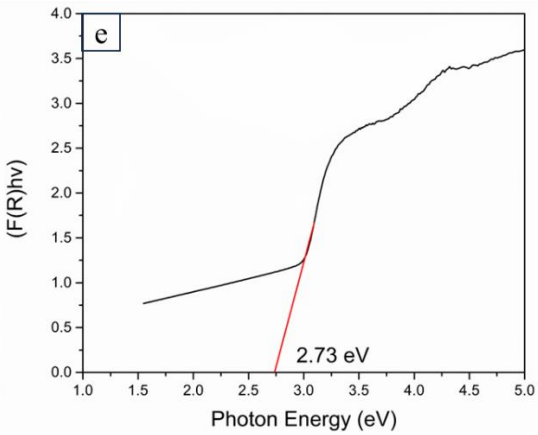

Figure 3.8. (a) UV DRS data in terms of reflectance. The plot of the Kubelka-Munk function versus the energy of exciting light that results in the band-gap of (b) ZTO, (c) composite I, (d) composite II, (e) composite III.

3.5.6 Photoluminescence Spectroscopy

The photoluminescence emission spectra have been widely employed to explore the effectiveness of charge carrier trapping, migration, and transfer, as well as to comprehend the fate of electron-hole pairs in semiconductors. In Figure 3.9, there are four emission bands observed in the visible region (excited at 400 nm), close to 423 nm, 460 nm, 485 nm, and 547 nm. The first band can be attributed to a transition caused by pure ZTO (2.9 eV), close to the band gap measured from DRS data (2.8 eV). The second emission at around 460 nm (~2.69 eV) showing in the PL spectra could be attributed to the transition from donor states to the valence band. The third emission band near 485 nm (~2.55 eV) could be attributed to the transition from donor to acceptor states [230]. The fourth emission band near 547 nm indicates (2.27 eV) ZTO, composite I, II, and III defects [231]. Figure 3.9 suggests that the samples prepared by the hydrothermal method have a higher reduction in emission intensity than other methods, which means there is an enhancement in carrier lifetime, leading to longer-lived carriers. Increased carrier lifetimes in these samples could be one reason for their improved photocatalytic activity. The increased lifetime can be attributed to better binding of the ZTO particles with the rGO sheets, as concluded from the XPS data.

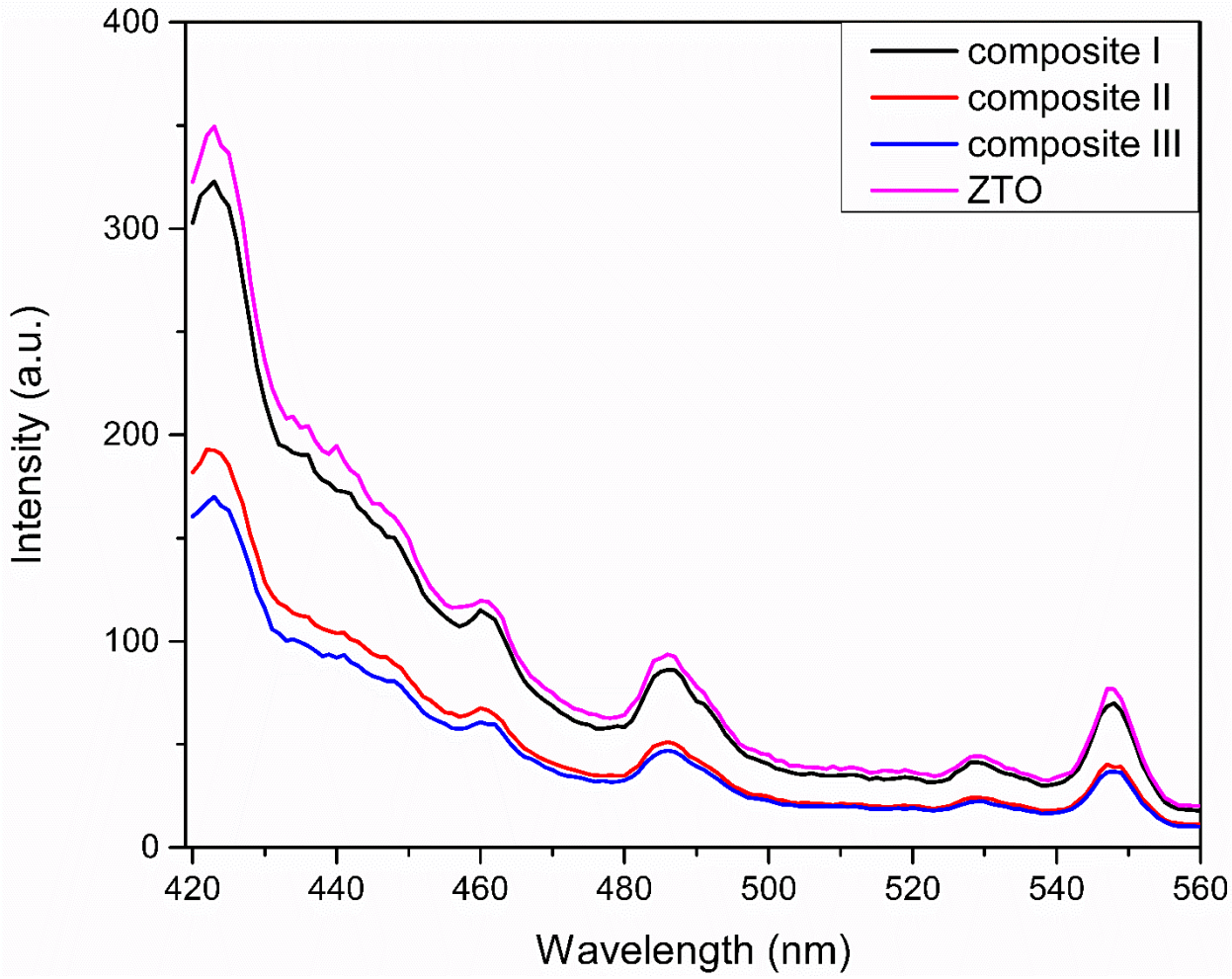

Figure 3.9. Photoluminescence spectra of ZTO, composite I, composite II, composite III.

3.5.7 Mott-Schottky Analysis

The Mott Schottky plot showing the variation of the inverse square of the measured capacitance against applied electrode voltage is presented in Figure 3.10. The flat-band potential (V_{fb}) is measured from the intercept of the linear part of the curve on the abscissa and the slope of the linear part is inversely proportional to donor density and is used to measure the donor density [232], [233]. V_{fb} is seen to shift negatively for the composites as compared to ZTO, revealing a smaller barrier for charge transfer in the composites. Graphene oxide sheets form an inherent barrier layer to block electron transfer from the

conduction band or trap sites of the composite to the electrolyte, retarding charge recombination in the composite/electrolyte interface [234]. The slopes of the composite II, and III showed a lower value, clearly indicating higher donor density [235]. The charge carrier density (N_d) of ZTO, composite I, composite II, and composite III are 2.02 x 10^{21} m^{-3}, 1.50 x 10^{21} m^{-3}, 7.95 x 10^{20} m^{-3}, and 6.76 x 10^{20} m^{-3} respectively.

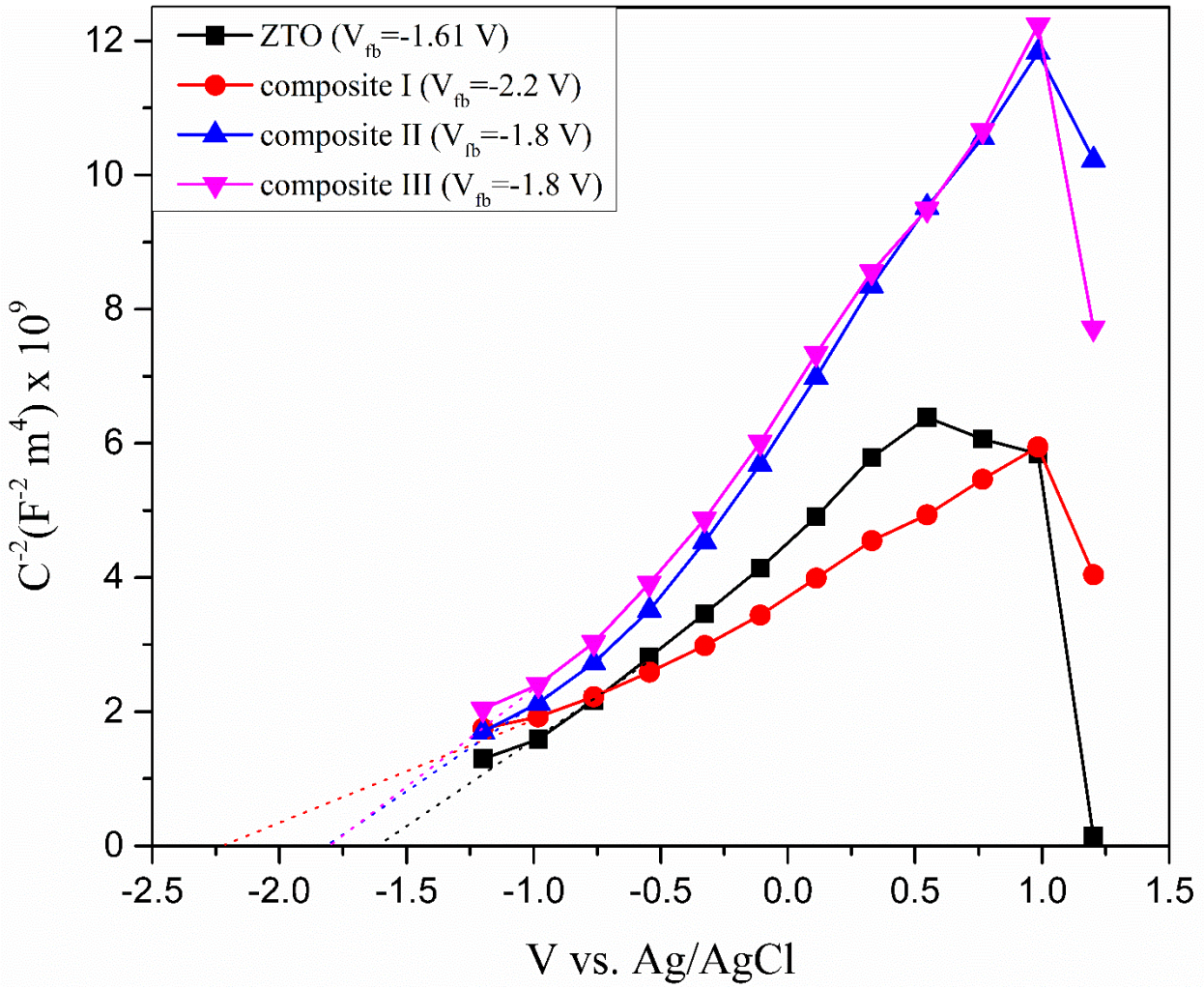

Figure 3.10. Mott- Schottky plot of ZTO, composite I, composite II, and composite III.

3.5.8 Nyquist plot from electrochemical impedance analysis

In order to compare the charge transfer resistance for various samples, the Nyquist plots determined from the electrochemical impedance data for different samples are plotted in Figure 3.11. The constant phase element is linked to a non-uniform current distribution

due to material heterogeneity and is comparable to double layer capacitance [236]. The lower arc radius of the materials signifies weaker interfacial charge transfer resistance, leading to a more rapid charge transfer mechanism [237].

A semicircular shape at the high frequency is observed for the composite I and II whereas a semicircle at high frequency and a linear rise at lower frequencies are observed in ZTO and composite III. The corresponding equivalent circuits (simple Randles circuit for ZTO and composite III and Randles circuit with Warburg elements included for composite I and composite II) used to determine the charge-transfer resistance (R_{ct}) by semi-circular fit of EIS data are also shown in Figure 3.11. We consider mass transfer resistance in modeling the equivalent circuits by including Warburg elements for composite III and ZTO samples, but not in composite I and II. However, since our main concern is the comparison of the charge transfer resistance, therefore ignoring Warburg impedance in composites I and II doesn't affect our analysis and conclusions. By fitting the semicircular part of the curve yield R_{ct} values of 1081.2 kΩ for composite I, and 1017.5 kΩ for composite II, 49.6 kΩ for ZTO, and a much smaller value of 3.1 kΩ for composite III.

The lowest value of R_{ct} for composite III is indicative of the most facile transfer of holes, which may be indicative of increased photoactivity.

Much higher values of R_{ct} for composite I and II compared to ZTO and composite III correlate with the presence of a higher fraction of Zn_2TiO_4 (and a smaller fraction of $ZnTiO_3$) in composite I and II and a smaller fraction of Zn_2TiO_4 (and a higher fraction of $ZnTiO_3$) in ZTO and composite III.

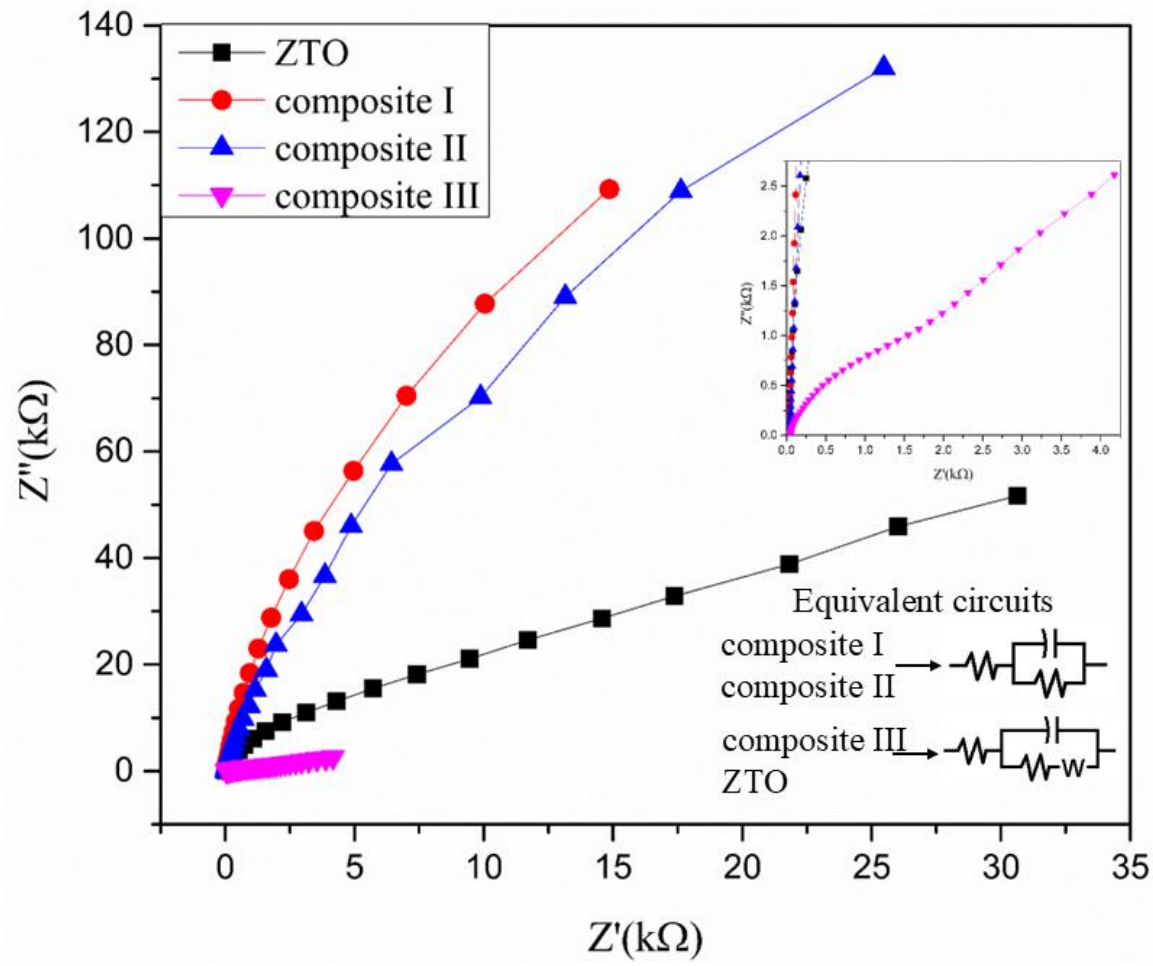

Figure 3.11. Nyquist plot of ZTO, composite I, composite II, and composite III.

3.6 Conclusion

In this chapter, the focus was on understanding how compositing GO with $ZnTiO_3$ modifies the structural, surface, and electronic properties of $ZnTiO_3$. Therefore, the application studies were not experimentally explored in this chapter. Instead, the results obtained here suggest that the composite may improve visible-light photocatalytic performance by enhancing charge separation, surface area, and interfacial electron transfer.

CHAPTER 4

Improving $ZnTiO_3$ dispersion in water and thereby its photocatalytic activity towards MB degradation by plasma exposure using custom designed set-up

4.1. Abstract

In this work, we show that photocatalytic activity of rhombohedral zinc titanate under visible light irradiation can be enhanced by nitrogen plasma exposure. The sol-gel prepared rhombohedral zinc titanate was treated with nitrogen plasma prepared in a custom-designed setup that allowed the plasma-treated particles to be immersed in liquid immediately after plasma treatment without bringing them into contact with the ambient environment. We found that plasma treatment resulted in an enhancement of the first-order rate constant of methylene blue (MB) degradation under visible light by approximately 56%. Characterizations of the particles using Scanning Electron Microscopy (SEM), X-ray Photoelectron Spectroscopy (XPS), X-Ray Diffraction (XRD), (Diffuse Reflectance Spectroscopy) DRS, and Brunauer–Emmett–Teller (BET) suggest that the enhancement can be ascribed to the creation of oxygen vacancies and enhancement in the surface area due to etching.

4.2. Introduction

The previous chapter established that different synthesis routes can be used to prepare composites of graphene oxide with $ZnTiO_3$, and that the resulting materials can be analysed to understand how the structural, surface, and electronic properties of $ZnTiO_3$ are modified by GO compositing. In the present chapter, the focus shifts from interfacial compositing to surface defect engineering, by improving the properties of $ZnTiO_3$ through nitrogen plasma treatment and examining how its structural, surface, and electronic characteristics are altered. By correlating plasma-induced changes in dispersion behaviour, surface area, and oxygen-vacancy formation with photocatalytic performance, this chapter evaluates plasma exposure as a complementary route for enhancing $ZnTiO_3$-based visible-light photocatalysts.

Photocatalytic materials significantly contribute to the treatment of water and effluents, antibacterial activity, and gas purification from industry, hence serving as a crucial component in environmental remediation[238]. Addressing both environmental pollution and the energy crisis through photocatalysis using semiconductor materials utilizing solar energy is an attractive route for achieving pollutant degradation, hydrogen production via CO_2 photoreduction, water splitting into bacterial disinfection, and hydrocarbon fuels[239]. $ZnTiO_3$ is a promising photocatalyst (semiconductor) that has been extensively studied for effluent treatment and the removal of contaminants from water[183], [207]. $ZnTiO_3$ among photocatalysts arises from its distinctive attributes, such as exceptional stability, accessibility, eco-friendliness, biological and chemical inertness, and cost-effectiveness[240]. Two important points to the utilization of $ZnTiO_3$ more effectively as a photocatalytic material: the first is the reduction in electron-hole pair recombination, which increases the generation of several reactive species such as OH during photodegradation processes, and the second is the improved optical response to

the UV spectrum due to its relatively low bandgap[241]. Surface engineering is a viable route for improving the photocatalytic activity of semiconductors, and methods such as UV irradiation, plasma treatment, and electron bombardment have been shown to favorably alter the surface characteristics of materials[242], [243], [244], [245], [246]. Plasma treatment is an attractive approach for surface alteration in catalyst manufacturing because it is simple, cost-effective, environmentally friendly, and energy efficient. In this method, the chemically active species comprising of excited ions, atoms, electrons, and radicals, distinguished by an extreme electron temperature ($1*10^4$ -$10*10^4$ K) and a low gas temperature (approximately room temperature), may readily interact with the material surfaces at low temperatures without compromising the underlying structure of the materials[247]. Recently, eco-friendly plasma surface treatments have been shown to markedly enhance the photodegradation effectiveness of photocatalytic materials[248]. Bharti et al. exposed Co and Fe doped titanium dioxide films to plasma treatment in atmospheric air, which enhanced their optical adsorption and absorbance range through the production of oxygen vacancies and Ti^{3+}[249]. Yamada et al. investigated the photocatalytic properties of nitrogen plasma-treated titanium dioxide films and showed an improvement in their visible light activity[250]. Karuppiah *et al.* discovered that plasma treatment may produce uniformly dispersed particles with a consistent shape, preventing agglomeration and enhancing the interaction between the component and the support in Ni/Al_2O_3-CeO_2[251]. To our knowledge, there are no existing studies on the impact of plasma treatment on the surface characteristics and photocatalytic efficacy of $ZnTiO_3$.

In this study, $ZnTiO_3$ synthesized by the sol-gel technique [207] underwent further plasma treatments in nitrogen using a custom-designed discharge plasma reactor, where the plasma-treated powder was immersed in a suitable solvent inside the reactor itself before

exposure to ambient conditions. When zinc titanate is exposed to plasma, the high-energy reactive species etch the surface, which increases the specific surface area and provides more active sites for the adsorption of dye molecules. Additionally, the plasma treatment introduces oxygen vacancies or functional groups that act as electron trap sites. These defects help capture photogenerated electrons, reducing the electron-hole recombination rate and leading to better charge separation. In the thesis, it is also noted that the treatment improves the suspension stability of the particles in water which is verified by zeta potential and reducing particle agglomeration, which further enhances light absorption and contact with the pollutant. Immersion inside the liquid in the reactor enables the isolation of the powder samples from the environment, thereby preventing the treated surface from reacting with atmospheric oxygen. A comparative study examining the impact of plasma on the chemistry of the surface, topography, and phase of $ZnTiO_3$ was investigated using X-ray photoelectron spectroscopy (XPS), scanning electron microscopy (SEM), and X-ray diffraction (XRD). The photodegradation effectiveness of $ZnTiO_3$ and plasma-treated $ZnTiO_3$ was examined based on their capacity to break down the Methylene Blue (MB) dye. We found that the plasma treatment improved the first order rate constant of photodegradation reaction from a value of 0.00538 min^{-1} to 0.00838 min^{-1} in the plasma treated samples. As expected, it was also found that the powder dispersion improved significantly after plasma treatment.

4.3. Experimental section

4.3.1. Materials

All materials were of analytical grade and were used without further purification. The zinc and titanium precursors were zinc acetate dihydrate from RFCL Limited in India and tetra butyl ortho titanate from TCI in Japan. SDFCL, India, supplied acetic acid glacial.

4.3.2. Zinc titanate synthesis

$ZnTiO_3$ particles were synthesized using the sol-gel method [2,12]. Zn $(CH_2COO)_2 \cdot 2H_2O$ (2.25 g) was combined with CH_3COOH (6.66 mL) under gentle stirring for 30 min at ambient temperature. Following the incorporation of the zinc salt into the CH_3COOH solution, Ti $\{OCH(CH_3)_2\}_4$ (3.40 mL) was introduced with continuous agitation at ambient temperature, resulting in a viscous, homogenous, white solution. Ten milliliters of deionized water were added into this combination, resulting in a clear and uniform solution. The reaction temperature increased to 60 °C and stirred for 2 hrs. Subsequently, the resultant solution was placed at an ambient temperature for 20 hrs. and transformed into a gel. After that it was subsequently calcined in an air muffle furnace at 800 °C for 3 hrs. The final product was pulverized using a crusher and pestle to obtain a fine powder, hereafter referred to as $ZnTiO_3$.

4.3.3. Plasma treatment of zinc titanate

Plasma treatment of $ZnTiO_3$ was conducted using a custom-designed plasma treatment apparatus fabricated by Excel Instruments (Maharashtra, India). The setup enables the isolation of the treated samples from the atmosphere by providing a liquid inlet port that enables the pouring of liquid over the sample after plasma treatment without breaking the vacuum. A liquid solvent, which is water in our case, was introduced into the reactor to immerse the samples before they were removed from the chamber. $ZnTiO_3$ was plasma-treated at an initial vacuum pressure of 10^{-2} Torr and at ambient temperature. The experimental setup is shown in Figure 4.1. The experiment was conducted in a stainless-steel reactor with two identical electrodes. The high-voltage electrode was linked to the power frequency output, whereas the low-voltage electrode was earthed. The plasma treatment reactor was powered by a pulsed DC power supply. Plasma-treated $ZnTiO_3$ was

mixed with deionized water under a vacuum of approximately 10^{-2} Torr. Viscosity and Dynamic Light Scattering (DLS) measurements of this suspension were performed to examine the effect of plasma treatment. After 60 min, the sample was recovered and dried at 60 °C, and the subsequently obtained powder was designated here as PT-$ZnTiO_3$.

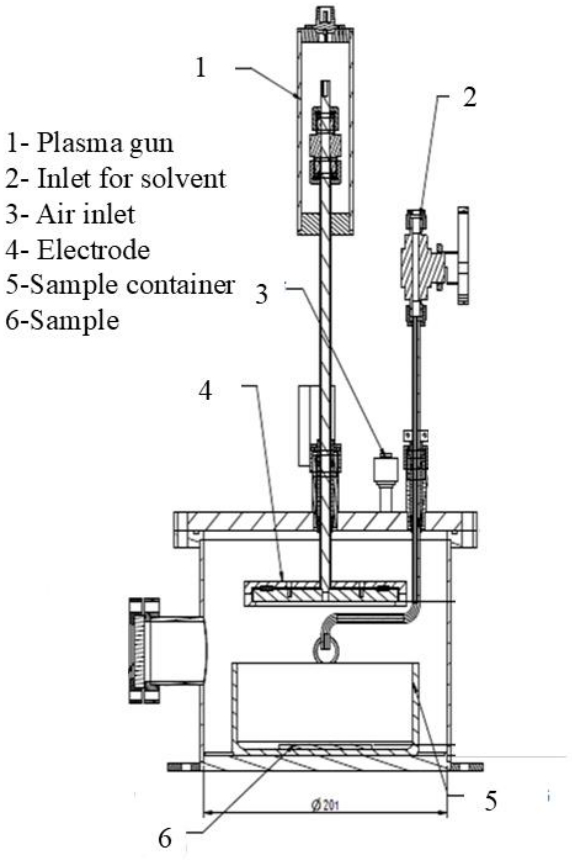

Figure 4.1. Customized plasma treatment Instrument.

4.3.4. Test for photocatalytic MB degradation

MB, which is known for its strong stability with photons and its solubility in water, was employed as a pollutant. For analysis, the photocatalyst (50 mg) was dispersed in 100 mL of MB (aq.) (40 mg/L) within a specially designed photocatalytic reactor, using light-emitting diodes (LEDs) as the light source. Before irradiation, the dispersion was agitated for 30 min in the dark to guarantee that MB attained the absorption-desorption equilibrium on the photocatalyst surface. Subsequently, the dispersions were treated with

visible white light LEDs. At specified intervals, 2 mL samples were collected and centrifuged to eliminate particles. The filtrates were examined by measuring the changes in the absorption of MB using a UV-Vis spectrophotometer.

4.4. Results and discussions

4.4.1. Suspension stability in water

Viscosity was measured by placing a suspension of $ZnTiO_3$ in DI water on a sample holder, and then a parallel plate geometry with a 50 mm diameter was used to measure viscosity at a constant shear rate of 10 s^{-1}. The effect of the plasma on the suspension viscosity of $ZnTiO_3$ is shown in Figure 4.2. As clearly shown, the suspension of $ZnTiO_3$ with plasma treatment shows nearly 2.75 mPa.s viscosity, and in the case of $ZnTiO_3$ without plasma treatment, it shows nearly the same viscosity as that of DI water, which is 0.8 mPa.s. PT-$ZnTiO_3$ shows nearly 3.5 times more viscosity than $ZnTiO_3$. Exposure to plasma leads to an altered electronic structure owing to the formation of oxygen vacancies. The chemically altered surface is exposed to water, which exposes it to the surroundings by breaking the vacuum. Therefore, we expect extensive hydroxylation of the particle surface in water, and thereby, the development of surface charge on these particles as compared to the untreated particles[252], [253]. Hence, the plasma-treated particles form a better dispersion in water because of the higher particle charge and higher viscosity. Although the viscosity showed a mildly decreasing trend with time, which can arise from particle aggregation, the aggregation kinetics were very slow.

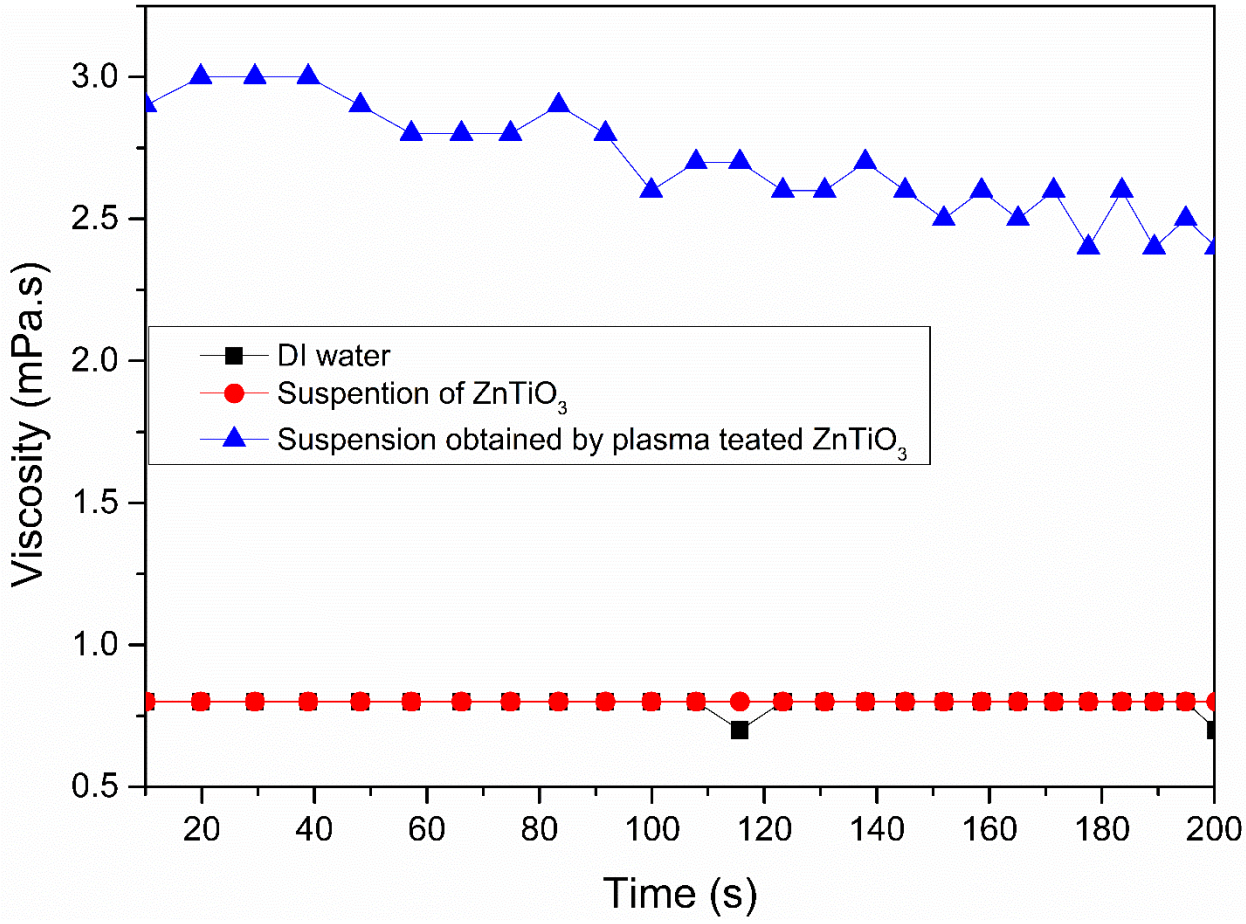

Figure 4.2. Viscosity of suspension of $ZnTiO_3$ and suspension obtained by plasma treatment of $ZnTiO_3$.

The development of particle charge upon plasma treatment was also evident from DLS analysis. Figure 4.3 shows the particle size distribution of $ZnTiO_3$ and PT-$ZnTiO_3$ obtained by the DLS method using water as the solvent. The average hydrodynamic diameters of $ZnTiO_3$ and PT-$ZnTiO_3$ were 550 and 500 nm, respectively. The PT-$ZnTiO_3$ samples show an increase in the fraction of smaller particles, which suggests the suppression of particle aggregation upon plasma treatment. The PT samples also show a wider variation in zeta potential values compared to the untreated particles, clearly suggesting a wide range of charges on them, which enhances their dispersion in water.

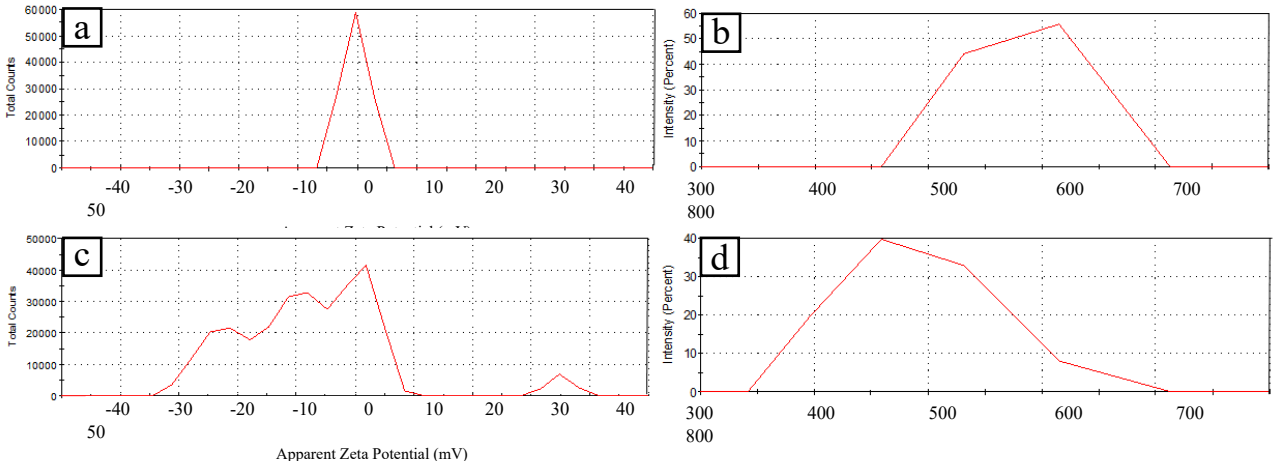

Figure 4.3. (a) Zeta potential of suspension of $ZnTiO_3$, (b) particle-size distribution of suspension of $ZnTiO_3$, (c) zeta potential of suspension of PT-$ZnTiO_3$, and (d) particle-size distribution of PT-$ZnTiO_3$ suspension.

4.4.2. Field Emission Scanning Electron Microscopy (FESEM) analysis

The surface appearance and microstructure of $ZnTiO_3$ and PT-$ZnTiO_3$ were examined using SEM. Compared to pure $ZnTiO_3$ (Figure 4.4(a, b)), which consists of a solid hexagonal particle, PT-$ZnTiO_3$ (Figure 4.4(c, d)) features nanopores on the surface of the $ZnTiO_3$ particle due to the bombardment of plasma on the surface of $ZnTiO_3$. EDX elemental analysis (Figure 4.5) revealed that a small amount of nitrogen was present in PT- $ZnTiO_3$ due to nitrogen plasma treatment, which may increase the efficiency of photocatalysis in plasma-treated samples[247], [254].

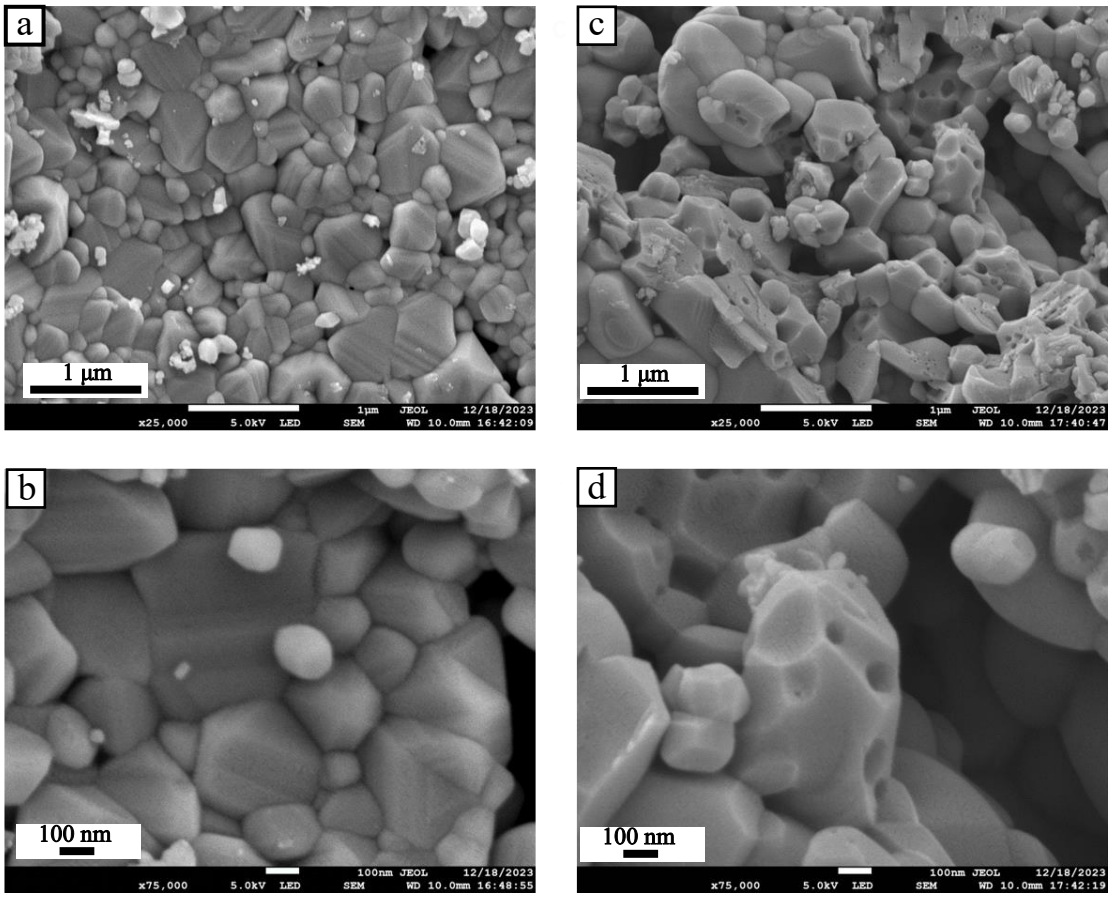

Figure 4.4.FESEM images of (a, b) ZnTiO3, and (c, d) PT- ZnTiO3. Lower panels correspond to higher magnification.

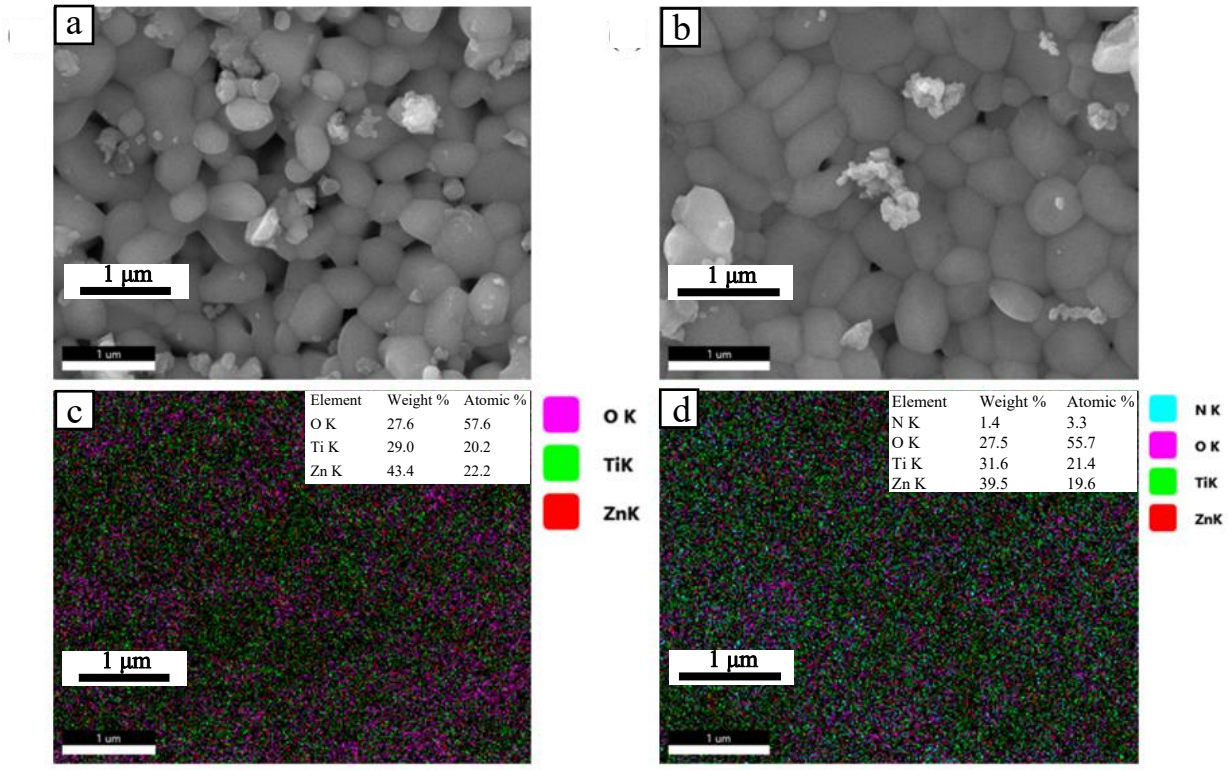

Figure 4.5. FESEM images of native and plasma treated ZnTiO3 are respectively shown in (a) and (b), and their elemental composition mapping obtained by EDX are shown in (c) and (d).

4.4.3. X-ray diffraction (XRD)

X-ray diffraction (XRD) patterns of pure $ZnTiO_3$ and PT-$ZnTiO_3$ are shown in Figure 4.6. Both samples show characteristic diffraction peaks at 21.19, 23.91, 32.8, 35.15, 40.45, 48.94, 53.44, 56.45, 61.97, and 63.39, consistent with the peaks of rhombohedral $ZnTiO_3$ (JCPDS 00-015-0591) with impurity phases of Zn_2TiO_4 (cubic), TiO_2 (rutile), and ZnO. Both samples exhibited identical peaks, indicating that plasma treatment did not alter the crystal structure and composition of phases present in $ZnTiO_3$ and PT- $ZnTiO_3$ are approximately same (Table 1).

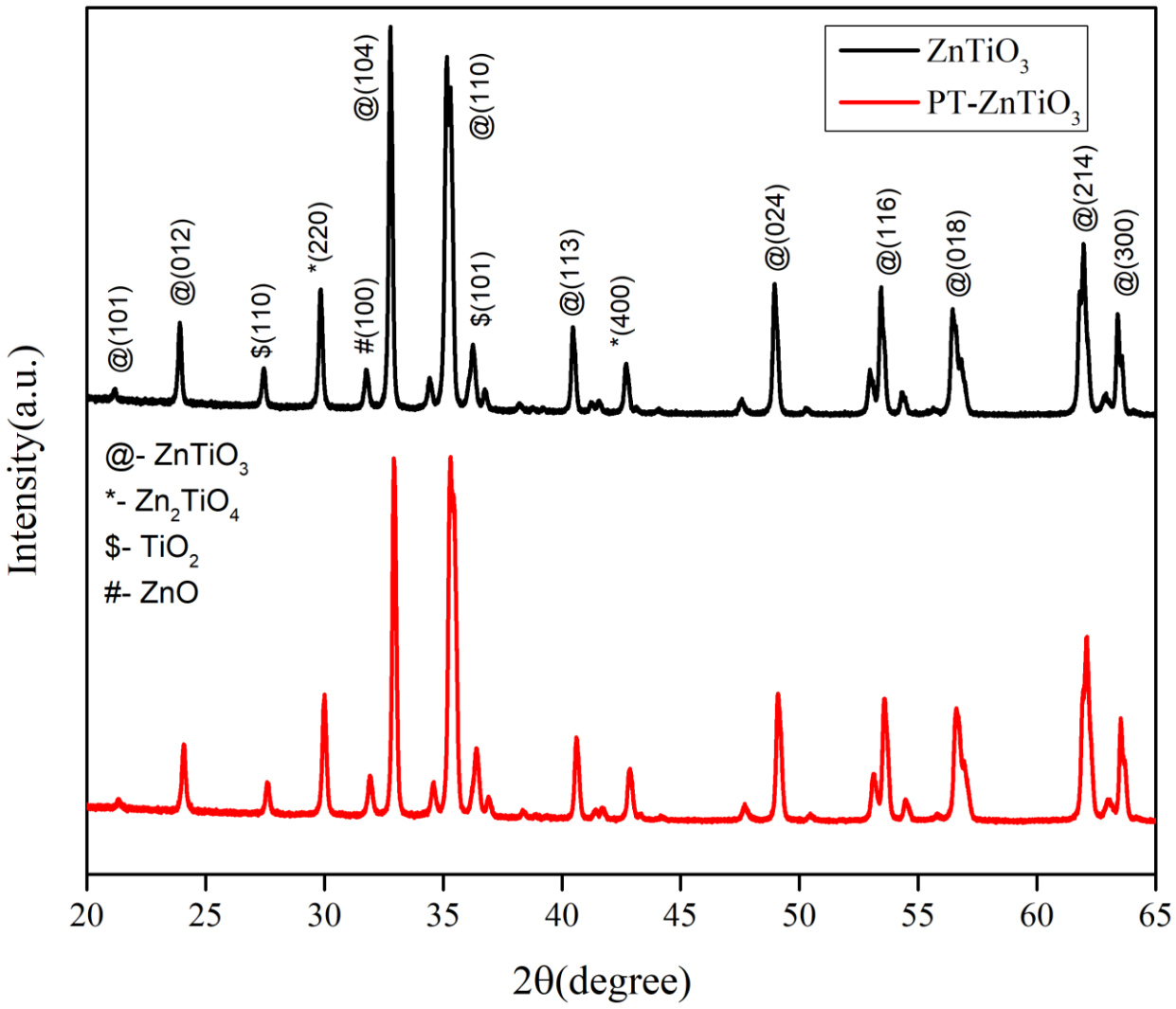

Figure 4.6. X-ray diffractogram of $ZnTiO_3$, and PT- $ZnTiO_3$.

Table 4.1. Composition of phases present in $ZnTiO_3$ and PT- $ZnTiO_3$.

Phases	$ZnTiO_3$ (untreated)	PT-$ZnTiO_3$
$ZnTiO_3$ (rhombohedral)	86.47%	86.56%
Zn_2TiO_4 (cubic)	6.97%	6.81%
TiO_2 (rutile)	4.87%	5.03%
ZnO (hexagonal)	1.68%	1.59%

4.4.4. Surface Area Analysis

Figure 4.7 illustrates N_2 adsorption-desorption for both native and plasma-treated PT-$ZnTiO_3$. These samples showed a type II isotherm, characterized by a very high adsorption capacity at elevated pressures (P/P_0:0.9-1), indicating the existence of macropores[255]. The hysteresis was found to be much higher in the plasma-treated samples, suggesting that these particles became mesoporous. The BET surface area of PT-$ZnTiO_3$ was determined to be 11.9 m^2 g^{-1}, around seven times higher than that of $ZnTiO_3$ (1.7 m^2 g^{-1}). The alterations in the morphology of the surface and the increase in the specific surface area are mostly due to the etching effect induced by plasma treatment, as confirmed by SEM imaging. [256]. The plasma contained abundant highly active and energetic molecules that contributed to the formation of pores in the $ZnTiO_3$ particles[257]. The increased specific surface area facilitates the absorption of more active species and reactants on the surface. Consequently, we expect that PT-$ZnTiO_3$ will exhibit superior photocatalytic activity compared to $ZnTiO_3$.

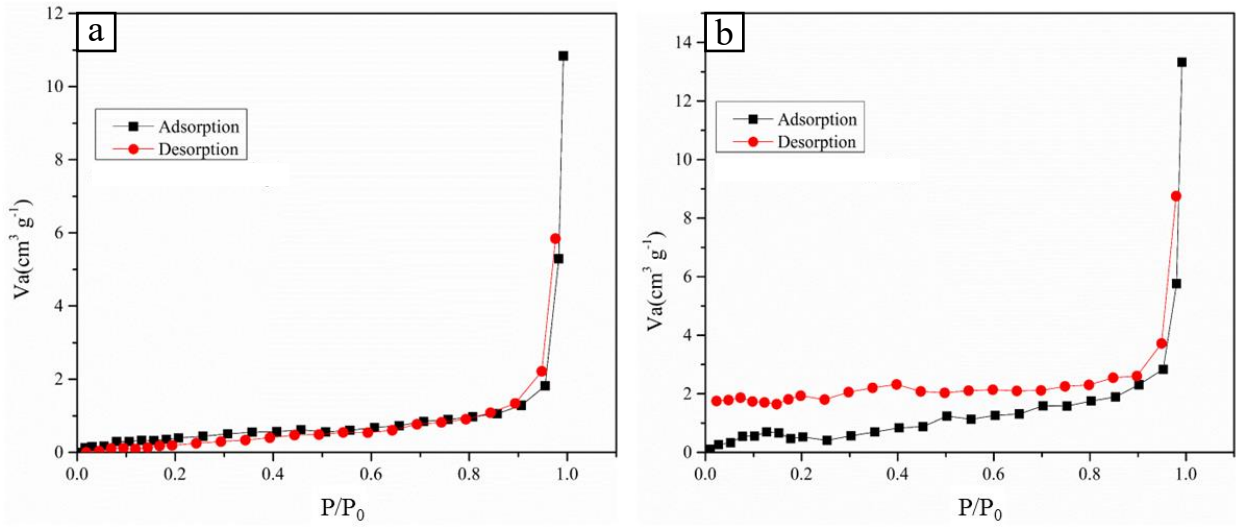

Figure 4.7. The BET surface area and isotherm of (a) $ZnTiO_3$, and (b) PT- $ZnTiO_3$.

4.4.5. Optical behaviour from UV-Vis Diffuse Reflectance Spectroscopy

The impact of plasma treatment on optical properties was examined using UV-Vis diffuse reflectance spectroscopy (DRS). Figure 4.8 (b) shows the Tauc plot obtained from the UV-Vis DRS (Figure 4.8 (a)) used to determine the bandgap. A small band gap reduction from 2.85 eV in untreated samples to 2.78 eV in the plasma treated samples is observed. Defects are known to significantly affect the bandgap and photocatalytic activity of $ZnTiO_3$ photocatalysts[258], [259]. Tay and Niu et al. indicated that oxygen vacancies may reduce the bandgap in $ZnTiO_3$ by creating gap states near the valence band, thereby inducing bandgap narrowing[258], [260]. Here, we conclude that exposure to plasma promotes the formation of oxygen vacancies in zinc titanate[260], a conclusion that is further supported by our XPS results.

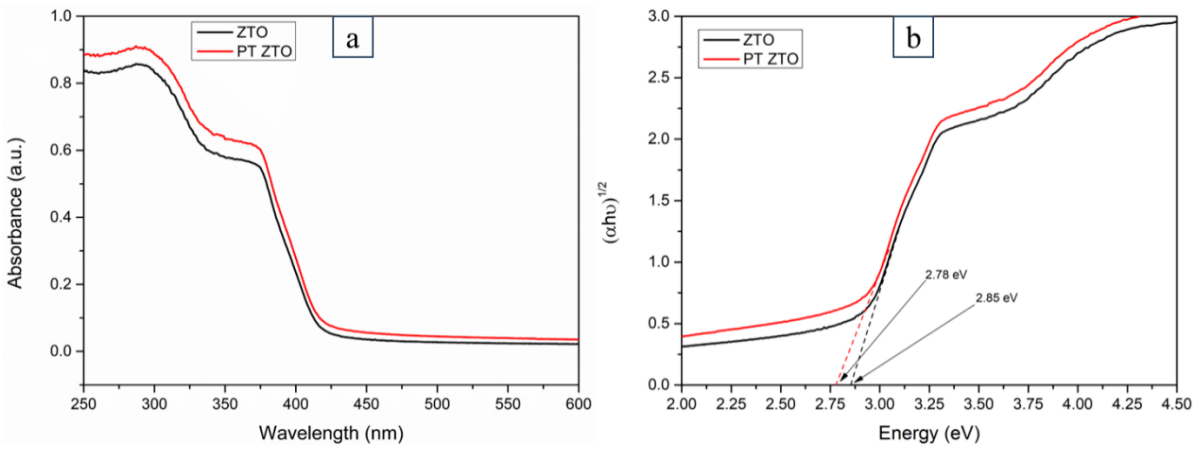

Figure 4.8. (a) UV–vis DRS, and (b) Tauc plots of $ZnTiO_3$ and PT-$ZnTiO_3$.

4.4.6. X-ray Photoelectron spectroscopy

The impact of plasma treatment on the chemical speciation and surface composition was further examined using XPS, and the data are presented in Figure 4.9. High-resolution O-1s spectrum of $ZnTiO_3$ and PT- $ZnTiO_3$ were fitted using Gaussian curves. The XPS data confirmed that the plasma treatment promoted the formation of oxygen vacancies in zinc

titanate, whereas the cations were hardly affected by the nitrogen plasma. The deconvoluted signal due to O1s in Figure 4.9 arises from two species: the metal-bonded oxygen (O-Zn and O-Ti) appearing at smaller binding energy values, and oxygen lying in the neighborhood of vacancies at a larger binding energy. In native $ZnTiO_3$ the first type (metal-bonded oxygen) appears at 529.36 eV and the second kind at 530.75 eV[226], [261]. The same two species are also found in the PT-$ZnTiO_3$ samples, as seen in Figure 4.9 (b), where the former appears at 529.48 eV and the latter at 531.06 eV. However, the second peak due to the oxygen near the vacancies was found to have nearly 17% larger FWHM and nearly 7% larger area in the PT samples as compared to the untreated samples, indicating a larger abundance of surface vacancies in PT-$ZnTiO_3$[262].

Additional evidence of significant oxygen vacancy formation in plasma-treated samples comes from the XPS signal of Zn^{2+} ions. The Zn 2p core-level XPS spectrum in Figure 4.9(c, d) shows that the otherwise symmetric peaks due to $2p_{1/2}$ and $2p_{3/2}$ electrons (centered around 1021 and 1044 eV) in $ZnTiO_3$ develop small shoulders towards the higher BE side in the PT-$ZnTiO_3$ samples. Deconvolution of the $2p_{1/2}$ and $2p_{3/2}$ peaks in the plasma-treated samples shows the presence of additional small peaks at 1022.4 and 1045.7 which may originate from the Zn^{2+} ions surrounded by oxygen vacancies[263]. The XPS spectra of the Ti 2p for $ZnTiO_3$ and PT-$ZnTiO_3$ are presented in the Figure 4.9(e, f), displaying two peaks at 463.68 eV and 457.8 eV, which correspond to the $Ti2p_{1/2}$ and $Ti2p_{3/2}$ electrons respectively. The nearly identical Ti signals in the two samples confirmed that the chemical environment of Ti^{4+} was not altered upon plasma treatment[261]. Thus, the XPS analysis lends support to the conclusion that the major effect brought about by the plasma treatment in $ZnTiO_3$ is the formation of oxygen vacancies.

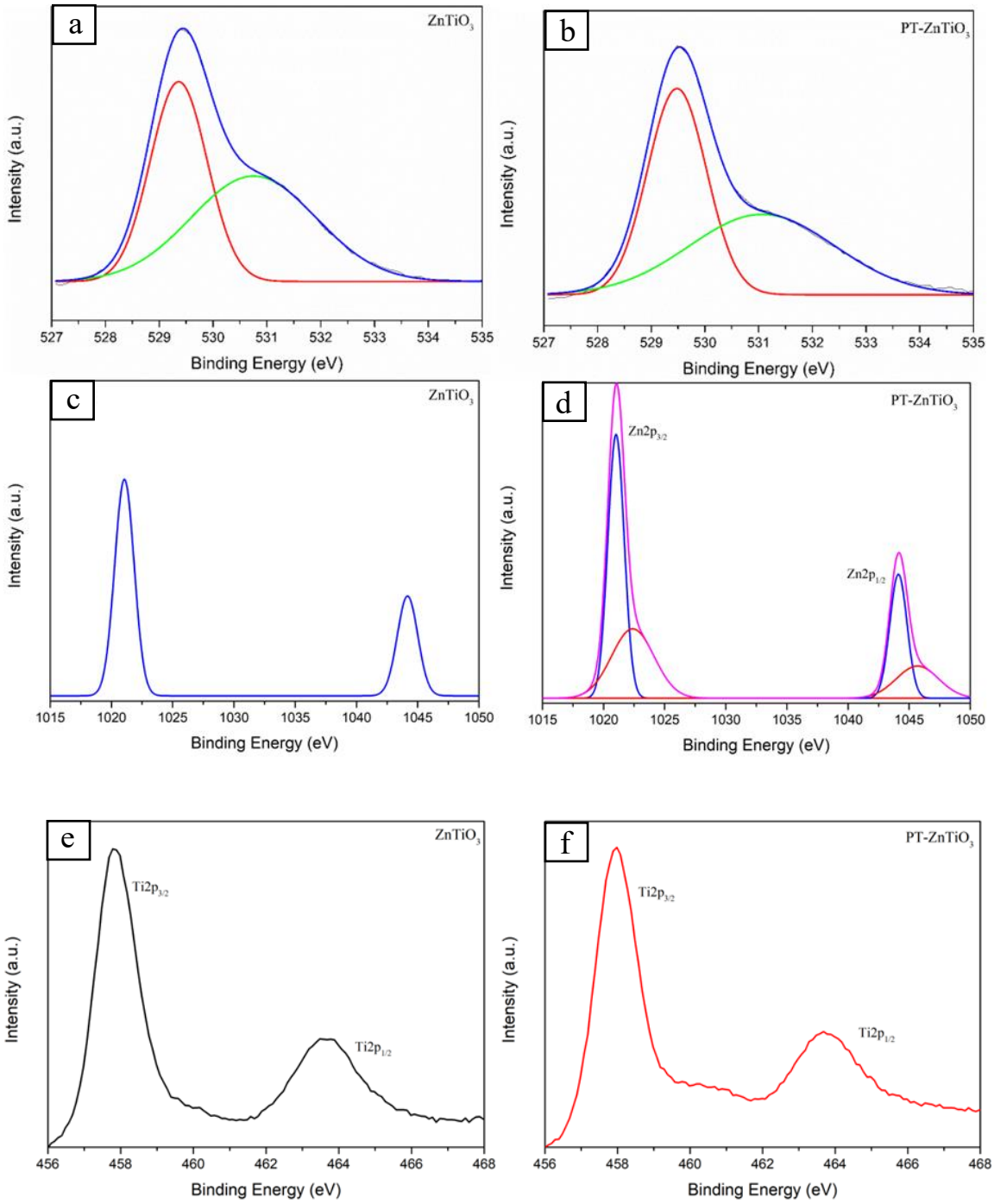

Figure 4.9. XPS signals from (a) O1s of $ZnTiO_3$, (b) O1s of PT-$ZnTiO_3$, (c) Zn2p of $ZnTiO_3$, (d) Zn2p of PT-$ZnTiO_3$, (e) Ti2p of $ZnTiO_3$, and (f) Ti2p of PT-$ZnTiO_3$.

4.5. Photocatalytic degradation of methylene blue

The photocatalytic activities of the native and plasma-treated zinc titanate were compared by studying their effects on the photocatalytic degradation of methylene blue (MB) under

visible light irradiation. Before irradiation, the suspensions were magnetically agitated in the dark for 30 min to achieve absorption-desorption equilibrium between the photocatalyst and methylene blue. Subsequently, the LED was turned on and the concentration of MB was monitored over time by measuring its absorption spectrum in the presence of the particles and using the peak absorbance at 600 nm at pH 12 for concentration measurement of the MB dye. The time dependence of the absorption spectra is presented in Figures 4.10 (a, b). The measured concentrations from the absorption curves are plotted against time in Figures 4.10 (c, d). The concentration dependence on time ($C(t)$) is fitted to the following first-order kinetics equation to extract the value of k:

$$-\ln(\frac{C}{C_0}) = kt \tag{4.1}$$

where, C_0 is the initial dye concentration. The kinetic rate constant was determined to be 0.00838 min^{-1} for PT-$ZnTiO_3$, which is around 1.56 times greater than those of $ZnTiO_3$ (0.00538 min^{-1}). The results indicated that plasma treatment markedly enhanced the photocatalytic activity of $ZnTiO_3$ by optimizing its surface characteristics, thereby enhancing the specific surface area. Based on the foregoing discussion of the characterization data of the zinc titanate particles, we conclude that exposure to nitrogen plasma enhances the photocatalytic activity of zinc titanate for two reasons: (i) it forms oxygen vacancies, which leads to a reduction in the observed bandgap caused by the gap states introduced by vacancy formation, and (ii) the plasma treatment significantly enhances the surface area by etching, generating more active sites for the catalytic reaction. The improved photocatalytic performance can be correlated with the combined influence of surface area, defect chemistry, and charge separation behavior induced by plasma treatment. The increase in accessible surface sites enhances adsorption of

methylene blue molecules, while the modified surface defects and oxygen vacancies promote charge trapping and reduce electron-hole recombination. In addition, the improved interfacial characteristics of the plasma-treated sample facilitate more efficient charge transfer during photocatalysis. Therefore, the enhanced degradation rate is not due to a single parameter, but rather to the synergistic effect of these structural and electronic modifications.

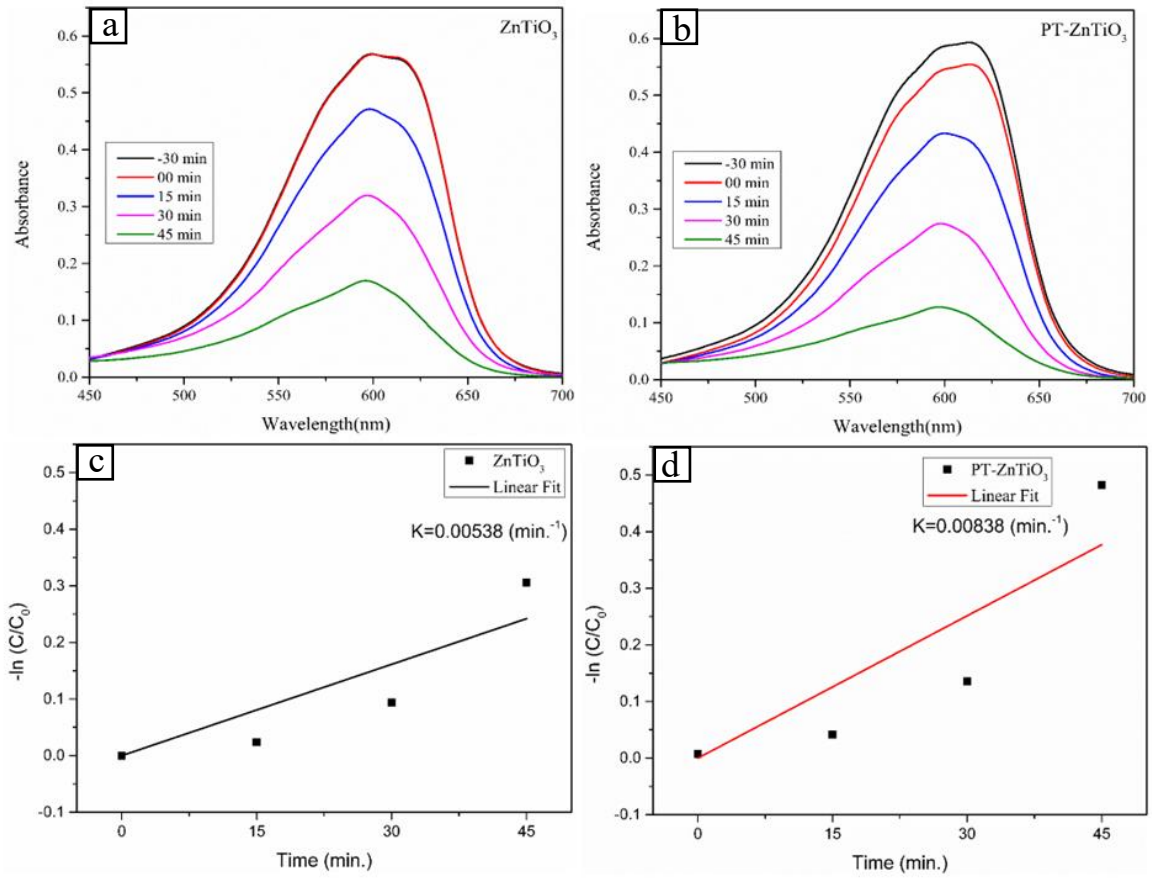

Figure 4.10. The absorption spectra of MB dye after varying time for (a) $ZnTiO_3$ and (b) PT-$ZnTiO_3$. First order kinetics fit for the degradation of MB for (c) $ZnTiO_3$ and (d) PT-$ZnTiO_3$.

Finally, Table 4.2 presents a comparison of the rate constants of the MB photocatalytic degradation reaction in the presence of other catalyst particles reported in the literature. The results indicate that the photodegradation of PT-$ZnTiO_3$ is suitable and shows

reasonable photodegradation performance for MB, showing better performance than many other photocatalysts.

Table 4.2. Comparison of degradation efficiency and kinetics for different photocatalysts.

Photocatalyst	Catalyst amount (mg/mL)	MB concentration (mg/L)	Irradiation time (min.)	Rate constant (min^{-1})	Reference
$ZnTiO_3$	0.5	40	45	0.00538	This work
PT-$ZnTiO_3$	0.5	40	45	0.00838	This work
Zn_3Ti_1-LDH	0.25	20	180	0.00637	[264]
$ZnTiO_3$	0.1	20	25	0.00399	[240]
10%PANI/ $ZnTiO_3$	0.1	20	25	0.00479	[240]
1%Ag/10%PANI/$ZnTiO_3$	0.1	20	25	0.00738	[240]
0.1 % of Ag-Fe co-doped $ZnTiO_3$	0.2	10	90	0.0011	[265]
0.3 % of Ag-Fe co-doped $ZnTiO_3$	0.2	10	90	0.0021	[265]
$ZnTiO_3$(hexagonal)-TiO_2(anatase)	1	10	120	0.0013	[266]

4.6. Conclusion

In this chapter, the main focus was on understanding how plasma treatment influences the structural and photocatalytic properties of $ZnTiO_3$. The results show that plasma treatment modifies the surface chemistry, defect concentration, and charge carrier

behavior of the material. These changes contribute to the improved photocatalytic degradation of methylene blue under visible-light irradiation. The observed enhancement in photocatalytic activity clearly indicates that plasma treatment is an effective surface modification strategy for $ZnTiO_3$.

CHAPTER 5

Synthesis and characterization of deep eutectic solvent-assisted Cu doped zinc titanate and its DFT study

5.1 Abstract

This study reports the successful synthesis of Cu-doped zinc titanate ($ZnTiO_3$) nanoparticles using a deep eutectic solvent (DES)-assisted approach for enhanced photocatalytic applications. The chloride-based DES system enabled controlled doping and uniform particle morphology at moderate temperatures, offering a greener alternative to conventional high-temperature solid-state methods. Comprehensive characterization through X-ray diffraction (XRD), scanning electron microscopy (SEM), UV-visible spectroscopy, and energy-dispersive X-ray spectroscopy (EDX) confirmed the successful incorporation of Cu dopants into the $ZnTiO_3$ lattice structure. Density functional theory (DFT) calculations revealed that Cu doping introduces intermediate energy states within the bandgap, effectively narrowing the optical bandgap from the pristine $ZnTiO_3$ value and enhancing visible light absorption. The modified electronic structure promotes efficient charge carrier separation and reduces electron-hole recombination rates. The synergistic combination of DES-mediated synthesis and strategic Cu doping presents a

promising pathway for developing high-performance photocatalysts for environmental remediation and solar energy conversion applications.

5.2 Introduction

The previous chapter established that graphene oxide compositing leads to significant modifications in the structural, surface, and electronic properties of $ZnTiO_3$, and also demonstrated the impact of plasma treatment. In the present chapter, the focus is on improving the properties of the $ZnTiO_3$ by Cu doping and examining how the deep eutectic solvent assists the doping process to further enhance the properties of $ZnTiO_3$. In addition, a DFT study is carried out to computationally understand how Cu incorporation improves the properties of the metal oxide with the help of density of states and band structure.

Transition metal doping has proven to be an effective strategy for enhancing photocatalytic performance by modulating the electronic structure and optical properties of semiconductor materials [148], [267], [268], [269]. Copper doping offers several advantages including the introduction of intermediate energy levels within the bandgap, enhanced visible light absorption, and improved charge carrier dynamics [270], [271]. The Cu^{2+} ions can act as electron traps, effectively reducing the recombination rate of photogenerated charge carriers and extending their lifetime for participating in redox reactions [272], [273], [274].

Conventional synthesis methods for doped zinc titanate materials typically require high-temperature solid-state reactions (nearly 900 °C), which often result in poor dopant distribution, large particle sizes, and high energy consumption [268], [270], [275]. Deep eutectic solvents (DESs) have emerged as environmentally supportive alternatives to traditional organic solvents, offering unique advantages including low toxicity,

biodegradability, tunable physicochemical properties, and the ability to facilitate controlled crystallization at moderate temperatures [276], [277], [278], [279], [280]. Choline chloride-based DES systems have demonstrated exceptional versatility in materials synthesis due to their hydrogen bonding networks that can stabilize precursor species and direct crystal growth [281], [282], [283], [284]. Despite the growing interest in both Cu-doped photocatalysts and DES-mediated synthesis, the integration of these approaches for $ZnTiO_3$ preparation remains largely unexplored.

In this work we investigate the DES-assisted synthesis of Cu-doped $ZnTiO_3$, combining experimental characterization with computational insights from density functional theory calculations. The study aims to elucidate the role of DES in facilitating uniform Cu doping, understanding the electronic structure modifications induced by Cu incorporation. The findings provide fundamental insights into the structure-property relationships of doped zinc titanate and demonstrate a sustainable synthetic approach for developing next-generation environmental remediation materials.

5.3 Experimental section

5.3.1 Materials

All materials were of analytical grade and were used without further purification. The zinc and titanium precursors were zinc acetate dihydrate from RFCL Limited in India and tetra butyl ortho titanate from TCI in Japan. SDFCL, India, supplied acetic acid glacial. Copper nitrate trihydrate purchased from MOLYCHEM, India.

5.3.2 Synthesis of zinc titanate (ZTO)

ZTO powder was synthesized using the sol-gel method. The mole ratio of Zn: Ti was determined to be 1:0.9 [119]. In a typical synthesis, 2.25 g of zinc acetate dihydrate and

3.14 mL of titanium tetra butoxide were dissolved in 3.33 mL of acetic acid (CH_3COOH) separately. Both solutions were mixed with magnetic stirring and heated to around 50 ◦C followed by mixing with deionized water (10 mL). After mixing deionized water, a transparent sol was obtained, which over time formed a gel. During the gel aging process, it was realized that maintaining a constant temperature is critical for getting a transparent and homogeneous gel. To remove excess solvent, dry for 10 h at 120 ◦C. The resulting gel was calcined at 800 ◦C equilibrated for 3 h at a heating rate of 10 ◦C/min to obtain the final powders.

5.3.3 Synthesis of Cu doped ZTO

Then, 70 mg Cu $(NO_3)_2 \cdot 3H_2O$ was added to 10 mL DI water under vigorous stirring at 75 °C. After 30 min, the Cu $(NO_3)_2 \cdot 3H_2O$ was dissolved entirely into DI water. Subsequently, 500 mg of ZTO was added to the DI water containing the dissolved Cu salt with 24 h of stirring. The obtained Cu/$ZnTiO_3$ slurry in DI water was washed with deionized water and ethanol using vacuum filtration. The collected product was dried overnight in a vacuum oven at 175 °C. The samples obtained are denoted $ZnTiO_3$/Cu (14% with DI).

5.3.4 Synthesis of DES

The DES were prepared using the quaternary ammonium salt of choline chloride and urea as hydrogen bond donors at a molar ratio of 1:2. The as-prepared DES solution was placed in a three-necked flask and kept under constant magnetic stirring at a temperature of 60 °C for 1 hr. After 1 hr the entire mixture was converted entirely into a viscous transparent liquid, which was used as an ionic solvent [285].

5.3.5 Synthesis of DES assisted Cu doped ZTO

Then, 70 mg Cu $(NO_3)_2 \cdot 3H_2O$ was added to 10 mL DES solution under vigorous stirring at 75 °C. After 30 min, the Cu $(NO_3)_2 \cdot 3H_2O$ was dissolved entirely into the DES solvent. Subsequently, 500 mg of ZTO was added to the DES containing the dissolved Cu salt with 24 h of stirring. The obtained Cu/$ZnTiO_3$ slurry was washed with deionized water and ethanol using vacuum filtration. The collected product was dried overnight in a vacuum oven at 175 °C. A similar procedure was employed by varying amount of Cu $(NO_3)_2 \cdot 3H_2O$ to 140 mg. The obtained sample are denoted $ZnTiO_3$/Cu (14% with DES) and $ZnTiO_3$/Cu (28% with DES) respectively.

5.4 Results and discussion

5.4.1 X-ray Diffraction (XRD)

Figure 5.1 is an X-ray Diffraction (XRD) pattern comparing the crystalline structures of pristine $ZnTiO_3$ and Cu-doped $ZnTiO_3$ synthesized with different Cu content and solvents. The peaks are indexed to four main phases, identified by rhombohedral $ZnTiO_3$ (JCPDS file number 00-015-0591/ R-3 space group symmetry) main phase in all samples, cubic Zn_2TiO_4 (JCPDS file number 00-002-1033 / Fd3m space group symmetry) as minor phase, tetragonal anatase TiO_2 (JCPDS file number 03-065-1118/ (P42/mnm) space group symmetry) and hexagonal ZnO (JCPDS file number 01-075-0576/ P63mc space group symmetry) as a secondary phase. The peaks in the pattern have been indexed according to these structures. The peaks positioned at the 2θ values of 24.11, 32.96, 35.38, 40.69, 49.23, 53.70, 56.70, 62.15, and 63.65^o correspond to $ZnTiO_3$ [119], 30.02, and 42.98 correspond to Zn_2TiO_4, 27.65, and 54.57 correspond to TiO_2 [286]and 31.98, 34.63, and 36.42 correspond to ZnO [287]. Percentage of phases presented in Table 5.1.

All samples show dominant $ZnTiO_3$ peaks, indicating it's the major crystalline phase. The pristine $ZnTiO_3$ has the sharpest and most intense peaks, showing high crystallinity. In Cu-doped samples slight peak broadening is observed, may indicate reduced crystallite size or increased lattice strain with increase in lattice constant (Table 5.2). The intensity of TiO_2 and ZnO peaks are somewhat suppressed in doped samples, suggesting improved phase purity with higher Cu doping or better dispersion with DES/DI.

Doping with Cu shows no new Cu phases appear, implies Cu is well incorporated (likely substituted or interstitial doped) rather than forming separate CuO phases [288]. Doping reduces secondary phase intensity, potentially enhances photocatalytic properties by reducing charge recombination sites [289].

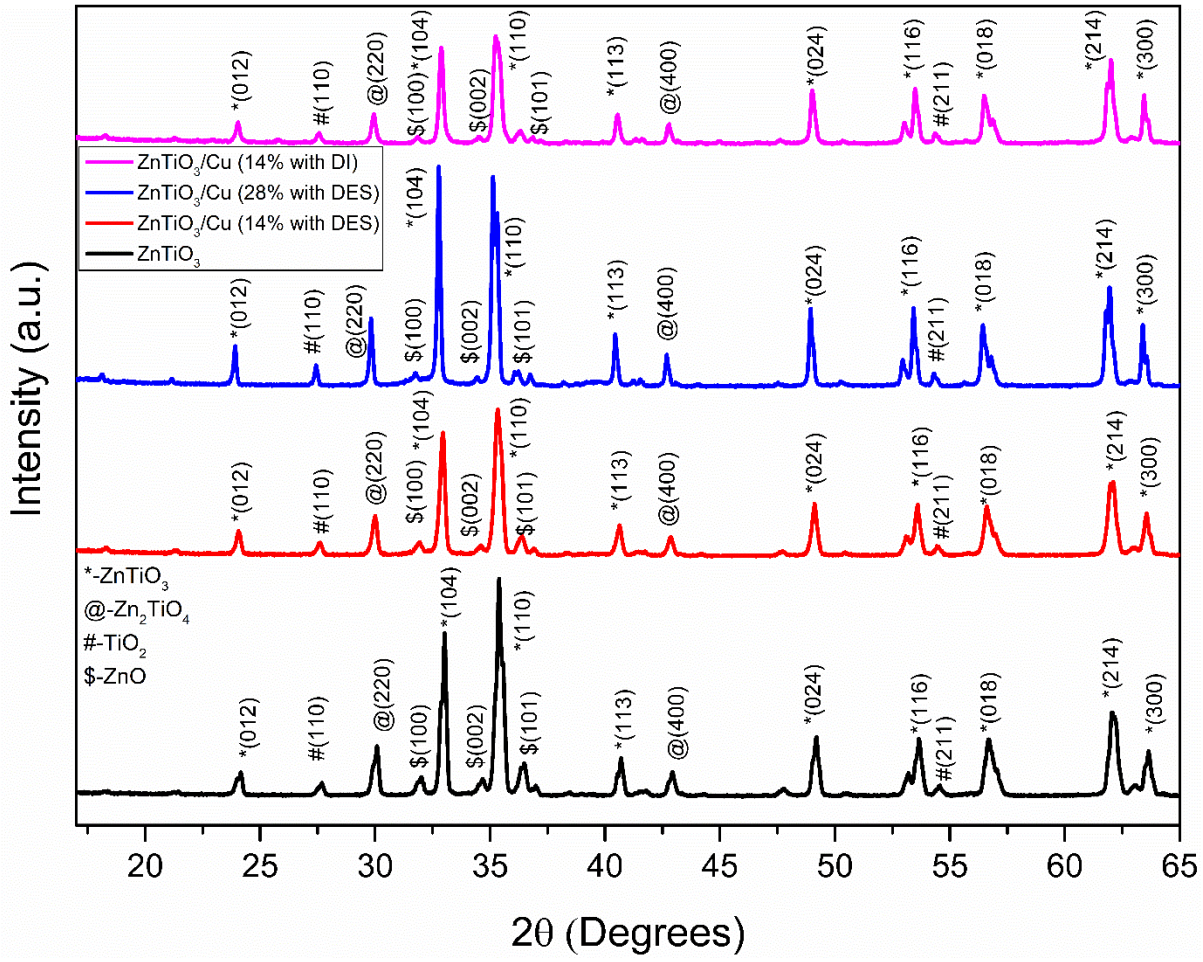

Figure 5.1. XRD patterns of $ZnTiO_3$, $ZnTiO_3$/Cu (14% with DES), $ZnTiO_3$/Cu (28% with DES), and $ZnTiO_3$/Cu (14% with DI).

Table 5.1. Calculation of the percentage of phase present in the sample.

Phases	$ZnTiO_3$	$ZnTiO_3$/Cu (14% with DES)	$ZnTiO_3$/Cu (28% with DES)	$ZnTiO_3$/Cu (14% with DI)
$ZnTiO_3$	83.54%	86.36%	88.21%	88.81%
Zn_2TiO_4	06.77%	06.45%	07.06%	06.01%
TiO_2	01.80%	02.35%	02.40%	02.40%
ZnO	07.87%	04.83%	02.32%	02.76%

Table 5.2. Calculation of lattice constants of different phases present in samples.

Phases	$ZnTiO_3$ (Rhombohedral) a=b≠c		Zn_2TiO_4 (Cubic) a=b=c	TiO_2 (Tetragonal) a=b≠c		ZnO (Hexagonal) a=b≠c	
Samples	a	c	a	a	c	a	c
$ZnTiO_3$	5.065	13.801	8.408	4.560	2.181	3.225	5.192
$ZnTiO_3$/Cu (14% with DES)	5.073	13.867	8.422	4.569	2.949	3.244	5.129
$ZnTiO_3$/Cu (28% with DES)	5.094	13.900	8.465	4.594	2.955	3.246	5.258
$ZnTiO_3$/Cu (14% with DI)	5.079	13.801	8.434	4.574	2.974	3.236	5.232

5.4.2 Field Emission Scanning Electron Microscopy (FESEM)

Figure 5.2(a, b) shows pristine zinc titanate exhibits well-defined with relatively uniform size distribution. Figure 5.2(c, d) the introduction of 14% copper using DES dramatically alters the morphological landscape. The sample displays extensive nanoparticle clustering and agglomeration. The morphology suggests that DES facilitates the uniform distribution of copper species, leading to enhanced interaction between the copper and zinc titanate. Figure 5.2 (e, f) shows with increase in copper content to 28%, the morphological characteristics become even more pronounced. The images show dense, highly aggregated structures forming extensive networks. The high copper content appears to promote extensive interconnectivity between particles, creating a three-dimensional porous network. Figure 5.2(g, h) shows sample synthesized with deionized water as the medium presents a markedly different morphology compared to its DES counterpart. The use of DI water instead of DES appears to promote nanoscale particle growth.

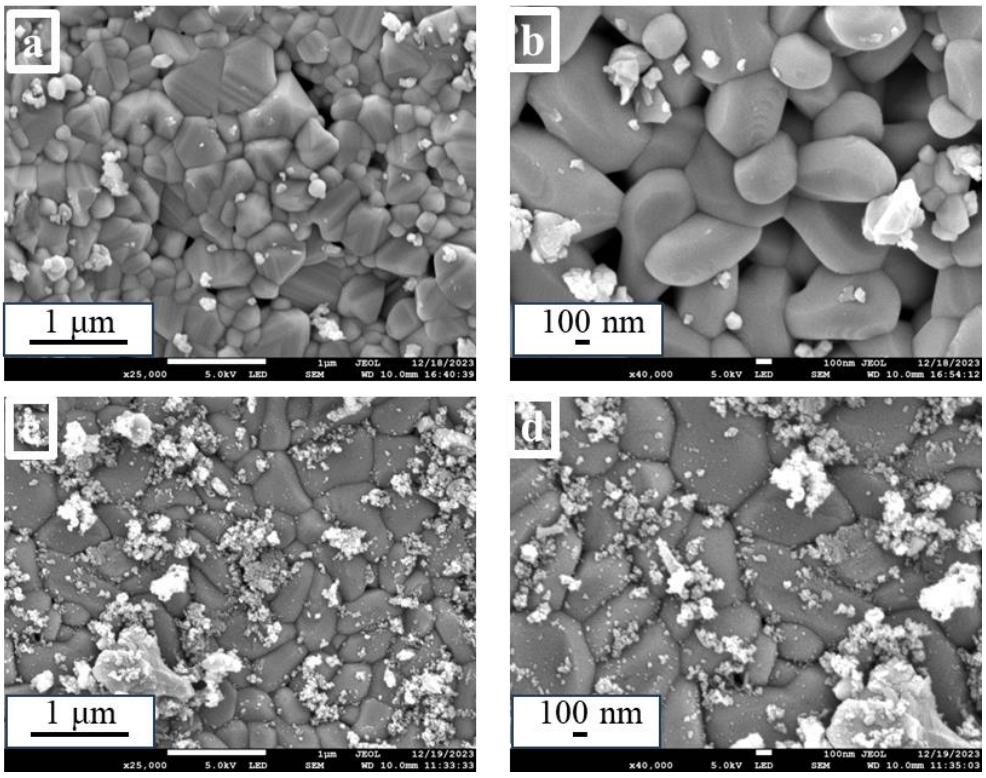

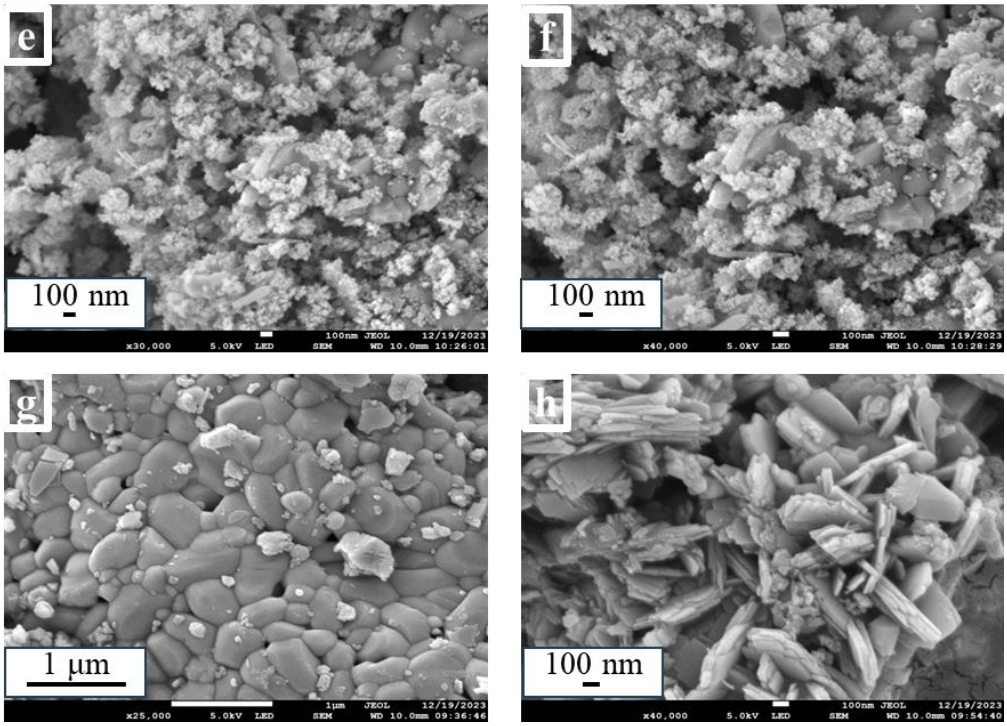

Figure 5.2. FESEM images of samples at smaller magnification (left column) and larger magnification (right column). Images of $ZnTiO_3$ (a, b), $ZnTiO_3$/Cu (14% with DES) (c, d), $ZnTiO_3$/Cu (28% with DES) (e, f), and $ZnTiO_3$/Cu (14% with DI) (g, h) samples.

In Figure 5.3(a, b) $ZnTiO_3$ shows Zn, Ti, O are uniformly distributed that supports homogeneous structure and No Cu signal detected. Figure 5.3(c, d) $ZnTiO_3$/Cu (14% with DES) shows well-dispersed across the sample, suggesting successful doping of copper and Zn, Ti, O still uniformly present that shows that DES route results in fine distribution of Cu. Figure 5.3(e, f) $ZnTiO_3$/Cu (28% with DES)shows that Cu intensity is higher and more concentrated, aligning with higher Cu loading. Distribution is relatively uniform, although some clustering likely occurs at high concentrations. In Figure 5.3(g, h) $ZnTiO_3$/Cu (14% with DI) shows Cu present but spread seems slightly less uniform compared to DES at same loading that suggests the solvent influences the copper dispersion.

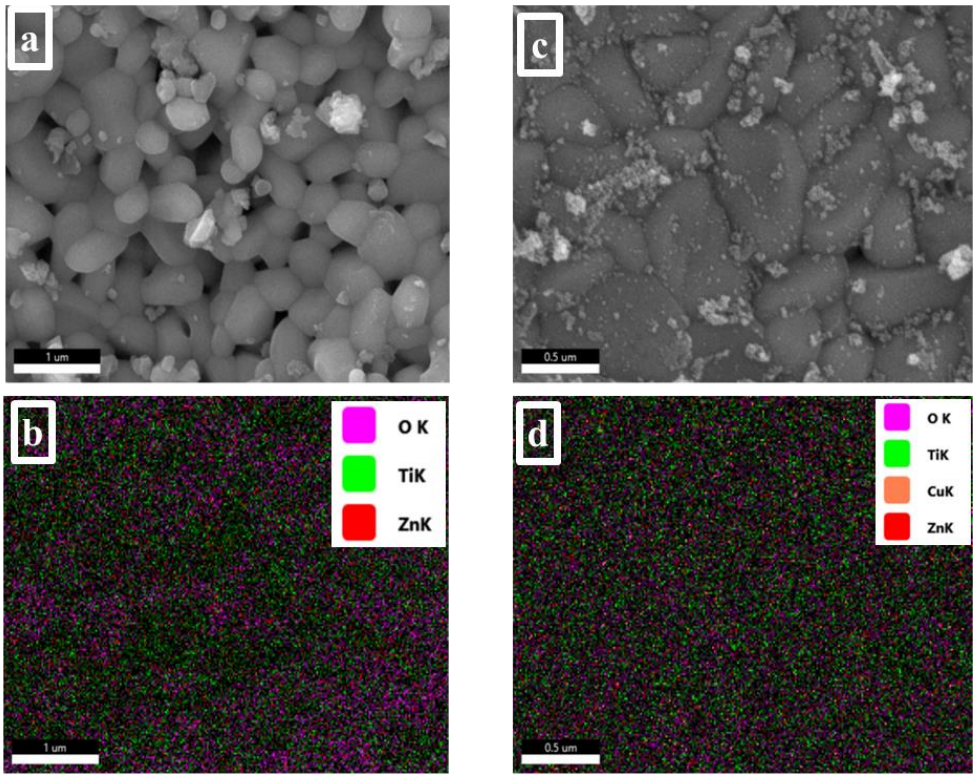
a
1 um
c
0.5 um
b
O K
TiK
ZnK
1 um
d
O K
TiK
CuK
ZnK
0.5 um

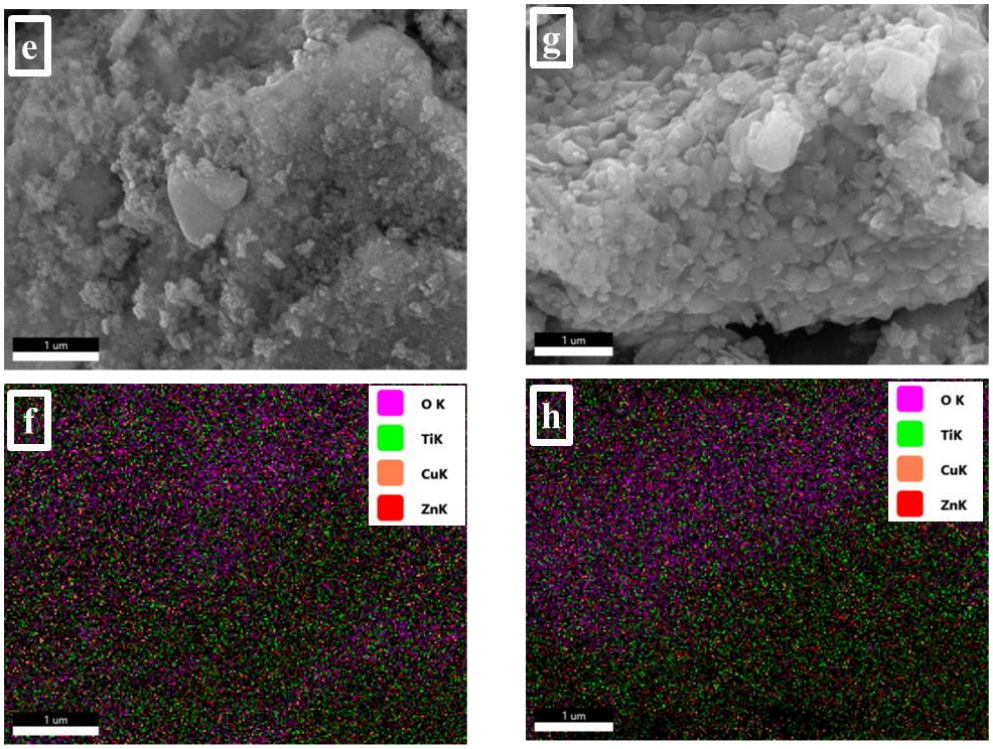

Figure 5.3. FESEM images of (a) $ZnTiO_3$, (c) $ZnTiO_3$/Cu (14% with DES), (e) $ZnTiO_3$/Cu (28% with DES), (g) $ZnTiO_3$/Cu (14% with DI), and their elemental composition mapping obtained by EDX are shown in (b) $ZnTiO_3$, (d) $ZnTiO_3$/Cu (14% with DES), (f) $ZnTiO_3$/Cu (28% with DES), (h) $ZnTiO_3$/Cu (14% with DI).

5.4.3 Optical behavior from UV-Vis Diffuse Reflectance Spectroscopy

This figure 5.4 (b) presents a Tauc plot vs Energy (eV) derived from UV-Vis DRS (figure 5.4 (a) for various Cu-doped $ZnTiO_3$ samples, showing the effect of Cu doping concentration and solvent type on the optical band gap. The band gap (E_g) is estimated by extrapolating the linear region of the curve to intersect the energy axis. Doping with Cu reduces the band gap is due to introduction of impurity levels (Cu 3d orbitals) near the valence or conduction band [290], [291], [292]. Slight lattice distortion that alters electronic transitions. Effect of Cu doping concentration increasing Cu from 14% to 28% (in DES) results in further band gap narrowing from 2.963 eV to 2.947 eV indicates that higher Cu content continues to contribute to electronic structure modification. DES-doped samples have lower band gaps compared to DI water. Suggests DES promotes

better Cu incorporation or defect formation, enhancing band gap reduction. DES may provide a more uniform or reactive medium during synthesis [293]. Shift toward lower energies (red shift) with doping and DES use. This implies enhanced visible-light absorption, desirable in photocatalysis or solar applications.

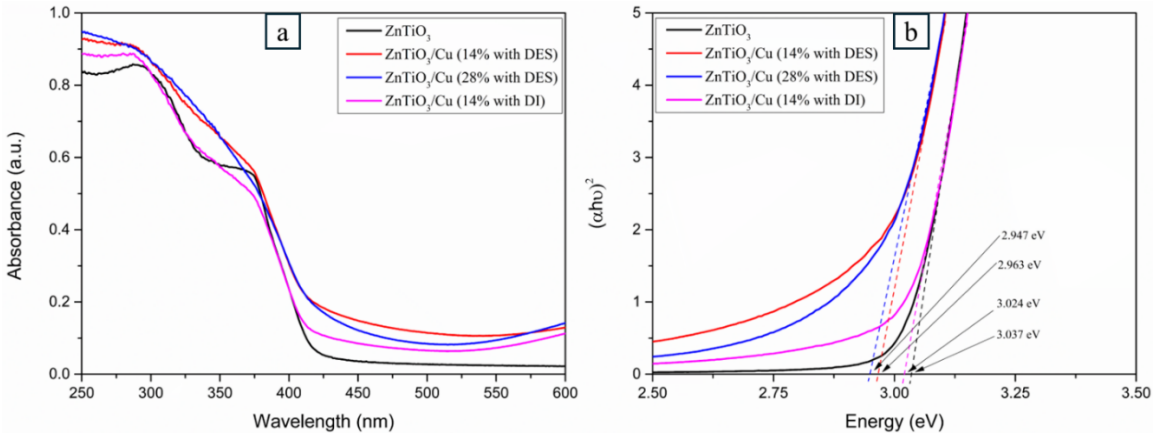

Figure 5.4. (a) UV-Vis DRS, and (b) The tauc plot versus the energy of exciting light results in the band-gap of $ZnTiO_3$, $ZnTiO_3$/Cu (14% with DES), $ZnTiO_3$/Cu (28% with DES), and $ZnTiO_3$/Cu (14% with DI).

5.4.4 Surface Area Analysis

Figure 5.5 depicts the nitrogen adsorption-desorption isotherms. An increased surface area of the $ZnTiO_3$/Cu compared to pure $ZnTiO_3$ is expected [294]. DES assisted Cu doping increases the surface area of $ZnTiO_3$ by controlling the nucleation and growth of nanoparticles (confirmed by FESEM images) and preventing their agglomeration [295]. The BET surface areas of $ZnTiO_3$, $ZnTiO_3$/Cu (14% with DES), $ZnTiO_3$/Cu (28% with DES), and $ZnTiO_3$/Cu (14% with DI) are found to be 1.1 m^2/g, 3.2 m^2/g, 4.7 m^2/g and 2.2 m^2/g, respectively, revealing a 96% increase in surface area in 14% Cu with DI, 180% increase in surface area in 14% Cu with DES and 269% increase in surface area in 28% Cu with DES.

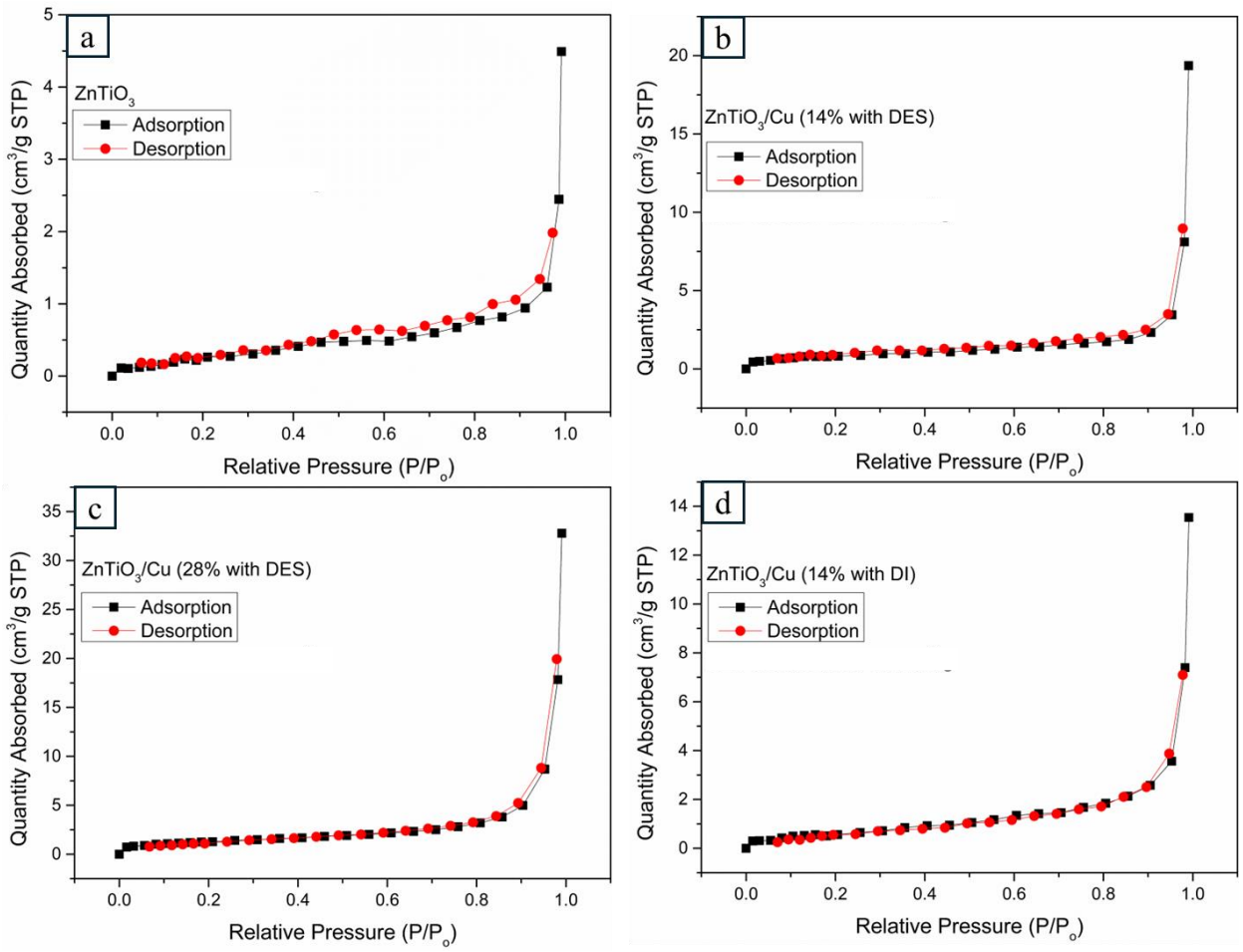

Figure 5.5. The BET isotherms of (a) $ZnTiO_3$, (b) $ZnTiO_3$/Cu (14% with DES), (c) $ZnTiO_3$/Cu (28% with DES), and (d) $ZnTiO_3$/Cu (14% with DI).

5.4.5 X-ray Photoelectron spectroscopy (XPS)

Figure 5.6 presents the O1s spectra from all the samples. Figure 5.6 shows two peaks in which first peak shows lattice oxygen and second peak shows OH [296], [297]. There is shift in lattice oxygen peak towards higher binding energy (Table 3) in $ZnTiO_3$/Cu (14% with DES), $ZnTiO_3$/Cu (28% with DES), and (d) $ZnTiO_3$/Cu (14% with DI) as compared to $ZnTiO_3$ by 1.2eV, 1.3eV and 0.2eV respectively. This shift in peak position towards higher binding energy may be due to more electronegativity of copper as compared to zinc [298].

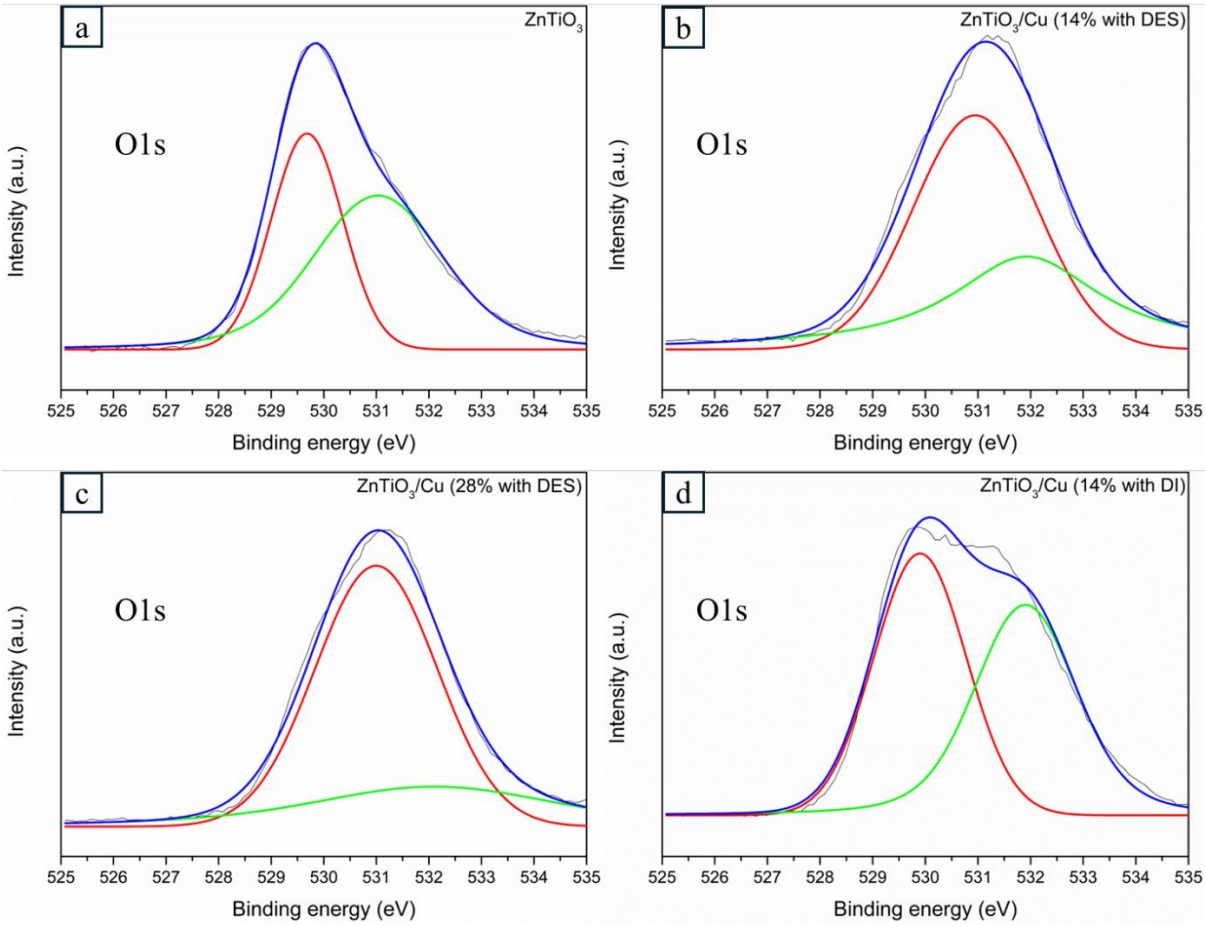

Figure 5.6. XPS of O1s of (a) $ZnTiO_3$, (b) $ZnTiO_3$/Cu (14% with DES), (c) $ZnTiO_3$/Cu (28% with DES), and (d) $ZnTiO_3$/Cu (14% with DI).

In figure 5.7 (a) Zn2p spectra exhibit $Zn2p_{3/2}$ and $Zn2p_{1/2}$ centered near 1021.4 eV and 1044.5 eV across all samples, consistent with Zn^{2+} in oxide environments [119]. In Figure 5.7 (b) Ti2p spectra are dominated by Ti^{4+} with $Ti2p_{3/2}$ near to 458.3 eV and $Ti2p_{1/2}$ near to 464 eV [299].

In Figure 5.8, Cu 2p spectra indicate that Cu is incorporated into $ZnTiO_3$ primarily as Cu^{+}/Cu^{2+} species substituting for cations in the oxide and forming surface Cu-O environments rather than remaining metallic. The main Cu $2p_{3/2}$ and Cu $2p_{1/2}$ component at ~932.5 eV and ~952 eV signifies lattice-incorporated Cu^{+} that can replace Zn^{2+} and introduce charge-compensating defects such as oxygen vacancies, which are beneficial

for charge transport and catalytic activity in doped oxides..Cu $2p_{3/2}$ and Cu $2p_{1/2}$ component at ~934.5 eV and ~954.5 eV characteristic of Cu^{2+} in octahedral or distorted CuO-like coordination, consistent with Cu^{2+} occupying surface or near-surface sites in the oxide framework and interacting strongly with the O sublattice. Compared with the main peaks, the satellite peaks at about ~940.8 eV, ~943.3 eV, ~960.7 eV and 962.9 eV are located at higher binding energy [300], [301], [302], [303], [304].

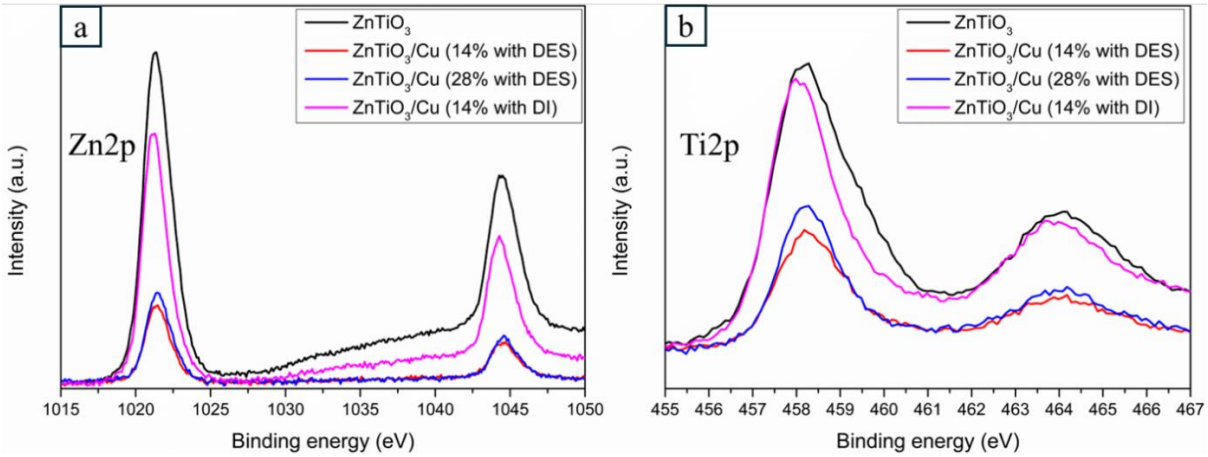

Figure 5.7. XPS of (a) Zn2p, (b) Ti2p for $ZnTiO_3$, $ZnTiO_3$/Cu (14% with DES), $ZnTiO_3$/Cu (28% with DES), and $ZnTiO_3$/Cu (14% with DI).

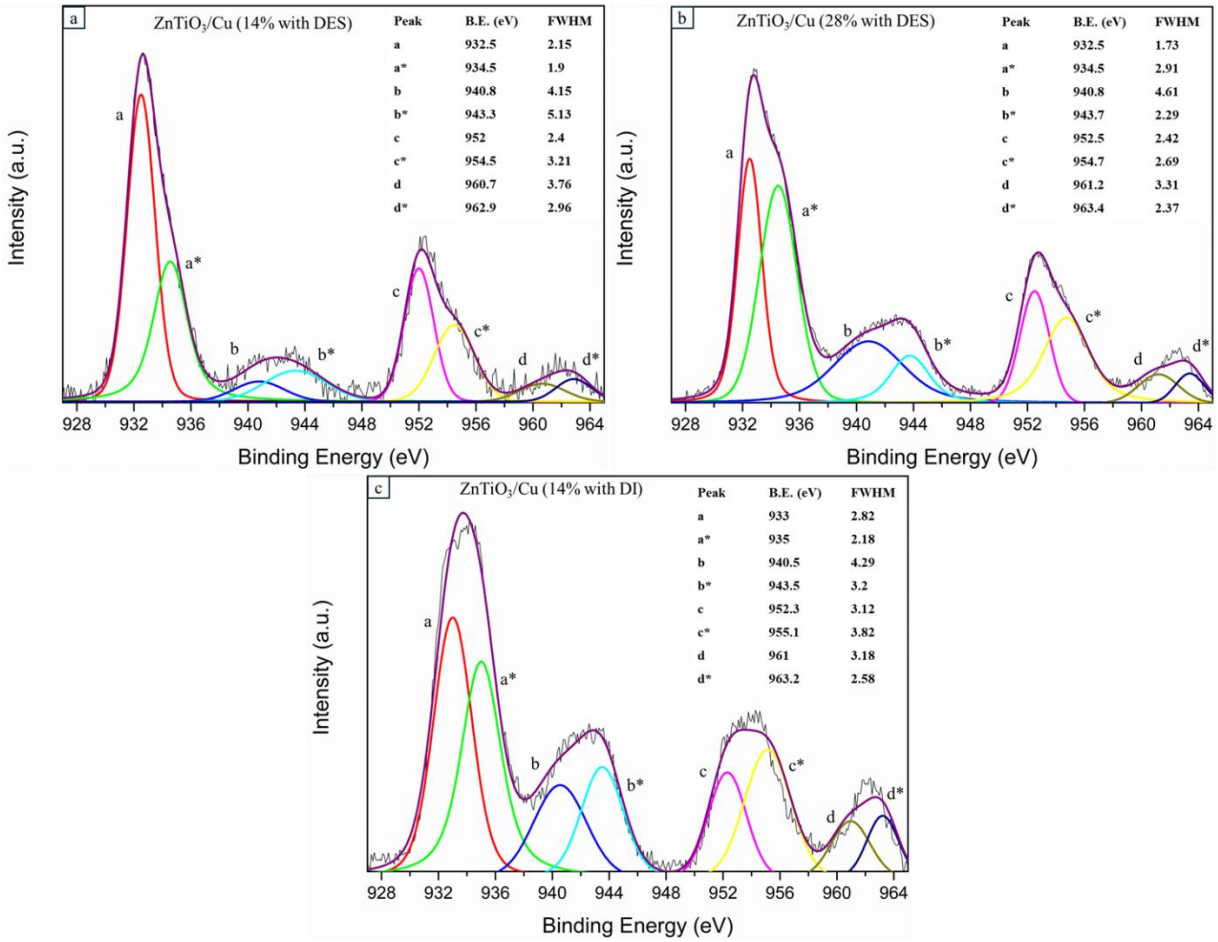

Figure 5.8. XPS of Cu2p for (a) $ZnTiO_3$/Cu (14% with DES), (b) $ZnTiO_3$/Cu (28% with DES), and (c) $ZnTiO_3$/Cu (14% with DI).

Table 5.3. Peak positions of XPS for $ZnTiO_3$, $ZnTiO_3$/Cu (14% with DES), $ZnTiO_3$/Cu (28% with DES), and $ZnTiO_3$/Cu (14% with DI).

Samples	O1s	Bonds	Ti2p	Bonds	Zn2p	orbital	Cu2p	Bonds
$ZnTiO_3$	529.7	Zn-O/Ti-O	458.3	$Ti2p_{3/2}$	1021.4	$Zn2p_{3/2}$	-	-
	531	O-H	464.1	$Ti2p_{1/2}$	1044.3	$Zn2p_{1/2}$	-	-
$ZnTiO_3$/ Cu (14% with DES)	530.9	Zn-O/Ti-O/Cu-O	458.2	$Ti2p_{3/2}$	1021.5	$Zn2p_{3/2}$	932.5	$Cu2p_{3/2}$
							934.5	$Cu2p_{3/2}$
	531.9	O-H	464.2	$Ti2p_{1/2}$	1044.7	$Zn2p_{1/2}$	940.8	satellite
							943.3	satellite
	-	-	-	-	-	-	952	$Cu2p_{1/2}$
							954.5	$Cu2p_{1/2}$
	-	-	-	-	-	-	960.7	satellite
							962.9	satellite
$ZnTiO_3$/ Cu (28% with DES)	531	Zn-O/Ti-O/Cu-O	458.3	$Ti2p_{3/2}$	1021.4	$Zn2p_{3/2}$	932.5	$Cu2p_{3/2}$
							934.5	$Cu2p_{3/2}$
	532.1	O-H	464.2	$Ti2p_{1/2}$	1044.6	$Zn2p_{1/2}$	940.8	satellite
							943.7	satellite
	-	-	-	-	-	-	952.5	$Cu2p_{1/2}$
							954.7	$Cu2p_{1/2}$
	-	-	-	-	-	-	961.2	satellite
							963.4	satellite
$ZnTiO_3$/ Cu (14% with DI)	529.9	Zn-O/Ti-O/Cu-O	458	$Ti2p_{3/2}$	1021.3	$Zn2p_{3/2}$	933	$Cu2p_{3/2}$
							935	$Cu2p_{3/2}$
	531.9	O-H	463.7	$Ti2p_{1/2}$	1044.3	$Zn2p_{1/2}$	940.5	satellite
							943.5	satellite
	-	-	-	-	-	-	952.3	$Cu2p_{1/2}$
							955.1	$Cu2p_{1/2}$
	-	-	-	-			961	satellite
							963.2	satellite

5.5 Computational section

5.5.1 Calculation method and crystal structure

In this chapter, DFT calculations were employed to model pure and Cu-doped $ZnTiO_3$, allowing us to analyze changes in lattice structure, band structure, density of states, and Fermi-level position induced by Cu substitution at the Zn site. Such calculations are widely used to explain how doping alters the electronic structure, introduces new states, shifts the band gap into the visible region, and improves charge separation, which in turn supports and rationalizes the experimentally observed trends in optical and photocatalytic properties.

We conducted a theoretical analysis using the pseudopotential DFT-based first-principle method [147] to simulate and analyze the structural, electrical, and optical characteristics of pure and doped $ZnTiO_3$. Quantum Espresso (QE) was utilized to conduct a computation-based analysis of properties [305]. The QE code package utilizes the Generalized Gradient Approximation (GGA) function for performing geometrical optimization and calculating various attributes. $ZnTiO_3$ has a hexagonal symmetrical structure at a temperature near to 900 °C, specifically belonging to the 'R-3' space group. Figure 5.9 depicts the arrangement of a unit cell of $ZnTiO_3$, which has a hexagonal structure. Figure 5.9 depicts a cell that contains 6 Zn atoms, 18 oxygen atoms, and 6 Ti atoms, for a total of 30 atoms. The copper (Cu) atom is doped for zinc (Zn). which means $ZnTiO_3$ has undergone A site doping. The process of doping Cu has been carried out using the formula $Zn_{0.833}Cu_{0.167}TiO_3$. The computation and analysis of QE were conducted using density functional theory, which incorporates the plane-wave pseudopotential method to provide fast and accurate findings. The electron-ion interaction has been

examined using the ultrasoft pseudopotential proposed by GGA. The energy cutoff was set at 340 eV, and a k mesh of 5 × 5 × 2 was used to produce Brillouin zone integrations for geometrical optimization and other calculations.

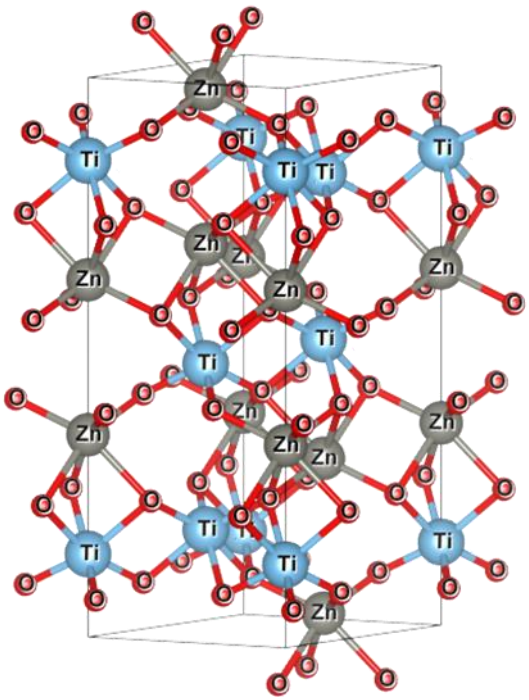

Figure 5.9. A schematic representation of the pure zinc titanate $ZnTiO_3$ using the VESTA package.

5.5.2 Structural properties

Figure 5.9 displays the structure of pure zinc titanate $ZnTiO_3$, which was plotted using the VESTA software [306]. The pure $ZnTiO_3$ possesses a hexagonal shape that is classified under the space group "R-3" (N◦ 148). The zinc atoms are located at the coordinates (0,0,0.36), and the titanium atoms are located at the coordinates (0,0,0.14). The oxygen atoms are situated in the coordinates (0.015, 0.370, 0.421). The experimental measurements provide information on the lattice parameters and symmetry space of $ZnTiO_3$. After the geometry optimization of Cu-doped $ZnTiO_3$, a reduction in the lattice parameters a=b=5.77 Å and c=12.88 Å was found. An investigation was conducted to

compare the lattice details of doped $ZnTiO_3$ using the process of geometric optimization. The $ZnTiO_3$ crystal has lattice parameters of a = b = 5.87 Å, c = 12.97 Å, and angles $\alpha = \beta = 90°$ and $\gamma = 120°$. The lattice parameter of the hexagonal phase $ZnTiO_3$ decreases after Cu doping. This is because the ionic radius of Cu^{2+} (0.73 Å) is less than that of Zn^{2+} (0.74 Å), and both ions occupy the A site of the hexagonal $ZnTiO_3$. After Cu doping, we observed a decrease in the lattice parameter and unit cell volume, with a minor fractional value.

5.5.3 Electronic properties

This study used GGA methods to show the electronic band structures and partial density of states (DOSs) of pure and doped $ZnTiO_3$. The aim was to investigate the behavior of the system and analyze its optoelectronic properties, both for pure and doped $ZnTiO_3$, along with high symmetry directions. The band structure of hexagonal $ZnTiO_3$ offers insight into its electrical structure and how it is altered by doping. Figure 5.10 depicts the band structure of undoped $ZnTiO_3$ and each $ZnTiO_3$ doped with Cu. Figure 5.10(a) and 5.10(b), represents undoped $ZnTiO_3$ and Cu doped $ZnTiO_3$. In figure 5.10(a) the valence band between the M and K points has a maximum level, whereas the conduction band at the M point has the lowest level. This indicates that the material has an indirect bandgap of 2.92 eV. This bandgap has been found in prior studies, which provides evidence for the high precision of our theoretical work. Figure 5.10 clearly shows that the expansion of valence bands does not go beyond 0 eV. The line corresponding to the 0 eV energy level denotes the Fermi energy level (E_f). In figure 5.10(b), Cu doped $ZnTiO_3$ has a indirect bandgap around the M point with a value of 2.44 eV. A material must possess an indirect bandgap to be considered a reliable tool for photocatalysis applications. This occurrence may be attributed to many factors. For instance, when a semiconductor has low doping

concentrations, atomic states (also known as localized states) are introduced inside the gap.

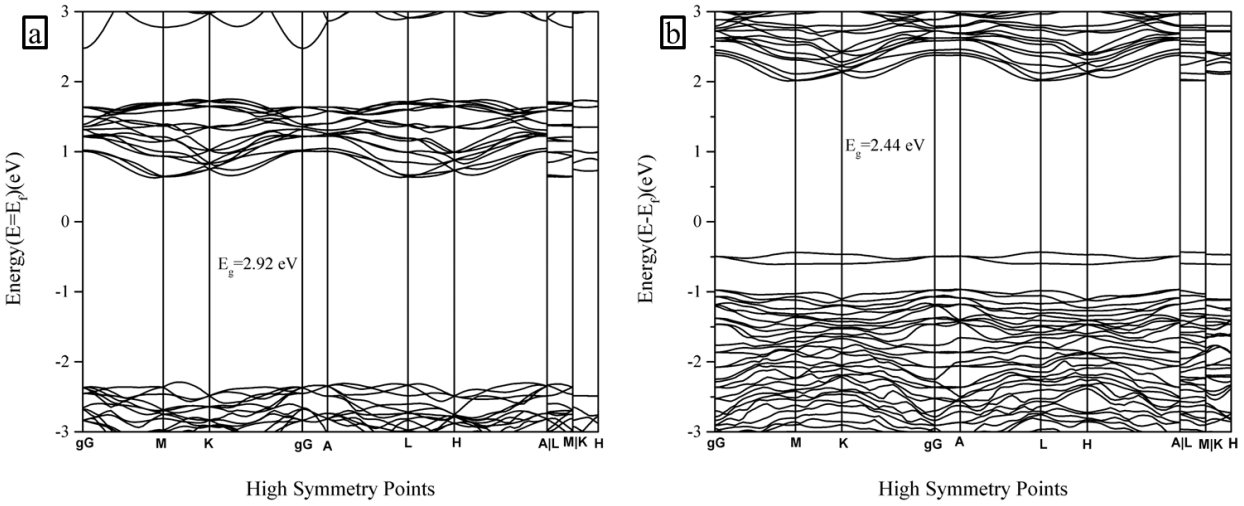

Figure 5.10. Band Structures of (a) $ZnTiO_3$ and (b) Cu doped $ZnTiO_3$.

Figure 5.11(a) and 5.11(b) illustrates the partial density of states (PDOS) for undoped $ZnTiO_3$ and Cu-doped $ZnTiO_3$ respectively. The analysis of the partial density of states revealed that the contribution of atomic orbitals had an impact on the total density of states. Figure 5.11(a) of the partial density of states (PDOS) shows that the valence band (VB) of undoped $ZnTiO_3$ is mostly made up of the oxygen 2p and zinc 3d states. On the other hand, the conduction band (CB) in undoped $ZnTiO_3$ is mostly dominated by the titanium 3d state, with minor contributions from the oxygen 2p and zinc 4s states. In figure 5.11(b), after doping, in valance band there is contribution from the oxygen 2p, copper 3d and zinc 3d state and in conduction band domination of titanium 3d state, with minor contributions from the oxygen 2p and zinc 4s states. When Cu replaces Zn, it affects the VB by introducing the copper 3d state and the CB by decreasing intensity of titanium 3d state. The presence of the dopant atom's orbitals in the valence band (VB) or conduction band (CB) might lead to changes in energy levels because of hybridization with the existing orbitals. The band gap reduces due to the metal nature of Cu.

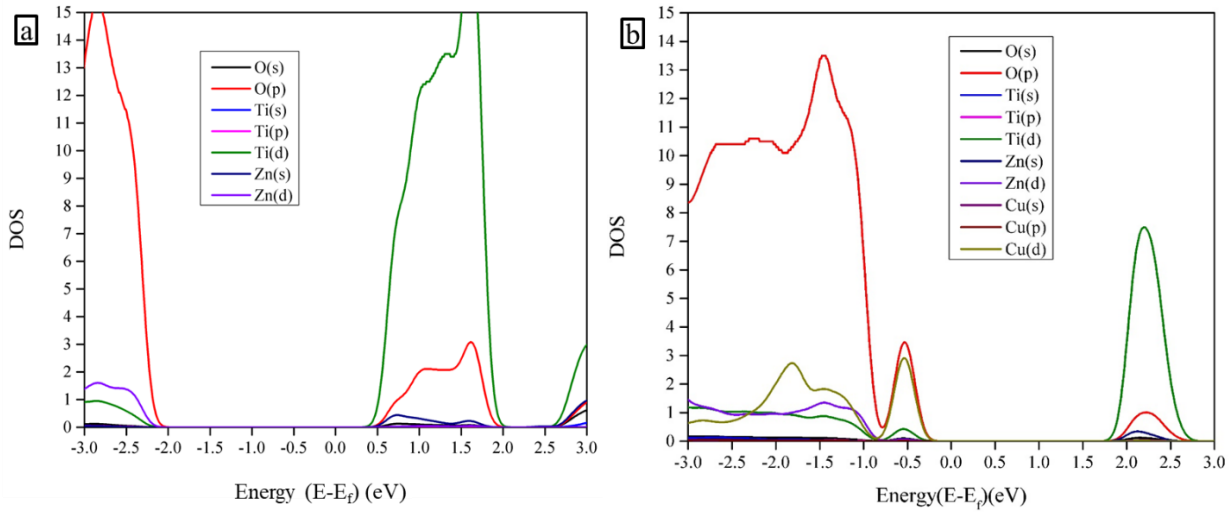

Figure 5.11. Partial density of states (PDOS) of (a) $ZnTiO_3$ and (b) Cu doped $ZnTiO_3$.

5.6 Conclusion

This study demonstrated that Cu doping, assisted by deep eutectic solvent, plays an important role in modifying the structural and functional properties of $ZnTiO_3$. The experimental results showed that the doping process influences the phase composition, crystallinity, surface characteristics, and optical behavior of the material. The DFT study further provided a theoretical explanation for these changes by showing how Cu incorporation affects the electronic structure and related properties of $ZnTiO_3$. Together, the experimental and computational findings establish that Cu doping is an effective approach for improving the properties of $ZnTiO_3$. This chapter therefore provides a clear understanding of the structure-property relationship and supports the potential of the modified material for future functional applications.

CHAPTER 6

The effect of Mg-doping on the structural and electronic properties of $ZnTiO_3$: A first-principles study and compared with experimental band gap of $ZnTiO_3$

6.1. Abstract

This work shows a detailed analysis of the structural and electronic properties of pure zinc titanate ($ZnTiO_3$) and magnesium (Mg)-doped $ZnTiO_3$ ($Zn_{1-x}Mg_xTiO_3$, where x = 0.167, 0.333, 0.5, and 0.667) and compared with experimental band gap of $ZnTiO_3$. We conducted the analysis using first-principles and density-functional-theory calculations using the Quantum Espresso package. The objective was to investigate the effect of Mg substitution on zinc titanate $ZnTiO_3$. In the pure $ZnTiO_3$ system, calculations reveal an indirect electronic structure gap. At a doping level of 0.333, $ZnTiO_3$ with Mg impurities have an indirect electronic structure gap of 1.81 electron volts (eV). The investigation of structural and electronic characteristics indicates that x = 0.333 Mg doped $ZnTiO_3$ significantly reduce the electronic structure gap of $ZnTiO_3$ while maintaining the same kind of electronic structure gap, which is an indirect electronic structure gap. The density functional theory study shows that Mg substitution in $ZnTiO_3$ change their electronic

structure and density of states and experimental band gap is nearly same as computational band structure gap which validates the exchange-correlation treatment and pseudopotentials employed for the band-structure calculation for this system.

6.2. Introduction

The previous chapter established that graphene oxide compositing leads to significant modifications in the structural, surface, and electronic properties of $ZnTiO_3$, and also demonstrated the impact of plasma treatment and Cu doping on $ZnTiO_3$-based systems. These results highlighted that both defect engineering and dopant-induced band structure modulation can be used to tune visible-light activity. Building on these insights, the present chapter extends the theoretical investigation to Mg doping in $ZnTiO_3$. Specifically, this chapter examines how the electronic properties, including band structure and density of states, evolve when Mg is incorporated into $ZnTiO_3$, and further explores the effect of varying the percentage of Mg doping on the overall performance of the material. This progression allows for a more comprehensive understanding of dopant-induced structural and electronic modifications.

Researchers have conducted limited experimental studies using Mg-doped $ZnTiO_3$ ceramic material. In a referenced work, Yin-Lai Chai et al. [307] experimented on Mg-doped $ZnTiO_3$. They found that it significantly enhances the electrical conductivity qualities of $ZnTiO_3$ ceramic, making it an excellent material option. The dopant's enhanced electrical properties make it suitable for photocatalytic applications, specifically dye degradation. Therefore, our investigation is centered around examining the characteristics of $ZnTiO_3$ ceramic with Mg atom doping to compare them with existing experimental literature on $ZnTiO_3$. Our goal is to determine the optimal concentration of the donor atom, making it a promising candidate for applications in

photocatalysis. An in-depth analysis of various theoretical and experimental research studies shows that the incorporation of donor atoms, such as Mg, can improve the structural and electronic properties of $ZnTiO_3$ ceramic.

This work presents a theoretical study on the doping of Mg atoms in $ZnTiO_3$ utilizing quantum espresso and experimental band gap of $ZnTiO_3$ [308], [309]. A First-Principles Density Functional Theory (DFT) study was conducted to investigate the impact of A site doping in pure $ZnTiO_3$ ceramic using the 3s element 'Mg'. The doping formula $Zn_{1-x}Mg_xTiO_3$ (x = 0.167, 0.333, 0.5, and 0.667) was employed to examine the changes in structural and electronic properties. Based on current research and literature, we identified three essential characteristics. We aimed to investigate the changes that occur when We add varying amounts of Mg as a dopant. Our objective is to analyze different doping and compare with experimental band gap studies on $ZnTiO_3$. This will help us identify the appropriate quantities of Mg that lead to enhanced structural and electrical characteristics.

6.3. Calculation method and crystal structure

We conducted a theoretical analysis using the pseudopotential DFT-based first-principle method [310], [311], [312] to simulate and analyze the structural and electrical characteristics of pure and doped $ZnTiO_3$ ceramic. Quantum Espresso (QE) was utilized to conduct a computation-based analysis of properties. The QE code package utilizes the Generalized Gradient Approximation (GGA) function for performing geometrical optimization and calculating various attributes. Computation and analysis incorporate the plane-wave pseudopotential method to provide fast and accurate findings.

All spin-polarized DFT calculations were performed with the GGA functional (PBE) using projector-augmented-wave (PAW). specific valence electron configurations are

$3d^{10}4s^2$, $3d^24s^2$, $2s^22p^4$ and $3s^2$ for Zn, Ti, O and Mg respectively. Plane-wave basis sets were converged to the kinetic-energy cutoff to 340 eV where changes were below 1meV $atom^{-1}$. So, kinetic-energy cutoff of 340 eV was adopted for all calculations. Brillouin-zone sampling employed Monkhorst-Pack meshes refined until energy changes were below 1meV $atom^{-1}$, yielding k=5×5×2 for geometrical optimization and other calculations.

$ZnTiO_3$ has a hexagonal symmetrical structure at a temperature of 900 °C, specifically belonging to the 'R-3' space group. Figure 6.1 depicts the arrangement of a unit cell of $ZnTiO_3$, which has a hexagonal structure. Figure 6.1 depicts a cell that contains 6 Zn atoms, 18 oxygen atoms, and 6 Ti atoms, for a total of 30 atoms. The Mg atom is doped for Zn. which means $ZnTiO_3$ has undergone A site doping. The process of doping Mg has been carried out using the formula $Zn_{1-x}Mg_xTiO_3$, where x takes the values of 0.167, 0.333, 0.500, and 0.667. The objective of this work is to determine the impact of Mg dopant on the properties of $ZnTiO_3$ ceramic. There are six Zn atoms in a unit cell that are being substituted by Mg atoms in a manner that keeps the concentration 'x'. To achieve a doping concentration of x = 0.167 (equivalent to 1/6), one Zn atom is substituted with Mg. The doping level of x is 0.333 (2/6), 0.500 (3/6), and 0.667 (4/6) correspondingly. The doping technique involves substituting a certain quantity of Zn with Mg.

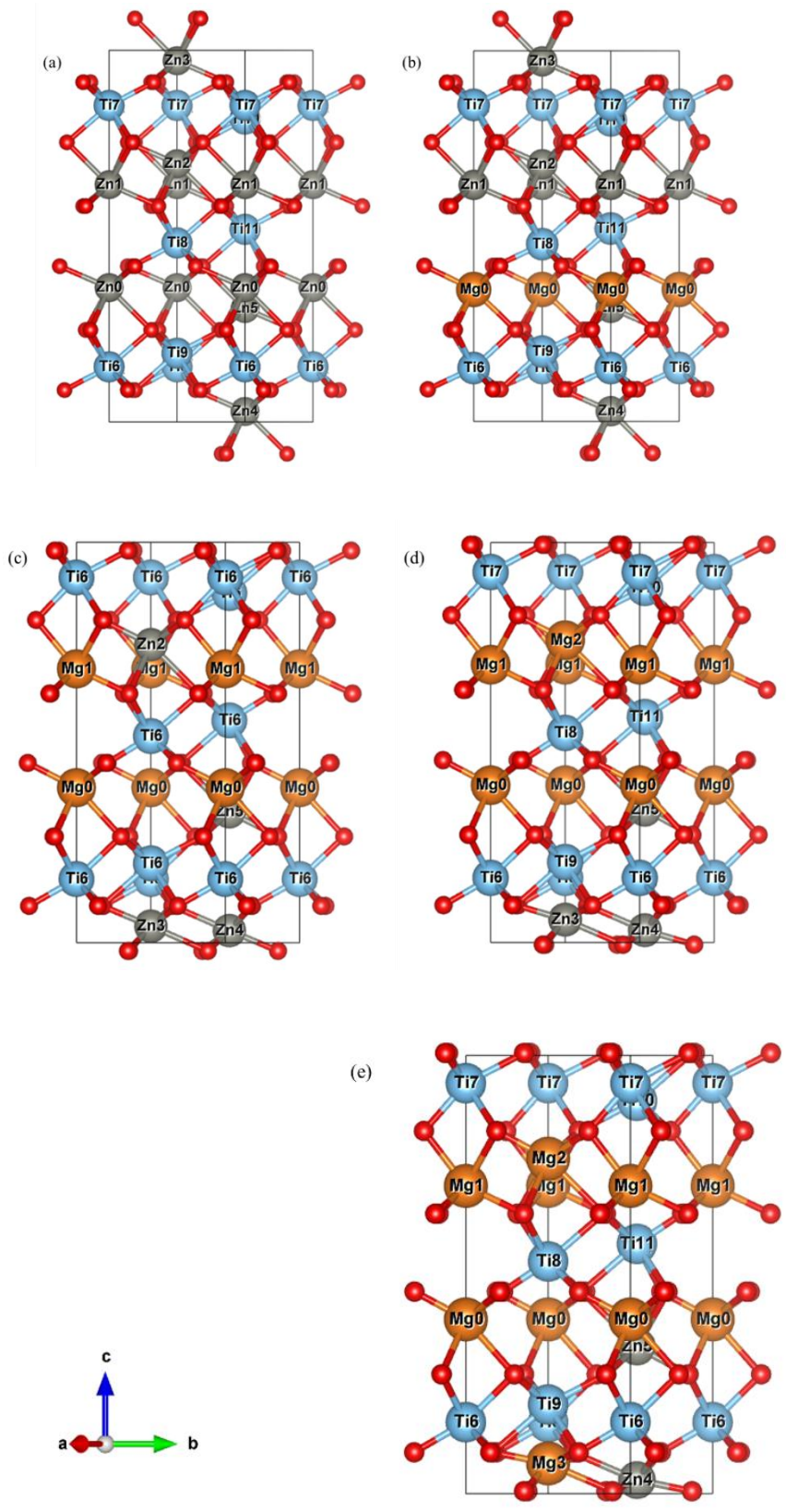

Figure 6.1. An optimized structures of $Zn_{1-x}Mg_xTiO_3$ where (a) x = 0, (b) x = 0.167, (c) x = 0.333, (d) x = 0.5, (e) x = 0.667 using the VESTA package.

6.4. Results and discussions

6.4.1. Structural properties

Figure 6.1 displays the optimized structure of pure zinc titanate $ZnTiO_3$, $Zn_{0.833}Mg_{0.167}TiO_3$, $Zn_{0.667}Mg_{0.333}TiO_3$, $Zn_{0.500}Mg_{0.500}TiO_3$ and $Zn_{0.333}Mg_{0.667}TiO_3$, which was plotted using the VESTA software. The pure $ZnTiO_3$ (Figure 6.1(a)) possesses a hexagonal shape that is classified under the space group "R-3" (No-148). The Zn atoms are located at the coordinates (0,0,0.36), and the Ti atoms are located at the coordinates (0,0,0.14). The oxygen atoms are situated in the coordinates (0.015, 0.370, 0.421). The experimental measurements [313] provide information on the lattice parameters and symmetry space of $ZnTiO_3$. Figure 6.1(b-e) shows geometry optimized structure of Mg-doped $ZnTiO_3$, a reduction in the lattice parameters a and c was found (Figure 6.2). An investigation was conducted to compare the lattice details of doped $ZnTiO_3$ using the process of geometric optimization. The $ZnTiO_3$ crystal has lattice parameters of a = b = 5.1292 Å, c = 14.1 Å, and angles $\alpha = \beta = 90°$ and $\gamma = 120°$. The lattice parameter of the hexagonal phase $ZnTiO_3$ decreases when the concentration of Mg increases. This is because the ionic radius of Mg^{2+} (0.66 Å) is less than that of Zn^{2+} (0.74 Å), and both ions occupy the A site of the hexagonal $ZnTiO_3$. The lattice parameters of $ZnTiO_3$ and geometrically optimized Mg-doped $ZnTiO_3$ are shown in Table 6.1. After Mg doping, we observed a decrease in the lattice parameter and unit cell volume, with a minor fractional value.

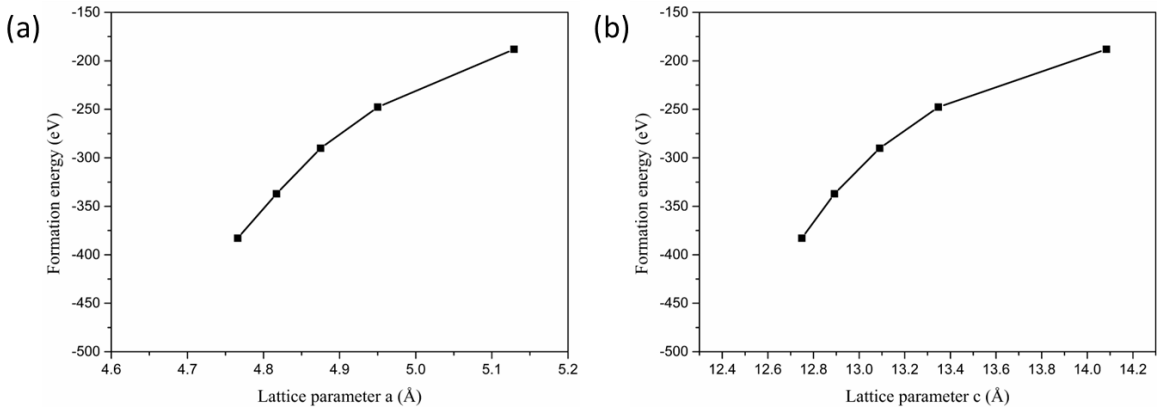

Figure 6.2. The formation energy of the Mg-doped $ZnTiO_3$ material as a function of the lattice parameters (a) a (Å) and (b) c (Å), using the GGA approximation.

Table 6.1. Lattice parameter of $ZnTiO_3$ and calculated lattice parameter of Mg-doped $ZnTiO_3$.

Composition	**a (Å)**	**c (Å)**
$ZnTiO_3$	5.1292	14.1
$Zn_{0.833}\,Mg_{0.167}\,TiO_3$	4.95	13.3
$Zn_{0.667}\,Mg_{0.333}\,TiO_3$	4.88	13.1
$Zn_{0.500}\,Mg_{0.500}\,TiO_3$	4.82	12.9
$Zn_{0.333}\,Mg_{0.667}\,TiO_3$	4.77	12.7

6.4.2. Electronic properties

This study used GGA methods to show the electronic band structures and partial density of states (PDOSs) of pure zinc titanate $ZnTiO_3$. The aim was to investigate the behavior of the system and analyze its electronic properties, both pure and doped $ZnTiO_3$, along with high symmetry directions. The band structure of hexagonal $ZnTiO_3$ offers insight

into its electrical structure and how it is altered by doping. Figure 6.3 depicts the band structure of undoped $ZnTiO_3$ and each $ZnTiO_3$ doped with Mg. The figure, labeled as Figure 6.3(a), represents undoped $ZnTiO_3$, and the subsequent figures are arranged based on the amount of doping. The valence band between the M and K points has a maximum level, whereas the conduction band at the M point has the lowest level. This indicates that the material has an indirect electronic structure gap (band gap) of 3.11 eV. This electronic structure has been found in prior studies, which provides evidence for the high precision of our theoretical work. Table 6.2 presents the computed electronic bandgap (E_g) and observed values for $ZnTiO_3$. Figure 6.3 clearly shows that the expansion of valence bands does not go beyond 0 eV. The line corresponding to the 0 eV energy level denotes the Fermi energy level (E_f). When doping Mg (x = 0.167), We observed a similar electronic structure. Still, there were noticeable changes in the band regions, as seen in Figure 6.3. Specifically, we observed an indirect electronic structure gap around the M point with a value of roughly 3.14 eV. When x = 0.500 and 0.667, Mg-doped $ZnTiO_3$ has a direct electronic structure gap. Therefore, it illustrates the conversion of the band position from close to the M point to the K-K point band position material following an increase in Mg-doping (Figure 6.3). There is a little increase in the valence band of Mg-doped $ZnTiO_3$ compared to $ZnTiO_3$. Similarly, the conduction band of the $ZnTiO_3$ compound moved downwards in comparison to the pure $ZnTiO_3$ compound, except for when x = 0.167. This resulted in a reduction of the electronic structure gap by nearly 0.98 eV. An uncommon scenario was seen when the value of x was 0.333. In this situation, an indirect electronic structure gap with a magnitude of 1.81 eV was identified, as depicted in Figure 6.3. Materials must possess an indirect electronic structure gap to be considered a reliable tool for photocatalysis applications. This occurrence may be attributed to many factors. For instance, when a semiconductor has low doping concentrations, atomic states

(also known as localized states) are introduced inside the gap. Increasing the doping concentration results in the overlap of atomic states, which in turn generates new impurity bands. The electronic structure gaps obtained in this investigation are presented in Table 6.2, along with the experimental data for $ZnTiO_3$. The absence of experimental values in Table 6.2 is a result of limited research publications on this doped material. Ultimately, our study objective was to examine the variation in electronic structure gap in $ZnTiO_3$ caused by Mg doping and to prevent any errors in the electronic structure calculation using the GGA technique.

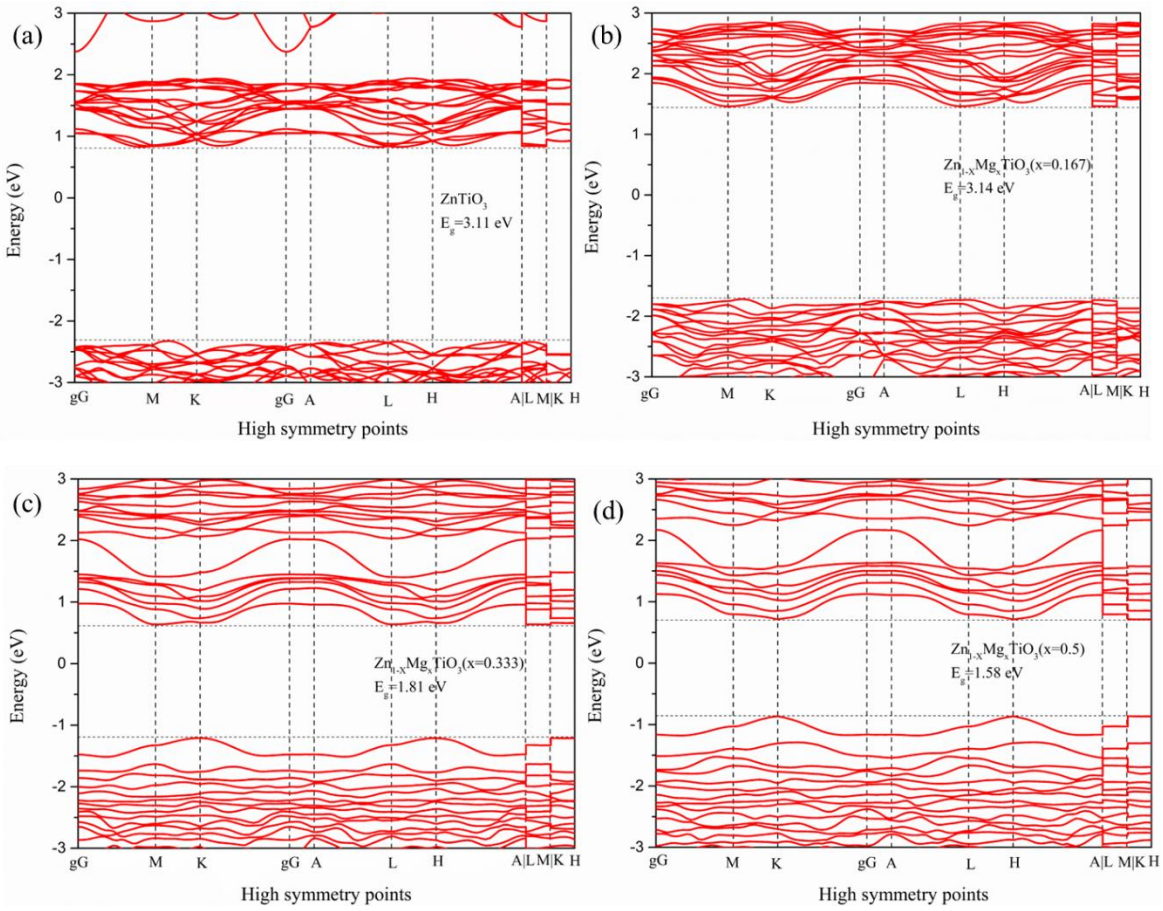

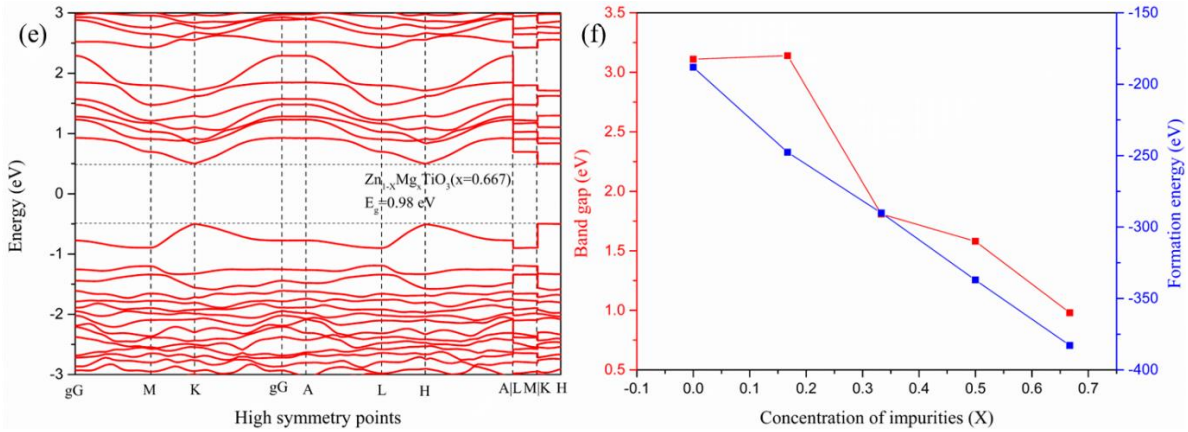

Figure 6.3. Band Structures of $Zn_{1-x}Mg_xTiO_3$ where (a) x = 0, (b) x = 0.167, (c) x = 0.333, (d) x = 0.5, (e) x = 0.667, and (f) formation energy and electronic structure gap of the doped $ZnTiO_3$ as a function of concentration (x) of impurities of Mg.

Figure 6.4 illustrates the partial density of states (PDOS) for undoped $ZnTiO_3$ and Mg-doped $ZnTiO_3$, shown sequentially based on doping. The analysis of the partial density of states revealed that the contribution of atomic orbitals impacted on the total density of states. Figure 6.4 of the partial density of states (PDOS) shows that the valence band (VB) of undoped $ZnTiO_3$ is mostly made up of the oxygen 2p and zinc 3d states. On the other hand, the conduction band (CB) in undoped $ZnTiO_3$ is mostly dominated by the titanium 3d state, with minor contributions from the oxygen 2p and zinc 4s states. After doping, there is little contribution from the Mg 3s state. A vertically dotted line in the image indicates the Fermi energy level, which is represented as a zero point on the energy scale. PDOS changes reflect band-structure rehybridisation originating from local structural relaxation and a more ionic Mg-O bond. Specifically, the different Mg-O versus Zn-O bond lengths/angles modify the octahedral crystal field around Ti and the O-site potential, which in turn alters O 2p-Ti 3d hybridisation. Two coupled effects are evident: (i) the O 2p manifold shows a slight downward shift because Mg-O is more ionic and lacks the shallow Zn 3d-O 2p repulsion present in Zn-O; and (ii) the Ti 3d band edge broadens and

its minimum moves downward due to changes in Ti-O bond lengths and Ti-O-Ti connectivity that enhance O 2p-Ti 3d mixing. The net outcome is a larger downward movement of the CBM than the VBM, leading to a reduced gap with increasing x. Consistent with Figure 6.3, the gap decreases from 3.11 eV (x = 0) to 1.81 eV (x = 0.333, indirect) and further to 0.98 eV (x = 0.667). The Fermi level remains within the gap; any apparent shift reflects the relative motion of the band edges under rehybridisation rather than carrier doping or metallicity. The diminishing intensity and slight rightward displacement of features associated with Zn-derived states at higher energies simply track the reduced Zn content and the altered crystal field. Mg-related spectral weight near the band edges remains negligible, consistent with its closed-shell 2+ configuration and the isovalent nature of the substitution. Finally, the calculated formation energy decreases with increasing x, indicating that Mg incorporation is thermodynamically favorable, in line with the greater ionicity of Mg-O bonding and the accompanying lattice relaxation.

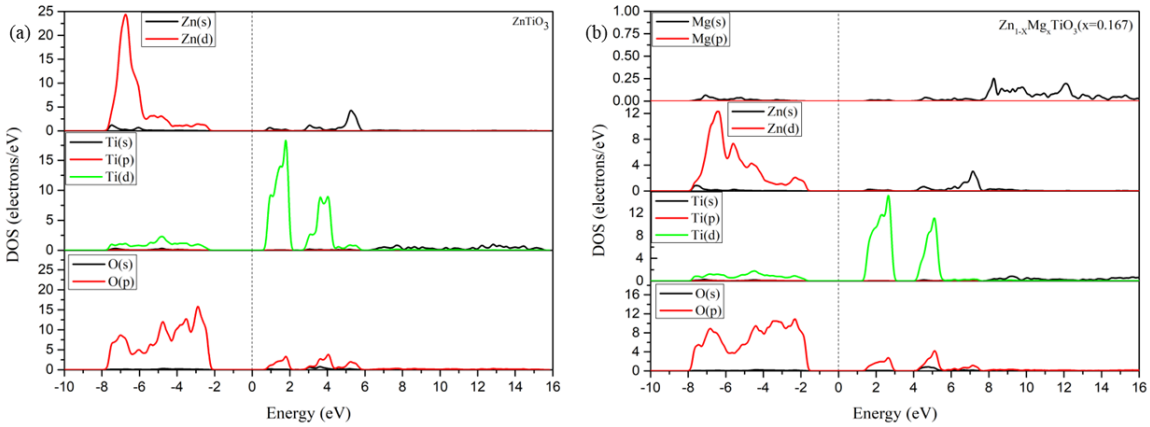

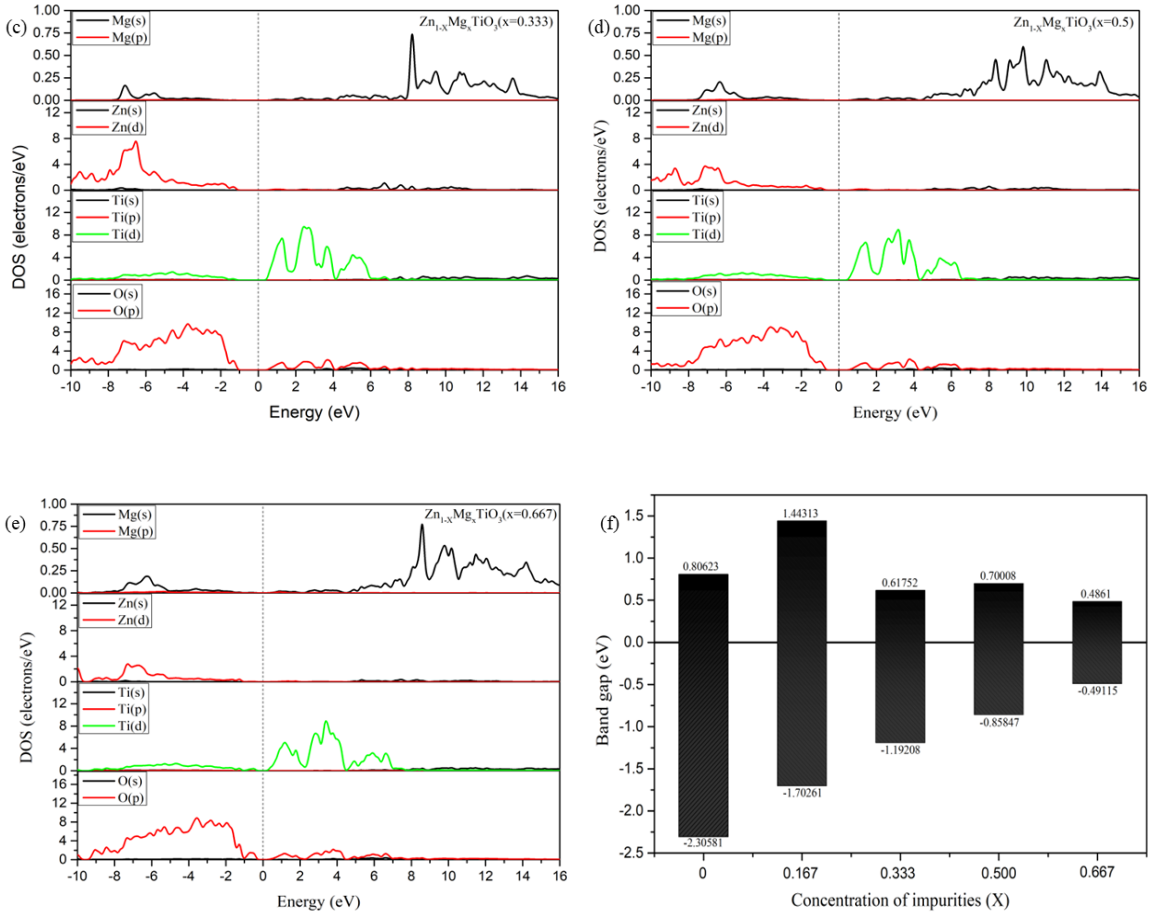

Figure 6.4. Partial density of states (PDOS) of $Zn_{1-x}Mg_xTiO_3$, where (a) x = 0, (b) x = 0.167, (c) x = 0.333, (d) x = 0.5, and (e) x = 0.667.

6.5. Experimental band gap

We perform synthesis of $ZnTiO_3$ with the help of our previous work. Figure 6.5(a) depicts the UV-Vis absorption spectra of $ZnTiO_3$ across the wavelength range of 200 to 800 nm. Significant absorption is detected for wavelengths in the visible spectrum, as illustrated in Figure 6.5(a). This is due to the absorption of incident photon energy by molecules in a lower energy state transitioning to higher energy levels. The experimental bandgap (E_g) is ascertained from a Tauc plot using given relation below.

$$\alpha = \frac{A(h\nu - E_g)^n}{h\nu} \tag{7.1}$$

where α represents the absorption coefficient, h denotes Planck's constant, ν signifies the frequency of light radiation, and E_g indicates the band gap energy, with "n" assuming the value of ½ for permitted direct transitions [314]. Graphs of $(\alpha h\nu)^2$ against $(h\nu)$ are constructed for $ZnTiO_3$. The band gap energy (E_g) is derived from the extension of the linear segments of the graphs to the x-axis. From Figure 6.5(b), it is found that the band energy gap (E_g) for $ZnTiO_3$ is around 3.04 eV. Here we only present experimental band gap of $ZnTiO_3$.

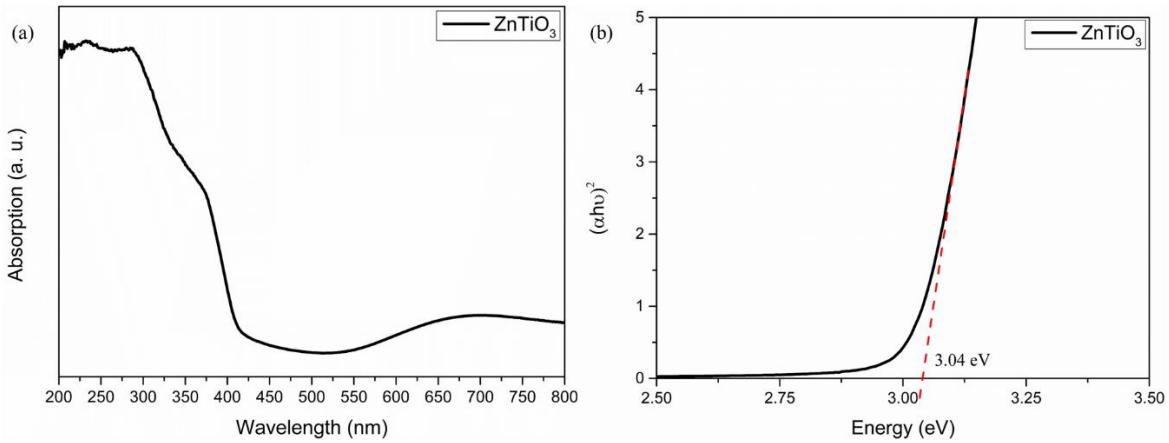

Figure 6.5. (a) absorption verses wavelength and (b) experimental band gap energy (E_g) for $ZnTiO_3$.

6.6. Comparison of band gap from theoretical, experimental and from literature

The theoretical electronic structure gap for $Zn_{1-x}Mg_xTiO_3$ is 3.11 eV at x=0, then drops to 0.98 eV at x=0.667, while the experimental band gap of $ZnTiO_3$ is 3.04 eV, close to theory and literature.

Table 6.2.Comparison tabulation of bandgap of $ZnTiO_3$ reported in the literature, experimental and theoretical bandgap of Mg-doped $ZnTiO_3$.

$Zn_{1-x}Mg_xTiO_3$	**Bandgap E_g (eV)**		
x	**Theoretical**	**Experimental**	**Literature**
0	3.11	3.04	~3.1 [315], [316]
0.167	3.14	-	-
0.333	1.81	-	-
0.5	1.58	-	-
0.667	0.98	-	-

6.7. Conclusion

This chapter investigated the effect of Mg doping on the electronic properties of $ZnTiO_3$ using density functional theory calculations. The results show that varying Mg concentration significantly influences the band structure and density of states of $ZnTiO_3$. These changes demonstrate that Mg incorporation is an effective approach for tuning the electronic behavior of $ZnTiO_3$. Therefore, this chapter provides a theoretical understanding of composition dependent electronic modulation in $ZnTiO_3$ and highlights the potential of Mg-doped metal oxide systems for further study and future applications.

CHAPTER 7

Photocatalytic performance of NiZnO/graphene oxide composites towards visible light induced degradation of methylene blue dye

7.1. Abstract

In this work, we prepare composites of NiO, ZnO, and GO with 1% and 10% GO and measure their photocatalytic activity in the MB degradation reaction under visible light illumination. The oxides are prepared by the sol-gel route, and GO is mixed using a hydrothermal method. The rate constant value in the 1% GO and 10% GO composites are, respectively, 1.76 and 2.35 times higher as compared to that in the binary composite of NiO-ZnO. The rate constants with our GO-based composites also compare favourably with previously reported composites. Structural and chemical characterizations performed using XRD, SEM, BET, XPS, DRS, and PL are correlated with their photocatalytic performance. It is found that GO is reduced in the composites to r-GO, and the NiO band gap decreases to the visible range, which we attribute to the bonding of the NiO particles with the GO sheets. We also propose that the composite forms a double heterojunction structure of r-GO/NiO/ZnO. Because of the work function difference between the GO and NiO, the bands bend-up from r-GO to NiO. Since NiO is a p-type semiconductor and ZnO an n-type, the bands bend-down from NiO to ZnO. The band structure thus formed leads to an efficient carrier separation. Overall, we attribute the

enhanced rate constants in our samples to the reduction in the NiO band gap so as to lie in the visible range, causing higher carrier generation, and the formation of double heterostructures, causing more effective carrier separation.

7.2. Introduction

The previous chapter established that graphene oxide compositing leads to significant modifications in the structural, surface, and electronic properties of $ZnTiO_3$, and also demonstrated the impact of plasma treatment and Cu and Mg doping on $ZnTiO_3$-based systems. These results highlighted that both defect engineering and dopant-induced band structure modulation can be used to tune visible-light activity. Building on these findings, the present chapter focuses on a different oxide platform by investigating NiO-ZnO in combination with graphene oxide, selected because both NiO and ZnO have been widely reported to exhibit promising photocatalytic activity under visible-light or near-visible irradiation.

NiO and ZnO, have been explored by numerous researchers for photocatalytic applications. These oxide semiconductors behave like p-type and n-type, respectively, owing to the dominant defects present in their crystals. The researchers have explored modifying its characteristics by compositing [317], [318]. H. A. Alshamsi et al. successfully synthesized NiZnO/TiO_2 by a mix of hydrothermal and ultrasonic techniques for the photocatalytic degradation of rhodamine B [319]. Jin Wang et al. create NiZnO thin films using photo-assisted metal-organic chemical vapor deposition to produce p-type NiZnO films with elevated hole concentrations [320]. Previous studies have demonstrated that graphene composites can improve light absorption capacity [208]. The transformation of GO to rGO enhances photoexcitation by restoring sp^2 π-bonded regions within an sp^3-insulating matrix, where disorder-induced localized states in the π–π* gap

yield broad optical absorption and emission [35]. GO-metal oxide composites enhance photocatalytic activity by facilitating electron transfer through oxygen-containing functional groups and π-d orbital overlap, enabling greater light absorption and efficient charge separation. Electrons on GO surfaces react with O_2 and H_2O, generating $-O_2^-$ and -OH radicals that effectively degrade pollutants[131]. Sadia Ameen et al. construct a highly efficient ZnO-GO nanohybrid photocatalyst using a chemical method for the photodegradation of crystal violet dye [139]. Ayesha Kiran et al. successfully synthesized NiO/GO for photocatalytic applications [142]. Metal-CNT composites can reduce electron-hole recombination [209].

In this work we have explored NiO-ZnO along with GO, presuming that use of such a system will result in simultaneously improving the three factors responsible for photocatalytic efficiency, namely the light absorption, charge separation, and specific surface area. NiO, being a p-type semiconductor, will form a p-n junction with the n-type ZnO, which will facilitate charge separation. Thus, with the formation of two heterojunctions of n-p-n type between GO/NiO/ZnO with enhanced charge generation in NiO due to bandgap shortening and enhanced charge separation due to two heterojunctions, and with GO imparting higher surface area and accessibility of the photogenerated charges, we can expect a high photocatalytic efficiency in these systems. Our photocatalysis studies indeed show that mixing GO with the NiZnO system enhances photocatalytic degradation of the methylene blue dye, and rate constant shown with 10% GO in NiZnO exceeds that of any of the binary composites such as NiO-ZnO, NiO-GO, and ZnO-GO.

7.3. Experimental section

7.3.1. Materials

Zinc nitrate hexahydrate (Zn $(NO_3)_2.6H_2O$, MW=297.48, purity-98%), terephthalic acid ($C_8H_6O_4$, MW=166.13, purity 98%), C-tab ($C_{19}H_{42}BrN$, MW=364.46, purity-98%), and nickel nitrate hexahydrate (Ni $(NO_3)_2.6H_2O$, MW=290.80, purity-98%) were procured from Molychem Limited. Solvents used during synthesis, DMF ($HCON(CH_3)_2$, MW=73.09, purity-99%) and methanol (CH_3OH, MW=32.04, purity-99%), were procured from Loba Chemie Pvt. Ltd. and Molychem Limited, respectively.

Sodium nitrate, graphite, potassium permanganate, hydrochloric acid, and hydrogen peroxide were purchased from Molychem, India. Sulphuric acid and phosphoric acid were purchased from Rankem, India.

7.3.2. Synthesis of NiZnO

For the synthesis of Ni-Zn oxide particles, 5 g (0.0300 mol) of terephthalic acid was dissolved completely in 100 mL of DMF at 45 °C at a stirring rate of 200 rpm (solution A). Concurrently, 5 g (0.01719 mol) of nickel nitrate hexahydrate and 5 g (0.1680 mol) of zinc nitrate hexahydrate salt precursors were dissolved in 100 mL of DI water at 45 °C (solution B). Separately, 5 g (0.01371 mol) of CTAB (cetyltrimethylammonium bromide) is dissolved in 100 mL of DI water at 45 °C at a stirring speed of 200 rpm (solution C). Solutions A, B, and C are combined in a stainless-steel reactor, and 500 mL of DI water is added to achieve a total solvent volume of 900 mL. The sealed stainless-steel reactor was placed on a magnetic stirrer with a heating plate at 75 °C and 200 rpm for 12 hours. After this period, the temperature of the reactor was raised to 120 °C to evaporate the remaining solvent. The obtained product was washed three times with DI water, methanol, and DMF (1:0.5:0.1) solution and dried in an oven at 80 °C for two hours [321].

After drying, the particles were calcined at 600 °C for two hours in a muffle furnace, giving the desired composite of NiO and ZnO is obtained [322] and will be referred to as NiZnO henceforth in this work.

7.3.3. Synthesis of graphene oxide (GO)

Graphene oxide (GO) was synthesized from graphite powder (GP) via a modified Hummer method. Under constant stirring, 6 g of sodium nitrate was mixed into 230 mL of concentrated sulphuric acid and phosphoric acid (9:1 weight ratio), followed by the addition of 10.0 g of graphite. After 4 hours, 30 g of $KMnO_4$ was gradually added to the above solution while maintaining a temperature below 20 °C. The mixture was stirred at 35 °C for 48 hours, and the resulting solution was diluted by vigorously stirring in 460 mL of water. To ensure that the reaction with $KMnO_4$ was completed, the suspension was treated with 5 mL of H_2O_2 solution (30%). The resulting mixture was filtered, and the graphite oxide residue was washed repeatedly with HCl and H_2O before drying; graphite oxide was thus obtained. We get graphene oxide after sonicating it several times.

7.3.4. Synthesis of NiZnO/graphene oxide (GO) composite

Initially, the obtained GO powder was dispersed in 40 mL of DI water by vigorously stirring for 4 hours and then sonicating for 2 hours. After that, NiZnO is dispersed in the previously obtained GO solution by vigorously stirring it for 4 hours and then sonicating for 2 hours. At last, we transferred this suspension into a 50 mL Teflon autoclave and held it at 180 °C for 12 hr. Then, final NiZnO/GO composites were obtained by centrifuge and dried at 60 °C. The samples with NiZnO:GO weight ratios of 100:1 and 100:10 are named here NiZnO/GO1 and NiZnO/GO10, respectively.

7.4. Results and discussion

7.4.1. X-ray diffraction (XRD)

Figure 7.1 displays the X-ray diffraction patterns of GO, NiZnO, NiZnO/GO1, and NiZnO/GO10. The identified phases in the composites were those of cubic NiO (JCPDS file number 03-065-2901), with Fm-3m space group symmetry, and hexagonal ZnO (JCPDS file number 01-079-0205) with P63mc space group. The peaks in the pattern have been indexed according to these structures. The peaks positioned at the 2θ values of 37.1, 43.1, 62.6, 75, and 79º correspond to cubic NiO [323] and 31.8, 34.5, 36.4, 47.7, 56.7, 63.1, 66.6, 68.2, 69.3, 72.9 and 77.2 correspond to hexagonal ZnO [324]. The relative fractions of each phase were determined by determining the areas beneath the corresponding peaks and are presented in Table 7.1. It is found that the NiO is the majority phase. We don't report here the fraction of r-GO composites since, owing to the small weight percentage, the XRD signal of r-GO is very weak compared to oxide peaks and hence susceptible to large errors. The nearly unchanged NiO and ZnO contents indicate that increasing the GO amount from 1% to 10% did not significantly alter the relative proportion of the oxide phase. In this system, GO mainly acts as an additional supporting or interfacial component rather than replacing or consuming NiO and ZnO, so the oxide composition remains essentially stable while only the GO fraction increases.

The GO samples have a distinct strong peak at a 2θ value approximately equal to 10.9° [213]. Our composite samples exhibit r-GO reflections at around 22°. The distinctive GO peak at 10.9° was not seen in the XRD diffraction patterns of the composites. The composite data exhibit faint signals at a 2θ value of 23° (Figure 7.2). These data indicate that in the composite samples, the GO has been reduced to r-GO. Yang et al. noted that GO is reduced when mixed with TiO_2, as signaled by a progressive attenuation of the GO

peak at about 10° as the TiO_2 fraction increased, with total disappearance of this peak at a GO: TiO_2 ratio of 1:2.5 [214]. In this work we have used a relatively very small fraction of GO compared to the metal oxides. The Scherrer equation yields the crystallite sizes in the three samples as (Table ST1, please see the Supplementary Document) 29.7 ± 2.47 nm, 27.3 ±1.55 nm, and 31.6 ± 2.20 nm for NiO, and 33.9 ± 1.15 nm, 30.5 ±0.98 nm, and 36.6 ± 1.30 nm for ZnO, respectively NiZnO, NiZnO/GO1, and NiZnO/GO10 samples. The crystallite size of the ZnO is 10-15% larger than NiO.

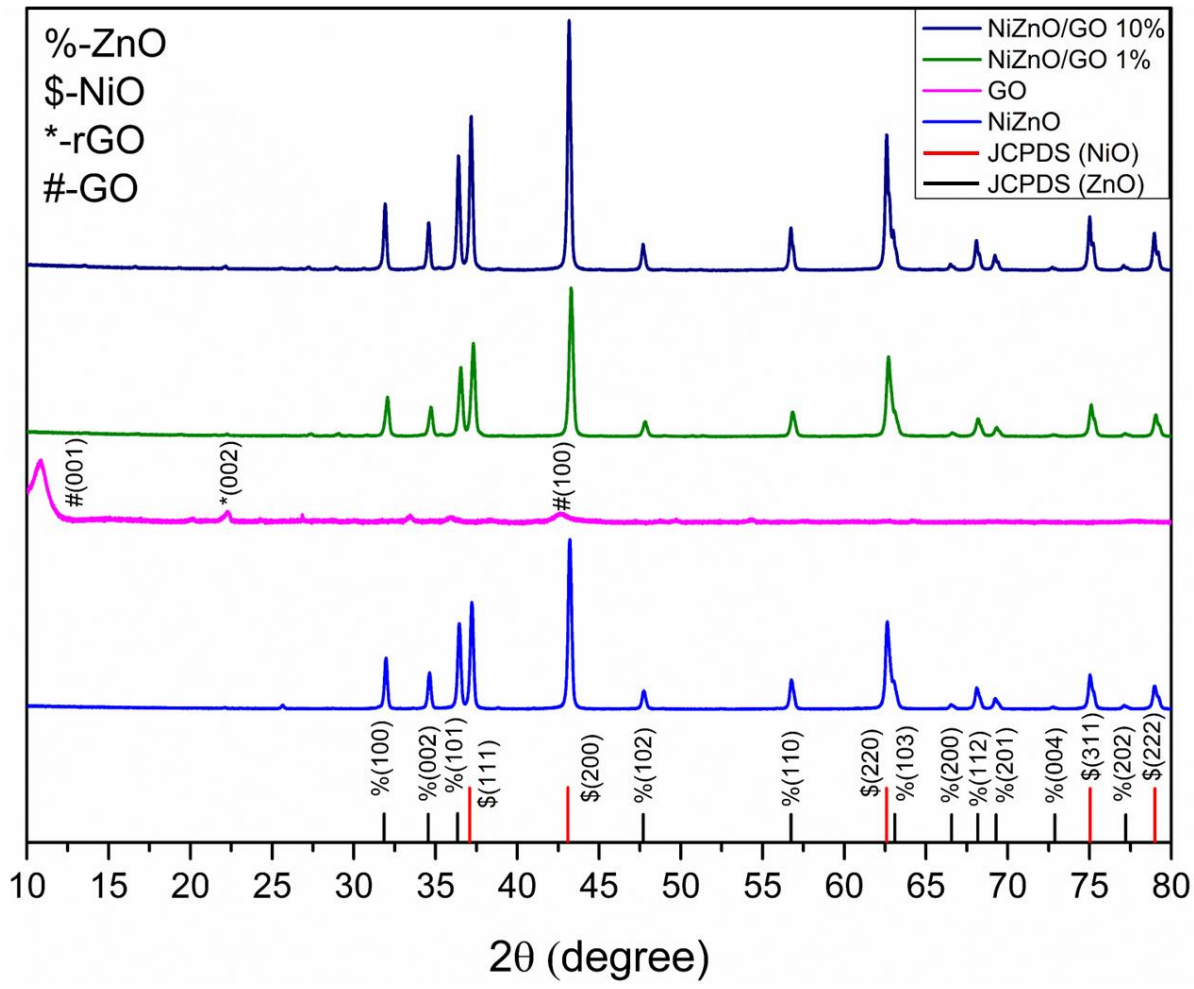

Figure 7.1. X-ray diffractogram of NiZnO, NiZnO/GO1, NiZnO/GO10, and GO.

Table 7.1.Percentage of phase present in the sample.

	NiZnO	NiZnO/GO 1	NiZnO/GO 10

NiO	65.43%	66.46%	67.32%
ZnO	34.57%	33.29%	32.50%

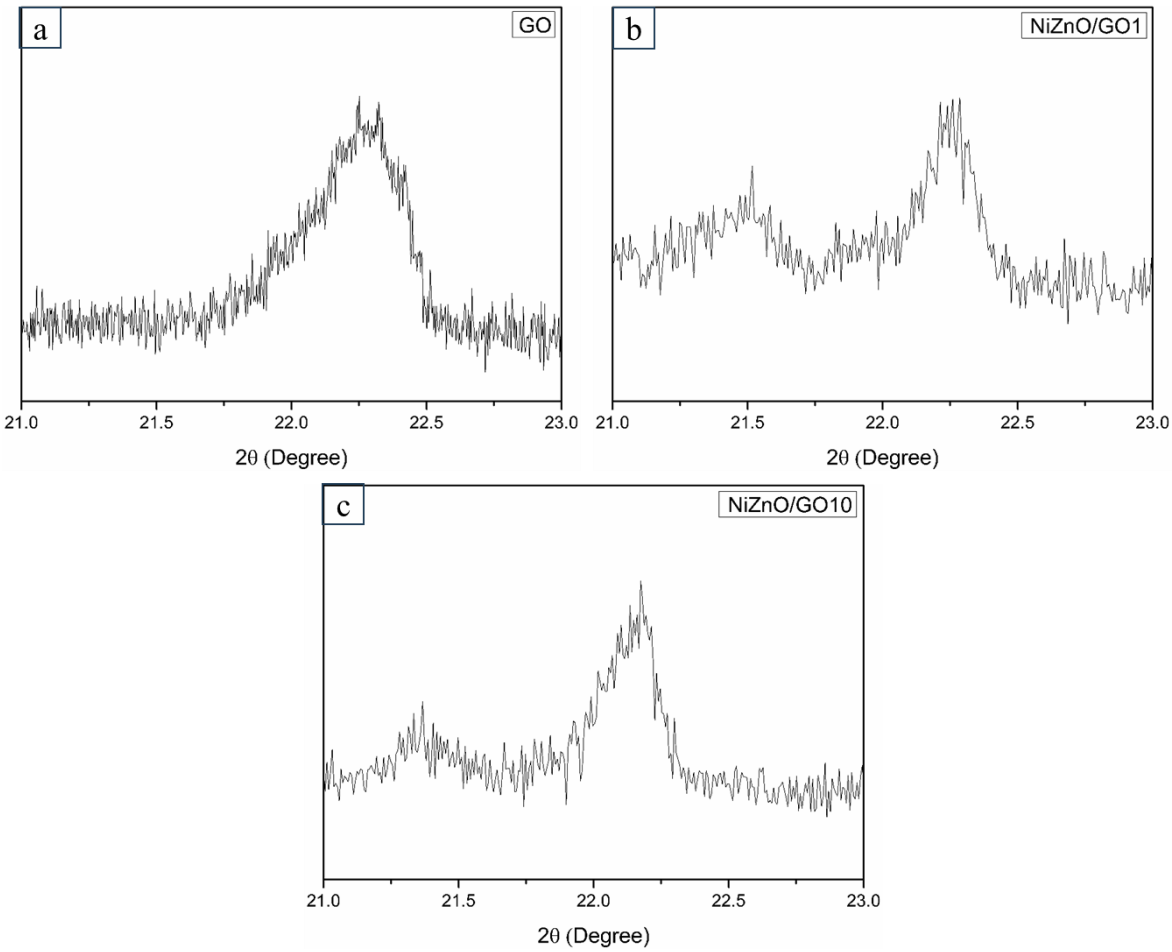

Figure 7.2. X-ray diffractogram for (a) GO, (b) NiZnO/GO1, and (c) NiZnO/GO10 in region 21-23°.

7.4.2. Surface Area Analysis

Figure 7.3 (a, c) depicts the nitrogen adsorption-desorption isotherms and (b, d) the BET plots of the composites. The huge surface area of graphene sheets has been extensively observed [325], [326]. Consequently, an increased surface area of the NiZnO/GO composite compared to pure NiZnO is expected. The BET surface areas of NiZnO and NiZnO/GO10 are found to be 2.1 m^2/g and 2.6 m^2/g, respectively, revealing a 27%

increase in surface area in the latter sample. We have not presented data for the 1% composite because the GO fraction is not significant, and therefore the surface area change also doesn't change appreciably.

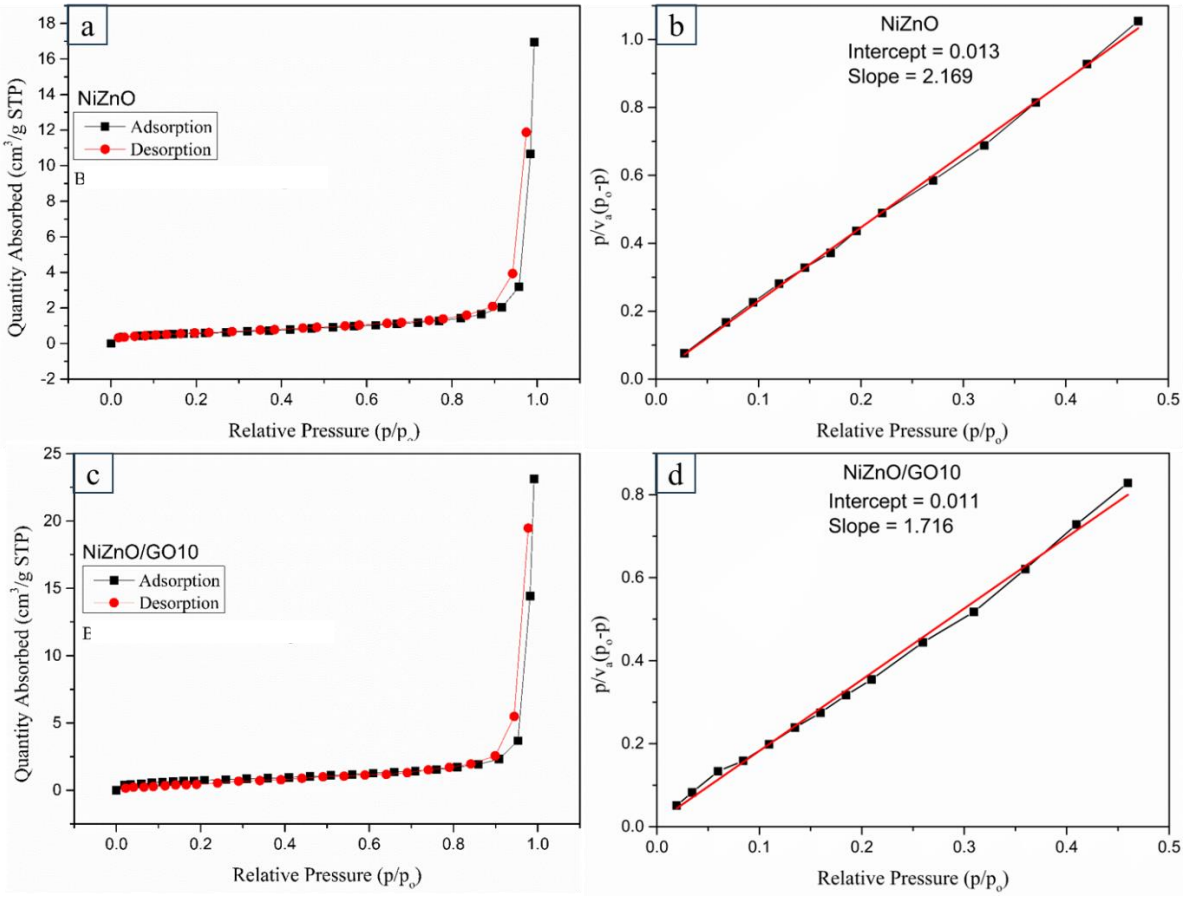

Figure 7.3. The BET isotherms of (a) NiZnO, (c) NiZnO/GO10 and BET plots of (b) NiZnO, (d) NiZnO/GO10.

7.4.3. Field Emission Scanning Electron Microscopy (FESEM) analysis

Figure 7.4 shows the FESEM images of GO and other composite samples. Figures 7.4(a) and 7.4(b) distinctly display GO sheets, exhibiting a C/O ratio of 1.9 as obtained from the EDX data (Figure 7.5(f)). The standard values of the C/O ratio are approximately 1.4 [49]. In the NiZnO/GO10 sample, oxide particles are visible on the graphene sheets, as

seen in Figures 7.4(g) and 7.4(h). Conversely, the NiZnO/GO1 sample did not show graphene oxide, due to a lesser quantity of GO, as shown in figures 7.4(e) and 7.4(f).

Figure 7.5 displays the EDX mapping of NiZnO along with the spot EDX for both NiZnO and GO. Figure 7.5 (a, b, c) shows that Ni and Zn are found in the NiZnO sample, while figure 7.5 (d, e) shows that small particles contain more Ni than Zn, and large particles contain more Zn than Ni. Figure 7.5 confirms elemental presence and visualizes its spatial distribution in samples before compositing. In this figure, the EDX of the r-GO composite is not presented because the GO fraction is very small, and therefore fraction of carbon detected by EDX will have a large error bar and will be inaccurate, giving no significantly new information. The objective in Figure 7.5 is solely to confirm the presence of Ni and Zn in as-prepared NiZnO, and carbon and oxygen in as-prepared GO.

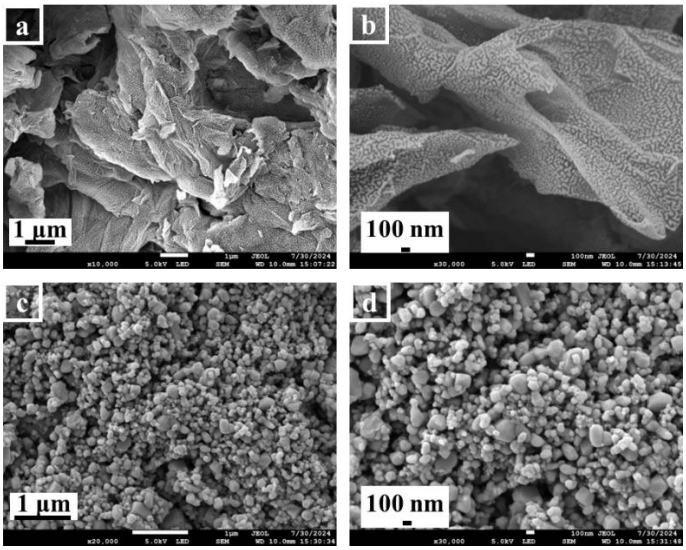

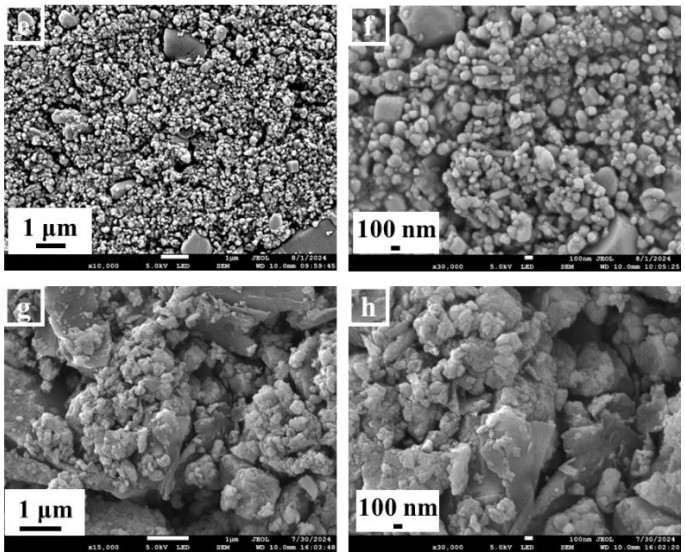

Figure 7.4. FESEM images of samples at smaller magnification (left column) and larger magnification (right column). Images of (a, b) GO, (c, d) NiZnO, (e, f) NiZnO/GO1, and (g, h) NiZnO/GO10 samples.

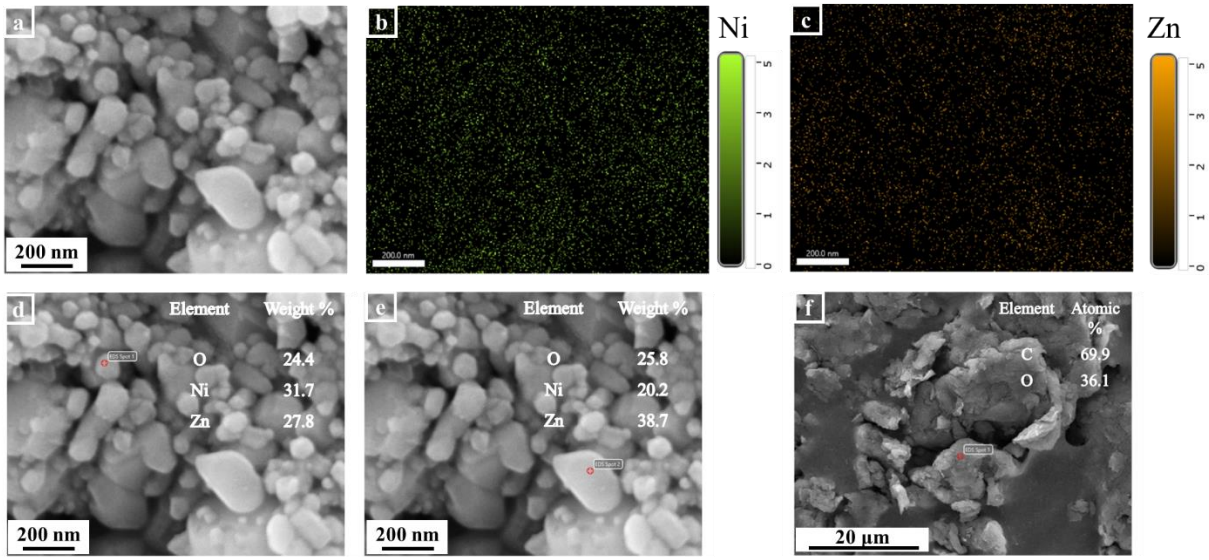

Figure 7.5. EDX mapping (a, b, c) of NiZnO and spot EDX (d, e) of NiZnO and (f) GO.

7.4.4. X-ray Photoelectron spectroscopy

XPS analysis is used for identifying the oxidation states of the atomic species, and in our samples, it helps to uncover the correlation between the atomic details and the observed photocatalytic behavior.

The O1s spectra for each sample are presented in Figure 7.6, showing distinct peaks of core electrons of oxygen from all the samples. It is clearly seen that the peak at around 532 eV in the GO sample attributed to the C=O group (Figure 7.6(a)) gets significantly diminished in the composite samples (Figures 7.6(c) and (d)), confirming loss of oxygen from the GO due to formation of r-GO. These C=O peaks also shift and broaden significantly in composite samples, which may be attributed to a bond formation of the residual C=O groups with Ni. In Ni-C=O bonds, the carbon atom forms a sigma bond with nickel, and nickel back-bonds with carbon by donating its 3d electrons to the π^* orbital of the C=O, and thereby the electron cloud of the C=O bond is pulled towards carbon, raising the oxidation state of oxygen and shifting the XPS peak of O1s electrons to higher binding energy values. In Figure 7.6(b), there are three components at about 529.20, 530.36, and 531.92 eV; the peaks at 529.20 and 530.36 correspond to lattice oxygen (Ni-O and ZnO, respectively), while 531.92 eV is attributed to chemisorbed oxygen (OH) species [130], [327], [328]. It can also be seen that the relative strength of the O1s signal from Ni-O bonds as compared to Zn-O bonds is reduced in the composite samples and shifted to slightly higher binding energy values. This suggests oxygen loss from the Ni-O framework. Thus, from the O1s spectra, we conclude that the presence of r-GO leads to nickel oxide losing its oxygen and forming a bond with the residual C=O of the r-GO. As argued later, this has important consequences in the photocatalytic activity of the composites because the Ni-C bond formation leads to shortening its bandgap, and oxygen loss leads to the presence of surface states, which plays an important role in optical absorption.

Figure 7.7 presents the C1s spectra from all the samples. Figure 7.7(a) shows three peaks at 284.90, 287.03, and 288.50 eV, which respectively correspond to the C-C, C-O-C or C=O, and O=C-OH functional groups of GO [328], [329]. The C1s electrons from both

C-O and C=O bonds exhibit markedly decreased signals in composited samples, indicating a drop in oxygen and confirming the formation of r-GO [223]. Figure 7.8 (a) shows the Zn 2p spectrum, with two peaks at 1044.0 eV and 1021.3 eV, which correspond to Zn $2p_{1/2}$ and Zn $2p_{3/2}$ in the ZnO form, respectively. There is no significant change in the Zn2p spectra from various samples except for a minor shift to higher binding energy in composite samples as compared to the NiZnO sample, which may be attributed to the oxygen loss from the ZnO framework. Peak positions for O1s, C1s, and Zn2p are presented in Table 7.2.

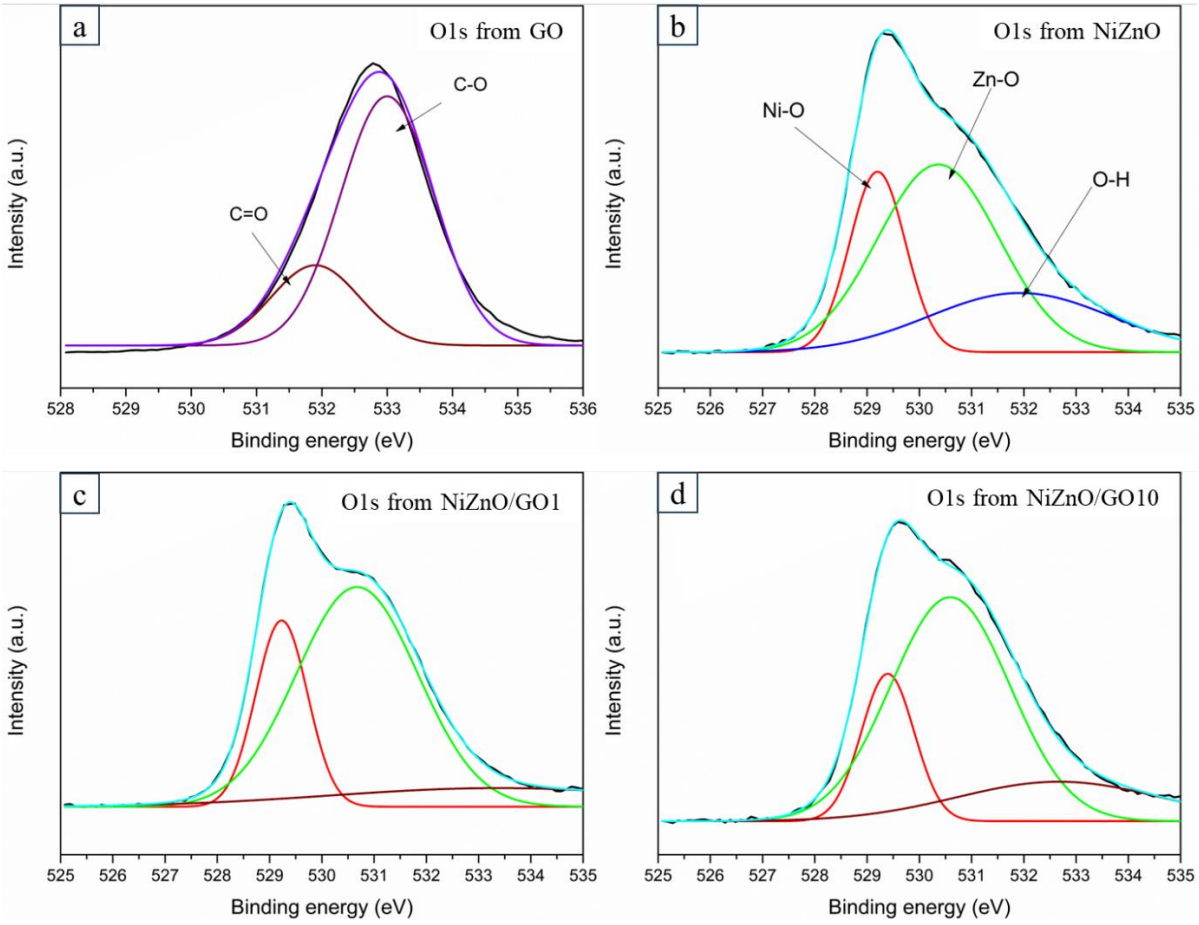

Figure 7.6. XPS of O1s of (a) GO, (b) NiZnO, (c) NiZnO/GO1, and (d) NiZnO/GO10.

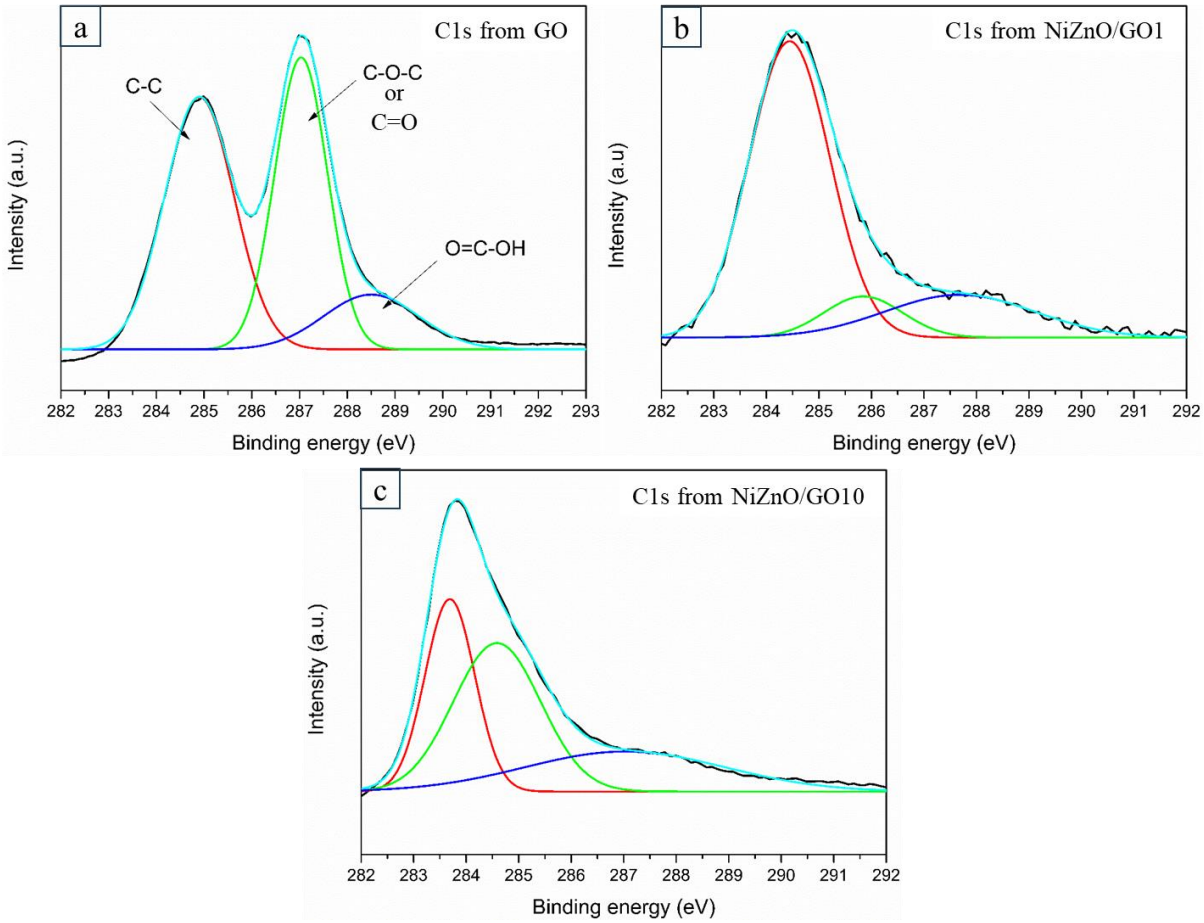

Figure 7.7. XPS of C1s of (a) GO, (b) NiZnO/GO1, and (c) NiZnO/GO10.

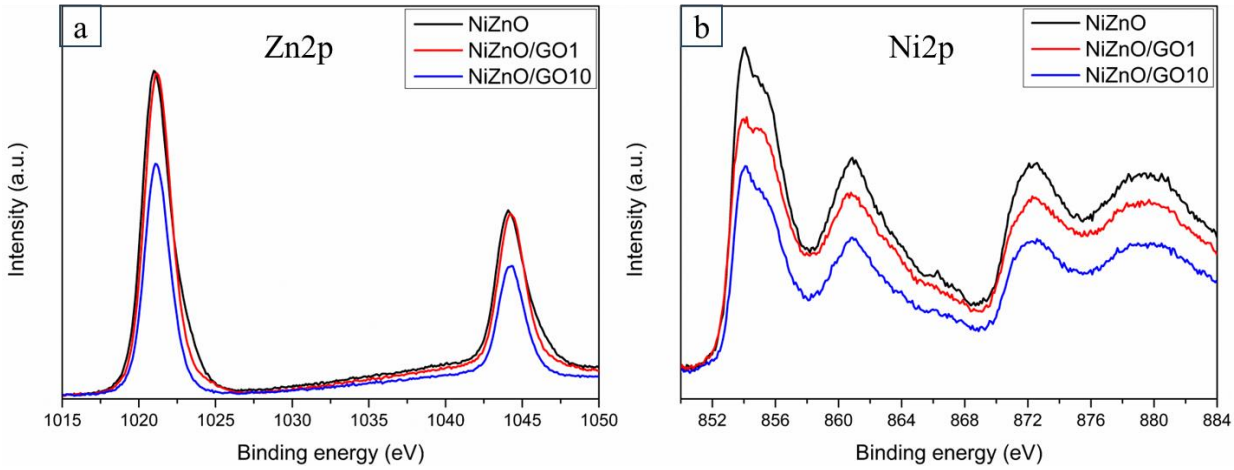

Figure 7.8.XPS of Zn2p of (a) NiZnO, NiZnO/GO1, and NiZnO/GO10 and XPS of Ni2p of (b) NiZnO, NiZnO/GO1, and NiZnO/GO10.

Table 7.2. Peak positions of XPS for NiZnO, NiZnO/GO1, and NiZnO/GO10.

Samples	O1s	Bonds	C1s	Bonds	Zn2p	orbital
NiZnO	529.20	Ni-O	-	-	1020.98	$Zn2p_{3/2}$
	530.36	Zn-O	-	-	1044.08	$Zn2p_{1/2}$
	531.92	O-H	-	-	-	-
NiZnO/GO1	529.23	Ni-O	284.44	C-C	1021.18	$Zn2p_{3/2}$
	530.67	Zn-O	285.84	C-O-C	1044.18	$Zn2p_{1/2}$
	533.39	C=O	287.68	O=C-OH (C=O)	-	-
NiZnO/GO10	529.39	Ni-O	283.69	C-C	1021.08	$Zn2p_{3/2}$
	530.59	Zn-O	284.58	C-O-C	1044.38	$Zn2p_{1/2}$
	532.67	C=O	287.02	C=O-OH (C=O)	-	-
GO	533	C=O	284.90	C-C	-	-
	531.9	C-O	287.03	C-O-C/C=O	-	-
			288.50	O=C-OH	-	-

The Ni 2p spectra are presented in Figure 7.8(b). Due to multi-peak structures observed in the Ni2p spectra, detailed deconvoluted spectra for each sample are shown separately in Figures 7.9(a), (b), and (c). The peak at the smallest binding energy clearly shows a shoulder and could be deconvoluted into two separate peaks, where the first peak at the lower binding energy corresponds to Ni^{2+} and the higher one to Ni^{3+}. Both Ni^{2+} and Ni^{3+} are present in all the samples. The presence of Ni^{3+} makes the NiO a p-type semiconductor, which forms a p-n junction with the ZnO particles, which aids in charge

separation and prevents recombination and thereby improves photocatalytic efficiency. Overall, the Ni2p peaks could be deconvoluted into eight sub-peaks, four of each arising due to Ni^{2+} and Ni^{3+}. For accurate determination of the double peak features of Ni $2p_{3/2}$ and Ni $2p_{1/2}$, the XPS spectra were deconvoluted using the Voigt peak fitting function. The perfect fit for 8 peaks noted as a, a*, b, b*, c, c*, d, and d* are located at BE of 854 (±0.2), 855.8 (±0.2), 860.9 (±0.2), 866 (±0.2), 871.3 (±0.2), 872.8 (±0.2), 878 (±0.2), and 880.9 (±0.2) eV, respectively. The peaks noted as a, a*, c, and c* represent core levels of Ni^{2+} ($2p_{3/2}$), Ni^{3+} ($2p^{3/2}$), Ni^{2+} ($2p_{1/2}$), and Ni^{3+} ($2p_{1/2}$), respectively. The deconvoluted shake-up satellite peaks due to hybridization or transition of charge between O (2p) → Ni (3d) [330] noted as b, b*, d, and d*, were observed at ~6.9 (±0.2), 10.2 (±0.2) eV, 6.9 (±0.3), and 8.1 (±0.2) eV higher in BE than that of Ni^{2+} ($2p_{3/2}$), Ni^{3+} ($2p_{3/2}$), Ni^{2+} ($2p_{1/2}$), and Ni^{3+} ($2p_{1/2}$) peaks, respectively. The presence of double peak features of Ni 2p along with their shake-up satellite peaks clearly confirms Ni^{2+} and Ni^{3+} [331]. These observations are in agreement with the peak positions are reported in previous studies for the presence of Ni^{2+} and Ni^{3+} oxidation states in stoichiometric and non-stoichiometric NiO [332].

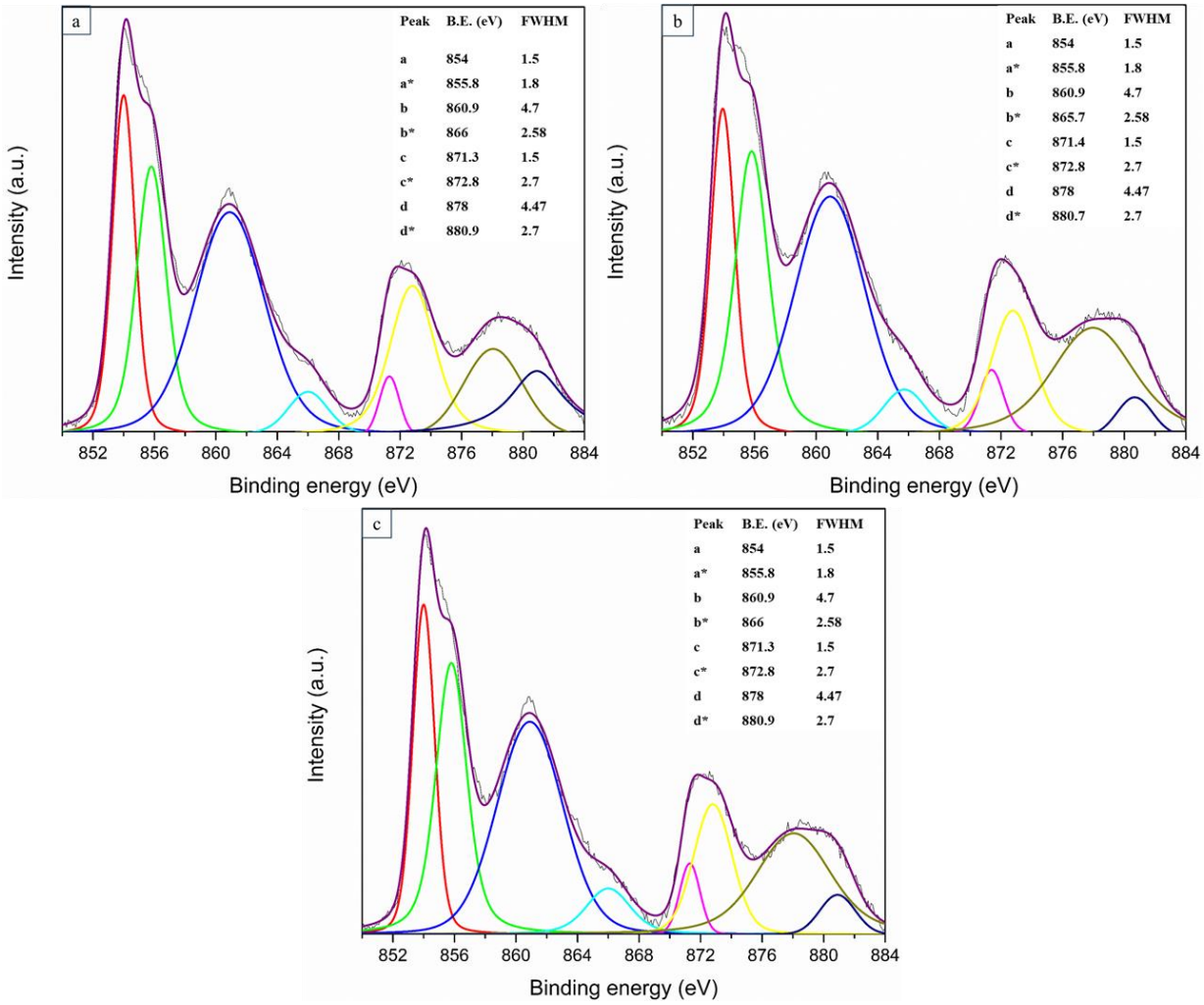

Figure 7.9. Images of XPS deconvolute of Ni2p for (a) NiZnO, (b) NiZnO/GO1, and (c) NiZnO/GO10.

7.4.5. Optical behavior from UV-Vis Diffuse Reflectance Spectroscopy

The influence of GO on optical characteristics was analyzed utilizing UV-Vis diffuse reflectance spectroscopy (DRS). The NiO and ZnO are wide bandgap materials, whereas the band gap of GO is tunable depending on the extent of oxidation of graphite or reduction of graphene oxide [132], [133], [135], [333]. The DRS spectra shown in Figure 7.10 are used to extract the bandgap values in NiZnO, NiZnO/GO1, and NiZnO/GO10, which are found to be 3.04 eV, 2.92 eV, and 2.69 eV, respectively, as ascertained from the Tauc plot based on the DRS data. The reduction in the bandgap is attributed to bandgap

shortening of NiO, which arises due to Ni-C bond formation, as also confirmed by the XPS data presented earlier. The bandgap of NiO observed in the composites (2.92 eV and 2.69 eV) lies in the visible region. Additionally, an increased fraction of GO causes the long absorption tail extending to large wavelengths to become stronger, suggesting the absorption is due to the short bandgap GO (Figure 7.10 (e)). The presence of oxygen vacancies in NiO and ZnO can also create surface states that may give rise to the long absorption tail [334]. The bandgap of the pure GO is observed to be 1.6 eV. Thus, on compositing, both NiO and GO act like absorbing media for visible light and are thereby expected to improve the photocatalytic activity.

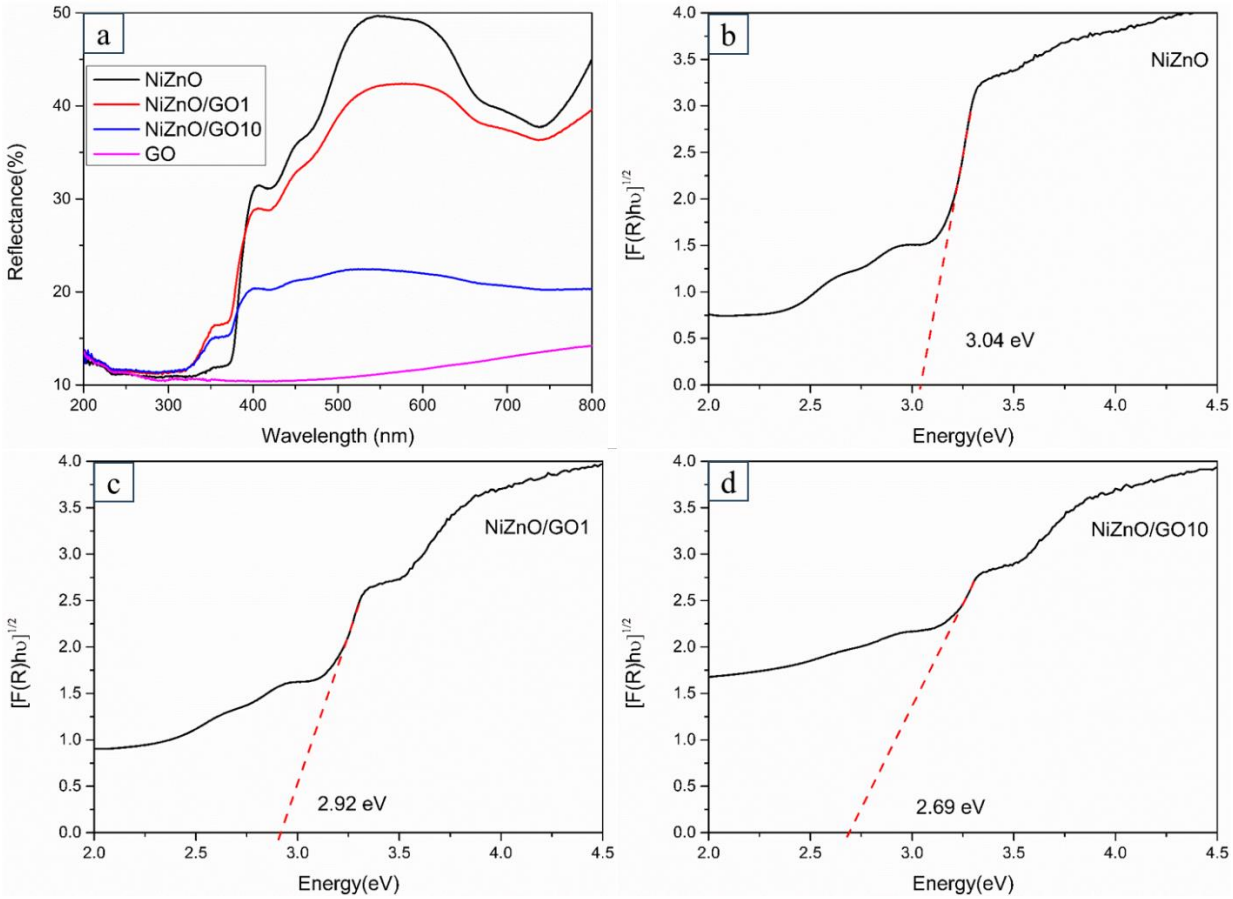

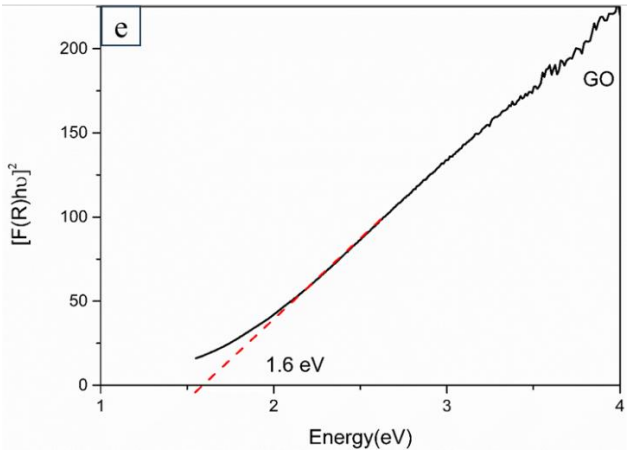

Figure 7.10. (a) UV DRS data in terms of reflectance. The plot of the Kubelka-Munk function versus the energy of exciting light that results in the band gap of (b) NiZnO, (c) NiZnO/GO1, (d) NiZnO/GO10, (e) GO.

We propose that the three components of GO, NiO, and ZnO form a sequentially adhered heterostructure with two heterojunctions, one between GO and NiO, and the other between NiO and ZnO.

We assume that r-GO prevalently binds with NiO and not the ZnO during the hydrothermal mixing. The reason behind this assumption is that (i) NiO fraction is much higher than ZnO in our samples, and (ii) Ni has an affinity to bind with C=O groups where the bond is stabilized by nickel transferring its d-electrons to the π^* orbital of the sp^2 hybridized carbon. This assumption is also supported by our XPS data where the oxygen signal from NiO systematically reduces in strength as compared to that from ZnO (Figure 7.6), suggesting increasing oxygen loss from NiO as r-GO content is increased, which can happen due to Ni-C bond formation. Bandgap narrowing in NiO upon binding with carbon (as observed in our DRS data) is also reported in literature [335], [336]. Thus, based on our data and prior works, we propose a double junction heterostructure formed of r-GO/NiO/ZnO where n-type r-GO binds with p-type NiO which subsequently binds with n-type ZnO. We argue in the following paragraphs that this structure will always

lead to separation of photogenerated electron-hole pairs and thereby enhanced photocatalytic activity.

Type II heterostructures [337], [338] and direct Z-scheme [339], [340], [341] are the two most common mechanisms forwarded to explain the photocatalysis in prior works. In the Type II heterostructures, the band bending due to intimate contact between the two particles causes photogenerated electrons and holes to roll down over the junction to lower energy levels on the other side leading to charge separation, whereas in direct Z-scheme, lower energy electrons and holes present on either side of the junction recombine leaving electrons and holes with higher energy values separated spatially. The interfacial electric field formed by band bending or the interfacial defect states promote the recombination. The Z-scheme is expected to be a more efficient mechanism for photocatalysis since the separated charges have higher redox potentials.

The relative positions of the Fermi levels and the band edges two materials are the crucial information needed for determining the possible pathways constituting the mechanism of catalysis. Difference in the Fermi level decides the interfacial electric field which in turn would decide which of the two mechanisms will be more likely to occur. Relative positions of the band edges will decide the separation bias of the electron hole pairs. In our system, we consider the r-GO to be a semiconductor whose band gap and the Fermi level depend upon the extent of reduction in GO [342]. Also, after binding with r-GO, the p-NiO undergoes bandgap narrowing, with its Fermi level moving up reducing its p-type character [343]. The work function of the r-GO can lie between 4.2-5.5 eV depending upon its extent of reduction, whereas the NiO work function can lie between 5.2-5.6 eV depending on the extent of vacancy creation. The work function of ZnO is close to 4.25 eV [344], [345], [346], [347], [348], [349]. Due to indeterminacy in the work functions of r-GO and NiO, there are two possibilities: the work function of r-GO is either smaller

or larger than the p-NiO. The band structures and resulting mechanisms of charge separation for both the cases are shown in Figure 7.11 (a) and (b). In both the cases, (i) the NiO bandgap decreases after binding with r-GO, so that photogeneration occurs in r-GO and NiO regions, and (ii) the NiO/ZnO forms a p-n junction, with band bending promoting the transfer of the photogenerated electrons in the NiO conduction band to ZnO conduction band. However, when the work function of r-GO is smaller than NiO, then r-GO/NiO also forms a p-n junction (Type II heterostructure), so that overall, the photogenerated electrons accumulate on r-GO and ZnO, and holes on NiO. On the other hand, if the work function of r-GO is higher than that of the NiO, then r-GO/NiO will an n-p direct Z-scheme heterojunction [350], where the direction of the interfacial electric field assists the recombination of photogenerated electrons in the r-GO conduction band and holes in the NiO valence band. The photogenerated electrons in the conduction band of the NiO transfer to the ZnO conduction band as in the first case. This mechanism leads to wider separation of the electrons and holes. In summary, the proposed double heterostructure will always give rise to charge separation, although the mechanisms will be different.

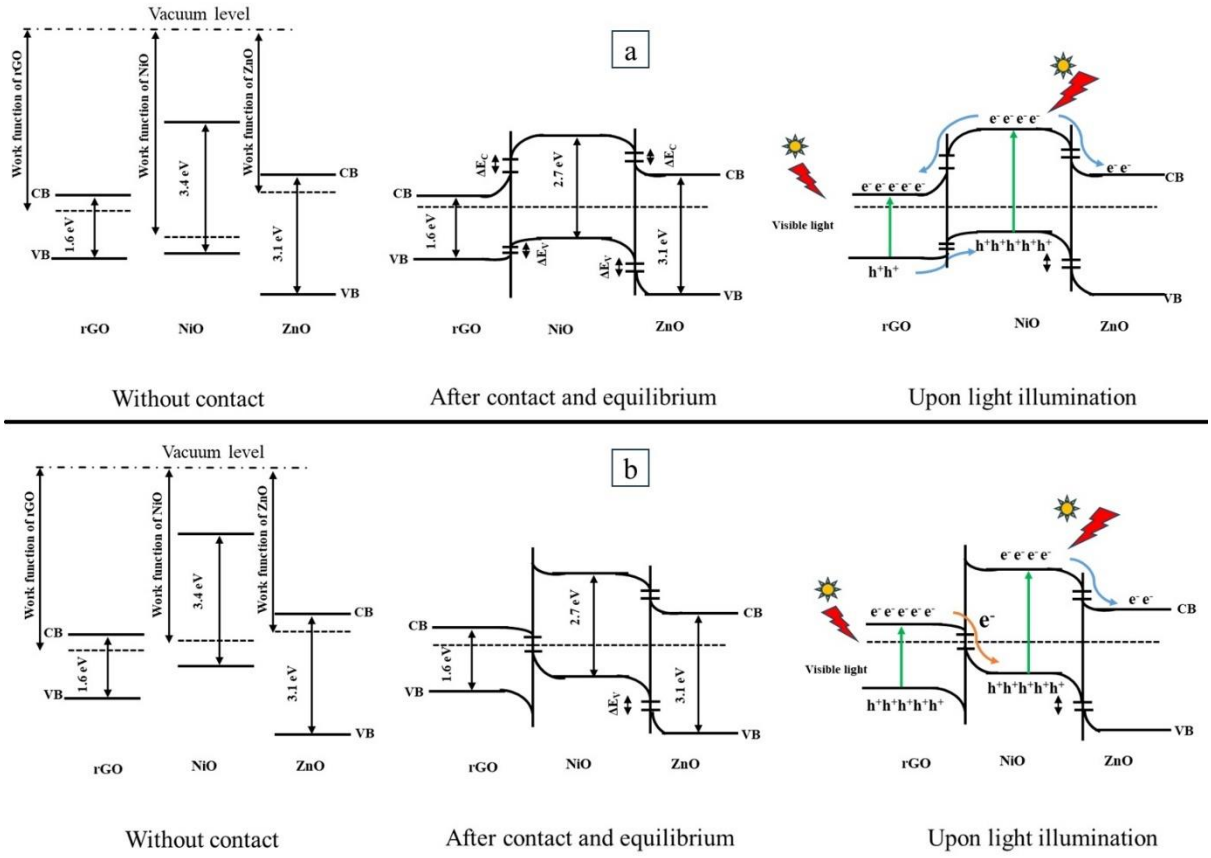

Figure 7.11. Mechanism of charge separation in r-GO/NiO/ZnO. (a) Type II heterojunction when r-GO work function is larger than that of NiO, and (b) direct Z-scheme, when work function of r-GO is smaller than that of NiO. The dashed lines imply the Fermi level. For representation, sample NiZnO/GO10 is considered here, with NiO band gap becoming 2.7 eV from 3.4 eV due to nickel binding with carbon of r-GO sheets after it is composited with the GO. The green vertical arrows represent carrier generation due to light illumination, blue arrows represent carriers moving across the junction to lower energy levels, and orange arrows represent recombination. Please see text for detail.

7.4.6. Photoluminescence Spectroscopy

The photoluminescence emission spectrum, closely linked to surface states and stoichiometric chemistry, is employed to evaluate the efficiency of charge carrier entrapment, migration, and transfer, as well as to clarify the dynamics of electron-hole

pairs in semiconductors. Figure 7.12 presents the photoluminescence emission spectra of NiZnO and NiZnO/GO samples, excited at 380 nm. All samples have photoluminescence bands centered at 410, 422, 444, 458, 487, and 522 nm. The various peaks can be attributed to defects in NiO and ZnO, as reported earlier in the literature. Without going into the details of the nature of the defects involved in giving rise to various emissions, we will only assign the PL peaks to either NiO or ZnO since the study of defects is not our objective here [351], [352], [353], [354]. An emission band at 410 nm can arise due to either NiO or ZnO. NiO is reported to give PL band at 411 and 414 nm [351], [353], whereas zinc interstitials (Zn_i) to VB transition in ZnO can give rise to a band at 422 nm [352]. The band at 444 and 458 nm can also be due to $3d^8$ electrons of Ni^{2+} of the bulk NiO [353], [355]. The emission band at 487 nm can be attributed to the Zn_i to zinc vacancy (V_{Zn}) in ZnO [354]. The band at 522 nm can be attributed to the transition from interstitial zinc (Zn_i) to V_o (the oxygen vacancy) in ZnO [354].

We notice that intensities of all the emission bands significantly reduce in NiZnO-GO10 samples, clearly suggesting enhanced carrier lifetimes in these composites. We attribute this to an efficient electron-hole separation effected by the two heterojunctions as depicted in the band diagram shown in Figure 7.12. The separation causes suppression in the disappearance of these carriers and thereby enhancement in the photocatalytic activity of the composite.

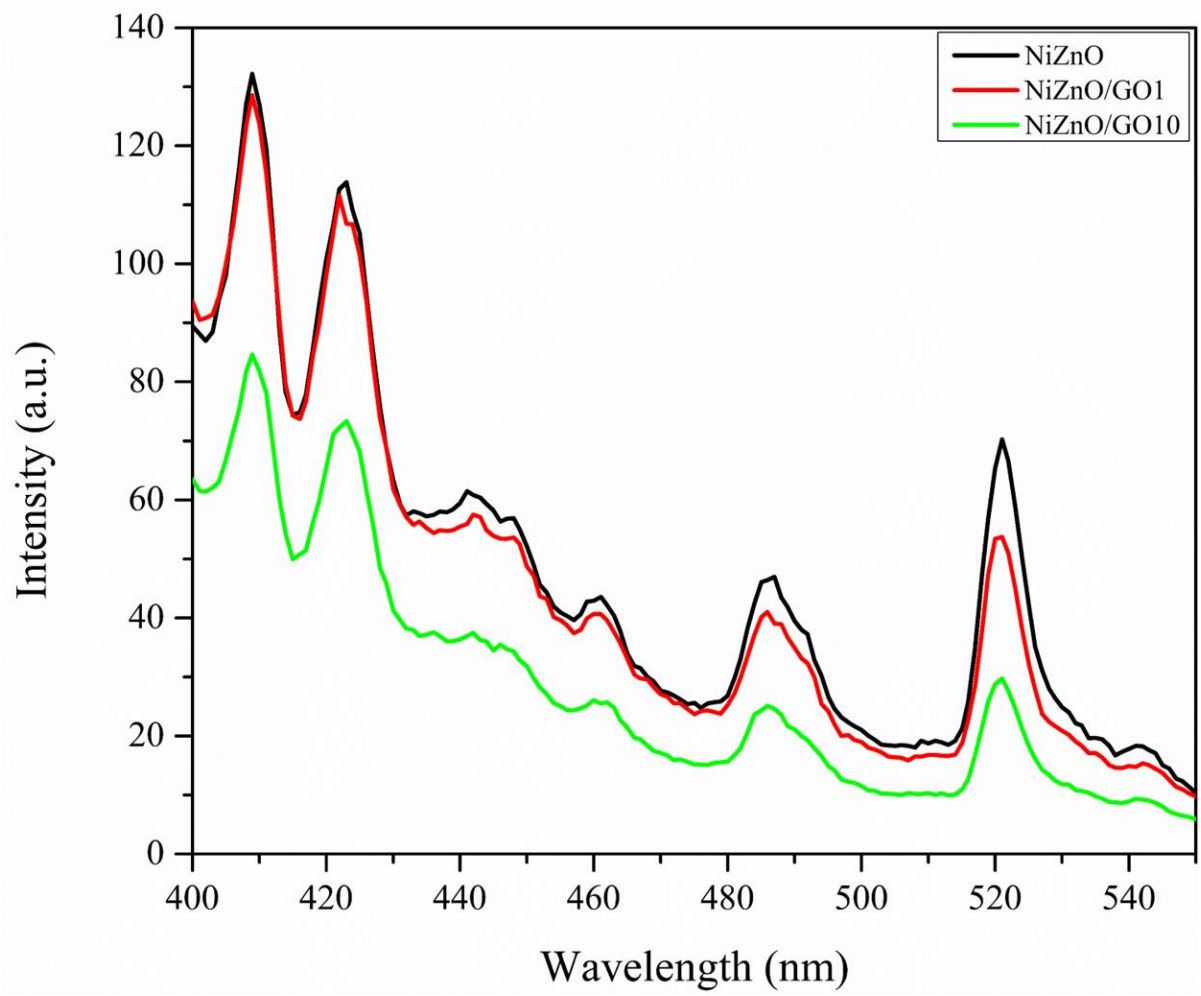

Figure 7.12. Photoluminescence spectra of NiZnO, NiZnO/GO1, and NiZnO/GO10 samples.

7.5. Photocatalytic performance

The photocatalytic effectiveness of NiZnO and NiZnO/GO was evaluated and compared by analyzing the kinetics of degradation of MB dye solution in the presence of the photocatalyst powder under visible light illumination. The concentration of the dye was measured using UV-Vis spectra of the MB dye solutions stirred in the presence of the equal amount of the photocatalyst at different time steps. The absorption peak of the MB solution is noted at 600 nm at a pH of 12. Prior to irradiation, the suspensions were magnetically stirred in darkness for 30 minutes to establish absorption-desorption equilibrium between the photocatalyst and methylene blue. We noted the occurrence of

adsorption events; nevertheless, our primary focus is only on photocatalytic degradation. The MB aqueous solution stays stable under visible light irradiation, indicating that MB self-degradation is almost undetectable in the absence of a photocatalyst. The concentration of MB markedly decreases in the presence of NiZnO and NiZnO/GO photocatalysts under the same testing conditions. The UV-Vis data and the corresponding kinetics data are presented in Figure 7.13. The degradation of MB is following a pseudo-first-order reaction. The kinetic rate constants are established as 0.029 min^{-1} for NiZnO, 0.063 min^{-1} for NiZnO/GO1, and 0.080 min^{-1} for NiZnO/GO10. The kinetic rate constant of NiZnO/GO10 is 1.76 times larger than that of NiZnO. Since the surface area did not change appreciably from NiZnO to the 1% GO samples, we attribute this increase mainly to the bandgap reduction and probable formation of the double heterojunctions. We also present in Table 7.3 a comparison of the rate constants of the MB degradation with photocatalysts attempted in other works and find that our values compare favourably with the other values.

Unlike the photocatalyst composites formed of bimetallic oxides or metal oxide with GO as reported earlier, our ternary composites of two metal oxides and GO are likely to form a double heterojunction. The GO interaction with the NiO also causes its bandgap reduction. We believe that these two factors influence the photocatalytic activity most and enhance the rate constants as compared to those reported in previous literature.

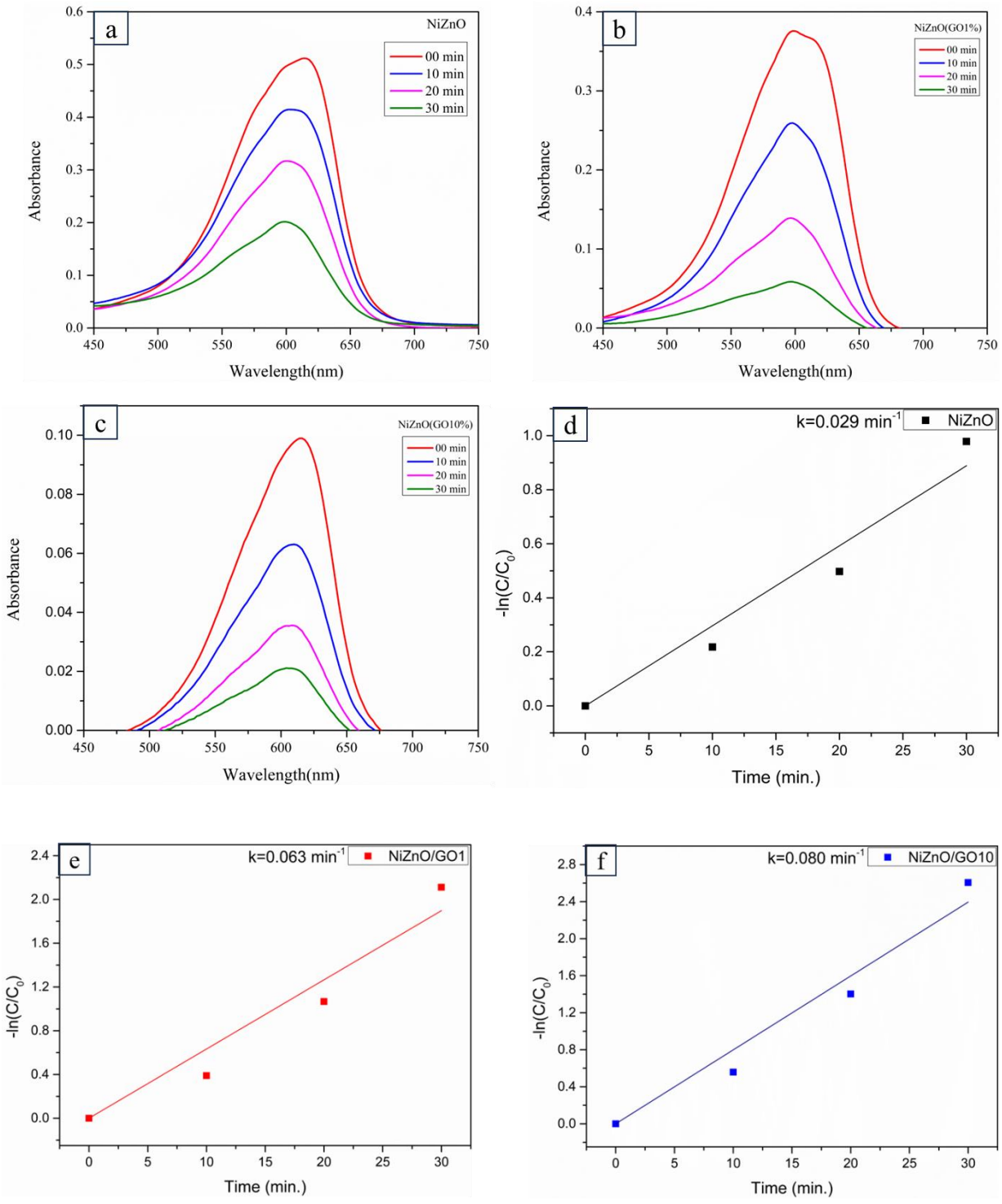

Figure 7.13. UV-Vis of degradation for (a) NiZnO, (b) NiZnO/GO1, and (c) NiZnO/GO10 and pseudo-first-order kinetic fit for the degradation of MB for (d) NiZnO, (e) NiZnO/GO1, and (f) NiZnO/GO10.

Table 7.3. Comparison of degradation kinetics rate constant for different photocatalysts.

Photocatalyst	Irradiation type	Irradiation time (min.)	Rate constant (min^{-1})	Reference
NiZnO	Visible	30	0.029	This work
NiZnO/GO1	Visible	30	0.063	This work
NiZnO/GO10	Visible	30	0.080	This work
NiO	Visible	90	0.00701	[356]
NiO/ZnO	Visible	90	0.00945	[356]
NiO/g-C_3N_4	Visible	90	0.01195	[356]
NiO/ZnO/g-C_3N_4	Visible	90	0.02396	[356]
ZnO	Visible	120	0.03126	[357]
ZnO/graphene	Visible	90	0.056	[140]
ZnO nanorods	UV	30 (UV light)	0.024	[326]
ZnO/GO (3 wt%) nanocomposite	UV	30 (UV light)	0.042	[326]
GO sheets	Visible	100	0.0024	[358]
flower-like ZnO particles	Visible	100	0.0077	[358]
ZnO/GO nanocomposite	Visible	60	0.064	[358]

7.6. Conclusion

This study demonstrates that the incorporation of GO into the NiO/ZnO composite plays an important role in modifying the structural, surface, and interfacial properties of the material. The results show that GO influences the morphology, surface area, functional groups, and band structure, which together affect the overall behavior of the composite. The formation of the hybrid structure improves charge separation and contributes to the observed performance. Therefore, this chapter clearly establishes the structure-activity relationship in the GO-modified NiO/ZnO system and provides a strong basis for understanding its potential in visible-light-driven applications.

CHAPTER 8

Solar-Powered Photocatalytic Reactor

8.1. Abstract

A solar-powered photocatalytic reactor system has been designed to treat wastewater through the synergistic integration of solar energy and oxidation processes. The system comprises a tilted-frame structure supporting an array of horizontally aligned photocatalytic tubes and high-efficiency microreactor modules, powered by a photovoltaic (PV) panel coupled with real-time monitoring and control electronics. Wastewater is continuously circulated through an inlet manifold that distributes flow evenly across multiple parallel channels, each lined with semiconductor photocatalysts (low-cost catalyst in primary tubes and engineered visible-light-active catalysts in secondary microreactors). Upon solar irradiation, photogenerated electron-hole pairs in the catalyst generate reactive oxygen species (OH and O^{2-} radicals) that initiate mineralization of pollutants. The microreactor modules employ ribbed patterned microchannels to maximize the catalyst-water interface, enhance mass transfer, and increase photon utilization through light scattering and refocusing. The PV-powered control system regulates pump operation, flow rate, and pressure via integrated sensors, while optionally augmenting solar radiation with monochromatic UV-LED arrays during low-light periods to maintain consistent photocatalytic activity. This configuration combines the economic benefits of solar-driven treatment with the efficiency of

microscale reactor engineering, enabling rapid and near-complete degradation of contaminants with minimal operational costs. The system is particularly suited for decentralized or remote wastewater treatment applications where grid electricity is unavailable or expensive, and where the modularity of parallel channels allows scalability and customization to varying flow rates and pollutant loads.

8.2. Introduction and main components

Previous chapters introduced the basic research background and identified the need to improve the functional properties of metal oxides for practical applications. The subsequent chapters developed this theme further by examining the synthesis, structural modification, and characterization of $ZnTiO_3$-based systems, including the effect of GO incorporation, Cu doping, DES-assisted modification, Mg doping, and DFT-based electronic analysis. Through these studies, it was established that compositional modification strongly influences crystallinity, morphology, band structure, density of states, and charge transport behavior. These findings collectively provided a clearer understanding of how material design can be used to tailor photocatalytic performance.

Building on this progression, Chapter 8 shifts the focus from material-level investigation to application-oriented design by considering the photoreactor as the next stage of the study. The purpose of this chapter is to translate the insights gained from the previous chapters into a practical reactor framework suitable for photocatalytic use. In this way, Chapter 8 extends the earlier work by using the material properties established in the preceding chapters as the basis for reactor design considerations.

Figure 8.1 shows solar-powered photocatalytic reactor featuring numerous tubular reactors arranged in series for optimal light utilization. Various perspectives (right, bottom, front, top, and left) illustrate the configuration of tubes, microreactor, and support

frame for secure installation. A photovoltaic panel is affixed to the top to provide sustainable electrical energy for pumps and control systems.

Main components of reactor are (Figure 8.2):

(a) Solar PV panel: supplies electrical power (for pump, control, possibly auxiliary LEDs/valves).

(b) Control/monitoring unit: flow, pressure, turbidity/TOC sensor display and control of valves/pump.

(c) Cylindrical tubes: inlet distribution and outlet collection headers; they distribute the incoming wastewater across multiple reaction tubes and then recombine the treated stream.

(d) Horizontal tubes: main photocatalytic reactor tubes where wastewater flows; inner wall are coated with photocatalyst.

(e) Micro reactors: micro reactors that expose wastewater on inner wall coating of highly effective photocatalyst (high cost photocatalyst) over immobilized photocatalyst to sunlight (or serve as additional heat/UV collection stages).

(f) Curved pipes: hydraulic connections between manifolds and reactor modules (inlet/outlet loops, by-pass lines).

(g) Blue frame: mechanical support structure that also fixes the tilt angle toward the sun.

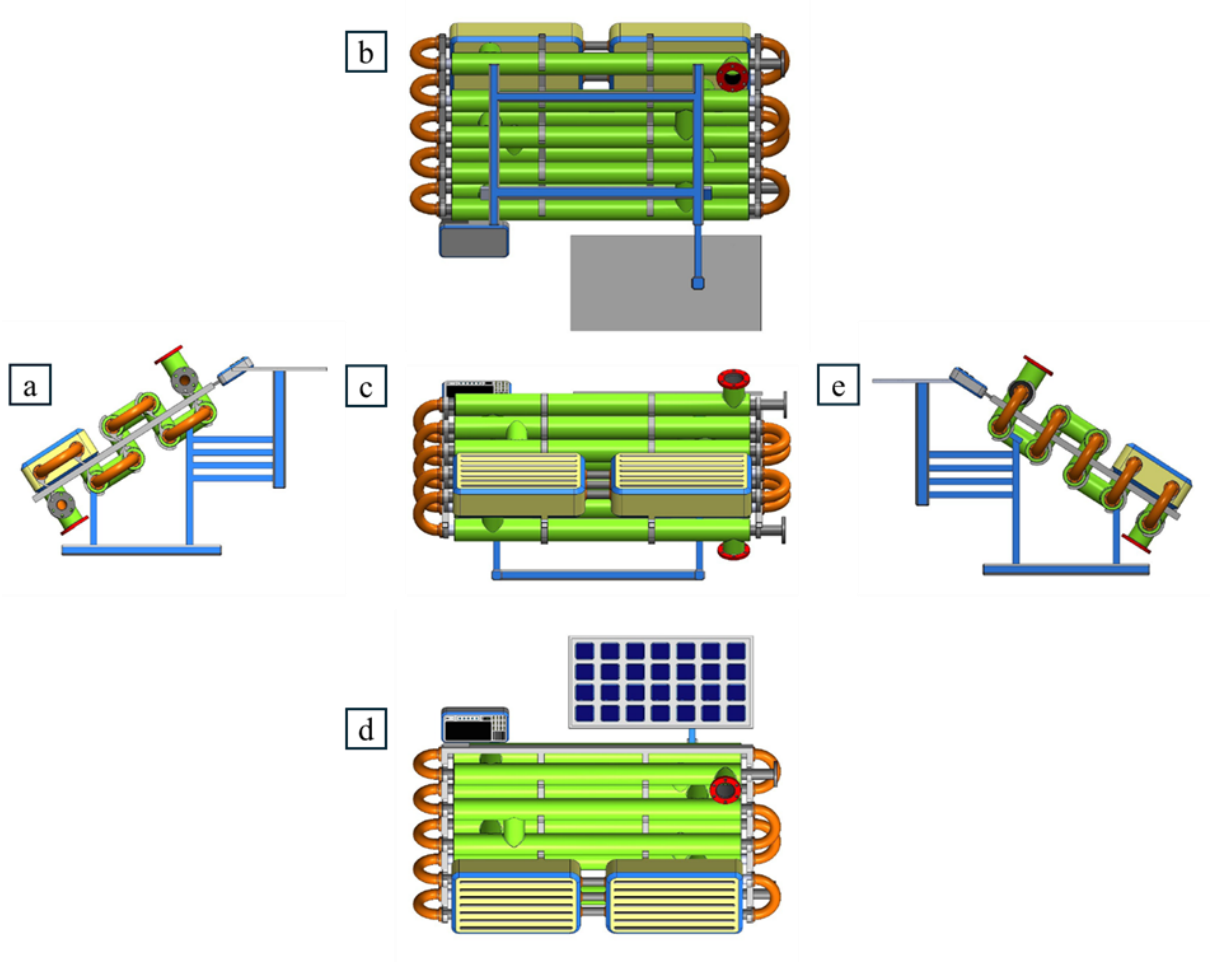

Figure 8.1. Design of Solar-Powered Photocatalytic Reactor (a) Right View, (b) bottom view, (c) front view, (d) top view and (e) left view.

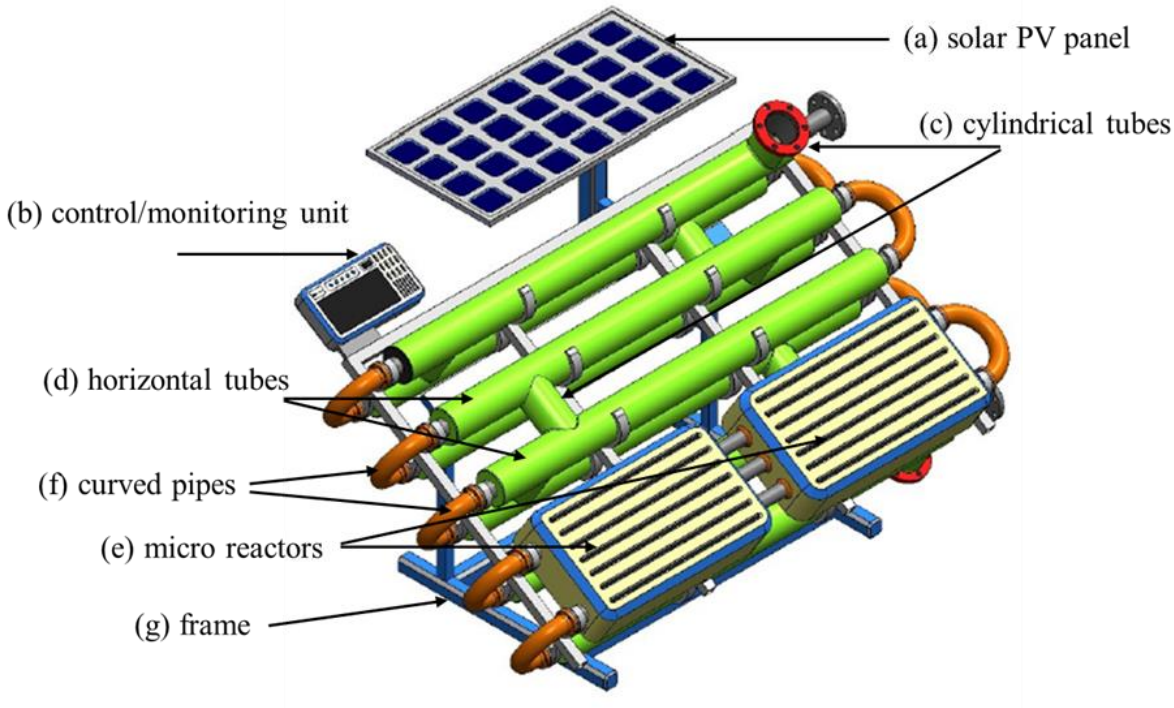

Figure 8.2. Perspective view of photocatalytic reactor.

8.3. System Configuration and Flow Path

The reactor comprises a tilted frame (g) supporting an array of horizontal tubes and microreactor modules, with a solar PV panel (a) mounted to power the system. Wastewater is first drawn into the system by a pump controlled by monitoring unit (b), which regulates flow rate and pressure via sensors and valves. The inlet tube (c) splits the incoming flow into multiple parallel channels feeding the horizontal tubes (d). Each tube's inner wall is coated with a low-cost semiconductor photocatalyst, and the tubes are aligned along the tilt of the frame to maximize sunlight exposure. After passing through the tubes, the water flows into two ribbed microreactor modules (e) containing a high efficiency photocatalyst. These microreactors consist of many small channels that greatly increase the photocatalytic surface area and induce mixing. The modules interconnect by curved pipes (f) and finally discharge into the outlet, which collects the treated effluent for onward flow. A PV-powered pump (within unit (b)) circulates the wastewater at a

controlled flow rate. Flow and pressure transducers in the inlet feed back to the control unit, which adjusts the pump or valves to maintain steady operation. This distributes the feed evenly into each tube so that each reactor channel receives the same volumetric flow, ensuring uniform residence time and illumination. In each tube, water flows along a transparent channel whose interior is coated with a catalyst film. Sunlight passing through the tube wall activates the catalyst on the inner surface. The distributed parallel-tube geometry effectively creates many microreactors in parallel, dramatically increasing the total catalyst–water interface and causing light to scatter among the channels. The microreactor modules present very high-surface-area photocatalyst in turbulent microchannels. By combining multiple small channels (microreactors), the system multiplies internal boundaries and light-path diversity

Finally, the treated water exits the microreactors and is collected into the outlet manifold, which merges the parallel flows and guides the effluent out of the system. Any remaining solids or catalyst residues are retained by the immobilized catalyst surfaces, avoiding downstream catalyst recovery issues. Throughout the flow path, the control/monitoring unit (b) continuously reads sensors (flow meters, pressure gauges, etc.) and can trigger alarms or adjust actuators if deviations occur. This ensures that the wastewater is distributed and exposed under the designed hydraulic and optical conditions.

The low-cost catalyst coatings in the tubes provide the initial stage of degradation, while the high-efficiency catalyst in the microreactors (often engineered for visible-light activation) drives further breakdown of the remaining pollutants. The large surface-to-volume ratios in the microchannels maximize catalyst-water contact, accelerating the reaction. As noted in similar systems, combining multiple microreactors significantly increases overall photocatalytic area and enhances light utilization and mass transfer, so that nearly complete degradation can occur rapidly within the series of tubes and

microchannels. The primary energy source is solar irradiation. The tilted frame (g) orients the tubes and modules to face the sun, maximizing incident sunlight on the catalyst surfaces.

8.4. Conclusion

This Chapter presents a solar-powered photocatalytic reactor design that connects the material development work of the thesis with a practical wastewater treatment application. The proposed system uses solar energy, photocatalyst-coated reactor elements, and a photovoltaic-assisted flow setup to improve light utilization, mass transfer, and treatment efficiency in a compact configuration.

Overall, this chapter shows that the photocatalysts developed in the thesis are not limited to laboratory testing but can also be considered for real-world remediation systems. The reactor concept is especially suitable for decentralized or off-grid wastewater treatment, and it strengthens the thesis by linking photocatalyst performance with an application-oriented engineering solution.

CHAPTER 9

Conclusions and Future Scope

9.1. Conclusions

In my thesis, I have explored methods to enhance visible light-induced photocatalytic activities in novel graphene oxide and metal oxides composites for removing hazardous chemicals from wastewater. This involved synthesizing and characterizing graphene oxide via modified hummers methods, metal oxide via sol-gel method and composite materials via hydrothermal methods, aiming for visible light-induced photocatalytic dye removal. Graphene oxide and oxide semiconductors composites show promise for environmental remediation due to their ability to release electrons from valence to conduction bands under electromagnetic radiation, triggering chemical reactions. Furthermore, computational methods like DFT method are also used to predict doping can enhance photocatalytic activity of $ZnTiO_3$. This versatility, including tunability of band gaps through doping and various processing methods leading to different morphologies, makes them effective for both photocatalysis and adsorption. Thus, this thesis concludes with the findings summarized in the following chapters:

9.1.1. Chapter 3

ZTO/GO composites with 1% GO were successfully synthesized by ambient mixing in solid and liquid states, and under hydrothermal conditions. XRD and XPS data show that

in all the three cases the GO is reduced to r-GO, but the samples prepared by hydrothermal method yields highest fraction of r-GO. Our characterization data suggest that the presence of GO leads to oxygen loss from the zinc titanate crystals also, which may subsequently cause the formation of Zn_2TiO_4 in samples (composite I (42.98%) and composite II (40.63%)) mixed under ambient conditions due to higher oxygen loss under ambient conditions. This phase transformation is suppressed in hydrothermally mixed samples. XRD data suggests that the hydrothermal mixing also leads to reduced crystallinity, as suggested by the enhanced FWHM of the XRD peaks in the composite III. An inefficient packing of atomic planes in composite III yields materials with the highest surface area among these samples. The specific BET surface area of ZTO, composite I, composite II, and composite III are respectively 1.0 m^2/g, 1.3 m^2/g, 1.3 m^2/g and 1.4 m^2/g, which suggests more active sites in composite III. The bandgaps measured for samples are 2.85 eV for ZTO, 2.81 eV for composite I, 2.59 eV for composite II, and 2.73 eV for composite III. Bandgap reduction is attributed to formation of oxygen vacancies in oxide, and since the composite II prepared by liquid state mixing under ambient conditions is likely to loose maximal oxygen from the lattice, we observe these samples to show smallest bandgap. The slopes of composite II and III showed a lower value in the Mott- Schottky plot, clearly indicating higher donor densities. R_{ct} values of 1081.2 kΩ for composite I, and 1017.5 kΩ for composite II, 49.6 kΩ for ZTO, and a much smaller value of 3.1 kΩ for composite III. The lowest value of R_{ct} in composite III, indicative of the most facile transfer of holes and thereby increased photoactivity, is attributed to better binding of the oxide particles with the r-GO. The analysis of the characterization data suggests that the composite III has a reduction in the band gap due to oxygen vacancies and a change in crystallinity, an increase in specific surface area, the binding of ZTO with the GO sheets, an increase in charge carrier density, and improved

charge transfer resistance. These results introduce a variety of possible applications in the field of photocatalysis.

9.1.2. Chapter 4

A custom-built plasma treatment setup was utilized to treat the sol-gel-synthesized zinc titanate particles using nitrogen plasma, wherein the particles were protected from exposure to the environment by immersing them in a liquid immediately after plasma treatment. This treatment enhanced the physical surface area and introduced oxygen vacancies. These two factors are attributed to the observed enhancement in the photocatalytic degradation performance of plasma-treated $ZnTiO_3$. The kinetic rate constants of plasma-treated $ZnTiO_3$ (PT-$ZnTiO_3$) under LED light irradiation increased by a factor of approximately 1.56 compared to the untreated $ZnTiO_3$.

9.1.3. Chapter 5

We have prepared a DES assisted Cu doped $ZnTiO_3$ and then performed DFT calculation. We prepared DES assisted Cu doping (14% and 28%) and DI assisted Cu doping with 14%. Our characterization data shows no new phases arise in XRD this confirms successful doping of copper which leads to shorten in band gap. DES assisted Cu doping shows particles in nanoscale and peak shift towards higher binding energy due to higher electronegativity of copper than zinc. We use first-principle DFT calculations with the GGA function to investigate the structural, electrical, and optical properties of $ZnTiO_3$ and Cu doped $ZnTiO_3$. The results are also in strong conformity with the experimental values of $ZnTiO_3$. The band structure and density of states have been computed for the unit cell of $ZnTiO_3$. Crucially, the $ZnTiO_3$ with doping exhibits an indirect bandgap. Additionally, the bandgap energy decreases after Cu doping. Overall, the reduced

bandgap and increases in surface area are the factors attributed to enhanced photocatalytic activity.

9.1.4. Chapter 6

This work presents an analysis and discussion of the impact of Mg substitution on the zinc titanate $ZnTiO_3$. We use first-principle DFT calculations with the GGA function to look into the structural and electrical properties of $ZnTiO_3$ and $ZnTiO_3$ that are doped with Mg. The results are also in strong conformity with the experimental values reported in the literature for $ZnTiO_3$. The band structure and partial density of states (PDOS) have been computed for the unit cell of $ZnTiO_3$. Crucially, the $ZnTiO_3$ with doping exhibits a direct electronic structure gap at the K-point, except for when x = 0.167 and 0.333. Additionally, the electronic structure gap energy drops as the concentration of Mg ions increases, except for when x = 0.167. Zinc titanate ($ZnTiO_3$) has an indirect electronic structure gap of 3.11 electron volts (eV) in its band structure, particularly near the M point. Experimental band gap of $ZnTiO_3$ (3.04 eV) agrees well with both the theoretical value (3.11 eV) and the cited literature (~3.1 eV), suggesting the baseline compound is captured reliably. The amounts of Mg substitution utilized are x = 0, 0.167, 0.333, 0.5, and 0.667. Mg substitution with x = 0.333 results in an electronic structure gap value of 1.81 eV with an indirect electronic structure gap. The data indicates that the value of x = 0.333 has a somewhat smaller electronic structure gap with an indirect electronic structure gap. This suggests that doped $ZnTiO_3$ is an appropriate choice for photocatalytic applications.

9.1.5 Chapter 7

In summary, we have prepared a composite of two oxide semiconductors, NiO and ZnO, and GO (with GO varying from 1 wt% to 10 wt%). These components were chosen so that they may form a double heterojunction structure and thereby improve the photocatalytic activity. The composite had NiO nearly twice as much in content as compared to ZnO. Our characterization data, when interpreted in light of the wisdom of previous work, suggest that GO is reduced to r-GO, the carbon from r-GO removes oxygen from NiO, with nickel forming bonds with the residual C=O groups, which shortens the NiO bandgap to visible light energies. This leads to enhanced optical absorption and creation of electron-hole pairs in the NiO part of the composite. Due to work function differences with GO and doping type differences from ZnO, two heterojunctions are proposed to form between GO/NiO and NiO/ZnO. These junctions lead to band-bending after contact formation, creating asymmetric energy barriers for electrons and holes, leading to their efficient separation. Overall, the reduced bandgap and enhanced charge separation are the factors attributed to the enhanced photocatalytic activity observed in our composites. The rate constant with NiZnO/GO1 under visible light irradiation is around 1.76 times greater, and with NiZnO/GO10 is around 2.35 times greater than that of NiZnO. The rate constants in our composites also compare favorably with composites studied earlier. Beyond an optimal graphene oxide (GO) loading, further addition typically decreases photocatalytic activity because excess GO introduces light shielding, aggregation/restacking, and active-site coverage that hinders charge generation and interfacial reactions.

9.1.6 Chapter 8

This chapter talks about the design of solar-powered photocatalytic reactor system that uses advanced microreactor engineering and solar energy to treat wastewater. This design uses cheap catalysts in the main tubes and high-efficiency visible-light-responsive catalysts in the microreactor modules. This makes the process more efficient at breaking down polutants while also lowering costs. The microchannels that run with the main channel speed up the mineralization of pollutants. This scalable, modular design offers a long-lasting, grid-independent solution that is perfect for remote locations and encourages eco-friendly ways to treat water.

9.2 Future Scope

Future studies in photocatalyst development should focus on the rational integration of multi-metal doping strategies to achieve synergistic control over electronic structures and charge carrier dynamics. By incorporating multiple dopants with complementary electronegativity and ionic radii, it becomes possible to modulate the band edge positions, suppress defect-mediated recombination, and enhance visible-light absorption. Such tailored multi-metal systems may unlock superior activity and stability compared to single-doped analogues, providing a pathway toward highly efficient and tunable photocatalysts.

Equally important is the advancement of scalable synthesis techniques. Plasma-assisted fabrication offers a promising route due to its rapid reaction kinetics, reduced thermal budget, and precise control over particle morphology and surface chemistry. Developing robust, continuous plasma processing setups suitable for large-scale production would bridge the current gap between laboratory innovation and industrial implementation of

photocatalytic materials. This direction aligns with the growing demand for economically viable and environmentally sustainable production technologies.

The integration of computational tools with experimental workflows will further accelerate discovery. Machine learning algorithms trained on density functional theory (DFT) datasets can identify patterns and correlations between structural features and photocatalytic performance, allowing predictive screening of new composite materials before synthesis. This data-driven approach could substantially reduce trial-and-error experimentation, enabling more directed material optimization and design.

Finally, expanding the practical application domains of these photocatalysts beyond traditional dye degradation remains crucial. Targeted exploration of solar-driven water splitting, carbon dioxide reduction, and hybrid photovoltaic-photocatalytic systems could advance sustainable energy conversion and environmental remediation technologies. Collectively, these research directions establish a comprehensive framework that integrates rational design principles, scalable manufacturing, and computational prediction for the next generation of visible-light-active photocatalysts.

References

[1] A. S. Kumar, D. P. Pabba, N. R. Reddy, and S. W. Joo, “Emerging photocatalytic systems for environmental and energy applications: A comprehensive review of mechanisms, materials, and future directions,” *J. Alloys Compd.*, vol. 1031, p. 180934, Jun. 2025, doi: 10.1016/J.JALLCOM.2025.180934.

[2] S. Banerjee, S. C. Pillai, P. Falaras, K. E. O’shea, J. A. Byrne, and D. D. Dionysiou, “New insights into the mechanism of visible light photocatalysis,” *Journal of Physical Chemistry Letters*, vol. 5, no. 15, pp. 2543–2554, Aug. 2014, doi: 10.1021/JZ501030X.

[3] F. Mohamadpour and A. M. Amani, “Photocatalytic systems: reactions, mechanism, and applications,” *RSC Adv.*, vol. 14, no. 29, pp. 20609–20645, Jul. 2024, doi: 10.1039/D4RA03259D.

[4] I. Abdelfattah and A. M. El-Shamy, “A comparative study for optimizing photocatalytic activity of TiO2-based composites with ZrO2, ZnO, Ta2O5, SnO, Fe2O3, and CuO additives,” *Sci. Rep.*, vol. 14, no. 1, pp. 1–26, Dec. 2024, doi: 10.1038/S41598-024-77752-5.

[5] C. B. Anucha, I. Altin, E. Bacaksiz, and V. N. Stathopoulos, “Titanium dioxide (TiO_2)-based photocatalyst materials activity enhancement for contaminants of emerging concern (CECs) degradation: In the light of modification strategies,” *Chemical Engineering Journal Advances*, vol. 10, p. 100262, May 2022, doi: 10.1016/J.CEJA.2022.100262.

[6] T. A. Khattab, M. S. Abdelrahman, and M. Rehan, “Textile dyeing industry: environmental impacts and remediation,” *Environmental Science and Pollution Research*, vol. 27, no. 4, pp. 3803–3818, Feb. 2020, doi: 10.1007/S11356-019-07137-Z.

[7] R. Ahmad, J. Guo, and J. Kim, “Structural characteristics of hazardous organic dyes and relationship between membrane fouling and organic removal efficiency in fluidized ceramic membrane reactor,” *J. Clean. Prod.*, vol. 232, pp. 608–616, Sep. 2019, doi: 10.1016/J.JCLEPRO.2019.05.244.

[8] B. A. Berehe *et al.*, “Enhanced photocatalytic degradation of methylene blue dye via valorization of a polyethylene terephthalate plastic waste-derived metal–organic framework-based ZnO@Co-BDC composite catalyst,” *Nanoscale Adv.*, vol. 7, no. 12, pp. 3834–3845, Jun. 2025, doi: 10.1039/D4NA01071J.

[9] Z. Kalaycıoğlu, B. Özuğur Uysal, Ö. Pekcan, and F. B. Erim, “Efficient Photocatalytic Degradation of Methylene Blue Dye from Aqueous Solution with Cerium Oxide Nanoparticles and Graphene Oxide-Doped Polyacrylamide,” *ACS*

Omega, vol. 8, no. 14, pp. 13004–13015, Apr. 2023, doi: 10.1021/ACSOMEGA.3C00198.

[10] S. Du and F. Zhang, "General applications of density functional theory in photocatalysis," *Chinese Journal of Catalysis*, vol. 61, pp. 1–36, Jun. 2024, doi: 10.1016/S1872-2067(24)60006-9.

[11] R. Gan *et al.*, "Machine learning and DFT-assisted design of A2B2X6 2D materials for photocatalytic CO2 reduction," *Mater. Today Commun.*, vol. 44, p. 112016, Mar. 2025, doi: 10.1016/J.MTCOMM.2025.112016.

[12] N. Baig, I. Kammakakam, W. Falath, and I. Kammakakam, "Nanomaterials: a review of synthesis methods, properties, recent progress, and challenges," *Mater. Adv.*, vol. 2, no. 6, pp. 1821–1871, Mar. 2021, doi: 10.1039/D0MA00807A.

[13] B. Blandón-González, A. F. Trompeta, and P. Mercader-Moyano, "Advanced materials: Introduction to nanotechnology," *Life Cycle Analysis Based on Nanoparticles Applied to the Construction Industry: A Comprehensive Curriculum*, pp. 59–74, Mar. 2025, doi: 10.1007/978-3-031-79115-4_4.

[14] P. M. Rajaitha *et al.*, "Unraveling highly efficient nanomaterial photocatalyst for pollutant removal: a comprehensive review and future progress," *Mater. Today Chem.*, vol. 23, p. 100692, Mar. 2022, doi: 10.1016/J.MTCHEM.2021.100692.

[15] M. B. Tahir, M. Sohaib, M. Sagir, and M. Rafique, "Role of Nanotechnology in Photocatalysis," *Encyclopedia of Smart Materials*, pp. 578–589, Jan. 2022, doi: 10.1016/B978-0-12-815732-9.00006-1.

[16] M. Baalousha, W. How, E. Valsami-Jones, and J. R. Lead, "Overview of Environmental Nanoscience," *Frontiers of Nanoscience*, vol. 7, pp. 1–54, Jan. 2014, doi: 10.1016/B978-0-08-099408-6.00001-3.

[17] M. H. Miah, M. U. Khandaker, M. B. Rahman, M. Nur-E-Alam, and M. A. Islam, "Band gap tuning of perovskite solar cells for enhancing the efficiency and stability: issues and prospects," *RSC Adv.*, vol. 14, no. 23, pp. 15876–15906, May 2024, doi: 10.1039/D4RA01640H.

[18] N. Abid *et al.*, "Synthesis of nanomaterials using various top-down and bottom-up approaches, influencing factors, advantages, and disadvantages: A review," *Adv. Colloid Interface Sci.*, vol. 300, p. 102597, Feb. 2022, doi: 10.1016/J.CIS.2021.102597.

[19] J. Abraham, R. Arunima, K. C. Nimitha, S. C. George, and S. Thomas, "One-dimensional (1D) nanomaterials: Nanorods and nanowires; nanoscale processing," *Nanoscale Processing*, pp. 71–101, Jan. 2021, doi: 10.1016/B978-0-12-820569-3.00003-7.

[20] Shreya, P. Phogat, R. Jha, and S. Singh, "Emerging advances and future prospects of two dimensional nanomaterials based solar cells," *J. Alloys Compd.*, vol. 1001, p. 175063, Oct. 2024, doi: 10.1016/J.JALLCOM.2024.175063.

[21] C. Verma, E. Berdimurodov, D. K. Verma, K. Berdimuradov, A. Alfantazi, and C. M. Hussain, "3D Nanomaterials: The future of industrial, biological, and environmental applications," *Inorg. Chem. Commun.*, vol. 156, p. 111163, Oct. 2023, doi: 10.1016/J.INOCHE.2023.111163.

[22] F. Wan, A. Thakur, and P. Thakur, "Classification of Nanomaterials (Carbon, Metals, Polymers, Bio-ceramics)," *Integrated Nanomaterials and their Applications*, pp. 37–55, Dec. 2023, doi: 10.1007/978-981-99-6105-4_3.

[23] M. Nikshitha, S. M. Sudhakara, and M. S. Shetty, "Organic-inorganic hybrids: A comprehensive review on synthesis and their potential applications," *Mater. Chem. Phys.*, vol. 331, p. 130181, Feb. 2025, doi: 10.1016/J.MATCHEMPHYS.2024.130181.

[24] A. T. Wassie, I. N. Ahmed, A. Bachheti, A. Husen, and R. K. Bachheti, "Role of Zinc Oxide Nanomaterials for Photocatalytic Degradation of Environmental Pollutants," pp. 287–311, 2024, doi: 10.1007/978-981-99-7673-7_14.

[25] K. Li, Y. De Rancourt De Mimérand, X. Jin, J. Yi, and J. Guo, "Metal Oxide (ZnO and TiO2) and Fe-Based Metal-Organic-Framework Nanoparticles on 3D-Printed Fractal Polymer Surfaces for Photocatalytic Degradation of Organic Pollutants," *ACS Appl. Nano Mater.*, vol. 3, no. 3, pp. 2830–2845, Mar. 2020, doi: 10.1021/ACSANM.0C00096.

[26] D. Bokov *et al.*, "Nanomaterial by Sol-Gel Method: Synthesis and Application," *Advances in Materials Science and Engineering*, vol. 2021, no. 1, p. 5102014, Jan. 2021, doi: 10.1155/2021/5102014.

[27] R. B. Kale, Y. J. Hsu, Y. F. Lin, and S. Y. Lu, "Hydrothermal synthesis, characterizations and photoluminescence study of single crystalline hexagonal ZnO nanorods with three dimensional flowerlike microstructures," *Superlattices Microstruct.*, vol. 69, pp. 239–252, May 2014, doi: 10.1016/J.SPMI.2014.03.003.

[28] V. C. A. Ajin and A. J. Lenus, "Engineering the role of oxygen vacancies in photocatalysts for environmental remediation and energy conversion applications: A comprehensive review," *Mater. Sci. Semicond. Process.*, vol. 197, p. 109705, Oct. 2025, doi: 10.1016/J.MSSP.2025.109705.

[29] R. Sahay, V. J. Reddy, and S. Ramakrishna, "Synthesis and applications of multifunctional composite nanomaterials," *International Journal of Mechanical and Materials Engineering*, vol. 9, no. 1, pp. 1–13, Dec. 2014, doi: 10.1186/S40712-014-0025-4.

[30] Mahnoor *et al.*, "A mechanistic overview on green assisted formulation of nanocomposites and their multifunctional role in biomedical applications," *Heliyon*, vol. 11, no. 3, p. e41654, Feb. 2025, doi: 10.1016/J.HELIYON.2025.E41654.

[31] B. Cao *et al.*, "Constructing BiOI/CeO2 p-n heterojunction with enhanced NOx photo-oxidative removal under visible light irradiation," *J. Alloys Compd.*, vol. 934, p. 167962, Feb. 2023, doi: 10.1016/J.JALLCOM.2022.167962.

[32] J. Kistner-Morris *et al.*, "Electric-field tunable Type-I to Type-II band alignment transition in MoSe2/WS2 heterobilayers," *Nature Communications 2024 15:1*, vol. 15, no. 1, pp. 1–7, May 2024, doi: 10.1038/s41467-024-48321-1.

[33] J. Low, S. Cao, J. Yu, and S. Wageh, "Two-dimensional layered composite photocatalysts," *Chemical Communications*, vol. 50, no. 74, pp. 10768–10777, Aug. 2014, doi: 10.1039/C4CC02553A.

[34] K. Chen, W. Dong, Y. Huang, F. Wang, J. L. Zhou, and W. Li, "Photocatalysis for sustainable energy and environmental protection in construction: A review on surface engineering and emerging synthesis," *J. Environ. Chem. Eng.*, vol. 13, no. 5, p. 117529, Oct. 2025, doi: 10.1016/J.JECE.2025.117529.

[35] P. Kumari, S. Chattopadhyay, and S. Samanta, "A comprehensive review on rare earth metal doped ZnS nanoparticles: structure, synthesis, properties, and applications in the realm of nanotechnology," *Discover Applied Sciences 2025 7:9*, vol. 7, no. 9, pp. 1–23, Aug. 2025, doi: 10.1007/S42452-025-07672-0.

[36] A. Tshikovhi, L. F. Koao, T. D. Malevu, E. C. Linganiso, and T. E. Motaung, "Dopants concentration on the properties of various host materials by sol-gel method: Critical review," *Results in Materials*, vol. 19, p. 100447, Sep. 2023, doi: 10.1016/J.RINMA.2023.100447.

[37] R. U. K. Shenoy, A. Rama, I. Govindan, and A. Naha, "The purview of doped nanoparticles: Insights into their biomedical applications," *OpenNano*, vol. 8, p. 100070, Nov. 2022, doi: 10.1016/J.ONANO.2022.100070.

[38] B. Abebe, N. K. Gupta, and D. Tsegaye, "A critical mini-review on doping and heterojunction formation in ZnO-based catalysts," *RSC Adv.*, vol. 14, no. 25, pp. 17338–17349, May 2024, doi: 10.1039/D4RA02568G.

[39] N. H. Alharthi, S. M. Almotairy, H. F. Alharbi, M. Shahinuzzaman, M. Luqman, and K. Sobayel, "Investigation on structural and opto-electronic properties of substitutional Sn doped WS2 by co-sputtering technique," *Journal of Materials Research and Technology*, vol. 15, pp. 846–854, Nov. 2021, doi: 10.1016/J.JMRT.2021.08.075.

[40] Y. Qin, B. Li, C. Zhou, and Y. Bai, "Interstitial/Substitutional Se Doping in Nanosheet Heterostructures for Sensing NH3: Experimental and Theoretical Study," *ACS Appl. Nano Mater.*, vol. 6, no. 20, pp. 19290–19299, Oct. 2023, doi: 10.1021/ACSANM.3C03772.

[41] A. K. De, S. Majumdar, S. Pal, S. Kumar, and I. Sinha, "Zn doping induced band gap widening of Ag2O nanoparticles," *J. Alloys Compd.*, vol. 832, p. 154127, Aug. 2020, doi: 10.1016/J.JALLCOM.2020.154127.

[42] D. P. Dutta, M. Ramakrishnan, M. Roy, and A. Kumar, "Effect of transition metal doping on the photocatalytic properties of FeVO4 nanoparticles," *J. Photochem. Photobiol. A Chem.*, vol. 335, pp. 102–111, Feb. 2017, doi: 10.1016/J.JPHOTOCHEM.2016.11.022.

[43] M. Sultana *et al.*, "Strategic development of metal doped TiO2 photocatalysts for enhanced dye degradation activity under UV–Vis irradiation: A review," *Current Research in Green and Sustainable Chemistry*, vol. 7, p. 100383, Jan. 2023, doi: 10.1016/J.CRGSC.2023.100383.

[44] P. Bouras, E. Stathatos, and P. Lianos, "Pure versus metal-ion-doped nanocrystalline titania for photocatalysis," *Appl. Catal. B*, vol. 73, no. 1–2, pp. 51–59, Apr. 2007, doi: 10.1016/J.APCATB.2006.06.007.

[45] M. A. Ahmed, S. A. Mahmoud, and A. A. Mohamed, "Interfacially engineered metal oxide nanocomposites for enhanced photocatalytic degradation of pollutants and energy applications," *RSC Adv.*, vol. 15, no. 20, pp. 15561–15603, May 2025, doi: 10.1039/D4RA08780A.

[46] Z. Liu, J. Zhang, Y. Lv, X. Zhou, and S. Li, "Impact of non-metal dopants on band-gap engineering and photocatalytic ability of λ-Ta2O5 from a hybrid density functional study," *J. Alloys Compd.*, vol. 700, pp. 1–11, Apr. 2017, doi: 10.1016/J.JALLCOM.2017.01.033.

[47] S. Sahoo, P. Mahamallik, R. Das, and S. Panigrahi, "A critical review on non-metal doped g-C3N4 based photocatalyst for organic pollutant remediation with sustainability assessment by life cycle analysis," *Environ. Res.*, vol. 258, p. 119390, Oct. 2024, doi: 10.1016/J.ENVRES.2024.119390.

[48] P. Basera, S. Saini, E. Arora, A. Singh, M. Kumar, and S. Bhattacharya, "Stability of non-metal dopants to tune the photo-absorption of TiO2 at realistic temperatures and oxygen partial pressures: A hybrid DFT study," *Sci. Rep.*, vol. 9, no. 1, pp. 1–13, Dec. 2019, doi: 10.1038/S41598-019-47710-7.

[49] M. Sajid, "Nanomaterials: types, properties, recent advances, and toxicity concerns," *Curr. Opin. Environ. Sci. Health*, vol. 25, p. 100319, Feb. 2022, doi: 10.1016/J.COESH.2021.100319.

[50] L. A. Kolahalam, I. V. Kasi Viswanath, B. S. Diwakar, B. Govindh, V. Reddy, and Y. L. N. Murthy, "Review on nanomaterials: Synthesis and applications," *Mater. Today Proc.*, vol. 18, pp. 2182–2190, Jan. 2019, doi: 10.1016/J.MATPR.2019.07.371.

[51] B. Mekuye and B. Abera, "Nanomaterials: An overview of synthesis, classification, characterization, and applications," *Nano Select*, vol. 4, no. 8, pp. 486–501, Aug. 2023, doi: 10.1002/NANO.202300038.

[52] B. H. Alshammari *et al.*, "Organic and inorganic nanomaterials: fabrication, properties and applications," *RSC Adv.*, vol. 13, no. 20, pp. 13735–13785, May 2023, doi: 10.1039/D3RA01421E.

[53] O. E. Semonin, J. M. Luther, and M. C. Beard, "Quantum dots for next-generation photovoltaics," *Materials Today*, vol. 15, no. 11, pp. 508–515, Nov. 2012, doi: 10.1016/S1369-7021(12)70220-1.

[54] R. K. Goyal, S. Maharaj, P. Kumar, and M. Chandrasekhar, "Exploring quantum materials and applications: a review," *Journal of Materials Science: Materials in*

Engineering 2025 20:1, vol. 20, no. 1, pp. 1–38, Jan. 2025, doi: 10.1186/S40712-024-00202-7.

[55] X. Hu *et al.*, "Structural regulation and application of transition metal dichalcogenide monolayers: Progress and challenges," *Coord. Chem. Rev.*, vol. 499, p. 215504, Jan. 2024, doi: 10.1016/J.CCR.2023.215504.

[56] J. Ye *et al.*, "Strongly-confined colloidal lead-halide perovskite quantum dots: from synthesis to applications," *Chem. Soc. Rev.*, vol. 53, no. 16, pp. 8095–8122, Aug. 2024, doi: 10.1039/D4CS00077C.

[57] J. A. Faucheaux, A. L. D. Stanton, and P. K. Jain, "Plasmon resonances of semiconductor nanocrystals: Physical principles and new opportunities," *Journal of Physical Chemistry Letters*, vol. 5, no. 6, pp. 976–985, Mar. 2014, doi: 10.1021/JZ500037K.

[58] A. Sahu and D. Kumar, "Core-shell quantum dots: A review on classification, materials, application, and theoretical modeling," *J. Alloys Compd.*, vol. 924, p. 166508, Nov. 2022, doi: 10.1016/J.JALLCOM.2022.166508.

[59] K. L. Kelly, E. Coronado, L. L. Zhao, and G. C. Schatz, "The optical properties of metal nanoparticles: The influence of size, shape, and dielectric environment," *Journal of Physical Chemistry B*, vol. 107, no. 3, pp. 668–677, Jan. 2003, doi: 10.1021/JP026731Y.

[60] M. Karmaoui *et al.*, "One-Step Synthesis, Structure, and Band Gap Properties of SnO2 Nanoparticles Made by a Low Temperature Nonaqueous Sol-Gel Technique," *ACS Omega*, vol. 3, no. 10, pp. 13227–13238, Oct. 2018, doi: 10.1021/ACSOMEGA.8B02122.

[61] A. D. Walter *et al.*, "Concentration-Dependent Control of the Band Gap Energy of a Low-Dimensional Lepidocrocite Titanate," *ACS Nano*, vol. 19, no. 4, pp. 4855–4866, Feb. 2025, doi: 10.1021/ACSNANO.4C16410.

[62] A. Qadoos, M. Rashid, M. N. Naeem, Z. Jiang, M. Moin, and M. Babar, "Bandgap engineering in graphene oxide (GO) via integrating DFT calculations with atmospheric-pressure microplasma (AMP) treatment for optoelectronic applications," *Hybrid Advances*, vol. 8, p. 100353, Mar. 2025, doi: 10.1016/J.HYBADV.2024.100353.

[63] A. Amirjani, N. B. Amlashi, and Z. S. Ahmadiani, "Plasmon-Enhanced Photocatalysis Based on Plasmonic Nanoparticles for Energy and Environmental Solutions: A Review," *ACS Appl. Nano Mater.*, vol. 6, no. 11, pp. 9085–9123, Jun. 2023, doi: 10.1021/ACSANM.3C01671.

[64] W. He *et al.*, "Localized surface plasmon resonance effect of bismuth nanoparticles in Bi/TiO2 catalysts for boosting visible light-driven CO2 reduction to CH4," *Applied Catalysis B: Environment and Energy*, vol. 344, p. 123651, May 2024, doi: 10.1016/J.APCATB.2023.123651.

[65] O. Gohar *et al.*, “Nanomaterials for advanced energy applications: Recent advancements and future trends,” *Mater. Des.*, vol. 241, p. 112930, May 2024, doi: 10.1016/J.MATDES.2024.112930.

[66] Q. Li, K. Wu, H. Zhu, Y. Yang, S. He, and T. Lian, “Charge Transfer from Quantum-Confined 0D, 1D, and 2D Nanocrystals,” *Chem. Rev.*, vol. 124, no. 9, pp. 5695–5763, May 2024, doi: 10.1021/ACS.CHEMREV.3C00742.

[67] M. D. Bhatt and J. S. Lee, “Effect of lattice strain on nanomaterials in energy applications: A perspective on experiment and theory,” *Int. J. Hydrogen Energy*, vol. 42, no. 25, pp. 16064–16107, Jun. 2017, doi: 10.1016/J.IJHYDENE.2017.03.142.

[68] M. Rizvi, H. Gerengi, and P. Gupta, “Functionalization of Nanomaterials: Synthesis and Characterization,” *ACS Symposium Series*, vol. 1418, pp. 1–26, Jun. 2022, doi: 10.1021/BK-2022-1418.CH001.

[69] M. A. Mimona *et al.*, “Quantum dot nanomaterials: Empowering advances in optoelectronic devices,” *Chemical Engineering Journal Advances*, vol. 21, p. 100704, Mar. 2025, doi: 10.1016/J.CEJA.2025.100704.

[70] P. Kumari, N. Bahadur, L. Kong, L. A. O’Dell, A. Merenda, and L. F. Dumée, “Engineering Schottky-like and heterojunction materials for enhanced photocatalysis performance – a review,” *Mater. Adv.*, vol. 3, no. 5, pp. 2309–2323, Mar. 2022, doi: 10.1039/D1MA01062J.

[71] M. R. Khan, T. W. Chuan, A. Yousuf, M. N. K. Chowdhury, and C. K. Cheng, “Schottky barrier and surface plasmonic resonance phenomena towards the photocatalytic reaction: study of their mechanisms to enhance photocatalytic activity,” *Catal. Sci. Technol.*, vol. 5, no. 5, pp. 2522–2531, Apr. 2015, doi: 10.1039/C4CY01545B.

[72] T. Lo Wong, C. Vallés, A. Nasser, and C. Abeykoon, “Effects of boron-nitride-based nanomaterials on the thermal properties of composite organic phase change materials: A state-of-the-art review,” *Renewable and Sustainable Energy Reviews*, vol. 187, p. 113730, Nov. 2023, doi: 10.1016/J.RSER.2023.113730.

[73] Z. Said *et al.*, “Nano-enhanced phase change materials: Fundamentals and applications,” *Prog. Energy Combust. Sci.*, vol. 104, p. 101162, Sep. 2024, doi: 10.1016/J.PECS.2024.101162.

[74] K. Rawat and M. Goyal, “Thermal conductivity dependence on shape and size in nanomaterials,” *Mater. Today Proc.*, vol. 81, no. 2, pp. 1132–1137, Jan. 2023, doi: 10.1016/J.MATPR.2021.04.409.

[75] P. Xiao *et al.*, “Anisotropic Thermal Conductivity of Crystalline Layered SnSe2,” *Nano Lett.*, vol. 21, no. 21, pp. 9172–9179, Nov. 2021, doi: 10.1021/ACS.NANOLETT.1C03018.

[76] T. Zhang *et al.*, “Boosting solar-driven thermal-assisted photocatalytic hydrogen production through device thermal management,” *Int. J. Hydrogen Energy*, vol. 51, pp. 921–934, Jan. 2024, doi: 10.1016/J.IJHYDENE.2023.07.103.

[77] Z. Chen *et al.*, “Extraordinary Thermal Stability and Sinter Resistance of Sub-2 nm Platinum Nanoparticles Anchored to a Carbon Support by Selenium,” *Nano Lett.*, vol. 24, no. 4, pp. 1392–1398, Jan. 2024, doi: 10.1021/ACS.NANOLETT.3C04601.

[78] N. Liang and Y. Zhao, “A review on thermal stability of nanostructured materials,” *J. Alloys Compd.*, vol. 938, p. 168528, Mar. 2023, doi: 10.1016/J.JALLCOM.2022.168528.

[79] U. Chadha *et al.*, “Complex Nanomaterials in Catalysis for Chemically Significant Applications: From Synthesis and Hydrocarbon Processing to Renewable Energy Applications,” *Advances in Materials Science and Engineering*, vol. 2022, no. 1, p. 1552334, Jan. 2022, doi: 10.1155/2022/1552334.

[80] K. Wieszczycka, K. Staszak, M. J. Woźniak-Budych, J. Litowczenko, B. M. Maciejewska, and S. Jurga, “Surface functionalization – The way for advanced applications of smart materials,” *Coord. Chem. Rev.*, vol. 436, p. 213846, Jun. 2021, doi: 10.1016/J.CCR.2021.213846.

[81] R. Yang, Z. Bao, and Y. Sun, “Probing and Leveraging the Structural Heterogeneity of Nanomaterials for Enhanced Catalysis,” *ACS Nanoscience Au*, vol. 3, no. 2, pp. 140–152, Apr. 2023, doi: 10.1021/ACSNANOSCIENCEAU.2C00057.

[82] D. Rosa, G. Manetta, and L. Di Palma, “Experimental assessment of the pH effect and ions on the photocatalytic activity of iron-doped titanium dioxide supported on polystyrene pellets: Batch and continuous tests,” *Chem. Eng. Sci.*, vol. 291, p. 119918, Jun. 2024, doi: 10.1016/J.CES.2024.119918.

[83] M. F. Hanafi and N. Sapawe, “Influence of pH on the photocatalytic degradation of methyl orange using nickel catalyst,” *Mater. Today Proc.*, vol. 31, pp. 339–341, Jan. 2020, doi: 10.1016/J.MATPR.2020.06.094.

[84] M. F. Hanafi and N. Sapawe, “Effect of pH on the photocatalytic degradation of remazol brilliant blue dye using zirconia catalyst,” *Mater. Today Proc.*, vol. 31, pp. 260–262, Jan. 2020, doi: 10.1016/J.MATPR.2020.05.746.

[85] N. Waiskopf *et al.*, “Photocatalytic reactive oxygen species formation by semiconductor-metal hybrid nanoparticles. Toward light-induced modulation of biological processes,” *Nano Lett.*, vol. 16, no. 7, pp. 4266–4273, Jul. 2016, doi: 10.1021/ACS.NANOLETT.6B01298.

[86] M. Sohail *et al.*, “Recent developments, advances and strategies in heterogeneous photocatalysts for water splitting,” *Nanoscale Adv.*, vol. 6, no. 5, pp. 1286–1330, Feb. 2024, doi: 10.1039/D3NA00442B.

[87] H. Sudrajat, D. Lisovytskiy, and J. C. Colmenares, “Improved charge carrier mobility in a copper oxide heterostructure enhances the photocatalytic partial oxidation of benzyl alcohol to benzaldehyde,” *Catal. Sci. Technol.*, vol. 14, no. 23, pp. 6893–6903, Nov. 2024, doi: 10.1039/D4CY00889H.

[88] Q. L. Liu, Z. Y. Zhao, and J. H. Yi, “Effects of crystal structure and composition on the photocatalytic performance of Ta–O–N functional materials,” *Physical*

Chemistry Chemical Physics, vol. 20, no. 17, pp. 12005–12015, May 2018, doi: 10.1039/C8CP00432C.

[89] R. Ghamarpoor, A. Fallah, and M. Jamshidi, "A Review of Synthesis Methods, Modifications, and Mechanisms of ZnO/TiO2-Based Photocatalysts for Photodegradation of Contaminants," *ACS Omega*, vol. 9, no. 24, pp. 25457–25492, Jun. 2024, doi: 10.1021/ACSOMEGA.3C08717.

[90] A. Kramell *et al.*, "Dyes of late Bronze Age textile clothes and accessories from the Yanghai archaeological site, Turfan, China: Determination of the fibers, color analysis and dating," *Quaternary International*, vol. 348, pp. 214–223, Oct. 2014, doi: 10.1016/J.QUAINT.2014.05.012.

[91] Z. C. Koren, "Modern chemistry of the ancient chemical processing of organic dyes and pigments," *ACS Symposium Series*, vol. 1211, pp. 197–217, 2015, doi: 10.1021/BK-2015-1211.CH007.

[92] K. Hübner, "History – 150 Years of mauveine," *Chemie in unserer Zeit*, vol. 40, no. 4, pp. 274–275, Aug. 2006, doi: 10.1002/ciuz.200690054.

[93] E. O. Alegbe and T. O. Uthman, "A review of history, properties, classification, applications and challenges of natural and synthetic dyes," *Heliyon*, vol. 10, no. 13, p. e33646, Jul. 2024, doi: 10.1016/J.HELIYON.2024.E33646.

[94] R. M. Christie, "Reactive dyes for textile fibres," *Colour Chemistry*, pp. 135–147, Mar. 2001, doi: 10.1039/9781847550590-00135.

[95] N. Nipu, L. Wei, J. Thomas, and J. A. Mennigen, "Methylene Blue Is a Widely Used Antifungal Agent That Confounds Behavioral Toxicity Assays in Larval Zebrafish," *Environ. Sci. Technol. Lett.*, vol. 12, no. 2, pp. 130–136, Feb. 2025, doi: 10.1021/ACS.ESTLETT.4C00955.

[96] M. A. Al-Ghouti and R. S. Al-Absi, "Mechanistic understanding of the adsorption and thermodynamic aspects of cationic methylene blue dye onto cellulosic olive stones biomass from wastewater," *Sci. Rep.*, vol. 10, no. 1, pp. 1–18, Dec. 2020, doi: 10.1038/S41598-020-72996-3.

[97] P. O. Oladoye, T. O. Ajiboye, E. O. Omotola, and O. J. Oyewola, "Methylene blue dye: Toxicity and potential elimination technology from wastewater," *Results in Engineering*, vol. 16, p. 100678, Dec. 2022, doi: 10.1016/J.RINENG.2022.100678.

[98] W. M. Kutayli and P. Silberstein, "Methemoglobinemia," *xPharm: The Comprehensive Pharmacology Reference*, pp. 1–5, Jan. 2007, doi: 10.1016/B978-008055232-3.63062-4.

[99] D. Mitoraj *et al.*, "Revisiting the problem of using methylene blue as a model pollutant in photocatalysis: The case of InVO4/BiVO4 composites," *J. Photochem. Photobiol. A Chem.*, vol. 366, pp. 103–110, Nov. 2018, doi: 10.1016/J.JPHOTOCHEM.2018.02.023.

[100] K. chawraba, M. Hamieh, H. Medlej, J. Lalevée, T. Hamieh, and J. Toufaily, "Advancing sustainable photocatalysis: Methylene blue-loaded SBA-15 for efficient pollutant degradation under visible LED light," *Results in Surfaces and Interfaces*, vol. 21, p. 100651, Oct. 2025, doi: 10.1016/J.RSURFI.2025.100651.

[101] "Recent advances on the removal of dyes from wastewater using various adsorbents: a critical review - Materials Advances (RSC Publishing) DOI:10.1039/D1MA00354B." Accessed: Oct. 13, 2025. [Online]. Available: https://pubs.rsc.org/en/content/articlehtml/2021/ma/d1ma00354b

[102] S. Satyam and S. Patra, "Innovations and challenges in adsorption-based wastewater remediation: A comprehensive review," *Heliyon*, vol. 10, no. 9, p. e29573, May 2024, doi: 10.1016/J.HELIYON.2024.E29573.

[103] S. Kainth, P. Sharma, and O. P. Pandey, "Green sorbents from agricultural wastes: A review of sustainable adsorption materials," *Applied Surface Science Advances*, vol. 19, p. 100562, Feb. 2024, doi: 10.1016/J.APSADV.2023.100562.

[104] M. U. Rehman, M. B. Taj, and S. A. C. Carabineiro, "Biogenic adsorbents for removal of drugs and dyes: A comprehensive review on properties, modification and applications," *Chemosphere*, vol. 338, p. 139477, Oct. 2023, doi: 10.1016/J.CHEMOSPHERE.2023.139477.

[105] R. Dewil, D. Mantzavinos, I. Poulios, and M. A. Rodrigo, "New perspectives for Advanced Oxidation Processes," *J. Environ. Manage.*, vol. 195, pp. 93–99, Jun. 2017, doi: 10.1016/J.JENVMAN.2017.04.010.

[106] A. S. Belousov *et al.*, "Environmental application of versatile Bi-based perovskite photocatalysts and their Z-scheme and S-scheme heterojunctions," *J. Environ. Chem. Eng.*, vol. 12, no. 5, p. 113309, Oct. 2024, doi: 10.1016/J.JECE.2024.113309.

[107] M. A. Hassaan, M. A. El-Nemr, M. R. Elkatory, S. Ragab, V. C. Niculescu, and A. El Nemr, "Principles of Photocatalysts and Their Different Applications: A Review," *Top. Curr. Chem.*, vol. 381, no. 6, pp. 1–54, Dec. 2023, doi: 10.1007/S41061-023-00444-7.

[108] A. Sreedhar *et al.*, "Green-synthesized metal oxide nanostructures for solar-driven photocatalysis: Advances, challenges, and environmental applications," *J. Alloys Compd.*, vol. 1036, p. 182080, Jul. 2025, doi: 10.1016/J.JALLCOM.2025.182080.

[109] M. R. Hoffmann, S. T. Martin, W. Choi, and D. W. Bahnemann, "Environmental Applications of Semiconductor Photocatalysis," *Chem. Rev.*, vol. 95, no. 1, pp. 69–96, 1995, doi: 10.1021/CR00033A004/ASSET/CR00033A004.FP.PNG_V03.

[110] M. I. Din, R. Khalid, J. Najeeb, and Z. Hussain, "Fundamentals and photocatalysis of methylene blue dye using various nanocatalytic assemblies- a critical review," *J. Clean. Prod.*, vol. 298, p. 126567, May 2021, doi: 10.1016/J.JCLEPRO.2021.126567.

[111] R. Mohammadzadeh Kakhki, “Beyond photosynthesis: Engineering self-healing photocatalytic systems for sustainability,” *Colloid Interface Sci. Commun.*, vol. 67, p. 100842, Jul. 2025, doi: 10.1016/J.COLCOM.2025.100842.

[112] A. Chakravorty and S. Roy, “A review of photocatalysis, basic principles, processes, and materials,” *Sustainable Chemistry for the Environment*, vol. 8, p. 100155, Dec. 2024, doi: 10.1016/J.SCENV.2024.100155.

[113] S. Ashu Abey, N. M. Reis, E. A. C. Emanuelsson, and A. J. Expósito, “Harnessing visible light: Advanced photocatalytic strategies for sustainable environmental reactions,” *Chemical Engineering Journal*, vol. 519, p. 164951, Sep. 2025, doi: 10.1016/J.CEJ.2025.164951.

[114] T. Wang *et al.*, “A new mechanism for visible light photocatalysis: generation of intraband by adsorbed organic compounds with wide-bandgap semiconductors,” *Environ. Sci. Nano*, vol. 11, no. 6, pp. 2415–2427, Jun. 2024, doi: 10.1039/D4EN00151F.

[115] A. Balapure, J. Ray Dutta, and R. Ganesan, “Recent advances in semiconductor heterojunctions: a detailed review of the fundamentals of photocatalysis, charge transfer mechanism and materials,” *RSC Applied Interfaces*, vol. 1, no. 1, pp. 43–69, Jan. 2024, doi: 10.1039/D3LF00126A.

[116] H. Dhila, A. Bhapkar, and S. Bhame, “Metal oxide/biochar hybrid nanocomposites for adsorption and photocatalytic degradation of textile dye effluents: A review,” *Desalination Water Treat.*, vol. 321, p. 101004, Jan. 2025, doi: 10.1016/J.DWT.2025.101004.

[117] R. Fatima, M. F. Warsi, S. Zulfiqar, S. A. Ragab, I. Shakir, and M. I. Sarwar, “Nanocrystalline transition metal oxides and their composites with reduced graphene oxide and carbon nanotubes for photocatalytic applications,” *Ceram. Int.*, vol. 46, no. 10, pp. 16480–16492, Jul. 2020, doi: 10.1016/J.CERAMINT.2020.03.213.

[118] H. He, “Metal oxide semiconductors and conductors,” *Solution Processed Metal Oxide Thin Films for Electronic Applications*, pp. 7–30, Jan. 2020, doi: 10.1016/B978-0-12-814930-0.00002-5.

[119] S. K. Pandey, V. Amoli, and A. Ranjan, “Synthesis and characterization of zinc titanate-graphene oxide composites prepared under ambient and hydrothermal conditions,” *Solid State Sci.*, vol. 166, p. 107969, Aug. 2025, doi: 10.1016/J.SOLIDSTATESCIENCES.2025.107969.

[120] Y. Yadawa, A. Verma, S. K. Pandey, and A. Ranjan, “PVP assisted sol-electrospraying, unlike sol electrospinning, yields highly pure rhombohedral zinc titanate particles that reduce 4-nitrophenol under visible light,” *J. Alloys Compd.*, vol. 981, p. 173618, Apr. 2024, doi: 10.1016/J.JALLCOM.2024.173618.

[121] E. E. El-Katori, E. A. Kasim, and D. A. Ali, “Sol–gel synthesis of mesoporous NiO/ZnO heterostructure nanocomposite for photocatalytic and anticorrosive

applications in aqueous media," *Colloids Surf. A Physicochem. Eng. Asp.*, vol. 636, p. 128153, Mar. 2022, doi: 10.1016/J.COLSURFA.2021.128153.

[122] K. H. Reddy, S. Martha, and K. M. Parida, "Fabrication of Novel p-BiOI/n-ZnTiO3 Heterojunction for Degradation of Rhodamine 6G under Visible Light Irradiation," *Inorg. Chem.*, vol. 52, no. 11, pp. 6390–6401, Jun. 2013, doi: 10.1021/IC400159M.

[123] F. H. DULlN and D. E. RASE, "Phase Equilibria in the System ZnO—TiO2," *Journal of the American Ceramic Society*, vol. 43, no. 3, pp. 125–131, Mar. 1960, doi: 10.1111/J.1151-2916.1960.TB14326.X.

[124] S. F. BARTRAM and R. A. SLEPETYS, "Compound Formation and Crystal Structure in the System ZnO-TiO2," *Journal of the American Ceramic Society*, vol. 44, no. 10, pp. 493–499, Oct. 1961, doi: 10.1111/J.1151-2916.1961.TB13712.X.

[125] O. Yamaguchi, M. Morimi, H. Kawabata, and K. Shimizu, "Formation and Transformation of ZnTiO3," *Journal of the American Ceramic Society*, vol. 70, no. 5, p. C-97-C-98, May 1987, doi: 10.1111/J.1151-2916.1987.TB05011.X.

[126] J. Li *et al.*, "Synthesis and characterization of rGO decorated cubic ZnTiO3 rods for solar light-induced photodegradation of rhodamine B," *New Journal of Chemistry*, vol. 43, no. 8, pp. 3374–3382, Feb. 2019, doi: 10.1039/C8NJ01971A.

[127] J. Lee, Y. Kang, and I. H. Jung, "Key phase diagram experiment of the ZnO-SnO2 system and thermodynamic modeling of the ZnO-SnO2-TiO2 system," *Physics and Chemistry of Minerals 2025 52:1*, vol. 52, no. 1, pp. 4-, Jan. 2025, doi: 10.1007/S00269-024-01308-2.

[128] E. G. Rini *et al.*, "Correlation of octahedral distortion with vibrational and electronic properties of LaFe1-xTixO3 nanoparticles," *J. Alloys Compd.*, vol. 830, p. 154594, Jul. 2020, doi: 10.1016/J.JALLCOM.2020.154594.

[129] A. Bouzaid, Y. Ziat, H. Belkhanchi, and H. Fatihi, "Boosting the photocatalytic hydrogen production via the S/Zr co-doping in a CaTiO3 perovskite: first-principles study of the optoelectronic, thermodynamic, and photocatalytic," *The European Physical Journal B 2025 98:7*, vol. 98, no. 7, pp. 1–19, Jul. 2025, doi: 10.1140/EPJB/S10051-025-01004-2.

[130] Z. Chen *et al.*, "ZnO/NiO heterostructures with enhanced photocatalytic activity obtained by ultrasonic spraying of a NiO shell onto ZnO nanorods," *Colloids Surf. A Physicochem. Eng. Asp.*, vol. 648, p. 129366, Sep. 2022, doi: 10.1016/J.COLSURFA.2022.129366.

[131] F. Khan, M. S. Khan, S. Kamal, M. Arshad, S. I. Ahmad, and S. A. A. Nami, "Recent advances in graphene oxide and reduced graphene oxide based nanocomposites for the photodegradation of dyes," *J. Mater. Chem. C Mater.*, vol. 8, no. 45, pp. 15940–15955, Nov. 2020, doi: 10.1039/D0TC03684F.

[132] M. Lundie, Ž. Šljivančanin, and S. Tomić, "Electronic and optical properties of reduced graphene oxide," *J. Mater. Chem. C Mater.*, vol. 3, no. 29, pp. 7632–7641, Jul. 2015, doi: 10.1039/C5TC00437C.

[133] U. A. Méndez-Romero, S. A. Pérez-García, X. Xu, E. Wang, and L. Licea-Jiménez, "Functionalized reduced graphene oxide with tunable band gap and good solubility in organic solvents," *Carbon N. Y.*, vol. 146, pp. 491–502, May 2019, doi: 10.1016/J.CARBON.2019.02.023.

[134] X. Chen, Z. Qu, Z. Liu, and G. Ren, "Mechanism of Oxidization of Graphite to Graphene Oxide by the Hummers Method," *ACS Omega*, vol. 7, no. 27, pp. 23503–23510, Jul. 2022, doi: 10.1021/ACSOMEGA.2C01963.

[135] N. Sharma, M. Arif, S. Monga, M. Shkir, Y. K. Mishra, and A. Singh, "Investigation of bandgap alteration in graphene oxide with different reduction routes," *Appl. Surf. Sci.*, vol. 513, p. 145396, May 2020, doi: 10.1016/J.APSUSC.2020.145396.

[136] R. Kaveh and H. Alijani, "An overview: recent development of semiconductor/graphene nanocomposites for photodegradation of phenol and phenolic compounds in aqueous solution," *Journal of Asian Ceramic Societies*, vol. 9, no. 1, pp. 343–365, Jan. 2021, doi: 10.1080/21870764.2020.1868385.

[137] N. T. Padmanabhan *et al.*, "Graphene coupled TiO2 photocatalysts for environmental applications: A review," *Chemosphere*, vol. 271, p. 129506, May 2021, doi: 10.1016/j.chemosphere.2020.129506.

[138] L. Yu, L. Wang, X. Sun, and D. Ye, "Enhanced photocatalytic activity of rGO/TiO2 for the decomposition of formaldehyde under visible light irradiation," *Journal of Environmental Sciences*, vol. 73, pp. 138–146, Nov. 2018, doi: 10.1016/J.JES.2018.01.022.

[139] S. Ameen, M. Shaheer Akhtar, H. K. Seo, and H. Shik Shin, "Advanced ZnO-graphene oxide nanohybrid and its photocatalytic Applications," *Mater. Lett.*, vol. 100, pp. 261–265, 2013, doi: 10.1016/j.matlet.2013.03.012.

[140] M. Ahmad *et al.*, "A facile one-step approach to synthesizing ZnO/graphene composites for enhanced degradation of methylene blue under visible light," *Appl. Surf. Sci.*, vol. 274, pp. 273–281, Jun. 2013, doi: 10.1016/j.apsusc.2013.03.035.

[141] K. Qi, B. Cheng, J. Yu, and W. Ho, "Review on the improvement of the photocatalytic and antibacterial activities of ZnO," Dec. 15, 2017, *Elsevier Ltd*. doi: 10.1016/j.jallcom.2017.08.142.

[142] A. Kiran *et al.*, "Green synthesis of NiO and NiO@graphene oxide nanomaterials using Elettaria cardamomum leaves: Structural and electrochemical studies," *Heliyon*, vol. 10, no. 20, Oct. 2024, doi: 10.1016/j.heliyon.2024.e38613.

[143] J. Ahmad, K. Majid, and M. A. Dar, "Controlled synthesis of p-type NiO/n-type GO nanocomposite with enhanced photocatalytic activity and study of temperature effect on the photocatalytic activity of the nanocomposite," *Appl. Surf. Sci.*, vol. 457, pp. 417–426, Nov. 2018, doi: 10.1016/J.APSUSC.2018.06.200.

[144] A. K. M. Hasan *et al.*, "Optoelectronic properties of electron beam-deposited NiOx thin films for solar cell application," *Results Phys.*, vol. 17, Jun. 2020, doi: 10.1016/j.rinp.2020.103122.

[145] V. Butera, “Density functional theory methods applied to homogeneous and heterogeneous catalysis: a short review and a practical user guide,” *Physical Chemistry Chemical Physics*, vol. 26, no. 10, pp. 7950–7970, Mar. 2024, doi: 10.1039/D4CP00266K.

[146] E. V. Ludeña, D. Arroyo, E. X. Salazar, and J. Vallejo, “The Kinetic Energy Pauli Enhancement Factor and Its Role in Determining the Shell Structure of Atoms and Molecules,” *Advances in Quantum Chemistry*, vol. 76, pp. 59–78, Jan. 2018, doi: 10.1016/BS.AIQ.2017.05.002.

[147] M. A. Lahmer, “Effect of doping with sulfur atoms on the electronic and photocatalytic properties of the ZnO(10$\bar{1}$0) surface: A DFT+U study,” *Computational Condensed Matter*, vol. 31, p. e00654, Jun. 2022, doi: 10.1016/J.COCOM.2022.E00654.

[148] K. Qi *et al.*, “Transition metal doped ZnO nanoparticles with enhanced photocatalytic and antibacterial performances: Experimental and DFT studies,” *Ceram. Int.*, vol. 46, no. 2, pp. 1494–1502, Feb. 2020, doi: 10.1016/J.CERAMINT.2019.09.116.

[149] K. R. Stoltz *et al.*, “Optimization of the U parameter in CoO groupings in ZnO (10$\bar{1}$0) and (11$\bar{2}$0) surfaces: A DFT+U and UPS study,” *Comput. Mater. Sci.*, vol. 198, Oct. 2021, doi: 10.1016/j.commatsci.2021.110700.

[150] N. Mushahary, A. Sarkar, F. Basumatary, S. Brahma, B. Das, and S. Basumatary, “Recent developments on graphene oxide and its composite materials: From fundamentals to applications in biodiesel synthesis, adsorption, photocatalysis, supercapacitors, sensors and antimicrobial activity,” *Results in Surfaces and Interfaces*, vol. 15, p. 100225, May 2024, doi: 10.1016/J.RSURFI.2024.100225.

[151] S. Sepeur, “Nanotechnology: Technical Basics and Applications,” p. 168, 2008, Accessed: Dec. 06, 2025. [Online]. Available: https://books.google.com/books/about/Nanotechnology.html?id=ZIBuXbgSPMoC

[152] J. Livage and D. Ganguli, “Sol–gel electrochromic coatings and devices: A review,” *Solar Energy Materials and Solar Cells*, vol. 68, no. 3–4, pp. 365–381, Jun. 2001, doi: 10.1016/S0927-0248(00)00369-X.

[153] J. Livage, M. Henry, and C. Sanchez, “Sol-gel chemistry of transition metal oxides,” *Progress in Solid State Chemistry*, vol. 18, no. 4, pp. 259–341, Jan. 1988, doi: 10.1016/0079-6786(88)90005-2.

[154] L. L. Hench and J. K. West, “The sol-gel process,” *Chem. Rev.*, vol. 90, no. 1, pp. 33–72, Jan. 2002, doi: 10.1021/CR00099A003.

[155] J. Livage, “Basic Principles of Sol-Gel Chemistry,” *Sol-Gel Technologies for Glass Producers and Users*, pp. 3–14, 2004, doi: 10.1007/978-0-387-88953-5_1.

[156] M. A. Meyers, A. Mishra, and D. J. Benson, “Mechanical properties of nanocrystalline materials,” *Prog. Mater. Sci.*, vol. 51, no. 4, pp. 427–556, May 2006, doi: 10.1016/J.PMATSCI.2005.08.003.

[157] K. N. Thakkar, S. S. Mhatre, and R. Y. Parikh, “Biological synthesis of metallic nanoparticles,” *Nanomedicine*, vol. 6, no. 2, pp. 257–262, Apr. 2010, doi: 10.1016/J.NANO.2009.07.002.

[158] C. M. Russo and W. G. Brose, “LA DOULEUR CHRONIQUE Cathy M. Russo, MD, et William G. Brose, MD,” no. 1, pp. 123–133, 1998, Accessed: Dec. 06, 2025. [Online]. Available: https://books.google.com/books/about/Elements_of_X_ray_Diffraction.html?id=XJVCgGFTODMC

[159] W. L. Bragg, “The diffraction of short electromagnetic Waves by a Crystal,” 1929. Accessed: Dec. 06, 2025. [Online]. Available: https://philpapers.org/rec/BRATDO-17

[160] D. J. Stokes, “Principles and Practice of Variable Pressure/Environmental Scanning Electron Microscopy (VP-ESEM),” *Principles and Practice of Variable Pressure/Environmental Scanning Electron Microscopy (VP-ESEM)*, pp. 1–221, Nov. 2008, doi: 10.1002/9780470758731.

[161] S. K. Kulkarni, “Nanotechnology: Principles and Practices, Third Edition,” *Nanotechnology: Principles and Practices, Third Edition*, pp. 1–403, Jan. 2014, doi: 10.1007/978-3-319-09171-6.

[162] S. Mourdikoudis, R. M. Pallares, and N. T. K. Thanh, “Characterization techniques for nanoparticles: comparison and complementarity upon studying nanoparticle properties,” *Nanoscale*, vol. 10, no. 27, pp. 12871–12934, Jul. 2018, doi: 10.1039/C8NR02278J.

[163] M. A. Isaacs *et al.*, “Advanced XPS characterization: XPS-based multi-technique analyses for comprehensive understanding of functional materials,” *Mater. Chem. Front.*, vol. 5, no. 22, pp. 7931–7963, Nov. 2021, doi: 10.1039/D1QM00969A.

[164] D. W. Ball, “Modern Spectroscopy, 4th ed. J. Michael Hollas. New York: John Wiley & Sons, Inc., 2004, 428 pp., $45.00, paperback. ISBN 0-470-84416-7.,” *Clin. Chem.*, vol. 50, no. 12, pp. 2469–2470, Dec. 2004, doi: 10.1373/CLINCHEM.2004.033902.

[165] H. Kisch, “Semiconductor Photocatalysis: Principles and Applications,” *Semiconductor Photocatalysis: Principles and Applications*, vol. 9783527335534, pp. 1–249, Apr. 2015, doi: 10.1002/9783527673315.

[166] A. A. Valeeva *et al.*, “Nonstoichiometric titanium dioxide nanotubes with enhanced catalytical activity under visible light,” *Scientific Reports 2018 8:1*, vol. 8, no. 1, pp. 9607-, Jun. 2018, doi: 10.1038/s41598-018-28045-1.

[167] S. Brunauer, P. H. Emmett, and E. Teller, “Adsorption of Gases in Multimolecular Layers,” *J. Am. Chem. Soc.*, vol. 60, no. 2, pp. 309–319, Feb. 2002, doi: 10.1021/JA01269A023.

[168] S. Brunauer, L. S. Deming, W. E. Deming, and E. Teller, “On a Theory of the van der Waals Adsorption of Gases,” *J. Am. Chem. Soc.*, vol. 62, no. 7, pp. 1723–1732, Jul. 2002, doi: 10.1021/JA01864A025.

[169] M. Thommes *et al.*, “Physisorption of gases, with special reference to the evaluation of surface area and pore size distribution (IUPAC Technical Report),” *Pure and Applied Chemistry*, vol. 87, no. 9–10, pp. 1051–1069, Oct. 2015, doi: 10.1515/PAC-2014-1117/XML.

[170] A. Hernández-Ramírez and I. Medina-Ramírez, “Photocatalytic semiconductors: Synthesis, characterization, and environmental applications,” *Photocatalytic Semiconductors: Synthesis, Characterization, and Environmental Applications*, pp. 1–289, Jan. 2015, doi: 10.1007/978-3-319-10999-2.

[171] S. Bhattacharjee, “DLS and zeta potential – What they are and what they are not?,” *Journal of Controlled Release*, vol. 235, pp. 337–351, Aug. 2016, doi: 10.1016/J.JCONREL.2016.06.017.

[172] J. Huang, Z. Li, B. Y. Liaw, and J. Zhang, “Graphical analysis of electrochemical impedance spectroscopy data in Bode and Nyquist representations,” *J. Power Sources*, vol. 309, pp. 82–98, Mar. 2016, doi: 10.1016/J.JPOWSOUR.2016.01.073.

[173] J. Wang and C. Zhu, “Visible-light photocatalyst design,” *Chem Catalysis*, vol. 2, no. 10, pp. 2414–2416, Oct. 2022, doi: 10.1016/J.CHECAT.2022.09.032.

[174] Y. Liu, W. Wang, X. Xu, J.-P. Marcel Veder, and Z. Shao, “Recent advances in anion-doped metal oxides for catalytic applications,” *J. Mater. Chem. A Mater.*, vol. 7, no. 13, pp. 7280–7300, 2019, doi: 10.1039/C8TA09913H.

[175] Z. Zhou, C. Lan, R. Wei, and J. C. Ho, “Transparent metal-oxide nanowires and their applications in harsh electronics,” *J. Mater. Chem. C Mater.*, vol. 7, no. 2, pp. 202–217, 2019, doi: 10.1039/C8TC04501A.

[176] S. C. Dixon, D. O. Scanlon, C. J. Carmalt, and I. P. Parkin, “n-Type doped transparent conducting binary oxides: an overview,” *J. Mater. Chem. C Mater.*, vol. 4, no. 29, pp. 6946–6961, 2016, doi: 10.1039/C6TC01881E.

[177] M. Khammar, F. Ynineb, S. Guitouni, Y. Bouznit, and N. Attaf, “Crystallite size and intrinsic strain contribution in band gap energy redshift of ultrasonic-sprayed kesterite CZTS nanostructured thin films,” *Appl. Phys. A Mater. Sci. Process.*, vol. 126, no. 6, Jun. 2020, doi: 10.1007/s00339-020-03591-6.

[178] Y. Cho, A. Yamaguchi, R. Uehara, S. Yasuhara, T. Hoshina, and M. Miyauchi, “Temperature dependence on bandgap of semiconductor photocatalysts,” *Journal of Chemical Physics*, vol. 152, no. 23, Jun. 2020, doi: 10.1063/5.0012330.

[179] M. Li and J. C. Li, “Size effects on the band-gap of semiconductor compounds,” *Mater. Lett.*, vol. 60, no. 20, pp. 2526–2529, Sep. 2006, doi: 10.1016/j.matlet.2006.01.032.

[180] E. M. Samsudin and S. B. Abd Hamid, “Effect of band gap engineering in anionic-doped TiO 2 photocatalyst,” *Appl. Surf. Sci.*, vol. 391, pp. 326–336, Jan. 2017, doi: 10.1016/j.apsusc.2016.07.007.

[181] S. K. Gharaei, M. Abbasnejad, and R. Maezono, “Bandgap reduction of photocatalytic TiO2 nanotube by Cu doping,” *Sci. Rep.*, vol. 8, no. 1, Dec. 2018, doi: 10.1038/s41598-018-32130-w.

[182] R. Sagheer, M. Khalil, V. Abbas, Z. N. Kayani, U. Tariq, and F. Ashraf, “Effect of Mg doping on structural, morphological, optical and thermal properties of ZnO nanoparticles,” *Optik (Stuttg).*, vol. 200, Jan. 2020, doi: 10.1016/j.ijleo.2019.163428.

[183] S. Singh, Y. Yadawa, and A. Ranjan, “Enhanced adsorption of methylene blue by mixed-phase bismuth ferrite prepared by non-aqueous sol-gel route,” *J. Environ. Chem. Eng.*, vol. 11, no. 1, p. 109229, Feb. 2023, doi: 10.1016/j.jece.2022.109229.

[184] R. Marschall and L. Wang, “Non-metal doping of transition metal oxides for visible-light photocatalysis,” *Catal. Today*, vol. 225, pp. 111–135, Apr. 2014, doi: 10.1016/j.cattod.2013.10.088.

[185] M. Valenti, M. P. Jonsson, G. Biskos, A. Schmidt-Ott, and W. A. Smith, “Plasmonic nanoparticle-semiconductor composites for efficient solar water splitting,” *J. Mater. Chem. A Mater.*, vol. 4, no. 46, pp. 17891–17912, 2016, doi: 10.1039/C6TA06405A.

[186] F. Han, V. S. R. Kambala, M. Srinivasan, D. Rajarathnam, and R. Naidu, “Tailored titanium dioxide photocatalysts for the degradation of organic dyes in wastewater treatment: A review,” *Appl. Catal. A Gen.*, vol. 359, no. 1–2, pp. 25–40, May 2009, doi: 10.1016/j.apcata.2009.02.043.

[187] R. Medhi, M. D. Marquez, and T. R. Lee, “Visible-Light-Active Doped Metal Oxide Nanoparticles: Review of their Synthesis, Properties, and Applications,” Jul. 24, 2020, *American Chemical Society*. doi: 10.1021/acsanm.0c01035.

[188] F. Esch *et al.*, “Electron Localization Determines Defect Formation on Ceria Substrates,” *Science (1979).*, vol. 309, no. 5735, pp. 752–755, Jul. 2005, doi: 10.1126/science.1111568.

[189] X. Chen, L. Liu, P. Y. Yu, and S. S. Mao, “Increasing Solar Absorption for Photocatalysis with Black Hydrogenated Titanium Dioxide Nanocrystals,” *Science (1979).*, vol. 331, no. 6018, pp. 746–750, Feb. 2011, doi: 10.1126/science.1200448.

[190] J. Di *et al.*, “Defect engineering in atomically-thin bismuth oxychloride towards photocatalytic oxygen evolution,” *J. Mater. Chem. A Mater.*, vol. 5, no. 27, pp. 14144–14151, 2017, doi: 10.1039/C7TA03624H.

[191] J. Di, J. Xia, H. Li, S. Guo, and S. Dai, “Bismuth oxyhalide layered materials for energy and environmental applications,” *Nano Energy*, vol. 41, pp. 172–192, Nov. 2017, doi: 10.1016/j.nanoen.2017.09.008.

[192] P. Bernard, P. Stelmachowski, P. Broś, W. Makowski, and A. Kotarba, “Demonstration of the Influence of Specific Surface Area on Reaction Rate in Heterogeneous Catalysis,” *J. Chem. Educ.*, vol. 98, no. 3, pp. 935–940, Mar. 2021, doi: 10.1021/acs.jchemed.0c01101.

[193] P. Raizada *et al.*, “Surface defect engineering of metal oxides photocatalyst for energy application and water treatment,” *Journal of Materiomics*, vol. 7, no. 2, pp. 388–418, Mar. 2021, doi: 10.1016/j.jmat.2020.10.009.

[194] D. G. Shchukin and R. A. Caruso, “Template Synthesis and Photocatalytic Properties of Porous Metal Oxide Spheres Formed by Nanoparticle Infiltration,” *Chemistry of Materials*, vol. 16, no. 11, pp. 2287–2292, Jun. 2004, doi: 10.1021/cm0497780.

[195] L. Mulky *et al.*, “An overview of hydrogen storage technologies – Key challenges and opportunities,” *Mater. Chem. Phys.*, vol. 325, p. 129710, Oct. 2024, doi: 10.1016/j.matchemphys.2024.129710.

[196] S. Gritschneder, Y. Namai, Y. Iwasawa, and M. Reichling, “Structural features of CeO2(11) revealed by dynamic SFM,” in *Nanotechnology*, Mar. 2005. doi: 10.1088/0957-4484/16/3/008.

[197] G. Lu, A. Linsebigler, and J. T. Yates, “Photooxidation of CH3Cl on TiOz(l10): A Mechanism Not Involving H2O,” 1995.

[198] K. Reuter, D. Frenkel, and M. Scheffler, “The steady state of heterogeneous catalysis, studied by first-principles statistical mechanics,” *Phys. Rev. Lett.*, vol. 93, no. 11, Sep. 2004, doi: 10.1103/PhysRevLett.93.116105.

[199] M. A. Henderson, J. M. White, H. Uetsuka, and H. Onishi, “Photochemical Charge Transfer and Trapping at the Interface between an Organic Adlayer and an Oxide Semiconductor,” *J. AM. CHEM. SOC*, vol. 125, pp. 14974–14975, 2003, doi: 10.1021/ja037764.

[200] M. A. Henderson, W. S. Epling, C. L. Perkins, C. H. F. Peden, and U. Diebold, “Interaction of molecular oxygen with the vacuum-annealed TiO2(110) surface: Molecular and dissociative channels,” *Journal of Physical Chemistry B*, vol. 103, no. 25, pp. 5328–5337, Jun. 1999, doi: 10.1021/jp990655q.

[201] M. Sander and T. Engel, “Surface Science Letters Atomic level structure of TiO,(110) as a function of surface oxygen coverage.”

[202] H. Uetsuka, H. Onishi, M. A. Henderson, and J. M. White, “Photoinduced redox reaction coupled with limited electron mobility at metal oxide surface,” *Journal of Physical Chemistry B*, vol. 108, no. 30, pp. 10621–10624, Jul. 2004, doi: 10.1021/jp0484027.

[203] K. Honkala *et al.*, “Ammonia Synthesis from First-Principles Calculations,” *Science (1979).*, vol. 307, no. 5709, pp. 555–558, Jan. 2005, doi: 10.1126/science.1106435.

[204] Bard Allen J. and Faulkner Larry R., *Electrochemical Methods: Fundamentals and Applications*, 2nd ed., vol. ISBN 9780471043720. Wiley, 2000.

[205] P. Tahay, Y. Khani, M. Jabari, F. Bahadoran, N. Safari, and A. Zamanian, “Synthesis of cubic and hexagonal ZnTiO3 as catalyst support in steam reforming of methanol: Study of physical and chemical properties of copper catalysts on the

H2 and CO selectivity and coke formation," *Int. J. Hydrogen Energy*, vol. 45, no. 16, pp. 9484–9495, Mar. 2020, doi: 10.1016/j.ijhydene.2020.01.149.

[206] L. L. Gonzales *et al.*, "Properties of zinc titanates synthesized by microwave assisted hydrothermal method," *Heliyon*, vol. 7, no. 3, Mar. 2021, doi: 10.1016/j.heliyon.2021.e06521.

[207] S. Perween and A. Ranjan, "Improved visible-light photocatalytic activity in ZnTiO3 nanopowder prepared by sol-electrospinning," *Solar Energy Materials and Solar Cells*, vol. 163, pp. 148–156, Apr. 2017, doi: 10.1016/j.solmat.2017.01.020.

[208] T. Hu, Y. Zhang, S. Guan, Y. Lu, and L. Hao, "Graphene coupled MoO3 films prepared by wetting-induced climbing and key role of graphene on photocatalytic activity enhancement," *Materials Science and Engineering: B*, vol. 286, p. 116012, Dec. 2022, doi: 10.1016/j.mseb.2022.116012.

[209] P. O. Agboola, S. Haider, and I. Shakir, "Copper sulfide and their hybrids with carbon nanotubes for photocatalysis and antibacterial studies," *Ceram. Int.*, vol. 48, no. 7, pp. 10136–10143, Apr. 2022, doi: 10.1016/j.ceramint.2021.12.225.

[210] T. A. Khalyavka *et al.*, "Photocatalytic hydrogen evolution and Rifampicinum destruction over carbon-modified TiO2," *Research on Chemical Intermediates*, vol. 48, no. 1, pp. 13–28, Jan. 2022, doi: 10.1007/s11164-021-04609-1.

[211] T. A. Khalyavka *et al.*, "Photocatalytic activity of TiO2 mechanochemically modified with carbon and/or thiourea under UV and visible irradiation in the destruction of Safranine T and Rifampicinum," *Reaction Kinetics, Mechanisms and Catalysis*, vol. 135, no. 6, pp. 3393–3409, Dec. 2022, doi: 10.1007/s11144-022-02317-4.

[212] R. Hummers, W. S.; Offeman and E., "Preparation of Graphitic Oxide," *J. Am. Chem. Soc.*, vol. 208, no. 1937, p. 1937, 1957.

[213] H. Saleem, M. Haneef, and H. Y. Abbasi, "Synthesis route of reduced graphene oxide via thermal reduction of chemically exfoliated graphene oxide," *Mater. Chem. Phys.*, vol. 204, pp. 1–7, Jan. 2018, doi: 10.1016/J.MATCHEMPHYS.2017.10.020.

[214] W. D. Yang, Y. R. Li, and Y. C. Lee, "Synthesis of r-GO/TiO2 composites via the UV-assisted photocatalytic reduction of graphene oxide," *Appl. Surf. Sci.*, vol. 380, pp. 249–256, Sep. 2016, doi: 10.1016/J.APSUSC.2016.01.118.

[215] W. Liu and G. Speranza, "Tuning the Oxygen Content of Reduced Graphene Oxide and Effects on Its Properties," *ACS Omega*, vol. 6, no. 9, pp. 6195–6205, Mar. 2021, doi: 10.1021/ACSOMEGA.0C05578.

[216] S. Alotibi *et al.*, "Optimizing thermal reduction of graphene oxide for enhanced solar-driven water purification using rGO-TiO2 nanocomposites," *Physica B Condens. Matter*, vol. 699, p. 416821, Feb. 2025, doi: 10.1016/J.PHYSB.2024.416821.

[217] H. H. Huang, K. K. H. De Silva, G. R. A. Kumara, and M. Yoshimura, “Structural Evolution of Hydrothermally Derived Reduced Graphene Oxide,” *Sci. Rep.*, vol. 8, no. 1, pp. 2–10, 2018, doi: 10.1038/s41598-018-25194-1.

[218] M. Acik *et al.*, “The role of oxygen during thermal reduction of graphene oxide studied by infrared absorption spectroscopy,” *Journal of Physical Chemistry C*, vol. 115, no. 40, pp. 19761–19781, Oct. 2011, doi: 10.1021/jp2052618.

[219] P. M. Botta, E. F. Aglietti, and J. M. P. López, “Mechanochemical effects on the kinetics of zinc titanate formation,” *J. Mater. Sci.*, vol. 39, no. 16/17, pp. 5195–5199, Aug. 2004, doi: 10.1023/B:JMSC.0000039209.48875.25.

[220] H. Nurdiansah *et al.*, “Temperature-tuned ZnO/rGO/TiO2 ternary all-solid-state Z-scheme heterojunction for enhanced photocatalytic degradation of rhodamine B,” *Case Studies in Chemical and Environmental Engineering*, vol. 14, p. 101414, Dec. 2026, doi: 10.1016/J.CSCEE.2026.101414.

[221] L. Chantelle *et al.*, “Zn2SnO4 and Zn2TiO4 inverse spinels: influence of the temperature on structural, microstructural and luminescent properties,” *J. Therm. Anal. Calorim.*, vol. 149, no. 10, pp. 4453–4468, May 2024, doi: 10.1007/s10973-024-13020-y.

[222] E. M. Aliyev *et al.*, “Covalently Modified Graphene Oxide and Polymer of Intrinsic Microporosity (PIM-1) in Mixed Matrix Thin-Film Composite Membranes,” *Nanoscale Res. Lett.*, vol. 13, 2018, doi: 10.1186/s11671-018-2771-3.

[223] V. R. Moreira *et al.*, “Graphene oxide in the remediation of norfloxacin from aqueous matrix: simultaneous adsorption and degradation process,” *Environmental Science and Pollution Research*, vol. 27, no. 27, pp. 34513–34528, Sep. 2020, doi: 10.1007/s11356-020-09656-6.

[224] S. M. Adyani and M. Ghorbani, “A comparative study of physicochemical and photocatalytic properties of visible light responsive Fe, Gd and P single and tri-doped TiO2 nanomaterials,” *Journal of Rare Earths*, vol. 36, no. 1, pp. 72–85, Jan. 2018, doi: 10.1016/j.jre.2017.06.012.

[225] G. L. Bhagyalekshmi, A. P. Neethu Sha, and D. N. Rajendran, “Luminescence kinetics of low temperature nano ZnTiO3:Eu3+ red spinel under NUV excitation,” *Journal of Materials Science: Materials in Electronics*, vol. 30, no. 11, pp. 10673–10685, Jun. 2019, doi: 10.1007/s10854-019-01413-x.

[226] R. Al-Gaashani, S. Radiman, A. R. Daud, N. Tabet, and Y. Al-Douri, “XPS and optical studies of different morphologies of ZnO nanostructures prepared by microwave methods,” *Ceram. Int.*, vol. 39, no. 3, pp. 2283–2292, Apr. 2013, doi: 10.1016/j.ceramint.2012.08.075.

[227] T. Cottre, M. Fingerle, M. Kranz, T. Mayer, B. Kaiser, and W. Jaegermann, “Interaction of Water with Atomic Layer Deposited Titanium Dioxide on p-Si Photocathode: Modeling of Photoelectrochemical Interfaces in Ultrahigh Vacuum

with Cryo-Photoelectron Spectroscopy," *Adv. Mater. Interfaces*, vol. 8, no. 11, Jun. 2021, doi: 10.1002/admi.202002257.

[228] M. Nowak, B. Kauch, and P. Szperlich, "Determination of energy band gap of nanocrystalline SbSI using diffuse reflectance spectroscopy," *Review of Scientific Instruments*, vol. 80, no. 4, pp. 4–7, 2009, doi: 10.1063/1.3103603.

[229] S. A. Mayén-Hernández *et al.*, "Optical and structural properties of ZnO + Zn 2TiO 4 thin films prepared by the sol-gel method," in *Journal of Materials Science: Materials in Electronics*, Nov. 2007, pp. 1127–1130. doi: 10.1007/s10854-007-9267-8.

[230] Y. Cong, J. Zhang, F. Chen, and M. Anpo, "Synthesis and characterization of nitrogen-doped TiO2 nanophotocatalyst with high visible light activity," *Journal of Physical Chemistry C*, vol. 111, no. 19, pp. 6976–6982, 2007, doi: 10.1021/jp0685030.

[231] E. Campos-González *et al.*, "Photoluminescence emission from nanostructured porous preparations of CdS–ZnTiO3 assembled nanoparticles," *Luminescence*, vol. 35, no. 5, pp. 781–787, 2020, doi: 10.1002/bio.3784.

[232] A. Hankin, F. E. Bedoya-Lora, J. C. Alexander, A. Regoutz, and G. H. Kelsall, "Flat band potential determination: Avoiding the pitfalls," *J. Mater. Chem. A Mater.*, vol. 7, no. 45, pp. 26162–26176, 2019, doi: 10.1039/c9ta09569a.

[233] S. Ottow, G. S. Popkirov, and H. Föll, "Determination of flat-band potentials of silicon electrodes in HF by means of ac resistance measurements," 1998.

[234] S. H. Kang, J. Y. Kim, Y. Kim, H. S. Kim, and Y. E. Sung, "Surface modification of stretched TiO2 nanotubes for solid-state dye-sensitized solar cells," *Journal of Physical Chemistry C*, vol. 111, no. 26, pp. 9614–9623, 2007, doi: 10.1021/jp071504n.

[235] T. Xu, L. Zhang, H. Cheng, and Y. Zhu, "Significantly enhanced photocatalytic performance of ZnO via graphene hybridization and the mechanism study," *Appl. Catal. B*, vol. 101, no. 3–4, pp. 382–387, 2011, doi: 10.1016/j.apcatb.2010.10.007.

[236] C. Karunakaran, P. Magesan, P. Gomathisankar, and P. Vinayagamoorthy, "Absorption, emission, charge transfer resistance and photocatalytic activity of Al2O3/TiO2 core/shell nanoparticles," *Superlattices Microstruct.*, vol. 83, pp. 659–667, Jul. 2015, doi: 10.1016/j.spmi.2015.04.014.

[237] N. Tian *et al.*, "In situ co-pyrolysis fabrication of CeO $_2$ /g-C $_3$ N $_4$ n–n type heterojunction for synchronously promoting photo-induced oxidation and reduction properties," *J. Mater. Chem. A Mater.*, vol. 3, no. 33, pp. 17120–17129, 2015, doi: 10.1039/C5TA03669K.

[238] K. K. Kefeni and B. B. Mamba, "Photocatalytic application of spinel ferrite nanoparticles and nanocomposites in wastewater treatment: Review," *Sustainable Materials and Technologies*, vol. 23, p. e00140, Apr. 2020, doi: 10.1016/j.susmat.2019.e00140.

[239] S. Ye, R. Wang, M.-Z. Wu, and Y.-P. Yuan, "A review on g-C3N4 for photocatalytic water splitting and CO2 reduction," *Appl. Surf. Sci.*, vol. 358, pp. 15–27, Dec. 2015, doi: 10.1016/j.apsusc.2015.08.173.

[240] M. Faisal, M. Jalalah, F. A. Harraz, A. M. El-Toni, J. P. Labis, and M. S. Al-Assiri, "A novel Ag/PANI/ZnTiO3 ternary nanocomposite as a highly efficient visible-light-driven photocatalyst," *Sep. Purif. Technol.*, vol. 256, p. 117847, Feb. 2021, doi: 10.1016/j.seppur.2020.117847.

[241] M. An *et al.*, "CdS QDs modified three-dimensional ordered hollow spherical ZnTiO3-ZnO-TiO2 composite with improved photocatalytic performance," *J. Alloys Compd.*, vol. 895, Feb. 2022, doi: 10.1016/j.jallcom.2021.162638.

[242] T. Tamai, I. Hashida, N. Ichinose, S. Kawanishi, H. Inoue, and K. Mizuno, "U.v.-irradiation of thin films of polystyrene derivatives: formation of carboxylic group and crosslinking from 4-trimethylsilylmethyl substituent," 1996.

[243] D. Zhang, S. M. Dougal, and M. S. Yeganeh, "Effects of UV irradiation and plasma treatment on a polystyrene surface studied by IR-visible sum frequency generation spectroscopy," *Langmuir*, vol. 16, no. 10, pp. 4528–4532, Jan. 2000, doi: 10.1021/la991353i.

[244] D. S. Dhawale, D. P. Dubal, R. R. Salunkhe, T. P. Gujar, M. C. Rath, and C. D. Lokhande, "Effect of electron irradiation on properties of chemically deposited TiO2 nanorods," *J. Alloys Compd.*, vol. 499, no. 1, pp. 63–67, Jun. 2010, doi: 10.1016/j.jallcom.2010.01.126.

[245] N. McEvoy, H. Nolan, N. Ashok Kumar, T. Hallam, and G. S. Duesberg, "Functionalisation of graphene surfaces with downstream plasma treatments," *Carbon N. Y.*, vol. 54, pp. 283–290, Apr. 2013, doi: 10.1016/j.carbon.2012.11.040.

[246] C. R. Vandenabeele and S. Lucas, "Technological challenges and progress in nanomaterials plasma surface modification – A review," Jan. 01, 2020, *Elsevier Ltd*. doi: 10.1016/j.mser.2019.100521.

[247] X. Liu, R. Hua, J. Niu, Z. Zhang, and J. Zhang, "N2 plasma treatment TiO2 nanosheets for enhanced visible light-driven photocatalysis," *J. Alloys Compd.*, vol. 881, p. 160509, Nov. 2021, doi: 10.1016/j.jallcom.2021.160509.

[248] K. N. Pandiyaraj *et al.*, "Dye wastewater degradation by the synergetic effect of an atmospheric pressure plasma treatment and the photocatalytic activity of plasma-functionalized Cu–TiO2 nanoparticles," *J. Hazard. Mater.*, vol. 405, Mar. 2021, doi: 10.1016/j.jhazmat.2020.124264.

[249] B. Bharti, S. Kumar, H. N. Lee, and R. Kumar, "Formation of oxygen vacancies and Ti3+ state in TiO2 thin film and enhanced optical properties by air plasma treatment," *Sci. Rep.*, vol. 6, Aug. 2016, doi: 10.1038/srep32355.

[250] K. Yamada *et al.*, "Preparation of N-doped TiO2 particles by plasma surface modification," *Comptes Rendus. Chimie*, vol. 9, no. 5–6, pp. 788–793, Sep. 2005, doi: 10.1016/j.crci.2005.05.016.

[251] J. Karuppiah and Y. S. Mok, "Plasma-reduced Ni/γ–Al 2 O 3 and CeO 2 –Ni/γ–Al 2 O 3 catalysts for improving dry reforming of propane," *Int. J. Hydrogen Energy*, vol. 39, no. 29, pp. 16329–16338, Oct. 2014, doi: 10.1016/j.ijhydene.2014.08.012.

[252] S. H. Nam and J. H. Boo, "Enhancement of photocatalytic activity of synthesized ZnO nanoparticles with oxygen plasma treatment," *Catal. Today*, vol. 265, pp. 84–89, May 2016, doi: 10.1016/j.cattod.2015.11.003.

[253] S. Y. Kim, K. Hong, K. Kim, H. K. Yu, W. K. Kim, and J. L. Lee, "Effect of N2, Ar, and O2 plasma treatments on surface properties of metals," *J. Appl. Phys.*, vol. 103, no. 7, 2008, doi: 10.1063/1.2874495.

[254] S. Singh, S. Perween, and A. Ranjan, "Enhancing the visible light induced photocatalytic activity in sol-electrospun zinc titanate nanopowders by nitrogen doping," *Journal of Physics and Chemistry of Solids*, vol. 158, Nov. 2021, doi: 10.1016/j.jpcs.2021.110221.

[255] Y. Mochizuki, J. Bud, E. Byambajav, and N. Tsubouchi, "Pore properties and CO2 adsorption performance of activated carbon prepared from various carbonaceous materials," *Carbon Resources Conversion*, Mar. 2024, doi: 10.1016/j.crcon.2024.100237.

[256] P. Kalita, P. Jyoti Boruah, R. Ruchel Khanikar, and H. Bailung, "Plasma–induced rapid crystallization and surface engraving of amorphous TiOx(OH)y to enhance adsorption and photocatalytic activity," *J. Photochem. Photobiol. A Chem.*, vol. 434, p. 114251, Jan. 2023, doi: 10.1016/j.jphotochem.2022.114251.

[257] N. Lu *et al.*, "Characterization of highly effective plasma-treated g-C3N4 and application to the photocatalytic H2O2 production," *Chemosphere*, vol. 241, p. 124927, Feb. 2020, doi: 10.1016/j.chemosphere.2019.124927.

[258] Z. Zafar *et al.*, "Recent Development in Defects Engineered Photocatalysts: An Overview of the Experimental and Theoretical Strategies," *ENERGY & ENVIRONMENTAL MATERIALS*, vol. 5, no. 1, pp. 68–114, Jan. 2022, doi: 10.1002/eem2.12171.

[259] S. Guan *et al.*, "Oxygen vacancies induced band gap narrowing for efficient visible-light response in carbon-doped TiO2," *Sci. Rep.*, vol. 13, no. 1, p. 14105, Aug. 2023, doi: 10.1038/s41598-023-39523-6.

[260] J. Wang *et al.*, "Oxygen vacancy induced band-gap narrowing and enhanced visible light photocatalytic activity of ZnO," *ACS Appl. Mater. Interfaces*, vol. 4, no. 8, pp. 4024–4030, Aug. 2012, doi: 10.1021/am300835p.

[261] X. Fan *et al.*, "Preparation and characterization of Ag deposited and Fe doped TiO2 nanotube arrays for photocatalytic hydrogen production by water splitting," *Ceram. Int.*, vol. 40, no. 10, pp. 15907–15917, Dec. 2014, doi: 10.1016/j.ceramint.2014.07.119.

[262] C. Kang *et al.*, "Hydrothermal synthesis of graphene-ZnTiO3 nanocomposites with enhanced photocatalytic activities," *Research on Chemical Intermediates*, vol. 44, no. 11, pp. 6621–6636, Nov. 2018, doi: 10.1007/s11164-018-3512-z.

[263] Y.-Y. Chen, J.-C. Hsu, C.-Y. Lee, and P. W. Wang, “Influence of oxygen partial pressure on structural, electrical, and optical properties of Al-doped ZnO film prepared by the ion beam co-sputtering method,” *J. Mater. Sci.*, vol. 48, no. 3, pp. 1225–1230, Feb. 2013, doi: 10.1007/s10853-012-6863-7.

[264] Q. Chen, L. Wu, X. Zhao, and X. J. Yang, “Fabrication of Zn-Ti layered double oxide nanosheets with ZnO/ZnTiO3 heterojunction for enhanced photocatalytic degradation of MO, RhB and MB,” *J. Mol. Liq.*, vol. 353, May 2022, doi: 10.1016/j.molliq.2022.118794.

[265] R. Abirami *et al.*, “An approach to enhance the photocatalytic activity of ZnTiO3,” *Ceram. Int.*, vol. 47, no. 13, pp. 18122–18131, Jul. 2021, doi: 10.1016/j.ceramint.2021.03.130.

[266] X. Li, J. Xiong, J. Huang, Z. Feng, and J. Luo, “Novel g-C3N4/h′ZnTiO3-a′TiO2 direct Z-scheme heterojunction with significantly enhanced visible-light photocatalytic activity,” *J. Alloys Compd.*, vol. 774, pp. 768–778, Feb. 2019, doi: 10.1016/j.jallcom.2018.10.034.

[267] Z. Suo, J. Dai, S. Gao, and H. Gao, “Effect of transition metals (Sc, Ti, V, Cr and Mn) doping on electronic structure and optical properties of CdS,” *Results Phys.*, vol. 17, p. 103058, Jun. 2020, doi: 10.1016/J.RINP.2020.103058.

[268] A. Khlyustova, N. Sirotkin, T. Kusova, A. Kraev, V. Titov, and A. Agafonov, “Doped TiO2: the effect of doping elements on photocatalytic activity,” *Mater. Adv.*, vol. 1, no. 5, pp. 1193–1201, Aug. 2020, doi: 10.1039/D0MA00171F.

[269] Y. Zhao, M. Tang, and L. He, “Transition metal (Mn, Fe, Co, Ni) and nitrogen co-doping for improving the photocatalytic activity of monolayer MoS2,” *Molecular Catalysis*, vol. 553, p. 113785, Jan. 2024, doi: 10.1016/J.MCAT.2023.113785.

[270] S. Baqi, M. T. Oo, and F. C. Chung Ling, “Unveiling the impact of Cu doping on charge carrier density and transfer in ZnO/ZnSe heterojunctions for PEC applications,” *Mater. Sci. Semicond. Process.*, vol. 198, p. 109780, Nov. 2025, doi: 10.1016/J.MSSP.2025.109780.

[271] T. K. Lih *et al.*, “Low intensity UV driven dual functional Cu doped BiVO4 for enhanced methylene blue degradation and Staphylococcus aureus inactivation,” *Scientific Reports 2025 15:1*, vol. 15, no. 1, pp. 1–18, Oct. 2025, doi: 10.1038/S41598-025-17994-Z.

[272] S. R. Al-Mhyawi *et al.*, “Impact of Heterovalent Cu2+ and Ag+ Doping on the Structural, Optoelectronic, and Photocatalytic Properties of ZnO for Enhanced Solar-Driven Hydrogen Evolution and Organic Pollutant Degradation,” *ACS Omega*, vol. 10, no. 37, pp. 42847–42861, Sep. 2025, doi: 10.1021/ACSOMEGA.5C05419.

[273] W. Van Der Stam *et al.*, “Tuning and Probing the Distribution of Cu+ and Cu2+ Trap States Responsible for Broad-Band Photoluminescence in CuInS2 Nanocrystals,” *ACS Nano*, vol. 12, no. 11, pp. 11244–11253, Nov. 2018, doi: 10.1021/ACSNANO.8B05843.

[274] J. Li, J. Zeng, L. Jia, and W. Fang, “Investigations on the effect of Cu2+/Cu1+ redox couples and oxygen vacancies on photocatalytic activity of treated LaNi1−xCuxO3 (x=0.1, 0.4, 0.5),” *Int. J. Hydrogen Energy*, vol. 35, no. 23, pp. 12733–12740, Dec. 2010, doi: 10.1016/J.IJHYDENE.2010.08.140.

[275] M. R. Mohammadi and D. J. Fray, “Low temperature nanostructured zinc titanate by an aqueous particulate sol–gel route: Optimisation of heat treatment condition based on Zn:Ti molar ratio,” *J. Eur. Ceram. Soc.*, vol. 30, no. 4, pp. 947–961, Mar. 2010, doi: 10.1016/J.JEURCERAMSOC.2009.09.031.

[276] J. Yu *et al.*, “Advances in deep eutectic solvent-mediated crystallization: toward green and tunable platforms for pharmaceutical and biomolecular applications,” *CrystEngComm*, vol. 27, no. 31, pp. 5238–5249, Aug. 2025, doi: 10.1039/D5CE00434A.

[277] M. Nawaz, M. Irfan, K. Zahra, H. Suleman, M. A. Bustam, and A. S. Maulud, “Quantifying green innovation: A bibliometric analysis of deep eutectic solvents and applications as eco-friendly solvents,” *Journal of Ionic Liquids*, vol. 5, no. 2, p. 100165, Dec. 2025, doi: 10.1016/J.JIL.2025.100165.

[278] N. F. A. Sani *et al.*, “Advancements in deep eutectic solvent-based membranes for the extraction, separation, and preconcentration of organic compounds,” *Advances in Sample Preparation*, vol. 14, p. 100181, May 2025, doi: 10.1016/J.SAMPRE.2025.100181.

[279] F. Oyoun *et al.*, “Deep Eutectic Solvents: An Eco-friendly Design for Drug Engineering,” *ChemSusChem*, vol. 16, no. 20, p. e202300669, Oct. 2023, doi: 10.1002/CSSC.202300669.

[280] A. K. Gomey, M. B. Haider, and R. Kumar, “Designing of energy-efficient deep eutectic solvents for CO2 capture: insights from physical and thermodynamic property evaluation,” *J. Mol. Liq.*, vol. 434, p. 127996, Sep. 2025, doi: 10.1016/J.MOLLIQ.2025.127996.

[281] J. Bhatt, D. Mondal, and K. Prasad, “Experimental evidence for the participation of deep eutectic solvents in silver chloride crystal formation at low temperature,” *J. Cryst. Growth*, vol. 442, pp. 95–97, May 2016, doi: 10.1016/J.JCRYSGRO.2016.03.007.

[282] M. R. Pinho *et al.*, “Choline Chloride- and Organic Acids-Based Deep Eutectic Solvents: Exploring Chemical and Thermophysical Properties,” *J. Chem. Eng. Data*, vol. 69, no. 10, pp. 3403–3414, Oct. 2024, doi: 10.1021/ACS.JCED.3C00706.

[283] A. Kityk, V. Pavlik, and M. Hnatko, “Exploring deep eutectic solvents for the electrochemical and chemical synthesis of photo- and electrocatalysts for hydrogen evolution,” *Int. J. Hydrogen Energy*, vol. 48, no. 100, pp. 39823–39853, Dec. 2023, doi: 10.1016/J.IJHYDENE.2023.07.158.

[284] F. G. Calvo-Flores and C. Mingorance-Sánchez, “Deep Eutectic Solvents and Multicomponent Reactions: Two Convergent Items to Green Chemistry

Strategies," *ChemistryOpen*, vol. 10, no. 8, pp. 815–829, Aug. 2021, doi: 10.1002/OPEN.202100137.

[285] A. K. Gomey, M. M. Tripathi, M. B. Haider, and R. Kumar, "Comparative analysis of isopropyl alcohol dehydration using ionic liquids and deep eutectic solvent," *Journal of Ionic Liquids*, vol. 3, no. 2, p. 100069, Dec. 2023, doi: 10.1016/J.JIL.2023.100069.

[286] R. A. Solano, A. P. Herrera, D. Maestre, and A. Cremades, "Fe-TiO2 Nanoparticles Synthesized by Green Chemistry for Potential Application in Waste Water Photocatalytic Treatment," *J. Nanotechnol.*, vol. 2019, no. 1, p. 4571848, Jan. 2019, doi: 10.1155/2019/4571848.

[287] "Crystallographic facet engineering of ZnO nanoparticles for photocatalytic organic pollutant degradation and antibacterial activity - Materials Advances (RSC Publishing) DOI:10.1039/D5MA00316D." Accessed: Oct. 09, 2025. [Online]. Available: https://pubs.rsc.org/en/content/articlehtml/2025/ma/d5ma00316d

[288] "Interstitial and substitutional doping of Mn 2+ in 2D PEA 2 PbBr 4 and BA 2 PbBr 4 perovskites - Chemical Communications (RSC Publishing) DOI:10.1039/D4CC04074K." Accessed: Oct. 09, 2025. [Online]. Available: https://pubs.rsc.org/en/content/articlehtml/2024/cc/d4cc04074k

[289] S. Li and B. Bergman, "Doping effect on secondary phases, microstructure and electrical conductivities of LaGaO3 based perovskites," *J. Eur. Ceram. Soc.*, vol. 29, no. 6, pp. 1139–1146, Apr. 2009, doi: 10.1016/J.JEURCERAMSOC.2008.08.017.

[290] Y. Zhao, Y. Zhang, Y. Zheng, F. Wang, and C. Li, "Effect of Cu doping on the electronic, magnetic and optical properties of GaN/AlN heterojunctions:A first-principles study," *Chem. Phys. Lett.*, vol. 878, p. 142262, Nov. 2025, doi: 10.1016/J.CPLETT.2025.142262.

[291] J. Dai, Z. Suo, Z. Li, and S. Gao, "Effect of Cu/Al doping on electronic structure and optical properties of ZnO," *Results Phys.*, vol. 15, p. 102649, Dec. 2019, doi: 10.1016/J.RINP.2019.102649.

[292] X. Zhao, C. Yang, T. Wang, X. Ma, S. Wei, and C. Xia, "3d transition metal doping-induced electronic structures and magnetism in 1T-HfSe 2 monolayers," *RSC Adv.*, vol. 7, no. 83, pp. 52747–52754, Nov. 2017, doi: 10.1039/C7RA11040E.

[293] M. S. Álvarez, M. A. Longo, A. Rodríguez, and F. J. Deive, "The role of deep eutectic solvents in catalysis. A vision on their contribution to homogeneous, heterogeneous and electrocatalytic processes," *Journal of Industrial and Engineering Chemistry*, vol. 132, pp. 36–49, Apr. 2024, doi: 10.1016/J.JIEC.2023.11.030.

[294] S. Sivakumar, Y. Robinson, and N. A. Mala, "Studies on photocatalytic performance and supercapacitor applications of undoped and Cu-doped ZnO nanoparticles," *Applied Surface Science Advances*, vol. 12, p. 100344, Dec. 2022, doi: 10.1016/J.APSADV.2022.100344.

[295] N. Mehrabi, U. F. Abdul Haq, M. T. Reza, and N. Aich, "Application of deep eutectic solvent for conjugation of magnetic nanoparticles onto graphene oxide for lead(II) and methylene blue removal," *J. Environ. Chem. Eng.*, vol. 8, no. 5, p. 104222, Oct. 2020, doi: 10.1016/J.JECE.2020.104222.

[296] K. Kotsis and V. Staemmler, "Ab initio calculations of the O1s XPS spectra of ZnO and Zn oxo compounds," *Physical Chemistry Chemical Physics*, vol. 8, no. 13, pp. 1490–1498, Mar. 2006, doi: 10.1039/B515699H.

[297] T. J. Frankcombe and Y. Liu, "Interpretation of Oxygen 1s X-ray Photoelectron Spectroscopy of ZnO," *Chemistry of Materials*, vol. 35, no. 14, pp. 5468–5474, Jul. 2023, doi: 10.1021/ACS.CHEMMATER.3C00801.

[298] M. H. Azarian, S. Nijpanich, N. Chanlek, and W. Sutapun, "Probing capping mechanisms and polymer matrix loading of biogenic vaterite CaCO3–Ag hybrid through X-ray photoelectron spectroscopy (XPS)," *RSC Adv.*, vol. 14, no. 21, pp. 14624–14639, May 2024, doi: 10.1039/D4RA01710B.

[299] W. Xie, R. Li, and Q. Xu, "Enhanced photocatalytic activity of Se-doped TiO2 under visible light irradiation," *Sci. Rep.*, vol. 8, no. 1, pp. 1–10, Dec. 2018, doi: 10.1038/S41598-018-27135-4.

[300] M. Fu, Y. Li, S. Wu, P. Lu, J. Liu, and F. Dong, "Sol–gel preparation and enhanced photocatalytic performance of Cu-doped ZnO nanoparticles," *Appl. Surf. Sci.*, vol. 258, no. 4, pp. 1587–1591, Dec. 2011, doi: 10.1016/J.APSUSC.2011.10.003.

[301] M. K. Gora *et al.*, "The study of optical, structural and magnetic properties of Cu-doped ZnO nanoparticles," *Journal of Materials Science: Materials in Electronics*, vol. 34, no. 4, pp. 1–21, Feb. 2023, doi: 10.1007/S10854-022-09713-5.

[302] W. Yuan, Y. Wu, C. Fang, X. Wang, X. Huang, and C. Li, "Engineering Nanowire Array Structure of Copper Oxide/Cuprous Oxide for Enhanced Oxygen Evolution Reaction," *J. Electrochem. Soc.*, vol. 167, no. 2, p. 022508, Jan. 2020, doi: 10.1149/1945-7111/AB6978.

[303] D. He, G. Wang, G. Liu, H. Suo, and C. Zhao, "Construction of leaf-like CuO–Cu2O nanocomposites on copper foam for high-performance supercapacitors," *Dalton Transactions*, vol. 46, no. 10, pp. 3318–3324, Mar. 2017, doi: 10.1039/C7DT00287D.

[304] D. He, S. Xing, B. Sun, H. Cai, H. Suo, and C. Zhao, "Design and construction of three-dimensional flower-like CuO hierarchical nanostructures on copper foam for high performance supercapacitor," *Electrochim. Acta*, vol. 210, pp. 639–645, Aug. 2016, doi: 10.1016/J.ELECTACTA.2016.05.196.

[305] P. Giannozzi *et al.*, "Advanced capabilities for materials modelling with Quantum ESPRESSO," *Journal of Physics: Condensed Matter*, vol. 29, no. 46, p. 465901, Oct. 2017, doi: 10.1088/1361-648X/AA8F79.

[306] K. Momma and F. Izumi, "VESTA 3 for three-dimensional visualization of crystal, volumetric and morphology data," *urn:issn:0021-8898*, vol. 44, no. 6, pp. 1272–1276, Oct. 2011, doi: 10.1107/S0021889811038970.

[307] Y. L. Chai, Y. S. Chang, K. T. Liu, and L. G. Teoh, "The structure and PTCR effects of Mg-doped ZnTiO 3 ceramics," *Ceram. Int.*, vol. 38, no. 5, pp. 3613–3618, Jul. 2012, doi: 10.1016/j.ceramint.2011.12.078.

[308] P. Giannozzi *et al.*, "QUANTUM ESPRESSO: a modular and open-source software project for quantum simulations of materials," *Journal of Physics: Condensed Matter*, vol. 21, no. 39, p. 395502, Sep. 2009, doi: 10.1088/0953-8984/21/39/395502.

[309] S. K. Pandey and A. Ranjan, "First-Principles Prediction of Enhanced Photocatalytic Activity in Cu-Doped ZnTiO3 by Replacing Zinc and Titanium," in *The 3rd International Electronic Conference on Processes—Green and Sustainable Process Engineering and Process Systems Engineering*, Basel Switzerland: MDPI, May 2024, p. 71. doi: 10.3390/proceedings2024105071.

[310] Z. Hasan, M. A. Rahman, D. K. Das, and H. K. Rouf, "Influence of Ca doping in structural, electronic, optical and mechanical properties of Ba1−xCaxTiO3 perovskite from first-principles investigation," *Sci. Rep.*, vol. 13, no. 1, Dec. 2023, doi: 10.1038/s41598-023-36719-8.

[311] O. Volnianska, "Computational studies of the electronic structure of copper-doped ZnO quantum dots," *Journal of Chemical Physics*, vol. 154, no. 12, Mar. 2021, doi: 10.1063/5.0039522.

[312] S. Idrissi, S. Ziti, H. Labrim, and L. Bahmad, "Sulfur doping effect on the electronic properties of zirconium dioxide ZrO2," *Materials Science and Engineering: B*, vol. 270, Aug. 2021, doi: 10.1016/j.mseb.2021.115200.

[313] S. Lei, H. Fan, X. Ren, J. Fang, L. Ma, and Z. Liu, "Novel sintering and band gap engineering of ZnTiO3 ceramics with excellent microwave dielectric properties," *J. Mater. Chem. C Mater.*, vol. 5, no. 16, pp. 4040–4047, 2017, doi: 10.1039/c7tc00815e.

[314] P. Kaur, S. Kumar, N. S. Negi, and S. M. Rao, "Enhanced magnetism in Cr-doped ZnO nanoparticles with nitrogen co-doping synthesized using sol–gel technique," *Applied Nanoscience (Switzerland)*, vol. 5, no. 3, pp. 367–372, Mar. 2015, doi: 10.1007/S13204-014-0326-1/FIGURES/4.

[315] ZHANG Xiao-Chao et al. "Electronic Structures and Optical Properties of Ilmenite-Type Hexagonal ZnTiO3," *Acta Phys. -Chim. Sin.*, vol. 27, no. 1, pp. 47-51, Jan. 2011, doi: 10.3866/PKU.WHXB20110102.

[316] J. Zhang, B. Xu, Y. S. Wang, Z. Qin, and S. H. Ke, "First-principles investigation of the ferroelectric, piezoelectric and nonlinear optical properties of LiNbO3-type ZnTiO3," *Sci. Rep.*, vol. 9, no. 1, pp. 1–14, Dec. 2019, doi: 10.1038/S41598-019-53986-6.

[317] C. Luo, D. Li, W. Wu, Y. Zhang, and C. Pan, "Preparation of porous micro-nano-structure NiO/ZnO heterojunction and its photocatalytic property," *RSC Adv.*, vol. 4, no. 6, pp. 3090–3095, 2014, doi: 10.1039/c3ra44670k.

[318] M. Hashim, M. Usman, S. Ahmad, R. Shah, A. Ali, and N. U. Rahman, "ZnO/NiO Nanocomposite with Enhanced Photocatalytic H2 Production," *International Journal of Photoenergy*, vol. 2024, 2024, doi: 10.1155/2024/2676368.

[319] H. A. Alshamsi and F. A. Jabir, "Green synthesis of Ni0.5Zn0.5O/TiO2 for photocatalytic, antibacterial and anticancer activities," *J. Mol. Liq.*, vol. 413, Nov. 2024, doi: 10.1016/j.molliq.2024.126037.

[320] J. Wang *et al.*, "P-Type NiZnO thin films grown by photo-assist metal-organic chemical vapor deposition," *J. Alloys Compd.*, vol. 579, pp. 160–164, 2013, doi: 10.1016/j.jallcom.2013.04.192.

[321] A. Nyabadza *et al.*, "A review of physical, chemical and biological synthesis methods of bimetallic nanoparticles and applications in sensing, water treatment, biomedicine, catalysis and hydrogen storage," *Adv. Colloid Interface Sci.*, vol. 321, p. 103010, Nov. 2023, doi: 10.1016/J.CIS.2023.103010.

[322] S. A. Farag, M. Farouk, and N. Shehata, "Evaluation of ZnO/NiO/kaolin nanocomposite as a sorbent/photocatalyst in hybrid water remediation process," *Appl. Water Sci.*, vol. 14, no. 12, pp. 1–25, Dec. 2024, doi: 10.1007/S13201-024-02282-4.

[323] M. Patel, H. S. Kim, and J. Kim, "All Transparent Metal Oxide Ultraviolet Photodetector," *Adv. Electron. Mater.*, vol. 1, no. 11, Nov. 2015, doi: 10.1002/AELM.201500232.

[324] J. Jassi, S. Deepa, C. S. Chitra Lekha, and N. M. Paul, "Influence of g-C3N4 on the structural, optical, and morphological features of g-C3N4/ZnO nanocomposites," *Results in Surfaces and Interfaces*, vol. 20, p. 100608, Aug. 2025, doi: 10.1016/J.RSURFI.2025.100608.

[325] B. Xue and Y. Zou, "High photocatalytic activity of ZnO–graphene composite," *J. Colloid Interface Sci.*, vol. 529, pp. 306–313, Nov. 2018, doi: 10.1016/J.JCIS.2018.04.040.

[326] J. Qin *et al.*, "A facile synthesis of nanorods of ZnO/graphene oxide composites with enhanced photocatalytic activity," *Appl. Surf. Sci.*, vol. 321, pp. 226–232, Dec. 2014, doi: 10.1016/J.APSUSC.2014.10.008.

[327] A. Yildiz, B. Kayhan, B. Yurduguzel, A. P. Rambu, F. Iacomi, and S. Simon, "Ni doping effect on electrical conductivity of ZnO nanocrystalline thin films," *Journal of Materials Science: Materials in Electronics*, vol. 22, no. 9, pp. 1473–1478, Sep. 2011, doi: 10.1007/s10854-011-0332-y.

[328] G. Qu *et al.*, "Graphene-Modified ZnO Nanostructures for Low-Temperature NO 2 Sensing," *ACS Omega*, vol. 4, no. 2, pp. 4221–4232, Feb. 2019, doi: 10.1021/acsomega.8b03624.

[329] O. Akhavan and E. Ghaderi, "Photocatalytic Reduction of Graphene Oxide Nanosheets on TiO2 Thin Film for Photoinactivation of Bacteria in Solar Light Irradiation," *Journal of Physical Chemistry C*, vol. 113, no. 47, pp. 20214–20220, 2009, doi: 10.1021/JP906325Q.

[330] K. Kaviyarasan, T. Sivasankar, V. K. Ponnusamy, and S. Anandan, "Ni–ZnO nanocomposites assembled under various morphologies like columnar, nanochains, and granular structure for removal of pollutants," *Mater. Chem. Phys.*, vol. 252, Sep. 2020, doi: 10.1016/j.matchemphys.2020.123299.

[331] J. S. Shaikh *et al.*, "Synthesis and characterization of Ru doped CuO thin films for supercapacitor based on Bronsted acidic ionic liquid," *Electrochim. Acta*, vol. 56, no. 5, pp. 2127–2134, Feb. 2011, doi: 10.1016/J.ELECTACTA.2010.11.046.

[332] P. Dubey, N. Kaurav, R. S. Devan, G. S. Okram, and Y. K. Kuo, "The effect of stoichiometry on the structural, thermal and electronic properties of thermally decomposed nickel oxide," *RSC Adv.*, vol. 8, no. 11, pp. 5882–5890, Feb. 2018, doi: 10.1039/C8RA00157J.

[333] S. Zainab, M. Azeem, S. U. Awan, S. Rizwan, N. Iqbal, and J. Rashid, "Optimization of bandgap reduction in 2-dimensional GO nanosheets and nanocomposites of GO/iron-oxide for electronic device applications," *Sci. Rep.*, vol. 13, no. 1, pp. 1–19, Dec. 2023, doi: 10.1038/S41598-023-33200-4.

[334] M. Ai, J. W. Zhang, Y. W. Wu, L. Pan, C. Shi, and J. J. Zou, "Role of Vacancies in Photocatalysis: A Review of Recent Progress," Nov. 16, 2020, *John Wiley and Sons Ltd*. doi: 10.1002/asia.202000889.

[335] K. Rahimi, H. Zafarkish, and A. Yazdani, "Reduced graphene oxide can activate the sunlight-induced photocatalytic effect of NiO nanowires," *Mater. Des.*, vol. 144, pp. 214–221, Apr. 2018, doi: 10.1016/J.MATDES.2018.02.030.

[336] P. Vivek, R. Sivakumar, E. Selva Esakki, and S. Deivanayaki, "Fabrication of NiO/RGO nanocomposite for enhancing photocatalytic performance through degradation of RhB," *Journal of Physics and Chemistry of Solids*, vol. 176, p. 111255, May 2023, doi: 10.1016/J.JPCS.2023.111255.

[337] R. Yang *et al.*, "One-step preparation (3D/2D/2D) BiVO4/FeVO4@rGO heterojunction composite photocatalyst for the removal of tetracycline and hexavalent chromium ions in water," *Chemical Engineering Journal*, vol. 390, p. 124522, Jun. 2020, doi: 10.1016/J.CEJ.2020.124522.

[338] I. Ahmad, M. Muneer, A. S. Khder, and S. A. Ahmed, "Novel Type-II Heterojunction Binary Composite (CdS/AgI) with Outstanding Visible Light-Driven Photocatalytic Performances toward Methyl Orange and Tetracycline Hydrochloride," *ACS Omega*, vol. 8, no. 25, pp. 22708–22720, Jun. 2023, doi: 10.1021/ACSOMEGA.3C01517.

[339] R. Yang, S. Zhong, L. Zhang, and B. Liu, "PW12/CN@Bi2WO6 composite photocatalyst prepared based on organic-inorganic hybrid system for removing pollutants in water," *Sep. Purif. Technol.*, vol. 235, p. 116270, Mar. 2020, doi: 10.1016/J.SEPPUR.2019.116270.

[340] C. Li *et al.*, "3D TiO2-x and Ag10Si4O13 nanoparticals embedded into 2D thin layer g-C3N4 to construct 3D/2D/3D double Z-scheme heterojunction for

enhanced photocatalytic activity and stability," *Surfaces and Interfaces*, vol. 64, p. 106477, May 2025, doi: 10.1016/J.SURFIN.2025.106477.

[341] G. Liao, C. Li, X. Li, and B. Fang, "Emerging polymeric carbon nitride Z-scheme systems for photocatalysis," *Cell Rep. Phys. Sci.*, vol. 2, no. 3, p. 100355, Mar. 2021, doi: 10.1016/J.XCRP.2021.100355.

[342] Abid, P. Sehrawat, S. S. Islam, P. Mishra, and S. Ahmad, "Reduced graphene oxide (rGO) based wideband optical sensor and the role of Temperature, Defect States and Quantum Efficiency," *Sci. Rep.*, vol. 8, no. 1, pp. 1–13, Dec. 2018, doi: 10.1038/S41598-018-21686-2.

[343] P. Mao, Y. Wei, H. Li, and J. Wang, "Junction diodes in organic solar cells," *Nano Energy*, vol. 41, pp. 717–730, Nov. 2017, doi: 10.1016/J.NANOEN.2017.10.027.

[344] S. Ji *et al.*, "Work function engineering of graphene oxide via covalent functionalization for organic field-effect transistors," *Appl. Surf. Sci.*, vol. 419, pp. 252–258, Oct. 2017, doi: 10.1016/J.APSUSC.2017.05.028.

[345] K. Ri, J. Ju, Y. Kim, and S. Jon, "Reduced graphene oxide prepared by microwave thermal reduction for performance improvement of AgNW/ATO-based flexible perovskite solar cells," *Appl. Phys. Lett.*, vol. 126, no. 15, p. 10, Apr. 2025, doi: 10.1063/5.0256713.

[346] X. Cheng *et al.*, "Fluorinated Reduced Graphene Oxide as an Efficient Hole-Transport Layer for Efficient and Stable Polymer Solar Cells," *ACS Omega*, vol. 2, no. 5, pp. 2010–2016, May 2017, doi: 10.1021/ACSOMEGA.7B00408.

[347] M. T. Greiner, M. G. Helander, Z. Bin Wang, W. M. Tang, and Z. H. Lu, "Effects of Processing Conditions on the Work Function and Energy-Level Alignment of NiO Thin Films," *Journal of Physical Chemistry C*, vol. 114, no. 46, pp. 19777–19781, Nov. 2010, doi: 10.1021/JP108281M.

[348] A. Douloumis, N. R. E. Vrithias, N. Katsarakis, I. N. Remediakis, and G. Kopidakis, "Tuning the workfunction of ZnO through surface doping with Mn from first-principles simulations," *Surf. Sci.*, vol. 726, p. 122175, Dec. 2022, doi: 10.1016/J.SUSC.2022.122175.

[349] M. Vorochta, V. Mansfeldova, S. Chakraborty, and L. Kavan, "Work function and electrochemistry of ZnO (wurtzite) single crystals (F-1:L07)," *Ceram. Int.*, vol. 51, no. 10, pp. 12346–12354, Apr. 2025, doi: 10.1016/J.CERAMINT.2024.11.066.

[350] X. Li *et al.*, "A review of material aspects in developing direct Z-scheme photocatalysts," *Materials Today*, vol. 47, pp. 75–107, Jul. 2021, doi: 10.1016/J.MATTOD.2021.02.017.

[351] S. Mochizuki and T. Saito, "Intrinsic and defect-related luminescence of NiO," *Physica B Condens. Matter*, vol. 404, no. 23–24, pp. 4850–4853, Dec. 2009, doi: 10.1016/j.physb.2009.08.166.

[352] F. Kayaci, S. Vempati, I. Donmez, N. Biyikli, and T. Uyar, "Role of zinc interstitials and oxygen vacancies of ZnO in photocatalysis: A bottom-up approach to control

defect density," *Nanoscale*, vol. 6, no. 17, pp. 10224–10234, Sep. 2014, doi: 10.1039/c4nr01887g.

[353] G. Vijaya Prasath, K. S. Usha, M. Karuppaiah, G. Ravi, and P. Krishnan, "Fabrication of heterostructure NiO/ZnO thin film for pseudocapacitor application," *J. Solgel Sci. Technol.*, vol. 104, no. 1, pp. 198–210, Oct. 2022, doi: 10.1007/s10971-022-05919-5.

[354] L. Kumar Jangir, Y. Kumari, A. Kumar, M. Kumar, and K. Awasthi, "Investigation of luminescence and structural properties of ZnO nanoparticles, synthesized with different precursors," *Mater. Chem. Front.*, vol. 1, no. 7, pp. 1413–1421, Jul. 2017, doi: 10.1039/c7qm00058h.

[355] Y. Wang, C. Ma, X. Sun, and H. Li, "Preparation and photoluminescence properties of organic–inorganic nanocomposite with a mesolamellar nickel oxide," *Microporous and Mesoporous Materials*, vol. 71, no. 1–3, pp. 99–102, Jun. 2004, doi: 10.1016/J.MICROMESO.2004.03.022.

[356] R. N. Jayaprakash, N. Dineshbabu, S. Selvaraj, S. Vignesh, T. Arun, and K. Ravichandran, "Hydrothermally constructed and visible-light activated efficient NiO/ZnO/g-C3N4 ternary nanocomposites for methylene blue dye degradation and antibacterial applications," *Inorg. Chem. Commun.*, vol. 159, p. 111643, Jan. 2024, doi: 10.1016/j.inoche.2023.111643.

[357] A. Bhapkar, R. Prasad, D. Jaspal, M. Shirolkar, Kh. Gheisari, and S. Bhame, "Visible light driven photocatalytic degradation of methylene blue by ZnO nanostructures synthesized by glycine nitrate auto combustion route," *Inorg. Chem. Commun.*, vol. 148, p. 110311, Feb. 2023, doi: 10.1016/j.inoche.2022.110311.

[358] B. Li, T. Liu, Y. Wang, and Z. Wang, "ZnO/graphene-oxide nanocomposite with remarkably enhanced visible-light-driven photocatalytic performance," *J. Colloid Interface Sci.*, vol. 377, no. 1, pp. 114–121, Jul. 2012, doi: 10.1016/J.JCIS.2012.03.060.

Appendix

Supporting Information

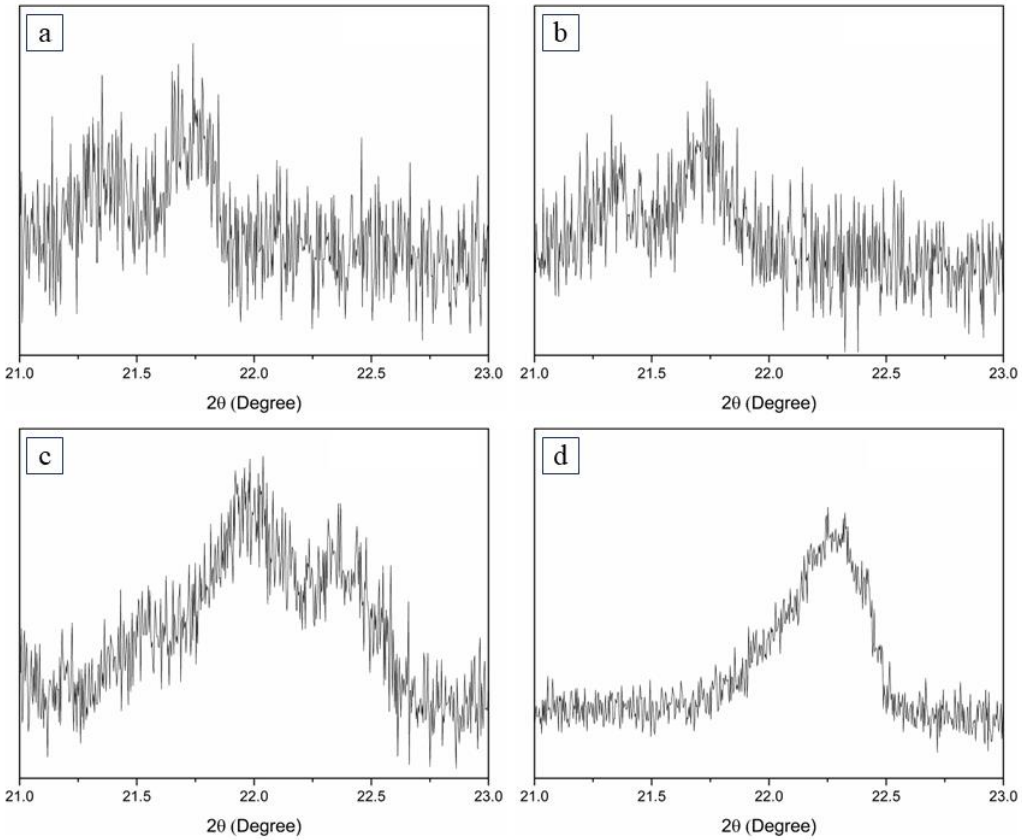

Figure S1. X-ray diffractogram for (a) composite I, (b) composite II, (c) composite III, and (d) GO in region 21-23 degree.

Table S1. FWHM values of ZTO, composite I, composite II, and composite III.

ZTO		composite I		Composite II		Composite III	
2θ	FWHM	2θ	FWHM	2θ	FWHM	2θ	FWHM
24.11277	0.21571	24.07749	0.19879	24.06353	0.21749	24.29003	0.28854
27.6284	0.22081	24.90788	0.19346	24.91321	0.18169	25.80727	0.32877
30.03453	0.21218	27.06895	0.20355	27.07411	0.19191	27.82536	0.3479
31.8662	0.22612	27.60692	0.19461	27.63168	0.19962	29.95574	0.37918
32.96258	0.21751	29.99835	0.20355	30.03124	0.19619	31.88918	0.60264
34.60715	0.2279	31.92924	0.22342	31.85963	0.22794	33.13984	0.36979
35.33916	0.22413	32.94043	0.20024	32.94288	0.2139	34.2	0.35822
36.42569	0.3541	34.59363	0.2447	34.63012	0.21992	35.70024	0.42235
38.56264	0.20442	35.37478	0.34519	35.32275	0.22631	36.49462	0.39821
42.91533	0.23032	36.39472	0.29174	36.40928	0.36498	40.84731	0.39348
50.78694	0.20654	36.94899	0.19451	36.94899	0.1947	41.64741	0.29138

53.14711	0.26898	40.62872	0.20688	40.65732	0.21172	44.32356	0.41367
53.57384	0.25719	41.41821	0.18228	41.43533	0.2098	48.2335	0.27369
56.63648	0.30146	42.86713	0.22608	42.89564	0.22551	49.27039	0.46958
62.1512	0.28788	44.14955	0.19009	44.05747	0.20333	53.80362	0.38616
73.47607	0.22906	47.70166	0.17999	47.72446	0.22554	54.62859	0.40144
		49.12526	0.2462	49.13442	0.33243	55.62767	0.42637
		53.13825	0.24595	53.15695	0.27279	56.99756	0.55618
		53.60448	0.26127	53.61784	0.22667	62.12822	0.4346
		54.73848	0.22755	54.49624	0.25305	63.71042	0.40108
		55.61352	0.18345	55.61352	0.16452		
		56.69613	0.46494	56.65617	0.3154		
		62.07319	0.37409	62.18402	0.30096		
		62.97094	0.24799	62.97094	0.30312		
		63.57563	0.29364	63.56598	0.23291		

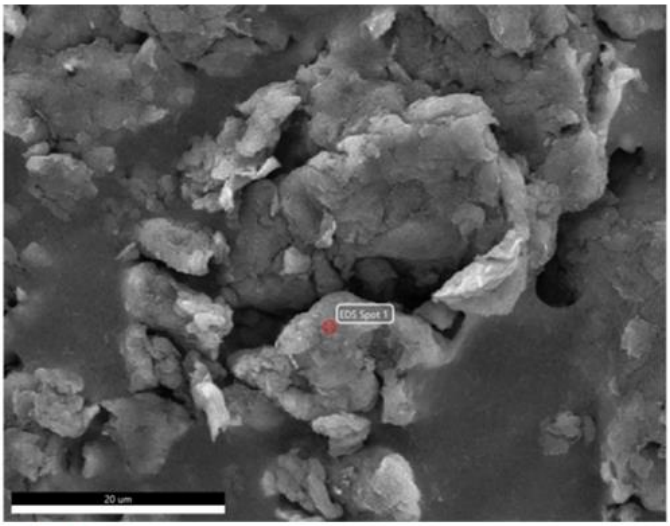

Element	Atomic %
C	69.9
O	36.1

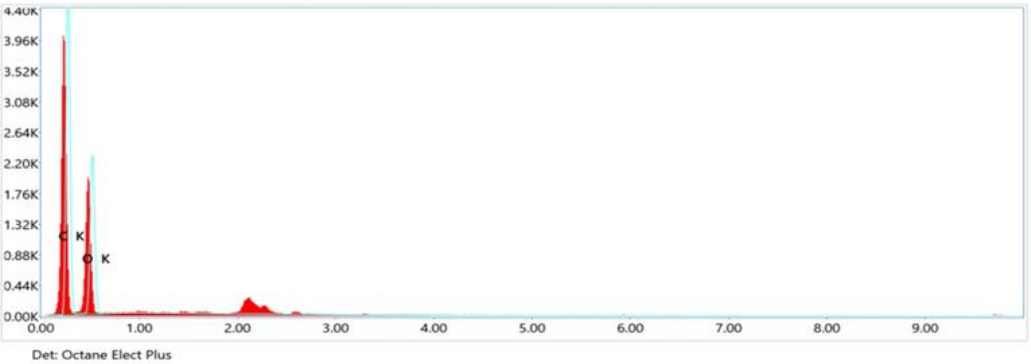

Figure S2. spot EDX of Graphene Oxide (GO).

Table S2. peak positions of XPS for ZTO, composite I, composite II, and composite III.

	Bonds	O1s	Bonds	C1s
ZTO	Lattice oxygen	530.19741	-	-
	O-H	531.93586	-	-
Composite I	Lattice oxygen	529.7632	C-C	284.52729
	O-H	531.57608	C-O-C	286.04897
			O=C-OH	288.21055
Composite II	Lattice oxygen	530.10684	C-C	284.88842
	O-H	531.59002	C-O-C	286.78724
			O=C-OH	288.71396
Composite III	Lattice oxygen	529.84924	C-C	284.50539
	O-H	531.66416	C-O-C	285.53575
			O=C-OH	288.12547
GO	C=O	533	C-C	284.90085
	C-O	531.9	C-O-C	287.03426
			O=C-OH	288.5

Table ST1. Crystalline size of NiZnO, NiZnO/GO1, and NiZnO/GO10

	NiZnO			NiZnO/GO1			NiZnO/GO10		
components	2θ (Degree)	FWHM (Degree)	crystalline size (nm)	2θ (Degree)	FWHM (Degree)	crystalline size (nm)	2θ (Degree)	FWHM (Degree)	crystalline size (nm)
ZnO	31.96	0.219	39.28	32.04	0.280	30.82	31.91	0.213	40.48
ZnO	34.63	0.228	38.09	34.71	0.270	31.51	34.58	0.217	39.98
ZnO	36.45	0.244	35.76	36.53	0.230	29.15	36.49	0.233	37.45
NiO	37.22	0.244	35.73	37.30	0.293	29.84	37.17	0.236	37.06
NiO	43.21	0.259	34.45	43.29	0.297	30.00	43.17	0.246	36.15
ZnO	47.74	0.274	33.06	47.82	0.306	29.62	47.70	0.252	35.89
ZnO	56.79	0.293	32.12	56.86	0.322	29.22	56.75	0.273	34.48
NiO	62.68	0.440	22.06	62.75	0.453	21.43	62.64	0.384	25.25
ZnO	66.57	0.295	33.59	66.63	0.309	32.07	66.53	0.271	36.57
ZnO	68.14	0.345	29.01	68.20	0.378	26.48	68.11	0.328	30.51
ZnO	69.28	0.340	29.63	69.33	0.351	28.66	69.24	0.314	32.02
NiO	75.07	0.368	28.40	75.13	0.378	27.64	75.04	0.350	29.85
ZnO	77.15	0.309	34.32	77.20	0.287	36.97	77.10	0.250	42.30
NiO	79.03	0.384	27.97	79.08	0.389	27.61	79.00	0.360	29.83
Average crystalline size (nm)	**NiO**		**29.7 ± 2.47**			**27.3 ±1.55**			**31.6 ± 2.20**
	ZnO		**33.9 ± 1.15**			**30.5 ±0.98**			**36.6 ± 1.30**

For calculation crystalline size were determined by using the Scherrer equation: -

$$D = \frac{k\lambda}{\beta\, Cos\theta}$$

where D is the crystalline size in nanometres,

λ is the wavelength of the radiation (0.154056 nm for CuKα radiation),

k is a constant equal to 0.94,

β is the peak width at half-maximum intensity (radian), and

θ is the half of peak position (radian).

Thesis outcomes

This thesis is based on the following publications, manuscripts and patent:

1. Synthesis and characterization of zinc titanate-graphene oxide composites prepared under ambient and hydrothermal conditions: **Sujeet Kumar Pandey**, Vipin Amoli, Amit Ranjan*, *Solid State Sciences*, Volume 166, 2025, 107969. https://doi.org/10.1016/j.solidstatesciences.2025.107969.

2. Photocatalytic performance of NiZnO/graphene oxide composites, towards visible light induced degradation of methylene blue dye: **Sujeet Kumar Pandey**, Bhupendra Kumar, V.S. Sistla, Amit Ranjan*, *Ceramics International,* https://doi.org/10.1016/j.ceramint.2025.11.325.

3. The effect of Mg-doping on the structural and electronic properties of $ZnTiO_3$: A first-principles study and compared with experimental band gap of $ZnTiO_3$: **Sujeet Kumar Pandey***, *Materials Research Express*, https://doi.org/10.1088/2053-1591/ae2430.

4. Improving zinc titanate dispersion in water and thereby its photocatalytic activity towards MB degradation by using custom designed plasma treatment set-up: **Sujeet Kumar Pandey,** Amit Ranjan*. **(Submitted to journal)**

5. Computational and experimental investigation of Cu doped $ZnTiO_3$ for photocatalytic applications, **Sujeet Kumar Pandey,** Amit Kumar Gomey, Rakesh Kumar, Amit Ranjan*. (**Submitted to journal**)

6. **Sujeet Kumar Pandey**, Aash Mohammad, Harikeshvar Pandey, Rohit Kumar Singh, Siddharth Atal, Indian design patent, Patent no.- 442388-001, 2024 (Granted).

Additional publication:

1. PVP assisted sol-electrospraying, unlike sol electrospinning, yields highly pure rhombohedral zinc titanate particles that reduce 4-nitrophenol under visible light, Yogendra Yadawa, Anil Verma, **Sujeet Kumar Pandey**, Amit Ranjan*, *Journal of Alloys and Compounds,* https://doi.org/10.1016/j.jallcom.2024.173618.

2. A transparent silicone tube coiled flow inverter impregnated with plasma treated zinc titanate particles on its inner surface as a novel continuous photocatalytic reactor, Anil Verma, **Sujeet Kumar Pandey**, K.D.P. Nigam, Amit Ranjan*,

Materials Science and Engineering: B, https://doi.org/10.1016/j.mseb.2025.119031.

List of Attended International Conferences/Workshop

International Conferences:

1. Poster presentation in Shaping the Energy Future: Challenges & Opportunities (SEFCO-2025) held at CSIR - Indian Institute of Petroleum, Dehradun, Uttarakhand, India.

   Title: - **Effect of doping with magnesium atoms on the properties of $ZnTiO_3$ by DFT study**

2. Oral presentation in International Conference on Renewable Energy with Sustainable Solutions (ICRESS 24) held at Department of Chemical Engineering Heritage Institute of Technology.

   Title: - **Prediction of enhanced photocatalytic activity in Cu doped ZnTiO3 by DFT study. (ISBN 978-93-340-9021-5)**

3. Oral presentation in Indian Institute of Chemical Engineers (IIChE)- Chemical Engineering Congress (CHEMCON 2023) held at Heritage Institute of Technology, Kolkata.

   Title: **- Plasma-treated zinc titanate with improved photocatalytic degradation of methylene blue under light emitting diodes (LEDs) (ISBN: 9789310 000719).**

4. Oral presentation in Indian Institute of Chemical Engineers (IIChE)- Chemical Engineering Congress (CHEMCON 2022) held at Harcourt Butler Technical University, Kanpur.

   Title: - **Zinc titanate/graphene oxide composites with improved photocatalytic activity for oxygen generation from water under visible light irradiation.**

5. Oral presentation at an international online conference on material science and technology (ICMT) organized by Mahatma Gandhi University, Kottayam, Kerala.

   Title: - **Photocatalytic hydrogen generation from water using $ZnTiO_3$ nanoparticles under visible light illumination.**

Workshop:

1. Attended one month workshop event on '**Density Functional Theory based Studies on Nanomaterials for Optoelectronic Devices**' at Chhattisgarh Swami Vivekanand Technical University (CSVTU), Bhilai, organized by the Centre for Skill Development and Informal Education (CSDIE) (2024).

2. Attended a one-week Karyashaala event on '**Quantum Chemical Calculations and Molecular Dynamics Simulations**' at the Department of Chemical Engineering, IIT Guwahati, sponsored by the Science and Engineering Research Board (SERB).

3. Attended a one-week workshop on '**Nanofiber technology and its commercial applications**' organized by E-Spin Nanotech in collaboration with MedTech, IIT Kanpur.

Awards and recognition:

1. Received third prize for idea titled '**Enhancing the properties of $ZnTiO_3$ for supercapacitor electrode material application**' in New Generation Ideation Contest-2023 organized by Hindustan Petroleum Green R & D Center.

2. Received '**Young Researcher Award-2024**' by scientific international publishing house.

Published Research Articles/Granted Patent

Research Paper 1

Solid State Sciences 166 (2025) 107969

Contents lists available at ScienceDirect

Solid State Sciences

journal homepage: www.elsevier.com/locate/ssscie

Synthesis and characterization of zinc titanate-graphene oxide composites prepared under ambient and hydrothermal conditions

Sujeet Kumar Pandey [a], Vipin Amoli [b], Amit Ranjan [a,*]

[a] Department of Chemical and Biochemical Engineering and Department of Basic Sciences and Humanities, Rajiv Gandhi Institute of Petroleum Technology, Jais, UP, 229304, India

[b] Department of Basic Sciences and Humanities, Rajiv Gandhi Institute of Petroleum Technology, Jais, UP, 229304, India

ARTICLE INFO

Keywords:
Graphene oxide
Zinc titanate
Hydrothermal

ABSTRACT

We prepare reduced graphene oxide-zinc titanate (ZTO) composite powders by mixing ZTO with 1 wt% graphene oxide (GO) in solid and liquid states under open environments, and under hydrothermal conditions. The treatment temperature was 400 °C in the first two cases and 180 °C in hydrothermal. Structural and chemical characterizations performed using XRD, SEM, BET, XPS, DRS, and PL are correlated with their photocatalytic performance. Mixing leads to significant structural and chemical changes in GO and ZTO particles but of different natures depending on the process. All the mixing routes reduce GO to r-GO. Unlike hydrothermal mixing, mixing under an open environment converts the rhombohedral $ZnTiO_3$ to cubic $Zn2TiO_4$ due to loss of oxygen. However, hydrothermal mixing leads to a loss in crystallinity of the $ZnTiO_3$ particles resulting into a larger specific surface area. XPS results suggest good binding between the r-GO sheets and the oxide particles. Liquid state mixing leads to the highest reduction in bandgap, probably due to maximal oxygen vacancy formation in this process. Mott-Schottky analysis is done to estimate the charge carrier density in all the samples. EIS shows that the hydrothermally prepared composite has the smallest R_{ct}. High surface area, less conversion to Zn_2TiO_4, changes in bandgap, good binding of ZTO with GO sheets, and more facile charge transfer in hydrothermally prepared composites have important implications in photocatalytic applications.

1. Introduction

Diverse categories of catalysts employed in photocatalysis include transition metal-centered complexes, organic photosensitizers, metal oxides, two-dimensional materials, quantum dots, and plasmonic metals [1,2]. Photocatalytic reactions involve charge generation on the catalyst and a subsequent charge transfer from the catalyst to the reacting species to trigger the desired reaction. Hence the concerned reactions are redox reactions. Metal oxides serve to be good photocatalytic materials because photogenerated electrons can help with reduction reactions, and holes in the valence band can help with oxidation reactions [3]. Moreover, metal oxides are the most prevalent minerals in the Earth's crust, resulting in lower prices relative to other wide-bandgap semiconductor materials. Certain metal oxides, like zinc oxide and tin oxide, demonstrate both conductivity and optical transparency, allowing the extensive application of transparent conducting oxides in optoelectronic devices [4,5]. Transparency to light and facile conduction of electrons are the features that make these metal oxide semiconductors especially attractive for optoelectronic processing.

The electron-hole generation depends on the bandgap, and it should be smaller than the photon energy, as it signifies the minimal energy necessary to elevate an electron to the conduction band, enabling its participation in electrical conductivity. For photocatalysis and photovoltaics, a more efficient absorption of solar light is preferable, one that spans a far broader spectrum of wavelengths. This deficiency is propelling the pursuit of broad-bandgap metal oxide materials exhibiting optical responses in the visible to near-infrared ranges. Bandgap in oxides has been engineered to adjust to the visible spectrum using several approaches such as varying processing conditions, particle size, [6–9] doping with metals, [10,11] non-metals, [12,13] and generation of vacancies [14,15]. Doping not only reduces the bandgap but also introduces new spectral characteristics in the visible to near-infrared ranges, hence enhancing overall absorption efficiency [16]. The investigation of emergent behavior via oxygen vacancy manipulation has catalyzed a surge of scientific interest [17–20].

To ensure that the diffusive transport occurs to the particle surface

* Corresponding author.
E-mail address: aranjan@rgipt.ac.in (A. Ranjan).

https://doi.org/10.1016/j.solidstatesciences.2025.107969
Received 20 January 2025; Received in revised form 9 April 2025; Accepted 12 May 2025
Available online 15 May 2025

ARTICLE IN PRESS

Ceramics International xxx (xxxx) xxx

Contents lists available at ScienceDirect

Ceramics International

journal homepage: www.elsevier.com/locate/ceramint

Photocatalytic performance of NiZnO/graphene oxide composites, towards visible light induced degradation of methylene blue dye

Sujeet Kumar Pandey, Bhupendra Kumar, Venkata Subbarayudu Sistla, Amit Ranjan *

Department of Chemical and Biochemical Engineering, Rajiv Gandhi Institute of Petroleum Technology, Jais, UP, 229304, India

ARTICLE INFO

Keywords:
NiO
ZnO
NiZnO
GO
Reduced GO
Visible light-induced photocatalysis
MB degradation

ABSTRACT

In this work, we prepare composites of NiO, ZnO, and GO with 1 % and 10 % GO and measure their photocatalytic activity in the MB degradation reaction under visible light illumination. The oxides are prepared by the sol-gel route, and GO is mixed using a hydrothermal method. The rate constant value in the 1 % GO and 10 % GO composites are, respectively, 1.76 and 2.35 times higher as compared to that in the binary composite of NiO-ZnO. The rate constants with our GO-based composites also compare favorably with previously reported composites. Structural and chemical characterizations performed using XRD, SEM, BET, XPS, DRS, and PL are correlated with their photocatalytic performance. It is found that GO is reduced in the composites to r-GO, and the NiO band gap decreases to the visible range, which we attribute to the bonding of the NiO particles with the GO sheets. We also propose that the composite forms a double heterojunction structure of r-GO/NiO/ZnO. Depending upon the work function difference between r-GO and NiO, which would depend on the extent of reduction of GO and extent of defect formation in NiO, the composite may form either a Type II p-n junction heterostructure or a direct Z-scheme heterostructure. In both possibilities the photogenerated charge separation is promoted. Therefore NiZnO/r-GO composite is a promising versatile material system for achieving photocatalytic degradation. Overall, we attribute the enhanced rate constants observed in our samples to the NiO band gap narrowing down to the visible range due to binding with the r-GO, causing higher carrier generation, and the formation of double heterostructures that leads to more effective carrier separation.

1. Introduction

Various kinds of catalysts utilized in photocatalysis include transition metal-centered complexes, organic photosensitizers, metal oxides, two-dimensional materials, quantum dots, and plasmonic metals [1,2]. Photocatalytic processes entail the creation of charge on the catalyst upon light illumination, followed by the transfer of this charge to the reacting species to initiate the desired reaction. Therefore, the overall processes being considered are redox reactions. However, photocatalysis involves multiple processes occurring on different timescales. The fastest processes (femtosecond charge generation and picosecond trapping) establish the initial charge-separated state. Intermediate processes (nanosecond recombination) represent competing loss pathways that reduce efficiency. The slowest processes (millisecond interfacial transfer) determine the overall photocatalytic rate and represent opportunities for improvement through surface modification or co-catalyst addition [3]. Photocatalytic efficiency can be increased by enhancing charge generation by light absorption using a suitable active material, achieving charge separation to minimize unproductive recombination pathways, and accelerating interfacial charge transfer.

Metal oxides are effective photocatalytic materials, as photogenerated electrons facilitate reduction events while holes in the valence band promote oxidation reactions [3–7]. Furthermore, metal oxides are the most abundant minerals in the Earth's crust, leading to reduced costs compared to other wide-bandgap semiconductor materials. Specific metal oxides, such as zinc oxide, titanium oxide, and nickel oxide, exhibit both conductivity and optical transparency, facilitating the widespread use of transparent conducting oxides in optoelectronic devices [8–10]. The characteristics of light transparency and efficient electron conduction render these metal oxide semiconductors very appealing for optoelectronic applications. Electron-hole creation is dependent upon the bandgap, which must be less than the photon energy, since its value indicates the minimum energy required to excite an electron to the conduction band. In photocatalysis and photovoltaics, enhanced absorption of solar light throughout a significantly wider spectrum of wavelengths is desirable. This shortcoming is driving the

* Corresponding author.
E-mail address: aranjan@rgipt.ac.in (A. Ranjan).

https://doi.org/10.1016/j.ceramint.2025.11.325
Received 19 September 2025; Received in revised form 4 November 2025; Accepted 23 November 2025
Available online 24 November 2025

Please cite this article as: Sujeet Kumar Pandey et al., *Ceramics International,* https://doi.org/10.1016/j.ceramint.2025.11.325

IOP Publishing *Mater. Res. Express* **12** (2025) 126301 https://doi.org/10.1088/2053-1591/ae2430

Materials Research Express

OPEN ACCESS

RECEIVED
8 September 2025

REVISED
5 November 2025

ACCEPTED FOR PUBLICATION
25 November 2025

PUBLISHED
3 December 2025

PAPER

The effect of Mg-doping on the structural and electronic properties of $ZnTiO_3$: a first-principles study and compared with experimental band gap of $ZnTiO_3$

Sujeet Kumar Pandey*

Department of Chemical and Biochemical Engineering, Rajiv Gandhi Institute of Petroleum Technology, Jais, Amethi 229304, India

* Author to whom any correspondence should be addressed.

E-mail: 20ce0012@rgipt.ac.in

Keywords: $ZnTiO_3$, Mg doped $ZnTiO_3$, band-gap engineering, density function theory

Abstract

This paper shows a detailed analysis of the structural and electronic properties of pure zinc titanate ($ZnTiO_3$) and magnesium (Mg)-doped $ZnTiO_3$ ($Zn_{1-x}Mg_xTiO_3$, where x = 0.167, 0.333, 0.5, and 0.667) and compared with experimental band gap of $ZnTiO_3$. We conducted the analysis using first-principles and density-functional-theory calculations using the Quantum Espresso package. The objective was to investigate the effect of Mg substitution on zinc titanate $ZnTiO_3$. In the pure $ZnTiO_3$ system, calculations reveal an indirect electronic structure gap. At a doping level of 0.333, $ZnTiO_3$ with Mg impurities have an indirect electronic structure gap of 1.81 electron volts (eV). The investigation of structural and electronic characteristics indicates that x = 0.333 Mg doped $ZnTiO_3$ significantly reduce the electronic structure gap of $ZnTiO_3$ while maintaining the same kind of electronic structure gap, which is an indirect electronic structure gap. The density functional theory study shows that Mg substitution in $ZnTiO_3$ change their electronic structure and density of states and experimental band gap is nearly same as computational band structure gap which validates the exchange–correlation treatment and pseudopotentials employed for the band-structure calculation for this system.

1. Introduction

The zinc titanate $ZnTiO_3$ has recently gained significant interest because of its superior microwave dielectric, and photocatalysis, making it a crucial ceramic compound [1–4]. In addition, nanotechnology has prioritized significant advancements in the process of semiconductor nanomaterials utilized in photocatalytic applications [5–7]. Furthermore, the advancement of renewable energy sources has generated significant interest in the application of prepared photocatalytic technology due to its high conversion efficiency and low manufacturing cost [1, 8]. The metal oxide layers, including Al_2O_3, TiO_2, ZnO, SiO_2, MgO_2, and $ZnTiO_3$, have been utilized as energy barriers to prevent charge recombination [6], [9–13]. Conversely, it is widely recognized that charge recombination results in the depletion of charge carriers, thereby reducing the photocatalytic efficiency. Scientists are currently researching the findings for additional properties and potential uses for $ZnTiO_3$ ceramics. Their profound enthusiasm for theoretical inquiry enables them to determine the approximate behavior of materials, while experimental studies aid in the more precise characterization of the substance. We combined these studies with the exploration of structural and electrical characteristics. In this work, we have specifically examined the alteration of characteristics resulting from doping. Several extensive studies have been conducted on $ZnTiO_3$. Researchers have shown significant interest in the $ZnTiO_3$ alteration. Researchers subject the compound $ZnTiO_3$ to doping with donor atoms and subsequently analyze its different characteristics. Doping induces a significant alteration in physical behavior and modifies features associated with the internal structure of $ZnTiO_3$. Researchers have conducted extensive studies on $ZnTiO_3$. In the ABO_3 structure of $ZnTiO_3$, Zn (Zinc) occupies the A site, and Ti (Titanium) occupies the B site. Doping mostly occurs

Patent

INTELLECTUAL PROPERTY INDIA
PATENTS | DESIGNS | TRADE MARKS
GEOGRAPHICAL INDICATIONS

सत्यमेव जयते

ORIGINAL
क्रम सं/ Serial No. : 193488

पेटेंट कार्यालय, भारत सरकार **The Patent Office, Government Of India**

डिजाइन के पंजीकरण का प्रमाण पत्र | Certificate of Registration of Design

डिजाइन सं. / Design No.	:	442388-001
तारीख / Date	:	28/12/2024
पारस्परिकता तारीख / Reciprocity Date*	:	
देश / Country	:	

प्रमाणित किया जाता है कि संलग्न प्रति में वर्णित डिजाइन जो *SOLAR-POWERED PHOTOCATALYTIC REACTOR* से संबंधित है, का पंजीकरण, श्रेणी 24-02 में 1.Mr. Sujeet Kumar Pandey 2. Mr. Aash Mohammad 3.Mr. Harikeshvar Pandey 4.Mr. Rohit Kumar Singh 5.Mr. Siddharth Atal के नाम में उपर्युक्त संख्या और तारीख में कर लिया गया है।

Certified that the design of which a copy is annexed hereto has been registered as of the number and date given above in class 24-02 in respect of the application of such design to *SOLAR-POWERED PHOTOCATALYTIC REACTOR* in the name of 1.Mr. Sujeet Kumar Pandey 2. Mr. Aash Mohammad 3.Mr. Harikeshvar Pandey 4.Mr. Rohit Kumar Singh 5.Mr. Siddharth Atal.

डिजाइन अधिनियम, 2000 तथा डिजाइन नियम, 2001 के अध्यधीन प्रावधानों के अनुसरण में।

In pursuance of and subject to the provisions of the Designs Act, 2000 and the Designs Rules, 2001.

जारी करने की तिथि : 27/02/2025
Date of Issue :

महानियंत्रक पेटेंट, डिजाइन और व्यापार चिह्न
Controller General of Patents, Designs and Trade Marks

*पारस्परिकता तारीख (यदि कोई हो) जिसकी अनुमति दी गई है तथा देश का नाम। डिजाइन का स्वत्वाधिकार पंजीकरण की तारीख से दस वर्षों के लिए होगा जिसका विस्तार, अधिनियम एवं नियम के निबंधनों के अधीन, पाँच वर्षों की अतिरिक्त अवधि के लिए किया जा सकेगा। इस प्रमाण पत्र का उपयोग विधिक कार्यवाहियों अथवा विदेश में पंजीकरण प्राप्त करने के लिए नहीं हो सकता है।

The reciprocity date (if any) which has been allowed and the name of the country. Copyright in the design will subsist for ten years from the date of Registration, and may under the terms of the Act and Rules, be extended for a further period of five years. This Certificate is not for use in legal proceedings or for obtaining registration abroad.

Curriculum vitae (CV)

Sujeet Kumar Pandey

+91-9685225095 | 20ce0012@rgipt.ac.in |
https://www.linkedin.com/in/sujeet-kumar-pandey-b2517092 |

EDUCATION

Doctor of Philosophy, Material Science 2020-Present
Rajiv Gandhi Institute of Petroleum Technology, Jais CPI: 8.4
Bahadurpur, Jais, Amethi, India-229304
Supervisor: -Prof. Amit Ranjan
Thesis: - **Design of composite materials for achieving enhanced photocatalytic performance under visible light and supercapacitor applications by using DFT calculations and various synthesis methods.**

Master of Technology, Material Science and Technology 2018-2020
National Institute of Technology, Kurukshetra CGPA: 8.9
Haryana, India-136119
Supervisor: - Dr. Yashashchandra Dwivedi
Co-supervisor: - Dr. Avanish Kumar Srivastava
Thesis: - **Study of graphene oxide and reduced graphene oxide for microwave absorption**

Bachelor of Engineering, Production Engineering 2012-2016
Lakshmi Narain College of Technology and Science affiliated to Percentage: 73%
Rajiv Gandhi Proudyogiki Vishwavidyalaya, Bhopal
India-462033

Publications/Patent

1. Synthesis and characterization of zinc titanate-graphene oxide composites prepared under ambient and hydrothermal conditions; Sujeet Kumar Pandey, Vipin Amoli, Amit Ranjan; Solid State Sciences, Volume 166, 2025, 107969, https://doi.org/10.1016/j.solidstatesciences.2025.107969.

2. Photocatalytic performance of NiZnO/graphene oxide composites, towards visible light induced degradation of methylene blue dye: **Sujeet Kumar Pandey**, Bhupendra Kumar, V.S. Sistla, Amit Ranjan*, Ceramics International, https://doi.org/10.1016/j.ceramint.2025.11.325.

3. The effect of Mg-doping on the structural and electronic properties of ZnTiO3: A first-principles study and compared with experimental band gap of ZnTiO3: **Sujeet Kumar Pandey***, Materials Research Express, https://doi.org/10.1088/2053-1591/ae2430.

4. PVP assisted sol-electrospraying, unlike sol electrospinning, yields highly pure rhombohedral zinc titanate particles that reduce 4-nitrophenol under visible light; Yogendra Yadawa, Anil Verma, **Sujeet Kumar Pandey**, Amit Ranjan; Journal of Alloys and Compounds, Volume 981,2024,173618, ISSN 0925-8388, https://doi.org/10.1016/j.jallcom.2024.173618.

5. A transparent silicone tube coiled flow inverter impregnated with plasma treated zinc titanate particles on its inner surface as a novel continuous photocatalytic reactor, Anil Verma, **Sujeet Kumar Pandey**, K.D.P. Nigam, Amit Ranjan*, Materials Science and Engineering: B, https://doi.org/10.1016/j.mseb.2025.119031.

6. Improving zinc titanate dispersion in water and thereby its photocatalytic activity towards MB degradation by using custom designed plasma treatment set-up; **Sujeet Kumar Pandey**, Amit Ranjan (Under Review).

7. **Sujeet Kumar Pandey**, Aash Mohammad, Harikeshvar Pandey, Rohit Kumar Singh, Siddharth Atal, Indian design patent, Patent no.- 442388-001, 2024 (Granted).

Conference/Workshop Attended

1. Attended SIESTA School 2024 organized by Catalan Institute of Nanoscience and Nanotechnology, Barcelona, Spain.
2. Attended one month workshop event on '**Density Functional Theory based Studies on Nanomaterials for Optoelectronic Devices'** at Chhattisgarh Swami Vivekanand Technical University (CSVTU), Bhilai, organized by the Centre for Skill Development and Informal Education (CSDIE).
3. Oral presentation in International Conference on Renewable Energy with Sustainable Solutions (ICRESS 24) held at Department of Chemical Engineering Heritage Institute of Technology.

   Title: - **Prediction of enhanced photocatalytic activity in Cu doped ZnTiO3 by DFT study. (ISBN 978-93-340-9021-5)**
4. Attended a one-week Karyashaala event on '**Quantum Chemical Calculations and Molecular Dynamics Simulations'** at the Department of Chemical Engineering, IIT Guwahati, sponsored by the Science and Engineering Research Board (SERB).
5. Oral presentation in Indian Institute of Chemical Engineers (IIChE)- Chemical Engineering Congress (CHEMCON 2023) held at Heritage Institute of Technology, Kolkata.

   Title: - **Plasma-treated zinc titanate with improved photocatalytic degradation of methylene blue under light emitting diodes (LEDs) (ISBN: 9789310 000719).**
6. Attended a one-week workshop on '**Nanofiber technology and its commercial applications'** organized by E-Spin Nanotech in collaboration with MedTech, IIT Kanpur.
7. Oral presentation in Indian Institute of Chemical Engineers (IIChE)- Chemical Engineering Congress (CHEMCON 2022) held at Harcourt Butler Technical University, Kanpur.

   Title: - **Zinc titanate/graphene oxide composites with improved photocatalytic activity for oxygen generation from water under visible light irradiation.**
8. Oral presentation at an international online conference on material science and technology (ICMT) organized by Mahatma Gandhi University, Kottayam, Kerala.

   Title: - **Photocatalytic hydrogen generation from water using $ZnTiO_3$ nanoparticles under visible light illumination.**
9. Poster presentation at a national conference on nanoscience and instrumentation technology organized by NIT Kurukshetra.

   Title: - **Study of graphene-based ink for radar radiation absorption.**
10. poster presentation at the international conference CHEMBIOEN (CHEMICAL, BIO, AND ENVIRONMENTAL ENGINEERING) organized by the chemical engineering department in NIT Jalandhar.

    Title: - **Study of piezoelectric material for energy harvesting.**

Technical Skills

1. **Experimental**: - Synthesis of composite semiconductor, Photocatalytic experiments, Kinetics studies of pollutants degradation.
2. **Instruments**: - Electron Beam Evaporation Beam Deposition, Rheometer, Electrospinning, Plasma treatment equipment, UV-VIS spectroscopy, Universal Testing Machine.
3. **Software**: - Quantum Espresso, Material Studio, Gaussian, Origin, MS Office.
4. **Mentoring**: - Mentored five undergraduate projects.

Academic Achievements

1. Received third prize for idea titled **'Enhancing the properties of $ZnTiO_3$ for supercapacitor electrode material application'** in New Generation Ideation Contest-2023 organized by Hindustan Petroleum Green R & D Center.
2. Internship in Defence Laboratory Jodhpur (DLJ) – DRDO.
   Title: - **graphene-based advance material for microwave/radar absorption**
3. Secured an All India Rank 314 in **GATE** (Graduate Aptitude Test in Engineering) 2018.
4. Internship in INDIAN RAILWAY (Diesel Locomotive).
   Title: - **Fuel Injection system.**